

## Metal sulfides for gas sensing applications: devices and mechanisms

Tang, Hongyu

**DOI**

[10.4233/uuid:c2137466-cdb5-42c4-9303-85e64b87acd5](https://doi.org/10.4233/uuid:c2137466-cdb5-42c4-9303-85e64b87acd5)

**Publication date**

2020

**Document Version**

Final published version

**Citation (APA)**

Tang, H. (2020). *Metal sulfides for gas sensing applications: devices and mechanisms*. [Dissertation (TU Delft), Delft University of Technology]. <https://doi.org/10.4233/uuid:c2137466-cdb5-42c4-9303-85e64b87acd5>

**Important note**

To cite this publication, please use the final published version (if applicable).  
Please check the document version above.

**Copyright**

Other than for strictly personal use, it is not permitted to download, forward or distribute the text or part of it, without the consent of the author(s) and/or copyright holder(s), unless the work is under an open content license such as Creative Commons.

**Takedown policy**

Please contact us and provide details if you believe this document breaches copyrights.  
We will remove access to the work immediately and investigate your claim.

**METAL SULFIDES FOR GAS SENSING  
APPLICATIONS: DEVICES AND MECHANISMS**



# **METAL SULFIDES FOR GAS SENSING APPLICATIONS: DEVICES AND MECHANISMS**

## **Proefschrift**

ter verkrijging van de graad van doctor  
aan de Technische Universiteit Delft,  
op gezag van de Rector Magnificus Prof.dr.ir. T.H.J.J. van der Hagen,  
voorzitter van het College voor Promoties,  
in het openbaar te verdedigen op maandag 15 juni 2020 om 12:30 uur

door

**Hongyu TANG**

Master of Science in Mechatronic Engineering,  
Guilin University of Electronic Technology, China  
geboren te Guilin, China.



致 我的父母

*To my parents*

*Youfa Tang, Qiulian Chen*



# CONTENTS

<b>Summary</b>	<b>xi</b>
<b>Samenvatting</b>	<b>xv</b>
<b>1 Introduction</b>	<b>1</b>
1.1 Background	2
1.2 Gas sensing transducers	3
1.2.1 Optical gas sensor	3
1.2.2 Physical gas sensors	4
1.2.3 Electrical gas sensors	5
1.3 Nanostructured materials-based gas sensor	7
1.3.1 Metal oxide-based nanomaterials for gas sensing	7
1.3.2 Carbon-based nanomaterials for gas sensing	9
1.3.3 Metal sulfide-based nanomaterials for gas sensing	10
1.4 Aim and scope of this dissertation	11
1.5 Outline of this dissertation	12
References	13
<b>2 Metal sulfide-based gas sensor: State-of-the-art</b>	<b>19</b>
2.1 Metal sulfide characteristics	20
2.2 Preparation methods for metal sulfide nanomaterials	21
2.2.1 Top-down approaches	21
2.2.2 Bottom-up strategies	24
2.3 Device fabrication	26
2.3.1 Suspension method	26
2.3.2 Transfer method	27
2.4 Sensing parameters	27
2.5 Various sensing concept of metal sulfide-based devices	29
2.5.1 Chemiresistor gas sensors	29
2.5.2 Schottky diode	32
2.5.3 Heterojunctions based gas sensor	33
2.5.4 Field-effect transistors (FETs)	35
2.6 Metal sulfides-based devices for NO <sub>2</sub> and humidity sensing applications	36
2.6.1 Nitric dioxide (NO <sub>2</sub> ) sensors	36
2.6.2 Humidity sensors	38
2.7 Conclusions	39
References	40

<b>3</b>	<b>SnS nanoflakes-based Schottky contacted humidity sensor</b>	<b>53</b>
3.1	Introduction . . . . .	54
3.2	Design and fabrication . . . . .	54
3.3	Characterization . . . . .	55
3.4	Humidity sensing performances . . . . .	56
3.5	Humidity sensing mechanism. . . . .	60
3.5.1	First principle analysis . . . . .	60
3.5.2	Schottky barrier analysis . . . . .	63
3.6	Applications . . . . .	63
3.6.1	Respiration monitoring . . . . .	63
3.6.2	Movement of fingertip . . . . .	65
3.6.3	A smart home system based on SnS nanoflakes-based sensor . . . . .	66
3.7	Conclusion . . . . .	67
	References . . . . .	68
<b>4</b>	<b>SnO<sub>x</sub>/SnS heterostructures gas sensor</b>	<b>71</b>
4.1	Introduction . . . . .	72
4.2	Fabrication of gas sensors . . . . .	73
4.3	Humidity sensing performances . . . . .	73
4.4	NO <sub>2</sub> gas sensing performance . . . . .	75
4.4.1	Characterization . . . . .	75
4.4.2	Gas sensing properties . . . . .	79
4.5	Gas sensing mechanism . . . . .	81
4.5.1	Computational methods . . . . .	81
4.5.2	Computational results . . . . .	82
4.6	Conclusion . . . . .	85
	References . . . . .	85
<b>5</b>	<b>WS<sub>2</sub>/IGZO heterojunction gas sensor</b>	<b>89</b>
5.1	Introduction . . . . .	90
5.2	Theoretical study of WS <sub>2</sub> /IGZO heterostructure . . . . .	91
5.2.1	Computational methods . . . . .	91
5.2.2	Tunable electrical and optical properties . . . . .	92
5.2.3	Gas sensing properties . . . . .	100
5.3	NO <sub>2</sub> gas sensor based on CVD-WS <sub>2</sub> /IGZO p-N heterojunction . . . . .	101
5.3.1	Design and fabrication . . . . .	101
5.3.2	Characterization . . . . .	103
5.3.3	Gas sensing properties of WS <sub>2</sub> /IGZO chemiresistor . . . . .	105
5.3.4	Gas sensing properties of WS <sub>2</sub> /IGZO TFT . . . . .	109
5.3.5	Gas sensing mechanism . . . . .	111
5.4	Conclusions . . . . .	114
	References . . . . .	115
<b>6</b>	<b>Conclusion and Recommendation</b>	<b>121</b>
	References . . . . .	124

---

<b>A</b>	<b>Appendix A</b>	<b>125</b>
A.1	Calculation methods . . . . .	125
A.2	Data of LOD calculation for SnO <sub>x</sub> /SnS sensor . . . . .	126
A.3	Data of LOD calculation for WS <sub>2</sub> /IGZO gas sensor . . . . .	127
	<b>Acknowledgements</b>	<b>129</b>
	<b>Curriculum Vitæ</b>	<b>133</b>
	<b>List of Publications</b>	<b>135</b>



# SUMMARY

Nanostructured materials have attracted more and more attention in the applications of gas sensing due to their high specific surface area, numerous surface-active sites, as well as the effect of crystal facets with high surface reactivity. These kinds of gas sensors are mainly used for detecting air quality, environment situation, and breath analysis. Among different gas sensors, metal sulfide-based sensors have generated considerable interest in recent years because of their excellent sensitivity, fast response, and good selectivity. Alternatively, driven by the increasing demand for environmental and health monitoring, the sensors are required to have low limit of detection (LOD) in ppb-level, higher response and selectivity, and real-time recording. There are several ways to improve the sensing performance, such as functionalizing metal sulfide (defects, dopants), constructing heterojunction (Schottky junction, p-n, n-n, and p-p semiconductor junction), and using field-effect transistor (FET) gas sensor. Herein, my research aims to explore high-performance gas sensors through these techniques and to research the fundamental mechanism of the gas sensing process for metal sulfides devices.

A comprehensive literature review of the state-of-the-art of metal sulfide-based gas sensor is presented in chapter 2. It includes the basic crystal structures, synthesis methods, device fabrication methods, and the gas sensing performances of various metal sulfide-based gas sensors. Since metal sulfides have a shallow valence band and different shapes, sizes, crystalline forms, chemical compositions, they have excellent sensing performance. It is found that the devices based on Schottky diode, metal oxide/metal sulfide heterojunction, and transistor have enhanced gas-sensing performance. Thus in this work, I analyzed the sensing behaviour of an SnS-Ti Schottky contact humidity sensor, an SnO<sub>x</sub>/SnS heterostructures-based NO<sub>2</sub> gas sensor with rich oxygen vacancies, and a WS<sub>2</sub>/IGZO-based thin film transistor for NO<sub>2</sub> gas sensing.

To improve the humidity sensing performance, an SnS-Ti Schottky-contacted sensor is designed and analyzed in chapter 3. The SnS nanoflakes were mechanically exfoliated and then transferred on a rigid or flexible substrate. The as-fabricated sensor exhibited high response of 67600% towards 10% RH and 2491000% towards 99% RH, wide RH range from 3% RH to 99% RH, and fast response/recovery time of 6 s /4 s. The flexible humidity sensor shows a similar performance. Through the density functional theory (DFT) analysis and band alignment analysis, it is found that excellent sensing performance is attributed to the Schottky nature of SnS-Ti contact. H<sub>2</sub>O absorption moves the Fermi level of SnS toward the conduction band, decreasing the Schottky barrier ( $\phi_B$ ) by  $\Delta\phi_B$ , resulting in thinning of the  $\phi_B$  and an increase of the device current. Different relative humidity levels induce different  $\Delta\phi_B$  and sensitivity. The recovery mechanism is also attributed to the  $\phi_B$ . When air flows out of the chamber, the water molecule shifts from the adsorption sites, and the conductivity decreases due to the increased  $\phi_B$ . To extend the device's application, a smart home system based on the sensors is proposed to process the signal from breath and finger touch experiments for noncontact controlling and respiration monitoring.

To further improve the LOD and sensitivity for humidity and NO<sub>2</sub> gas, four types of SnS-based gas sensors, including liquid phase exfoliated (LPE) SnS nanosheets, SnO<sub>2</sub> nanosheets, SnO<sub>2</sub>/SnS nanocomposites, and SnO<sub>x</sub>/SnS heterostructure, are explored and comparatively analyzed in chapter 4. The results show that the sensor based on SnO<sub>x</sub>/SnS heterostructure that formed by the post-oxidation of LPE-SnS nanosheets in air, has excellent humidity sensing response among these four types of sensors. Accordingly, the SnO<sub>x</sub>/SnS is also used for detecting NO<sub>2</sub> gas, which exhibits a high response of 161% towards 1 ppb NO<sub>2</sub>, wide detecting range (from 1 ppb to 1 ppm), an ultra-low theoretical LOD of 5 ppt, and excellent repeatability. To the best of my knowledge, such a LOD is the lowest among metal sulfide-based and metal oxide-based gas sensors. The sensor also shows excellent gas selectivity to NO<sub>2</sub> with comparison to several other gas molecules, such as NO, H<sub>2</sub>, CO, NH<sub>3</sub>, and H<sub>2</sub>O. The gas sensing mechanism analysis based on experiments and DFT calculations reveals that oxygen vacancies provide more adsorption sites, superior band gap modulation, and more active charge transfer in the sensing interface layer.

Metal oxide/metal sulfide heterojunction is a great potential candidate for gas sensing applications. Thus we vertically stacked a p-type narrow bandgap semiconductor (WS<sub>2</sub>) and an N-type wide bandgap semiconductor (IGZO) to form a type I heterojunction WS<sub>2</sub>/IGZO in chapter 5. The straddling gap results in both electrons and holes accumulating on the same side, and sensitive to the external stimulations. First of all, the structural, electronic, and optical properties of WS<sub>2</sub>/IGZO heterostructure are analyzed by DFT calculation under different E-field, mechanical strain, and gas molecules. The results demonstrate that the band gap of WS<sub>2</sub>/IGZO heterostructure shows a near-linear decrease with the increase of the E-field both in the negative and positive direction, resulting in a semiconductor-metal transition, revealing an application for the FET. The heterostructure exhibits broad spectral responsivity (from visible light to deep UV wavelengths) and enhanced optical properties under mechanical strain. The tensile strain can weaken the photoresponse of the heterostructure to the UV light and improve the response for the visible light; while for compressive strain, the heterostructure shows a sharp absorption peak in UV light. Moreover, the gas adsorption energy of NH<sub>3</sub> and NO<sub>2</sub> on the WS<sub>2</sub>/IGZO heterostructure are calculated, which shows high gas adsorption energy with NO<sub>2</sub>, indicating the potential application in NO<sub>2</sub> gas sensor.

The unique and tunable properties based on DFT calculation endow that the WS<sub>2</sub>/IGZO heterostructure is a good candidate for transistor and gas sensors. Thus, CVD-WS<sub>2</sub>/IGZO heterojunction-based devices are designed and investigated in two modes, chemiresistor, and transistor mode. The device has a maximum response of 18170% in the chemiresistor mode, and 499400% in the transistor mode under 300 ppm NO<sub>2</sub> after applying -20 V gate bias. The heterojunction device is much better than that of only WS<sub>2</sub> and IGZO. Moreover, the sensor shows excellent gas selectivity toward NO<sub>2</sub> with comparison to several gas vapors such as CO, NH<sub>3</sub>, and humidity. The superior gas sensing performance could benefit from the heterojunction of WS<sub>2</sub> and IGZO and the external electric field under the back gate voltage. In addition, the transistor notably presents a typical ambipolar-behaviour under dry air, while the transistor becomes p-type as the amount of NO<sub>2</sub> increases. The mobility, on/off ratio, and subthreshold slope of the device is modulated by the NO<sub>2</sub> gas concentration. The unique tunable behaviour can be associated with the doping effects of NO<sub>2</sub> on the heterojunction and the modulated Schottky barrier value at the WS<sub>2</sub> and IGZO

with a metal contact interface.

This thesis is concluded with summarizing the main obtained results and providing suggestions for future research opportunities in the field of 2D/nano- metal sulfides materials-based devices. The research for 2D/nanomaterials based device is still at an early stage. It is full of challenges to exploring high-quality materials suitable for gas sensors to guarantee the reliability and long-term stability of the device, to evaluate/test the sample accurately, and to integrate the sensor with the existing system. These fundamental research challenges need to be resolved in the future.



# SAMENVATTING

Nano gestructureerd materiaal krijgt steeds meer aandacht in toepassingen van gas detectie vanwege de hoge specifieke oppervlakte, aantal oppervlakte-actieve plaatsen en het effect van kristal facetten met hoge oppervlakte reactiviteit. Dit type gas sensor wordt voornamelijk gebruikt voor het detecteren van lucht kwaliteit, omgeving situatie en adem analyse. Van de verschillende gas sensoren hebben de metaal sulfide gebaseerde sensors een aanzienlijke interesse gegenereerd over de jaren vanwege de excellente gevoeligheid, snelle respons en goede selectiviteit. Daarnaast neemt de vraag naar milieu en gezondheid monitoring toe, waarbij sensoren een laag detectie limiet op ppb niveau, hogere respons en selectiviteit en real-time registratie dienen te hebben. Er zijn verschillende manieren om de detectie prestatie te verbeteren zoals het functionaliseren van metaal sulfide (defecten, doteermiddelen), het construeren van heterojuncties (Schottky junctie, p-n, n-n en p-p halfgeleider juncties) en het gebruiken van veld-effect transistors (FET) gas sensors. Hierin richt mijn onderzoek zich op het verkennen van hoge-prestatie gas sensors door middel van deze technieken en het uitzoeken van de fundamentele mechaniek van het gas detectie proces voor metaal sulfide apparaten.

Als eerste is een uitgebreid literatuur onderzoek naar de nieuwste metaal sulfide gebaseerde gas sensor gepresenteerd in deze thesis. Het bevat de basis kristal structuren, synthese methoden, fabricatie methoden van het apparaat en de gas detectie prestatie van verschillende metaal sulfide gebaseerde gas sensors. Aangezien metaal sulfides een lage valentie band, verschillende vormen, groottes, kristal vormen en chemische composities hebben, is de gas detectie prestatie excellent. Na het vergelijken van de gas detectie prestatie van verschillende op metaal sulfide gebaseerde gas sensors, is gebleken dat de apparaten gebaseerd op de Schottky diode, metaal oxide/metaal sulfide heterojunctie en transistor een verbeterde gas detectie prestatie hebben. Ik heb daarom in dit werk het detectie gedrag van de SnS-Ti Schottky contact luchtvochtigheid sensor geanalyseerd en gebruik gemaakt van  $\text{SnO}_x/\text{SnS}$  heterostructuren met overvloedige OV's om de  $\text{NO}_2$  detectie respons te verhogen en de LOD te verlagen. Tenslotte is een op  $\text{WS}_2/\text{IGZO}$  heterojunctie gebaseerde dunne film transistor voorgesteld ten behoeve van het verbeteren van de prestaties voor  $\text{NO}_2$  gas detectie.

Om de luchtvochtigheid detectie te verbeteren, is een SnS-Ti Schottky gecontacteerde sensor ontworpen en gefabriceerd. De SnS nano vlokken werden mechanisch geëxfolieerd en vervolgens getransfereerd op een stug of flexibel substraat. The gefabriceerde sensor toonde een hoge response van 67600% richting 10% RH en 2491000% richting 99% RH, groot RH bereik van 3% RH tot 99% RH en snelle response/herstel tijd van 6 s/4 s. De flexibele luchtvochtigheid sensor laat een vergelijkbare prestatie zien. Gebruik makend van de dichtheidsfunctionaaltheorie (DFT) analyse en band uitlijning analyse, werd gevonden dat de excellente detectie prestatie is toegeschreven aan het Schottky gedrag van het SnS-Ti contact.  $\text{H}_2\text{O}$  absorptie verplaatst het Fermi niveau van SnS richting de conductie band, wat de Schottky barrière ( $\phi_B$ ) verlaagt met  $\Delta\phi_B$ , wat resulteert in een dunnere  $\phi_B$  en een

verhoogde apparaat stroom. Verschillende RH niveaus induceren verschillende  $\Delta\phi_B$  en gevoeligheid. Het herstel mechanisme is ook toegerekend aan de  $\phi_B$ . Wanneer lucht uit de kamer stroomt, verplaatsen de water moleculen van de adsorptie locaties en wordt de geleiding verlaagd vanwege een verhoogde  $\phi_B$ . Om de toepassingen van het apparaat te verbreden, werd een smart home systeem gebaseerd op de sensors voorgesteld om het signaal te verwerken van adem en vinger aanraking experimenten voor contactloze controle en ademhaling monitoring.

Om het detectie limiet van gas detectie response voor luchtvochtigheid en  $\text{NO}_2$  gas te verbeteren, zijn vier typen op SnS gebaseerde gas sensors verkend en vergeleken, met inbegrip van vloeibare fase geëxfolieerde (LPE) SnS nano vellen,  $\text{SnO}_2$  nano vellen,  $\text{SnO}_2/\text{SnS}$  nano composieten en  $\text{SnO}_x/\text{SnS}$  heterostructuren. De resultaten laten zien dat de sensor gebaseerd op de  $\text{SnO}_x/\text{SnS}$  heterostructuur die geformeerd is bij de post-oxidatie van LPE-SnS nano vellen in lucht, de meest excellente luchtvochtigheid detectie response heeft van de vier typen sensor. Daarnaast is  $\text{SnO}_x/\text{SnS}$  ook gebruikt voor  $\text{NO}_2$  gas detectie, wat een hoge respons van 161% richting 1 ppb  $\text{NO}_2$  toont, breed detectie bereik (van 1 ppb tot 1 ppm), een ultra laag theoretisch detectie limiet van 5 ppt en excellente herhaalbaarheid. Naar mijn beste weten is dit detectie limiet de laagste onder de op metaal sulfide en metaal oxide gebaseerde gas sensors. De sensor toont ook een superieure gas selectiviteit naar  $\text{NO}_2$  in vergelijking met verschillende andere gas moleculen, zoals  $\text{NO}$ ,  $\text{H}_2$ ,  $\text{CO}$ ,  $\text{NH}_3$  en  $\text{H}_2\text{O}$ . De gas detectie mechanisme analyse gebaseerd op experimenten en DFT berekeningen, onthult dat zuurstof leegtes zorgen voor meer adsorptie locaties, superieure band kloof modulatie en meer actieve lading overdracht in de detectie interface laag.

Metaal oxide/metaal sulfide heterojuncties zijn een geweldige potentiële kandidaat voor gas detectie applicaties. Daarom hebben we een p-type smalle band kloof halfgeleider ( $\text{WS}_2$ ) en een n-type brede band kloof halfgeleider (IGZO) verticaal gestapeld, om een type I heterojunctie  $\text{WS}_2/\text{IGZO}$  te vormen. De grensoverschrijdende kloof resulteert in zowel elektronen als gaten accumulatie aan dezelfde zijde en gevoeligheid voor de externe stimulaties. Allereerst zijn de structurele, elektronische en optische eigenschappen van  $\text{WS}_2/\text{IGZO}$  heterostructuren geanalyseerd door middel van DFT berekeningen onder verschillende elektrische velden, mechanische stress en gas moleculen. The resultaten demonstreren dat de band kloof van  $\text{WS}_2/\text{IGZO}$  heterostructuren een nagenoeg lineaire afname heeft met toenemend elektrisch veld in de negatieve en positieve richting, resulterend in een halfgeleider-metaal transitie, wat een toepassing voor de FET onthult. De heterostructuur toont een brede spectrale responsiviteit (van zichtbaar licht tot diepe UV golflengtes) en verbeterde optische eigenschappen onder mechanische spanning. De trekspanning kan de fotorespons van de heterostructuur verzwakken voor UV licht en versterken voor zichtbaar licht; terwijl voor drukspanning de heterostructuur een scherpe absorptie piek laat zien voor UV licht. Bovendien is de gas adsorptie energie van  $\text{NH}_3$  en  $\text{NO}_2$  op de  $\text{WS}_2/\text{IGZO}$  heterostructuur berekend, wat een hoge gas adsorptie energie laat zien voor  $\text{NO}_2$ , wijzend op de potentiële toepassing als  $\text{NO}_2$  gas sensor.

De unieke en afstembare eigenschappen gebaseerd op de DFT berekening laten zien dat de  $\text{WS}_2/\text{IGZO}$  heterostructuur een goede kandidaat is voor transistors en gas sensors. De op CVD- $\text{WS}_2/\text{IGZO}$  heterojunctie gebaseerde apparaten zijn dus ontworpen en onderzocht in twee modi; de chemristor en TFT modus. Het apparaat heeft een maximum response van 18170% in de chemristor modus en 499400% in de TFT modus bij 300 ppm  $\text{NO}_2$  na

het toepassen van een -20 V gate bias. Het heterojunctie apparaat is veel beter dan enkel WS<sub>2</sub> of IGZO. Bovendien toont de sensor excellente gas selectiviteit naar NO<sub>2</sub> in vergelijking met verschillende gas dampen zoals CO, NH<sub>3</sub> en luchtvochtigheid. De superieure gas detectie prestatie kan profiteren van de heterojunctie van WS<sub>2</sub> en IGZO en het externe elektrisch veld op de back gate spanning. Daarnaast presenteert de transistor typisch ambipolair gedrag bij droge lucht, terwijl de transistor p-type wordt als de hoeveelheid NO<sub>2</sub> toe neemt. De mobiliteit, aan/uit ratio en onderdrempel helling worden gemoduleerd door de NO<sub>2</sub> gas concentratie. Het unieke en afstembare gedrag kan worden geassocieerd met de doping effecten van NO<sub>2</sub> op de heterojunctie en de gemoduleerde Schottky barrière op de WS<sub>2</sub> en IGZO metaal contact interface.

Dit proefschrift wordt afgesloten met een samenvatting van de voornaamste resultaten en geeft suggesties voor toekomstige onderzoeksmogelijkheden in het vakgebied van op 2D/nano-metaal sulfides materiaal gebaseerde apparaten. Het onderzoek naar op 2D/nano materialen gebaseerde apparaten is nog een vroeg stadium. Het zit vol met uitdagingen om materialen van hoge kwaliteit te ontdekken die geschikt zijn voor gas sensors die de betrouwbaarheid en stabiliteit op lange termijn garanderen, het nauwkeurig evalueren/testen van stalen en het integreren van de sensor in bestaande systemen. Deze fundamentele onderzoek uitdagingen moeten worden opgelost in de toekomst.



# 1

## INTRODUCTION

## 1.1. BACKGROUND

IN the 17th century, lots of researchers studied gases emitted from chemical reactions, such as fermentation and combustion. Jan Baptist van Helmont, is considered the father of the pneumatic chemistry, he was the first person to recognize the existence of vaporous substances distinct from the atmosphere, to describe these substances he coined the word “gas”. [1] Nowadays, gas sensors play a crucial role in our daily lives, such as the detection of air quality, environment monitoring, and breath analysis. According to the report of “Environmental Gas Sensors 2020-2030” from IDTechEx in Figure 1.1, it is found that there will be a large growth of gas sensors market in the coming years and the total market for environmental sensors will be over \$3.8 billion by 2030. [2] An ideal gas sensor can detect different gases simultaneously with high sensitivity and selectivity, has a small size, low-cost and low power consumption (<10 mW). [3] Typically, the atmospheric pollutants include nitrogen dioxide (NO<sub>2</sub>), nitrogen monoxide (NO), ammonia (NH<sub>3</sub>), sulfur dioxide (SO<sub>2</sub>), carbon monoxide (CO), carbon dioxide (CO<sub>2</sub>), and volatile organic compounds (VOCs). [4] When these pollutants exceed the recommended exposure limits, they have negative effects on the environment and human health (Table 1.1).

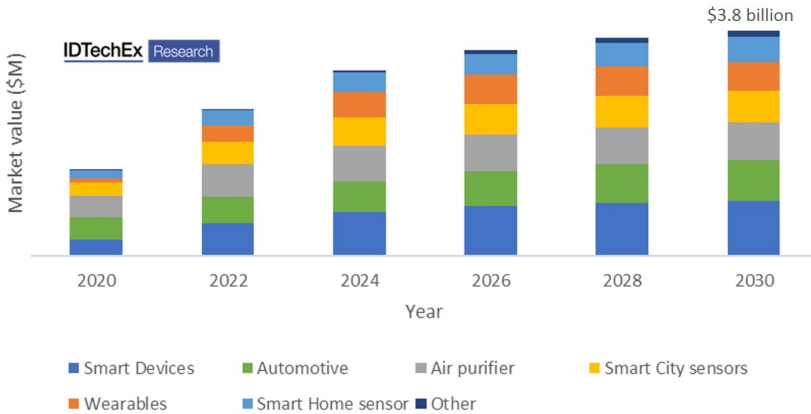


Figure 1.1: 2020-2030 Environmental Gas Sensor Market in Value. [2]

Nitrogen dioxide (NO<sub>2</sub>), one of the most abundant air pollutants and mainly emitted by fossil fuel burning, road traffic, indoor combustion source [5], and biomass burning. [6] When NO<sub>2</sub> exceeded the recommended exposure limits, it can induce acidification (acid rain), eutrophication (disruption of ecosystems due to excessive nutrients), and global warming. Besides, after exposure to low concentration NO<sub>2</sub> for a long time, the risk of asthma or lung disease will be increased. The World Health Organization (WHO) recommends an ambient air quality guideline of 40 µg/m<sup>3</sup> (21 ppb) annual average NO<sub>2</sub> concentrations. [7, 8] Under this context, many efforts were focused on developing a miniaturized, highly sensitive, and reversible NO<sub>2</sub> gas sensor with a low limit of detection (LOD) operating at room temperature.

Alternatively, driven by the increasing demand for health monitoring and controlling, high sensitive humidity sensors are in great demand. Various humidity sensors by detect-

ing the variation of their capacitances, resistances, impedance or piezoelectricity have been reported.[9–12] Currently, searching to adapt sensing materials with a high surface to volume ratio is of great importance to realizing high-quality humidity sensor with repeatable utilization and short response times.

Table 1.1: The environmental and human health impact of different air pollutants, and their maximum permissible limits set by the Gothenburg Protocol or the Paris Climate Agreement.[13, 14]

Gas	Environmental and human health impact	8 hours (ppm)	Short-term (ppm)	VOI (ppb)
NO <sub>2</sub>	Indirect GHG, Acidification, Eutrophication, Cardiovascular mortality, Asthma, Lung function	0.5	1	21
NH <sub>3</sub>	Toxic, PM2.5 precursor	20	50	20000
H <sub>2</sub> S	SO <sub>2</sub> precursor, Toxic	5	10	5000
SO <sub>2</sub>	Indirect GHG, Acidification, PM Precursor, Cardiovascular mortality	0.5	1	7.5
CO	Indirect GHG, Toxic, Birth weight, Asthma, Cardiovascular disease, Cardiac disease, Psychiatric admissions, etc.	20	100	4000
CO <sub>2</sub>	GHG -Climate Change, can potentially impact health	5000	/	400000

Notes: GHG = Green House Gas, PM = Particulate Matter, VOI= Value of Interest; Short term = 15 minutes.

## 1.2. GAS SENSING TRANSDUCERS

In general, a gas sensor is composed of a receptor and a transducer, as shown in Figure 1.2. The receptor is mostly provided with a material or a materials system, which interacts with some target gases.[15] It induces a change in properties, such as electrode potential, dielectric constant, mass, and work function. The transducer is a device that translates such variation on a specific property into an electrical signal (sensor response). Typically, gas sensors can be classified into optical, physical, and electrical sensors based on the type of transduction mechanism. The criteria to evaluate an efficient gas sensor rely on various parameters, such as sensitivity, selectivity, response and recovery times, long-term stability, and power consumption.

### 1.2.1. OPTICAL GAS SENSOR

Optical gas sensors monitor the optical properties of a gas species at defined wavelengths. The optical absorption/emission distribution with wavelength and intensity provides a “fingerprint” for any concentration gas species present.[16] Most of the optical gas sensors are based on non-absorption and absorption techniques (see Figure 1.3). Based on optical non-absorption techniques, chemiluminescence (CL) is often used for low concentrations NO<sub>x</sub> sensing,[17] and ultraviolet fluorescence (UVF) is used for detecting low levels of SO<sub>x</sub>.[18] Photoionisation detectors (PIDs) are usually hand-held instruments that for the detection of VOCs. On the other hand, absorption technique-based optical sensors, such as non-dispersive infra-red (NDIR), Fourier transform infrared (FTIR), photoacoustic spectroscopy (PAS), and cavity ring-down spectroscopy (CRDS), are mainly based on the Beer-Lambert absorption law. Optical gas sensors often have high selectivity and fast response and recovery. However, the required volume of the gas sensor is relatively large. The

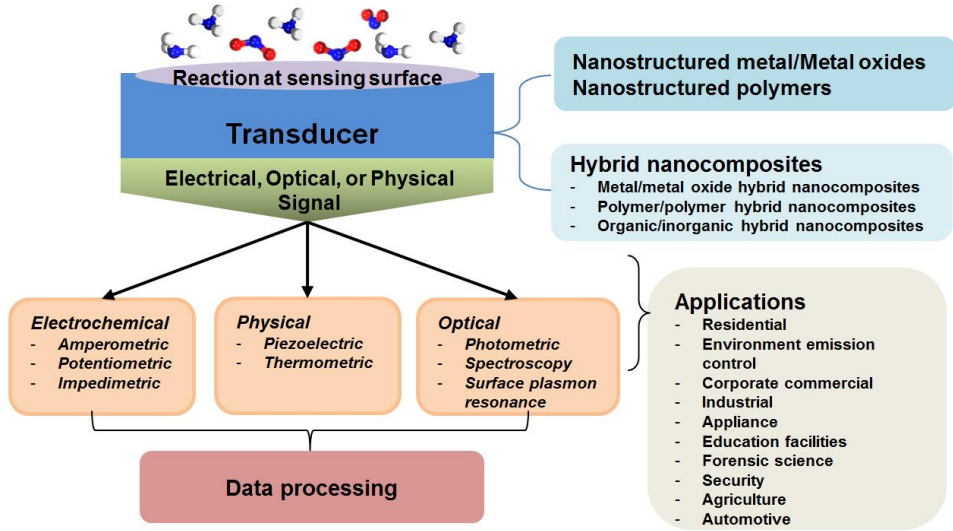


Figure 1.2: Schematic of gas sensor techniques.

gas should have visible absorption, emission, or scattering in the convenient region of the optical spectrum.

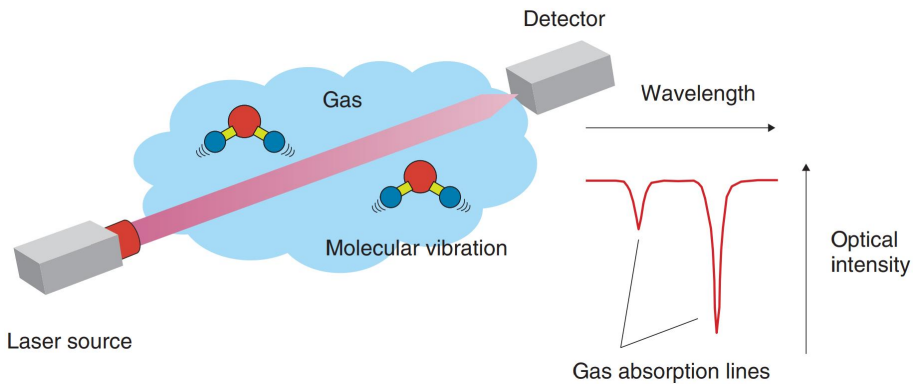


Figure 1.3: A typical laser-based trace gas sensor.[19]

### 1.2.2. PHYSICAL GAS SENSORS

Physical gas sensors include piezoelectric and thermometric (TE) sensors, which detect changes in the mass of the sensitive area exposed to the target gas, and the temperature variations arising from chemical reactions, respectively (see Figure 1.4).[20] There are three types of piezoelectric sensors, including quartz crystal microbalance (QCM), surface acoustic wave (SAW), and microcantilever, which are based on the shift of the resonant frequency induced by the gas adsorption on the surface of piezoelectric materials. Piezoelectric de-

devices have high sensitivity and fast response times and their fabrication is compatible with current planar IC technologies.[21] However, they suffer from a weak signal to noise performance due to the high operating frequencies, and the complicated and expensive IC system. Besides, it is challenging to realize the batch-to-batch reproducibility of piezoelectric gas sensors and the replacement of damaged sensors. TE devices can detect a temperature difference between the hot and cold parts of the TE film, which is generated by the interaction with a gas and TE film.[22] Another TE device is utilizing the differences in the thermal conductivity of certain gases. Once a gas with a higher/lower thermal conductivity is injected, the temperature of the device changes compared to the reference, and a signal is detected. This kind of gas sensor has high accuracy, but too expensive.



Figure 1.4: A typical physical gas sensor.[20]

### 1.2.3. ELECTRICAL GAS SENSORS

**Electrochemical gas sensors.** Electrochemical gas sensors measure the concentration of a target gas by oxidizing or reducing the target gas at an electrode and measuring the resulting current. They can be divided into three main classes according to the operating principle: amperometric, potentiometric, and conductometric sensors.[23] A typical sensor consists of two or three electrodes and electrolyte, in which the electrodes are separated by a solid, liquid, or polymer electrolyte (see Figure 1.5a). The chemical reactions occur at the sensing electrode that is commonly made of noble metals or carbon. The counter electrode is used to close the circuit with the sensing electrode and measure the electrical signal. The reference electrode is used to stabilize the sensing electrode's potential when the sensor requires an external voltage bias. The gas enters the sensor through a capillary barrier, then passes through a hydrophobic membrane and finally contacts the sensing electrode. These sensors have low power consumption but a short lifetime.

**Chemiresistor gas sensors.** The chemiresistor gas sensor directly interacts with the target gas, which results in the change of the resistance. These devices cover a wide range of sensing methods and employ different types of materials such as metals, semiconductors, and polymers(see Figure 1.5b). Noble metals such as Pt, Pd or Ir have widely used in gas sensing due to their obvious resistance variations toward gas molecules.[24] They are mostly made on glass, silicon, or ceramic substrates. Their gas sensing performances are affected by the thickness of the thin film, defect density, morphology, and operating temperature. Polymer-based gas sensors are in most cases organic macromolecules made of carbon and hydrogen atoms with minor amounts of other atoms e.g., oxygen, nitrogen, sulphur, phosphorus, and halogens.[25] To change their conductivities, p- or n-type electrically conducting polymers are synthesized by chemical, electrochemical, photochemical, and interfacial doping methods and widely applied for chemiresistors. The semiconductor-based gas sensor is the main electrical gas sensor due to its high sensitivity, fast response, and low cost.[26] Traditional semiconducting gas sensors are made from metal oxide (MOX),

such as aluminium oxide ( $\text{Al}_2\text{O}_3$ ),[27] zinc oxide ( $\text{ZnO}$ ),[28] tin oxide ( $\text{SnO}_2$ ),[29] titanium oxide ( $\text{TiO}_2$ ),[30] tungsten oxide ( $\text{WO}_3$ ),[31] etc. The sensing mechanism is related to adsorbed oxygen ions on the oxide surface. Oxygen molecules take electrons from the surfaces of MOX and ionize them into oxygen species such as  $\text{O}^{2-}$ ,  $\text{O}^-$ , and  $\text{O}_2^-$ . [32] Due to the dominant role of oxygen ions, the MOX sensors are typically operated at elevated temperatures ( $\sim 300\text{-}400^\circ\text{C}$ ). [33] To ensure the materials sensitive to the target analytes, external heaters are applied to the sensor for keeping high operation temperature. However, it increases the power consumption and decreases its thermal stability, limiting these sensors commercially available.

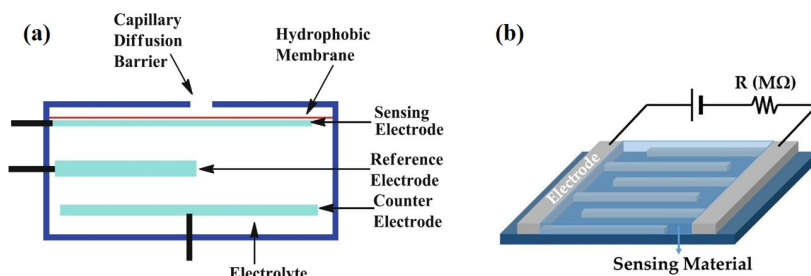


Figure 1.5: Schematic view of an (a) electrochemical gas sensor and (b) chemiresistor sensor.[34]

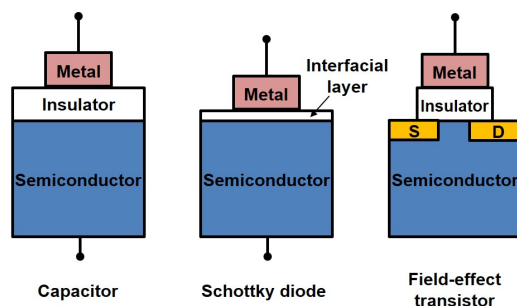


Figure 1.6: Schematic figure of field effect gas sensors.[35]

**Field-effect gas sensors.** Field-effect gas sensors are attributed to the considerable sensitivity of different types of chemically sensitive gates, such as palladium gate metal-oxide-semiconductor structures, metal gates, etc.[36] There are mainly three kinds of field effect gas sensors, Schottky diodes, capacitors, and transistors.[35] In the Schottky diode, the gas species that react with the sensing layer may induce both a resistivity change and a field effect. The capacitor only gives a response to gas species that give rise to field-effect changes of the gate metal, which makes the response, i.e., the drop in the capacitance-voltage ( $C$ - $V$ ) curve directly comparable to that of the transistor device. The transistors are operated in the constant current mode, for which the direct-current (DC) gate voltage change is reflected in the response of the output signal. The transistor device is by far the most stable and easy to operate, once the more complicated processing is made.

Table 1.2: Types of solid state gas sensors with the corresponding physical change used as gas detection principle, and their advantages and disadvantages.[16, 34, 37]

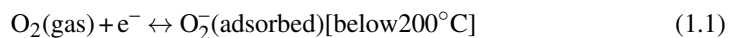
Type of devices	Physical change	Advantages	Disadvantages
Optical sensors (fibre optic or thin film)	Optical parameters: SPR, absorption, reflection, fluorescence, interferometry, or refractive index.	Rapid, high selectivity of measuring gas concentration with good sensitivity.	Specified gases for the optical spectrum, bulky
Physical sensors: QCM, SAW, microcantilevers	Mass	High accuracy	Slowly acting, expensive, bulky.
Electrochemical gas sensors	Electromotive force or electrical current in a solid state electrochemical cell	Highly specific, and operating at a convenient wavelength.	Slowly acting, non-reversible, poor selectivity.
Chemiresistor gas sensors	Electrical conductivity	Low cost, high sensitivity, simplicity in function.	High working temperature, long-time instabilities, sensitive to water vapour, poor selectivity.
Field effect gas sensors: diodes, transistors, capacitors	Work function (electrical polarisation)	Low cost, high sensitivity.	Poisoning can occur. It is non-reversible.

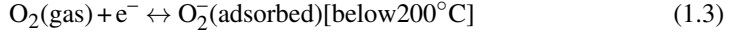
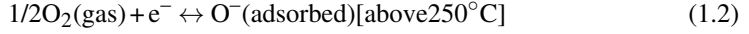
## 1.3. NANOSTRUCTURED MATERIALS-BASED GAS SENSOR

The traditional gas sensors have some shortcomings, such as large size, non-sufficient sensitivity, long response and recovery time, high working temperature, and poor selectivity. Therefore, nanoscience and nanotechnology have been proposed for overcoming these disadvantages.[38] Nanostructured materials, i.e. 2D layered materials and nanomaterials, often show strong in-plane ionic or covalent bonding and weak out of the plane van der Waal or hydrogen bonding. They have great potential for the sensing layers, which stem from the high specific surface area, numerous surface active sites, as well as the effect of crystal facets with high surface reactivity. Therefore, the interaction between gas molecules and materials mainly takes place on the surface. The number of atoms residing at a material's surface is critical for controlling the sensor performance. Consequently, gas sensors based on graphene,[39] carbon nanotube,[40], metal oxides (MOX)[41], and metal sulfides[42] exhibit better performances.

### 1.3.1. METAL OXIDE-BASED NANOMATERIALS FOR GAS SENSING

In general, the physical fundamentals, such as surface morphology, crystalline structure, energy band, charge transportation, etc., play an important role in adjusting the sensing performance of nanostructured MOX-based devices. The oxygen ions are formed by drawing electrons from the conduction band of the MOX, and different forms are possible depending on the operating temperature.[43] Below 200 °C, electrons are attached to oxygen molecules as shown in Eq.1.1 Above 250 °C, the oxygen molecules are dissociated into oxygen ion atoms with an electric charge by pulling electrons from MOX as shown in Eq.1.2 and 1.3.





The interaction between the oxygen ions and gas analytes can be divided into two main categories depending on the majority carrier, electrons or holes (see Figure 1.7). When the majority carriers are electrons, the MOX is considered to be n-type, while the majority carriers are holes in the p-type MOX sensors. For instance, the electrons in the conduction band of the n-type MOX are decreased due to the reactions of Eq.(1.1-1.3), resulting in increased resistance at the operating temperature. Once the target gas is introduced, the electrons from the reducing gas are transferred to the conduction band of the MOX, causing the sensor's resistance to decrease. It should be noted that the opposite resistance change occurs with an oxidizing gas. The categorized sensing behavior of n-type and p-type sensing materials to reducing and oxidizing gases is compared elsewhere.  $NO_x$  is considered an oxidizing gas due to unpaired electrons around the N atom, while  $NH_3$  acts as a reducing gas due to its lone electron pair. MOX have advantages of high sensitivities and low cost; however, large power consumption, high operation temperature and low selectivity are their drawbacks.

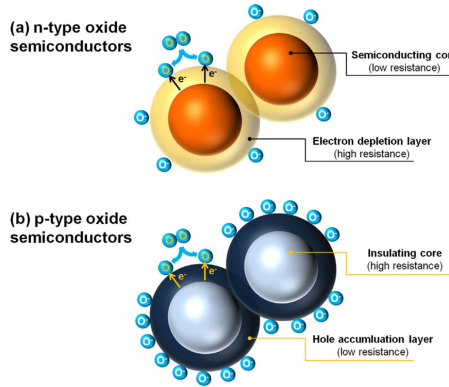
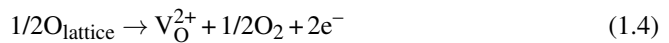


Figure 1.7: Formation of electronic core-shell structures in (a) n-type and (b) p-type oxide semiconductors.[32]

Thus defects are introduced to MOX, which play a critical role in determining their electronic properties, as Kolmakov and Moskovis noted in their classic review of one dimensional MOX gas sensors.[44] Oxygen vacancy is the most common type of defect in MOX gas sensors. It can increase the concentration of surface adsorbed oxygen, or modify the baseline resistance of the device, further improving gas sensing performance. For example, when an oxygen vacancy is created and fully ionized in an n-type oxide such as  $SnO_2$ , two electrons are released into the conduction band as illustrated in Eq.1.4.[45]



where  $O_{\text{lattice}}$  is oxygen on a lattice site,  $V_O^{2+}$  are ionized oxygen vacancies in  $SnO_2$ ,  $O_2$  is oxygen in the atmosphere and  $e^-$  are electrons. In this case the oxygen vacancy is con-

sidered to be a bulk donor with the defect state lying below the conduction band minimum (CBM), where the difference in energy between the CBM and the defect level is equal to the defect ionization energy. Eq.1.4 represents an equilibrium between the bulk material and surrounding atmosphere. The groups of Epifani[29] and Li[46] have proved that SnO<sub>2</sub> with oxygen vacancies (OVs) for NO<sub>2</sub> gas detection exhibited an ultrahigh response at room temperature.

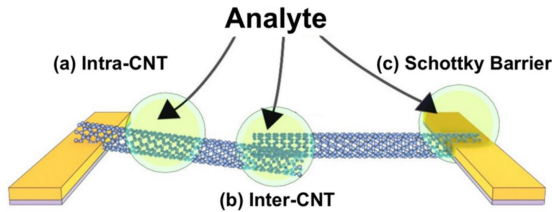


Figure 1.8: Mechanism of gas sensing operating on p-type CNT semiconductors with reducing/oxidizing type gases.[47]

### 1.3.2. CARBON-BASED NANOMATERIALS FOR GAS SENSING

The most studied carbon-based nanomaterials (CNMs) in the past decade are graphene and derivatives (such as graphene oxide (GO) and reduced graphene oxide (rGO)), and carbon nanotubes (CNTs), which can be used for chemical gas sensors.[48] The outstanding characteristics of CNMs, such as mesoporous nature, large specific surface area, enhanced electron transport properties, and good signal-to-noise ratio, ensuring gas sensing.

Unlike MOX-based devices, the gas sensing of CNMs is mainly based on the charge transfer processes, in which the sensing materials act as charge acceptors or donors.[49] Graphene is an atomic-thin layered carbon 2D materials with a large surface-to-volume ratio, which behaves like a p-type semiconductor. Schedin *et al.*[50] first reported a graphene-based gas sensor through mechanical exfoliation method, which can detect sub-ppb of gas molecules. Yavari *et al.*[51] demonstrated room temperature detection of NO<sub>2</sub> (100 ppb) and NH<sub>3</sub> (500 ppb) with graphene films synthesized by chemical vapor deposition (CVD). However, direct preparation of graphene is costly and hence in many cases it is prepared from GO by rGO. Pristine rGO can detect NH<sub>3</sub> and NO<sub>x</sub>, and rGO with functionally modified surface (such as rGO/ZnO, rGO/Pt, rGO/Ni) are known to detect VOCs (acetone, phenol, nitrobenzene, etc.).[52]

Similar to graphene, the charge transfer between CNT and gas molecules adsorbed at the surface acts like a p-type semiconductor at room temperature.[53] The sensing performance of CNT-based sensor depends on impurities, chirality, and defects in the structure, which exhibits negligible interactions with the major breath gases (such as N<sub>2</sub>, O<sub>2</sub>, and H<sub>2</sub>O) but significant interacts with NH<sub>3</sub> and NO<sub>x</sub>. [54] The sensing mechanisms of CNT-based sensors involve three aspects, the adsorption at the sidewall or the length of the CNT (intra-CNT), at the CNT-CNT interface (inter-CNT), and at the interface between the metallic electrode and the CNT (Schottky barrier), as shown in Figure 1.8a. Rigoni *et al.*[55] recently demonstrated chemiresistive sensors comprising pristine SWCNTs with 20 ppb sensitivity to NH<sub>3</sub> and a LOD of 3 ppb, Figure 1.8b,c. However, the pristine CNMs sensors

are often inert toward environmental contaminants. Other reactive nanomaterials (i.e. metals, metal oxides or metal sulfides) are introduced to construct hybrids for increasing the gas sensing performance.[56] CNMs-based gas sensors operate at room temperature with superior sensitivity, but long recovery time, low selectivity, and complex processing.

### 1.3.3. METAL SULFIDE-BASED NANOMATERIALS FOR GAS SENSING

Alongside graphene, metal sulfides are the most studied 2D materials. Typical metal sulfide semiconductors, like molybdenum disulfide ( $\text{MoS}_2$ ) and tungsten disulfide ( $\text{WS}_2$ ) are layered metal disulfide materials, which made of stacked planes of covalently bonded S and metal atoms, and weak van der Waals (vdWs) interlayer bonds. Therefore, the mechanical exfoliation or electrochemical intercalation techniques that first used to distil graphene can be applied for thinning metal sulfides down to 2D materials. It is known that many MOX exhibit a wide band gap because their valence band comprises a deep 2p oxygen orbital, and hole carriers have a comparatively heavy effective mass owing to the localized nature of the oxygen 2p state.[33] In contrast to MOX, metal sulfides often have a shallow valence band, and due to their small effective mass, they exhibit a robust quantum size effect.[57] In addition, because of their availability in a variety of shapes, sizes, crystalline forms, chemical compositions, and their excellent response to external stimulation, metal sulfide materials have a range of potential novel properties that can contribute to gas sensing.

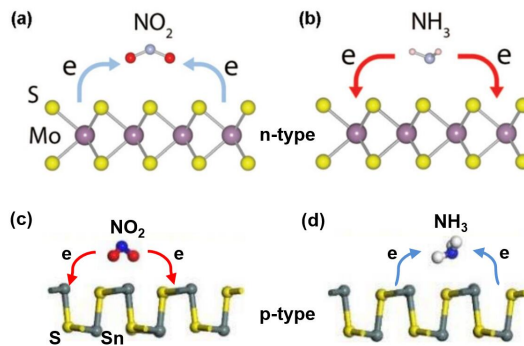


Figure 1.9: Gas sensing mechanism of (a-b)  $\text{MoS}_2$  (n-type metal sulfide)[43] and (c-d)  $\text{SnS}$  (p-type metal sulfide)[58] in the presence of  $\text{NO}_2$  and  $\text{NH}_3$  molecules.

Similar to the CNMs-based gas sensor, the sensing metal sulfide materials act as charge acceptors or donors. When exposing to different gases, the charge transfer reaction occurs between the sensing materials and the adsorbed gases, accompanied by different transfer directions and quantities of charges, which leads to different changes of the material resistance. If the sensing materials are re-exposed to air, desorption of gas molecules occurs, causing the sensing material resistance to returning to the initial state. As shown in Figure 1.9, when n-type  $\text{MoS}_2$  exposes to these electron-accepted gas  $\text{NO}_2$ , the electron charges transfer from  $\text{MoS}_2$  to the sensitive gases, leading to a decreased carrier density in  $\text{MoS}_2$ . As a result, the resistance of n-type  $\text{MoS}_2$  increases. On the contrary,  $\text{NH}_3$  molecules adsorbed on the  $\text{MoS}_2$  act as charge donors and transfer electrons to the  $\text{MoS}_2$  monolayer, increasing the electron carrier density of the n-type  $\text{MoS}_2$  monolayer and re-

ducing its resistance.[59] Due to the high-speed charge transfer and the high adsorption energy between them and gas molecules, the LOD of the MoS<sub>2</sub> gas sensor can reach 49.96 ppb.[60] In post-transition metal sulfide, tin sulfide (SnS) is a p-type semiconductor that belongs to a family of layered group IV monosulfide and has similar puckered structures as black phosphorus.[10, 61] The anisotropic crystal structure can enable unique response to external stimulation. Thus, SnS nanoflakes have been used for sensing toxic and VOC gas, like NO<sub>2</sub>, acetone, and alcohol.[62]

The advantages and disadvantages of MOX, CNM, and metal sulfides-based gas sensors are listed in Table 1.3. Metal sulfides-based sensor can work at room temperature with high sensitivity which is superior than that of MOX. The sensing performances of metal sulfides are similar with CNM-based devices, except for their sizeable and tuneable bandgaps, which makes such materials suitable for the applications of transistors, further inducing unique sensing behaviours. In addition to intrinsic metal sulfides, lots of researchers used different advanced methods to improve their sensing properties. For instance, functionalizing metal sulfide (e.g. by defects or dopants), constructing heterojunction (Schottky junction, p-n, n-n, and p-p semiconductor junction), and using transistor. In the next chapter, I will make a full comparison of the gas sensing performances between different types of metal sulfide-based sensors, including the crystal structure, synthesis methods, gas sensing behaviours, and mechanisms.

Table 1.3: Advantages and disadvantages of metal oxide, CNM, and metal sulfides gas sensors

Type of devices	Advantages	Disadvantages
Metal oxide	Short response time, low cost, long-term stability, scalable fabrication.	Low electron mobility at low temperature, high operating temperature, high power consumption, low gas response
CNM	High electron mobility at low temperature, low energy consumption, high gas response, mechanical flexibility, scalable fabrication.	Low selectivity, long recovery time, relatively high cost, lack of long-term stability, lack of scalable fabrication
Metal sulfide	High electron mobility at low temperature, low energy consumption, high gas response, good compatibility, mechanical flexibility.	Sluggish recovery, relatively high cost, lack of long-term stability, lack of scalable fabrication

## 1.4. AIM AND SCOPE OF THIS DISSERTATION

In this dissertation, scientific research has been conducted on metal sulfide-based devices for the detection of humidity and NO<sub>2</sub> gases in real-time. The aim of this dissertation is to answer the following research questions:

Main question: How to improve the gas sensing performance of the pristine metal sulfide-based sensor?

Answer: Typically, there are three methods to improve the pristine nanomaterials-based gas sensor. One is a morphological design of nanostructures, such as surface treatment for increasing the surface area or introducing defects to enhance the adsorption energy (Chapter 4). The second method is using the bandgap alignment technique to modulate the charge transfer density and bandgap barrier of in the interface the metal-semiconductor or semiconductor-semiconductor contact (Chapter 3, 4, and 5). The third method is using a

transistor-based sensor. FET devices can directly transform the interactions between target molecules and channel materials into readable electrical signals (Chapter 5).

According to the main question, four sub-questions are derived and discussed as follow:

Q1: How does the Schottky barrier improve the gas sensing response of the pristine metal sulfide-based sensor?

A1: Due to different band gaps and work functions, metal and metal sulfides would join together to form Schottky junction at the interface. A thicker electron depletion layer forms on the surface region of metal-metal sulfides compared with the pure one. The target gases can react with more adsorbed oxygen ions. Thus, more trapped electrons can return to the conduction band of the metal sulfides resulting in a more considerable change in resistance, namely a higher response. To know the mechanism, I fabricated a humidity sensor based on SnS-metal Schottky contact (Chapter 3).

Q2: How does heterojunction improve the limit of detection of the metal sulfide-based sensor?

A2: Most of the heterostructures-based device exhibit band offset where the carriers (i.e., electrons) at the higher energy level flow across the interface to the unoccupied states until the Fermi energy equilibrates. It induces fast charge transfer in the interface, which is so sensitive to the change of environment, such as gas or other chemical molecules (Chapter 4 and 5).

Q3: What are the effects of defects or oxygen vacancies on the gas sensing performance of the metal sulfide-based sensor?

A3: To improve gas sensing performance, I made a MOX/metal sulfide heterostructure in Chapter 4. These heterostructures have numerous oxygen vacancies (OVs), which is the most common type of defect in oxides. It can increase the concentration of surface adsorbed oxygen and modify the baseline resistance of the device. Thus the device shows high gas sensing response and ultralow limit of detection.

Q4: What is the difference between the gas sensing performances of the metal sulfide-based devices in chemiresistor mode and transistor mode?

A4: To know the gas sensing performance of the metal sulfide-based device in chemiresistor mode and transistor mode, a thin film transistor was fabricated and measured the gas response without and with applying back gate voltage, respectively (Chapter 5).

## 1.5. OUTLINE OF THIS DISSERTATION

Following, a summary of the topics treated in each chapter of this thesis is given:

Chapter 2 presents a state-of-the-art metal sulfides-based gas sensor. This chapter starts with introducing the synthesis method of nanostructured metal sulfides, and their applications in gas sensors. It also points out the bottleneck of metal sulfides-based gas sensors and presents the way of improved gas sensing performance.

Chapter 3 begins with the contribution of the thesis. This chapter presents a high-performance SnS nanoflakes-based humidity sensor which is benefited from its Schottky nature of SnS-metal contact. The gas sensing mechanism is analyzed through DFT and Schottky barrier theory. It also shows a flexible humidity sensor with a polyimide substrate. The envisioned applications of the device in the detection of breathing patterns and non-contact fingertips movement are introduced and discussed towards its potential use in the smart home system.

Chapter4 presents ultrasensitive NO<sub>2</sub> gas sensor based on OV<sub>s</sub> rich SnO<sub>x</sub>/SnS nanostructure, which can detect ppb-level NO<sub>2</sub> gas concentration at room temperature. In this chapter, design, fabrication, and simulation of the device are reported systematically in detail. The potential applications of the device are discussed.

Chapter5 starts with the first principle analysis of the tunable behaviour of WS<sub>2</sub>/IGZO heterostructure under external stimulation (such as electric field, strain, and gas molecules). Based on the theoretical review, the WS<sub>2</sub>/IGZO device is fabricated and used for gas sensing. It also comparatively analyzes the tunable polarity transport behaviour under the different gas concentrations with chemiresistor and transistor mode, respectively.

Chapter 6 gives the main conclusions of the thesis and recommendations for future research.

## REFERENCES

- [1] Ghenadii Korotcenkov. Handbook of gas sensor materials. *Properties, Advantages and Shortcomings for Applications*, 2, 2013.
- [2] Luyun Jiang. Environmental gas sensors 2020-2030: Technologies, manufacturers, forecasts. <https://www.idtechex.com/en/research-report/environmental-gas-sensors-2020-2030/718>, 2020.
- [3] Shaobin Feng, Fadi Farha, Qingjuan Li, Yueliang Wan, Yang Xu, Tao Zhang, and Huansheng Ning. Review on smart gas sensing technology. *Sensors*, 19(17), 2019.
- [4] Abdolkarim Afroozeh, Elnaz Akbari, and P. Yupapin. Recent advance in gas sensing by using two-dimensional transition metal disulfides materials. *Journal of Nanoelectronics and Optoelectronics*, 14(9):1225–1229, 2019.
- [5] Chester W. Spicer, Donald V. Kenny, Gerald F. Ward, and Irwin H. Billick. Transformations, lifetimes, and sources of NO<sub>2</sub>, HONO, and HNO<sub>3</sub> in indoor environments. *Air & Waste*, 43(11):1479–1485, 1993.
- [6] Adeel Afzal, Nicola Cioffi, Luigia Sabbatini, and Luisa Torsi. NO<sub>x</sub> sensors based on semi-conducting metal oxide nanostructures: Progress and perspectives. *Sensors and Actuators B: Chemical*, 171-172:25–42, 2012.
- [7] World Health Organization. WHO air quality guidelines for particulate matter, ozone, nitrogen dioxide and sulfur dioxide: global update 2005: summary of risk assessment. Report, Geneva: World Health Organization, 2006.
- [8] Mohammad Javad Mohammadi, Gholamreza Goudarzi, Abdolkazem Neisi, Kamran Ahmadi-Angali, Hamed Saki, Ali Akbar Babaei, Babak Mohammadi, Hassan Dehdashti Rad, Mohsen Borhani, and Mehrdad Sharifi. Estimation of health effects attributed to NO<sub>2</sub> exposure from the use of airq model in ahvaz. *Apadana Journal of Clinical Research*, 2(1):5–12, 2013.
- [9] Tie Li, Lianhui Li, Hongwei Sun, Yan Xu, Xuwen Wang, Hui Luo, Zheng Liu, and Ting Zhang. Porous ionic membrane based flexible humidity sensor and its multifunctional applications. *Advanced Science*, 4(5):1600404, 2017.
- [10] Zhen Tian, Chenglei Guo, Mingxing Zhao, Ranran Li, and Jiamin Xue. Two-dimensional SnS: A phosphorene analogue with strong in-plane electronic anisotropy. *ACS Nano*, 11(2):2219–2226, 2017.

- [11] Jing Zhao, Na Li, Hua Yu, Zheng Wei, Mengzhou Liao, Peng Chen, Shuopei Wang, Dongxia Shi, Qijun Sun, and Guangyu Zhang. Highly sensitive MoS<sub>2</sub> humidity sensors array for non-contact sensation. *Advanced Materials*, 29(34):1702076, 2017.
- [12] Yanlong Tai and Gilles Lubineau. Human-finger electronics based on opposing humidity-resistance responses in carbon nanofilms. *Small*, 13(11):1603486, 2017.
- [13] Buckley David, Black Nicola Charlotte Grant, Castanon Eli, Melios Christos, Hardman Melanie, and Kazakova Olga. Frontiers of graphene and 2D material-based gas sensors for environmental monitoring. *2D Materials*, 2020.
- [14] Jean-Claude JUNCKER. European commission directive (eu) 2017/164, 2017.
- [15] Noboru Yamazoe and Kengo Shimano. *Chapter One - Fundamentals of semiconductor gas sensors*, pages 3–38. Woodhead Publishing, 2020.
- [16] John P. Dakin and Paul Chambers. Review of methods of optical gas detection by direct optical spectroscopy, with emphasis on correlation spectroscopy. In F. Baldini, A. N. Chester, J. Homola, and S. Martellucci, editors, *Optical Chemical Sensors*, pages 457–477. Springer Netherlands, 2004.
- [17] Robert Bogue. Detecting gases with light: a review of optical gas sensor technologies. *Sensor Review*, 35(2):133–140, 2015.
- [18] Hiroshi Nakamura, Ichiro Asano, Hideki Ohashi, and Masayuki Adachi. Development of a new UVF analyzer with O<sub>3</sub> injection for measurement of SO<sub>x</sub> and trs in vehicle emission, 2004.
- [19] R. Yoshimura, M. Kohtoku, K. Fujii, T. Sakamoto, and Y. Sakai. Highly sensitive laser based tracegas sensor technology and its application to stable isotope ratio analysis. *NTT Technical Review*, 12(4):1–6, 2014.
- [20] Hassan Shokry Hassan and Marwa Farouk Elkady. *Semiconductor Nanomaterials for Gas Sensor Applications*, pages 305–355. Springer International Publishing, Cham, 2020.
- [21] K. Arshak, E. Moore, G. M. Lyons, J. Harris, and S. Clifford. A review of gas sensors employed in electronic nose applications. *Sensor Review*, 24(2):181–198, 2004.
- [22] Elisabetta Comini, Guido Faglia, and Giorgio Sberveglieri. *Solid state gas sensing*, volume 20. Springer Science & Business Media, 2008.
- [23] A. Md Khan, V. Mulpuri Rao, and Qiliang Li. Recent advances in electrochemical sensors for detecting toxic gases: NO<sub>2</sub>, SO<sub>2</sub> and H<sub>2</sub>S. *Sensors*, 19(4), 2019.
- [24] D. Kohl. The role of noble metals in the chemistry of solid-state gas sensors. *Sensors and Actuators B: Chemical*, 1(1):158–165, 1990.
- [25] Ilaria Fratoddi, Iole Venditti, Cesare Cametti, and Maria Vittoria Russo. Chemiresistive polyaniline-based gas sensors: A mini review. *Sensors and Actuators B: Chemical*, 220:534–548, 2015.
- [26] M. Andersson, A. Lloyd Spetz, and D. Puglisi. *Chapter Ten - Recent progress in silicon carbide field effect gas sensors*, pages 309–346. Woodhead Publishing, 2020.

- [27] M. M. Arafat, A. S. M. A. Haseeb, S. A. Akbar, and M. Z. Quadir. In-situ fabricated gas sensors based on one dimensional core-shell  $\text{TiO}_2\text{-Al}_2\text{O}_3$  nanostructures. *Sensors and Actuators B: Chemical*, 238:972–984, 2017.
- [28] Hongye Yuan, Saif Abdulla Ali Alateeqi Aljneibi, Jiaren Yuan, Yuxiang Wang, Hui Liu, Jie Fang, Chunhua Tang, Xiaohong Yan, Hong Cai, Yuandong Gu, Stephen John Pennycook, Jifang Tao, and Dan Zhao. ZnO nanosheets abundant in oxygen vacancies derived from metal-organic frameworks for ppb-level gas sensing. *Advanced Materials*, 31(11):1807161, 2019.
- [29] Mauro Epifani, Joan Daniel Prades, Elisabetta Comini, Eva Pellicer, Manuel Avella, Pietro Siciliano, Guido Faglia, Albert Cirera, Roberto Scotti, Franca Morazzoni, and Joan Ramon Morante. The role of surface oxygen vacancies in the  $\text{NO}_2$  sensing properties of  $\text{SnO}_2$  nanocrystals. *The Journal of Physical Chemistry C*, 112(49):19540–19546, 2008.
- [30] C. Garzella, E. Comini, E. Tempesti, C. Frigeri, and G. Sberveglieri.  $\text{TiO}_2$  thin films by a novel sol-gel processing for gas sensor applications. *Sensors and Actuators B: Chemical*, 68(1):189–196, 2000.
- [31] S. S. Shendage, V. L. Patil, S. A. Vanalakar, S. P. Patil, N. S. Harale, J. L. Bhosale, J. H. Kim, and P. S. Patil. Sensitive and selective  $\text{NO}_2$  gas sensor based on  $\text{WO}_3$  nanoplates. *Sensors and Actuators B: Chemical*, 240:426–433, 2017.
- [32] Hyo-Joong Kim and Jong-Heun Lee. Highly sensitive and selective gas sensors using p-type oxide semiconductors: Overview. *Sensors and Actuators B: Chemical*, 192:607–627, 2014.
- [33] Yonghui Deng. *Semiconducting Metal Oxides for Gas Sensing*. Springer, 2019.
- [34] Haleh Nazemi, Aashish Joseph, Jaewoo Park, and Arezoo Emadi. Advanced micro- and nano-gas sensor technology: A review. *Sensors*, 19(6), 2019.
- [35] Anita Lloyd Spetz, Magnus Skoglundh, and Lars Ojamae. *FET Gas-Sensing Mechanism, Experimental and Theoretical Studies*, pages 1–27. Springer US, Boston, MA, 2009.
- [36] I. Lundström, S. Shivaraman, C. Svensson, and L. Lundkvist. A hydrogen sensitive MOS field effect transistor. *Applied Physics Letters*, 26(2):55–57, 1975.
- [37] Simone Capone, A. Forleo, L. Francioso, R. Rella, P. Siciliano, J. Spadavecchia, D. S. Presicce, and Antonella M. Taurino. Solid state gas sensors: state of the art and future activities. *Journal of Optoelectronics and Advanced Materials*, 5(5):1335–1348, 2003.
- [38] Jun Zhang, Xianghong Liu, Giovanni Neri, and Nicola Pinna. Nanostructured materials for room-temperature gas sensors. *Advanced Materials*, 28(5):795–831, 2016.
- [39] Yu Pang, Jinming Jian, Tao Tu, Zhen Yang, Jiang Ling, Yuxing Li, Xuefeng Wang, Yancong Qiao, He Tian, Yi Yang, and Tian-Ling Ren. Wearable humidity sensor based on porous graphene network for respiration monitoring. *Biosensors and Bioelectronics*, 116:123–129, 2018.
- [40] Leandro Sacco, Salome Forel, Ileana Florea, and Costel-Sorin Cojocaru. Ultra-sensitive  $\text{NO}_2$  gas sensors based on single-wall carbon nanotube field effect transistors: Monitoring from ppm to ppb level. *Carbon*, 157:631–639, 2020.
- [41] G. Korotcenkov. Metal oxides for solid-state gas sensors: What determines our choice. *Materials Science and Engineering: B*, 139(1):1–23, 2007.

- [42] H. Tae Kim, H. Yeon Kim, Y. Seo Park, Y. Soo Kim, and W. Ho Jang. Two-dimensional transition metal disulfides for chemoresistive gas sensing: Perspective and challenges. *Chemosensors*, 5(2), 2017.
- [43] Eunji Lee, Young Soo Yoon, and Dong-Joo Kim. Two-dimensional transition metal dichalcogenides and metal oxide hybrids for gas sensing. *ACS Sensors*, 3(10):2045–2060, 2018.
- [44] Andrei Kolmakov and Martin Moskovits. Chemical sensing and catalysis by one-dimensional metal-oxide nanostructures. *Annual Review of Materials Research*, 34(1):151–180, 2004.
- [45] Atanu Bag and Nae-Eung Lee. Gas sensing with heterostructures based on two-dimensional nanostructured materials: a review. *Journal of Materials Chemistry C*, 2019.
- [46] Yuxiang Li, Baiyi Zu, Yanan Guo, Kun Li, Haibo Zeng, and Xincun Dou. Surface superoxide complex defects-boosted ultrasensitive ppb-level NO<sub>2</sub> gas sensors. *Small*, 12(11):1420–1424, 2016.
- [47] Vera Schroeder, Suchol Savagatrup, Maggie He, Sibbo Lin, and Timothy M. Swager. Carbon nanotube chemical sensors. *Chemical Reviews*, 119(1):599–663, 2019.
- [48] Esraa Gabal, Somenath Chatterjee, Farah K. Ahmed, and Kamel A. Abd-Elsalam. 7 - Carbon nanomaterial applications in air pollution remediation, pages 133–153. Elsevier, 2020.
- [49] Shengxue Yang, Chengbao Jiang, and Su-huai Wei. Gas sensing in 2D materials. *Applied Physics Reviews*, 4(2):021304, 2017.
- [50] F. Schedin, A. K. Geim, S. V. Morozov, E. W. Hill, P. Blake, M. I. Katsnelson, and K. S. Novoselov. Detection of individual gas molecules adsorbed on graphene. *Nature Materials*, 6(9):652–655, 2007.
- [51] Fazel Yavari and Nikhil Koratkar. Graphene-based chemical sensors. *The Journal of Physical Chemistry Letters*, 3(13):1746–1753, 2012.
- [52] Cherukutty Ramakrishnan Minitha, Velunair Sukumaran Anithaa, Vijayakumar Subramaniam, and Ramasamy Thangavelu Rajendra Kumar. Impact of oxygen functional groups on reduced graphene oxide-based sensors for ammonia and toluene detection at room temperature. *ACS Omega*, 3(4):4105–4112, 2018.
- [53] O. K. Varghese, P. D. Kichambre, D. Gong, K. G. Ong, E. C. Dickey, and C. A. Grimes. Gas sensing characteristics of multi-wall carbon nanotubes. *Sensors and Actuators B: Chemical*, 81(1):32–41, 2001.
- [54] Michael F. L. De Volder, Sameh H. Tawfik, Ray H. Baughman, and A. John Hart. Carbon nanotubes: Present and future commercial applications. *Science*, 339(6119):535, 2013.
- [55] Federica Rigoni, Silvia Tognolini, Patrizia Borghetti, Giovanni Drera, Stefania Pagliara, Andrea Goldoni, and Luigi Sangaletti. Enhancing the sensitivity of chemiresistor gas sensors based on pristine carbon nanotubes to detect low-ppb ammonia concentrations in the environment. *Analyst*, 138(24):7392–7399, 2013.
- [56] Zhangyuan Zhang, Xuming Zou, Lei Xu, Lei Liao, Wei Liu, Johnny Ho, Xiangheng Xiao, Changzhong Jiang, and Jinchai Li. Hydrogen gas sensor based on metal oxide nanoparticles decorated graphene transistor. *Nanoscale*, 7(22):10078–10084, 2015.

- [57] Sundaram Chandrasekaran, Lei Yao, Libo Deng, Chris Bowen, Yan Zhang, Sanming Chen, Zhiqun Lin, Feng Peng, and Peixin Zhang. Recent advances in metal sulfides: from controlled fabrication to electrocatalytic, photocatalytic and photoelectrochemical water splitting and beyond. *Chemical Society Reviews*, 48(15):4178–4280, 2019.
- [58] F. Hu, H. Tang, C. Tan, H. Ye, X. Chen, and G. Zhang. Nitrogen dioxide gas sensor based on monolayer SnS: A first-principle study. *IEEE Electron Device Letters*, 38(7):983–986, 2017.
- [59] Qu Yue, Zhengzheng Shao, Shengli Chang, and Jingbo Li. Adsorption of gas molecules on monolayer MoS<sub>2</sub> and effect of applied electric field. *Nanoscale Research Letters*, 8(1):425, 2013.
- [60] M. Donarelli, S. Prezioso, F. Perrozzi, F. Bisti, M. Nardone, L. Giancaterini, C. Cantalini, and L. Ottaviano. Response to NO<sub>2</sub> and other gases of resistive chemically exfoliated MoS<sub>2</sub>-based gas sensors. *Sensors and Actuators B: Chemical*, 207:602–613, 2015.
- [61] A. S. Rodin, Lidia C. Gomes, A. Carvalho, and A. H. Castro Neto. Valley physics in tin (II) sulfide. *Physical Review B*, 93(4):045431, 2016.
- [62] Jun Wang, Gang Lian, Zhenghao Xu, Chen Fu, Zhaojun Lin, Liyi Li, Qilong Wang, Deliang Cui, and Ching-Ping Wong. Growth of large-size SnS thin crystals driven by oriented attachment and applications to gas sensors and photodetectors. *ACS Applied Materials & Interfaces*, 8(15):9545–9551, 2016.



# 2

## METAL SULFIDE-BASED GAS SENSOR: STATE-OF-THE-ART

*In this chapter, I present the state-of-the-art of metal sulfide-based gas sensors. Firstly, the underlying crystal structure and characteristics are generally described. Secondly, the top-down and bottom-up synthesis methods are present systematically. Then, various gas-sensing concepts of metal sulfide-based devices, including chemiresistor, functionalized-metal sulfides, Schottky diode, heterojunction, and FET sensor, are comparatively present. Finally, the challenges and perspectives of metal sulfide-based gas sensors are discussed to confirm our research objective further.*

## 2.1. METAL SULFIDE CHARACTERISTICS

**S**ULFIDE is the simplest inorganic sulfur anion with the chemical formula, or a compound containing one or more  $S^{2-}$  ions.[1] Metal sulfides are compounds in which the sulfur anion is combined with a metal or semi-metal cation or cations to form  $M_xS_y$  (i.e., MS,  $M_2S$ ,  $M_3S_4$ , and  $MS_2$ ). Usually, different metal sulfides having the same stoichiometric proportion possess similar crystal structures.[2] As shown in Figure 2.1, metal monosulfides mostly correspond to group VIII, IB, IIB, IIIA, and IVA metal. Monolayer group VIII, IB, and IIB monosulfides (e.g., ferrous sulfide (FeS) and zinc sulfide (ZnS)) show tetrahedral crystal habits.[3] Gallium sulfide (GaS), one of group IIIA monosulfides, present a hexangular crystal structure with four sequential atom planes in the order of S-M-M-S.[4] The crystal structures of group IVA monosulfides (e.g., germanium sulfide (GeS), tin sulfide (SnS) and lead sulfide (PbS)) are constituted by the puckered M-S atom permutation.[5, 6] It is analogous to the crystal structure of black phosphorus (BP). However, group IVA monosulfides are much more stable than black phosphorus. Common S-M-M-S monolayers of group IIIA monosulfides present mirror-plane symmetry. Group IVA monosulfides with BP-like crystal structures also exhibit excellent anisotropy, which is sensitive to external stimulation.[7, 8]

										IIIA	IVA	VA			
										B	C	N	O		
										Al	Si	P	S		
IVB	VB	VIB	VIIB	VIII				IB	IIB						
Ti	V	Cr	Mn	Fe	Co	Ni	Cu	Zn	Ga	Ge	As	Se			
Zr	Nb	Mo	Tc	Ru	Rh	Pd	Ag	Cd	In	Sn	Sb	Te			
Hf	Ta	W	Re	Os	Ir	Pt	Au	Hg	Tl	Pb	Bi	Po			

Figure 2.1: Periodic table with symbols indicating metal sulfide.

Layered  $MS_2$  materials with various elemental compositions have been extensively investigated, and the elements from group IVB-VIIB and IVA can be used to form metal disulfides.[9] Monolayer  $MS_2$  possesses a sandwich crystal structure where one M atomic layer is located between two S atomic layers. Generally, they have 1H and 1T phases, which depend on the metal coordination by the six S atoms. As shown in Figure 2.2, the 1H phase has hexagonal symmetrical triangular prism coordination, and the S atoms in different atomic layers of the 1H phase crystal are equivalent and mirror-symmetric. The crystal structure of the 1T phase has octahedral coordination and tetragonal symmetry. In contrast to the 1H phase, the arrangement of S atoms destroys the mirror symmetry. Crystal structure plays a decisive role in the performance of metal sulfides. Materials of the same composition with different crystal phases have different properties. 2H phase group VIB disulfides are usually semiconducting, however, the corresponding 1T, 1T', and Td phase crystals are metallic. Group IVA disulfides, such as  $GeS_2$ , and  $SnS_2$ , are usually semiconductors. Semiconducting metal disulfides, such as  $MoS_2$ ,  $WS_2$ , and  $SnS_2$ , have been investigated

for application in FETs. Compared to other disulfides, group VIB disulfides possess high carrier mobility. Table 2.1 introduces the characteristics and applications of nanostructured metal monosulfides and metal disulfides. It is found that numerous metal sulfides possess several crystal phases, which can be controlled by altering the fabrication processes and external stimulations.[2, 10, 11] Based on phase engineering, Kappera *et al.*[12] demonstrated that the metallic 1T phase of MoS<sub>2</sub> in contact with metal electrodes has lower contact resistances of 200-300  $\Omega \cdot \mu\text{m}$ , which is superior than that of only 2H phase (semiconducting) MoS<sub>2</sub>, suggesting that the 1T/2H interface controls carrier injection into the channel.

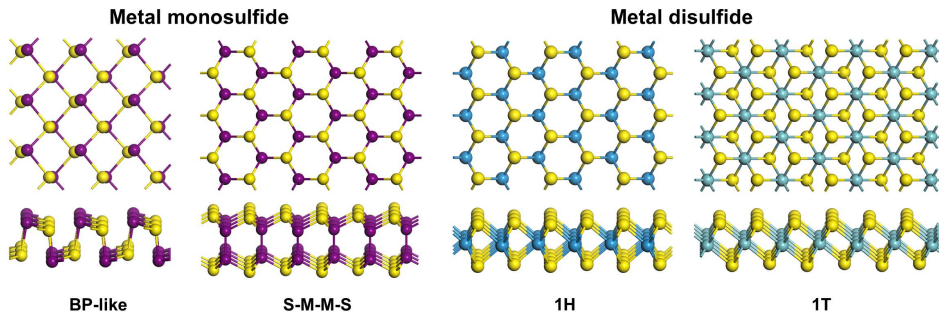


Figure 2.2: Representative crystal structures of metal sulfides.

## 2.2. PREPARATION METHODS FOR METAL SULFIDE NANOMATERIALS

To transform its electronic and optical properties into applications, many methods have been developed to prepare metal sulfides with customized nanostructures. In general, the existing techniques for the synthesis of metal sulfides are physical and chemical. To facilitate the classification, we divide the current preparation methods into two technologies based on "top-down" and "bottom-up" manufacturing methods.

### 2.2.1. TOP-DOWN APPROACHES

Typically, for most of the metal sulfides, there is strong covalent bonding in the hexagonal layer and weak van der Waals (vdW) interaction between the adjacent layers. It is an excellent way to achieve nano-sized materials with high quality through a top-down approach, which refers to slicing or successive reduction of their parent bulk crystals, including sputtering, electrospinning, lithography, ball milling, and exfoliation methods. Because the exfoliation method is simple, low-cost, and provides high-quality 2D metal sulfides materials, here I mainly introduce different exfoliation methods.

#### MECHANICAL EXFOLIATION

Mechanical exfoliation (ME) has been used for achieving high-quality graphene successfully, which is a simple, low-cost and efficient method.[34–36] Consequently, lots of researchers employed the Scotch-tape method for exfoliating other layered materials. Usually, the bulk materials of MoS<sub>2</sub> or WS<sub>2</sub> are used as the starting materials, where parts are

Table 2.1: Characteristics and applications of nanostructured metal sulfides.

	Crystal structure	Electric conductivity	con-	Band gap [eV]	Fabrication method	Application	Ref.
SnS	Orthorhombic	p-type		Indirect 1.1	PVD	photodetectors, gas sensor	[13]
GaS	Hexagonal	Semiconductor		Indirect 2.52	LPE	Hydrogen evolution reaction	[14]
GeS	Orthorhombic	p-type		Indirect 2.34	CVD	FET	[15]
ZnS	Hexagonal	n-type		Direct 3.7	Hydrothermal	Gas or optical sensor	[16]
CdS	Hexagonal	n-type		Direct 2.42	Spray pyrolysis	Solar cells, gas sensor	[17]
CuS	Hexagonal	p-type		Direct 2.5	Deposition	Solar cells, gas sensor	[18]
PbS	Hexagonal	n-type		Bulk 0.37; 3 nm 1.30	Deposition	Solar cell, photonics, gas sensor	[8]
NiS	Rhombohedral	p-type		0.5	Hydrothermal	Photocatalyst	[19]
MoS <sub>2</sub>	2H hexagonal	(2H) Semiconductor		(Bulk) Indirect 1.29	CVD, ME	FET, optical or gas sensor, supercapacitor	[20]
	1T	(1T) Metal		Direct 1.8			[21]
WS <sub>2</sub>	2H hexagonal	(2H) n-type		(Bulk) Indirect 1.3	CVD, ME	FET, photodetector,	[22]
	1T	(1T) Metal		Direct 2.1		Gas sensor	
SnS <sub>2</sub>	4H hexagonal	n-type		Indirect 2.308	CVD, ME	FET, photovoltaics,	[23]
				Indirect 2.033		Photodetector	
ZrS <sub>2</sub>	1T rhombohedral	n-type		Indirect 1.7	CVD	Photovoltaics	[24]
HfS <sub>2</sub>	1T rhombohedral	Semiconductor		Indirect 2.0	ME	FET, phototransistor	[25]
NbS <sub>2</sub>	2H hexagonal	Metal		0.73	CVD	Superconductivity	[26]
TaS <sub>2</sub>	1T rhombohedral	Metal		0.7	CVD	Photodetector,	[27]
	2H hexagonal					Superconductivity	
VS <sub>2</sub>	1T rhombohedral, 2H hexagonal	Metal		0.3	LPE	Gas sensor, supercapacitors, ion battery	[28]
TiS <sub>3</sub>	Monoclinic	n-type		Direct 1.13	ME, CVT	Photodetector, gas sensor	[29]
ZrS <sub>3</sub>	Monoclinic	n-type		Direct 2.56	CVT	Photodetector	[30]
HfS <sub>3</sub>	Monoclinic	Semiconductor		/	CVT	Transistor, photodetector	[31]
TaS <sub>3</sub>	Orthorhombic	Metal		/	/	Transistor, gas sensor	[32]
In <sub>2</sub> S <sub>3</sub>	Tetragonal	n-type		Direct 2.02	CVD	Photodetector, gas sensor	[33]

peeled off several times with adhesive tape and pushed into the substrate surface.[37] After releasing the tape, nanostructured metal sulfides contact the substrate due to the vdW force to the substrate surface (see Figure 2.3a). Li *et al.*[38] prepared three layers TaS<sub>2</sub> nanoflakes on SiO<sub>2</sub>/Si substrate by the Scotch tape-based ME method. Similarly, SnS thin flakes were obtained via tape exfoliation and Au-exfoliation and then transferred onto SiO<sub>2</sub>/n++Si substrates, where a single crystal of SnS was used as the functional material for FETs.[39] ME produces single-crystal flakes of high purity and cleanliness that are suitable for fundamental characterization and for fabricating individual devices.[21, 40] The thickness and size of the nanomaterials synthesis by ME method cannot be systematically controlled, limiting their use in large-scale fabrications. Besides, the ME-metal sulfide flakes need to be transferred to the other substrate for further use.

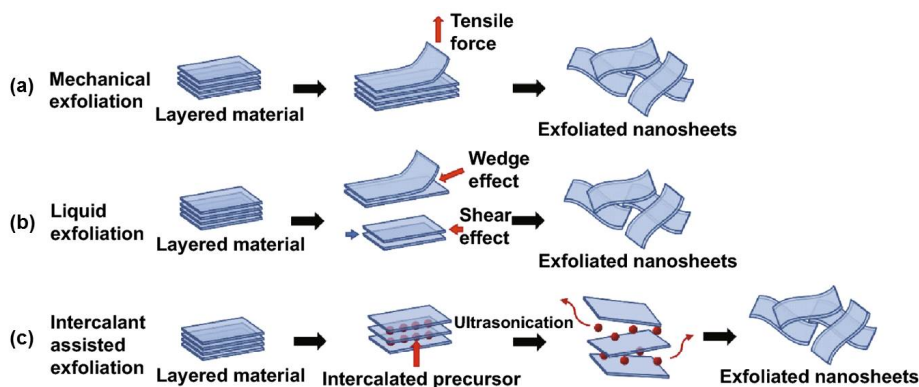


Figure 2.3: Schematic representation of various “top-down” fabrication techniques for large-scale synthesis of electrode materials: (a) Mechanical exfoliation, whereby a tensile force (possibly produced by Scotch tape) can peel off the constituent layers. (b) Liquid exfoliation where the sheets are sheared off by sonicating the bulk material in a liquid medium. (c) Intercalant-assisted exfoliation where a metal ion (usually Li<sup>+</sup>) is used to intercalate into the bulk precursor in a liquid media coupled with ultrasonication, which shears the sheets apart.[41]

### LIQUID PHASE EXFOLIATION

Liquid phase exfoliation (LPE) is another typical method of fabricating nanomaterials, which exfoliates bulk metal sulfides materials in solutions.[42, 43] There are two ways to exfoliate them. One is the exfoliation through mechanical ways such as sonication, stirring, shearing, grinding, and bubbling (see Figure 2.3b). It is a high yield method to obtain exfoliated nanosheets with a reasonable and controllable flake size. LPE nanosheets can easily be used to realize hybrid films and composites by mixing two dispersions. N-methyl-2-pyrrolidone (NMP),[44, 45] dimethylformamide (DMF),[46] dimethyl sulfoxide (DMSO)[47] are typically used as solvents for the exfoliation of metal disulfides. However, because their boiling points are high, it is hard to remove them from the exfoliation solvents and difficult to achieve pristine flakes.

The other method is ionic intercalation, where lithium ions are typically used to intercalate between the metal sulfides layers and enlarge the interlayer spacing (see Figure 2.3c). Matte *et al.*[48] introduced an ion intercalation method to produce monolayer MoS<sub>2</sub> and WS<sub>2</sub>. MoS<sub>2</sub> and WS<sub>2</sub> powder were mixed with n-butyllithium/ hexane solution firstly, and

then soaking the precursor for 72 h at 373 K. However, with the ion intercalation method it is difficult to control the size of the flakes, and it has a low productive.

### 2.2.2. BOTTOM-UP STRATEGIES

The nanostructured metal sulfides flakes based on top-down methods are mostly thick and small. It is necessary to develop methods for synthesizing large-area and uniform layers, so that it can be used in the wafer-scale fabrication of electronic devices and flexible, transparent optoelectronics. Here, the bottom-up method is the build-up of a nanomaterial atom by atom, molecule by molecule or cluster by cluster.

#### CHEMICAL VAPOUR DEPOSITION

Chemical vapour deposition (CVD) has been one of the most current research methods for synthesizing large-area graphene[49, 50] and graphene analogs like boron nitride[51, 52]. For large area metal sulfides fabrication, it begins with solid-state precursors of metal, such as molybdenum trioxide ( $\text{MoO}_3$ ),[53] tungsten trioxide ( $\text{WO}_3$ ),[54] molybdenum pentachloride ( $\text{MoCl}_5$ ),[55] germanium chloride ( $\text{GeCl}_4$ ),[56] stannic iodide ( $\text{SnI}_2$ ),[57] or metal of Mo and Zn.[58, 59] Then,  $\text{H}_2\text{S}$ -gas or vaporized solid S is used as the sulfur source for fabricating metal sulfide thin films on the substrates. The substrates are often silicon, silicon dioxide, silicon nitride, and sapphire. In order to achieve high crystalline and stoichiometric layers, the growth temperatures for CVD are 700-1000 °C (see Figure 2.4a). And the addition of a metal catalyst, such as Au, is encouraged to obtain high-quality films.[60, 61] Recently, Lim *et al.*[62] synthesized wafer-scale, homogeneous, and stoichiometric  $\text{MoS}_2$  layers at a low temperature of 450 °C through a plasma-enhanced CVD (PECVD) technique by using solution-processed  $(\text{NH}_4)_2\text{MoS}_4$  thin films (see Figure 2.4b). Whitham *et al.*[56] deposited  $\text{GeS}_2$  thin films on silicon wafers at a lower temperature of 130 °C through this method, which makes it possible to deposit on plastic and flexible substrates.

Metal-organic CVD (MOCVD) is another way to prepare single crystal epitaxial films, where organometallic materials are used as precursors. This method has been used in the fabrication of  $\text{MoS}_2$ ,[67]  $\text{WS}_2$ , [68]  $\text{SnS}_x$ ,[69, 70]  $\text{ReS}_2$ [71] and  $\text{CdS}$  [72] thin films. Kang *et al.*[66] successfully fabricated monolayer films of  $\text{MoS}_2$  and  $\text{WS}_2$  on a 4-inch  $\text{SiO}_2$  substrate, where they used gas-phase precursors of molybdenum hexacarbonyl [ $\text{W}(\text{CO})_6$ ],  $(\text{C}_2\text{H}_5)_2\text{S}$  and  $\text{H}_2$ . The monolayer metal sulfide films synthesized by MOCVD can be used immediately for the batch fabrication of integrated circuitry consisting of photodetectors, light emitting diodes, and FETs on a wafer scale.

Atomic layer deposition (ALD) is a subclass of the CVD technique, which enabled precise film thickness control because it is grown by exposing the substrate surface to sequential and repeated precursor vapours of gas molecules.[73, 74] ALD is associated with non-overlapping sequential pulses, where the molecules react with the substrate surface in a self-limiting mode. Therefore, based on this method, various inorganic films on wafer-scale can be fabricated with layer-by-layer precision, including oxides, nitrides, metals, and chalcogenides thin films.[75, 76] Recently,  $\text{MoS}_2$  growth by ALD using  $\text{Mo}(\text{CO})_6$  and dimethyldisulfide ( $\text{CH}_3\text{SSCH}_3$ , DMDS) as Mo and S precursors on a  $\text{SiO}_2/\text{Si}$  substrate at 100 °C has been demonstrated.[77] Other metal sulfides, such as  $\text{WS}_2$ ,  $\text{SnS}_2$ ,  $\text{SnS}$ , and  $\text{ZnS}$ , have been successfully deposited on  $\text{SiO}_2$  substrates.[78, 79]

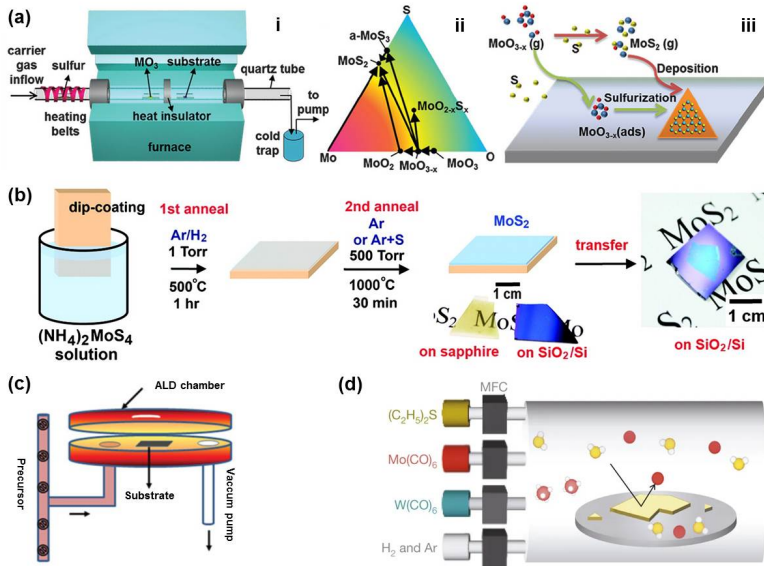


Figure 2.4: Three types of growth routes for TMDs. (a) LPCVD for the growth of MoS<sub>2</sub> from MoO<sub>3</sub> precursors.[63] (b) PECVD synthesis of MoS<sub>2</sub> from (NH<sub>4</sub>)<sub>2</sub>MoS<sub>4</sub> precursor.[64] (c) Schematic diagram of the ALD system.[65] (d) Diagram of our MOCVD growth setup.[66]

The greatest advantage of the CVD method is that the large-size single layer or few-layer 2D metal sulfides can be synthesized. However, it is still difficult to prepare heterostructures (i.e. MoO<sub>3x</sub>/W<sub>x</sub>S<sub>2</sub> monolayer or multilayers) because WO<sub>3</sub> or MoO<sub>3x</sub> requires a higher temperature of 1000 °C for vaporization.

### PULSED LASER DEPOSITION.

Pulsed laser deposition (PLD) is a physical vapor deposition (PVD) method, which can reproduce the components of the target precisely onto the substrate. Unlike CVD, it has a lot of advantages, including low cost, high growth rate, good control of thickness and morphology, low growth temperature, and its ability to grow on the chemically active surface.[80, 81] Recently, Serrao *et al.*[82] prepared highly crystalline thin films of MoS<sub>2</sub> on aluminium oxide (Al<sub>2</sub>O<sub>3</sub>)(0001), gallium nitride (GaN)(0001) and silicon carbide-6H (SiC-6H)(0001) substrates. Serna *et al.*[83] realized the deposition of MoS<sub>2</sub> layers on single-crystal (sapphire and quartz), polycrystalline (HfO<sub>2</sub>), and amorphous (SiO<sub>2</sub>) substrates. Loh *et al.*[84] report the fabrication of ultrathin layers of hybrid 2H-1T WS<sub>2</sub> grown by PLD on substrates of the noble metals Ag and Au. Similarly, SnS epitaxial films were grown on MgO(100) substrates by PLD using a H<sub>2</sub>S gas as an S source. By using a Nd:YAG laser to irradiate the metal sulfides target, nanoparticles (NPs) of SnS<sub>2</sub> and ZnS thin films have been synthesized with pulsed laser ablation technique.[85, 86] Thermal evaporation is one of the simplest techniques of PVD. Shimizu *et al.*[87] used thermal evaporation to synthesize gold (Au) mediated hexagonal wurtzite structured ZnS nanostructures including nanobelts, nanosheets, and nanorods. A one-step thermal evaporation synthesis of ZnO-ZnS heterostructure nanowire (NW) arrays was also carried out using ZnS powders.[88]

However, there are many sulfur defects generated from the pulsed laser, when the growth temperature is less than 300 °C.

## 2

### HYDROTHERMAL AND SOLVOTHERMAL SYNTHESIS.

The hydrothermal technique is one of the best methods to produce a variety of pure and nanostructured materials with desired properties. Generally, metal salts are used as precursors in the hydrothermal system, which reacts with sulfur or other sulfide source materials in a stainless-steel autoclave at  $\sim 80$ -200 °C. The properties of the particles can be controlled by changing the pressure and temperature conditions.[89, 90] Yan *et al.*[91] developed WS<sub>2</sub> quantum dots (QDs) with high quality via ultrasonication and a hydrothermal process from bulk WS<sub>2</sub>. The solvothermal method is similar to the hydrothermal method except that an organic solvent is used, instead of water, as the precursor medium. Unlike the hydrothermal approach, the reaction temperature is above the critical point of the solution; therefore, the pressure is high.[92, 93] Bhord *et al.*[94] reported the synthesis of SnS nanorods through a simple solvothermal method, which was carried out using precursors of stannous chloride (SnCl<sub>2</sub>·H<sub>2</sub>O), sodium sulfide (Na<sub>2</sub>S) and the solvent of dimethylformamide (DMF). Hydrothermal and solvothermal methods are widely used for synthesizing porous and heterostructured materials, but randomly aligned nanostructures can be obtained.

Other bottom-up methods, such as combustion, micro-emulsion, precipitation, sulfidation, microwave irradiation, electrodeposition, and spray pyrolysis, are used for synthesizing metal sulfides. Moreover, a variety of other techniques, i.e., ion exchange method, template engaged technique, and self-assembly method, etc. have been applied for preparing metal sulfides.

In my work, high-quality single-crystal SnS nanoflakes were obtained through ME methods; to achieve large surface area and high-quality materials, I used LPE method for preparing SnS nanosheets which were the foundation materials of SnO<sub>x</sub>/SnS heterostructures; to improve charge transfer in the interface, few-layer WS<sub>2</sub> thin film that grown through CVD method was adapted for forming WS<sub>2</sub>/IGZO heterojunction.

## 2.3. DEVICE FABRICATION

In order to fabricate metal sulfides-based devices, suspension and transfer methods are often required.

### 2.3.1. SUSPENSION METHOD

There are two suspension methods for fabricating the device. One is dip coating metal sulfide nanoflakes, nanosheets, nanorods, or nanotubes to the substrate with pre-made electrodes (see Figure 2.5a). The other way is evaporating/sputtering metal (Ti, Cr, Au, Pt, and Pb) to the top of metal sulfide thin film that was synthesized on the substrate through bottom-up methods (see Figure 2.5b). The metal sulfide-based transistor can be obtained through the same process, as shown in Figure 2.5c,d). It is an efficient way to fabricate the device through the suspension method, however, the uniformity of nanomaterials coverage in the electrodes is uncontrolled.

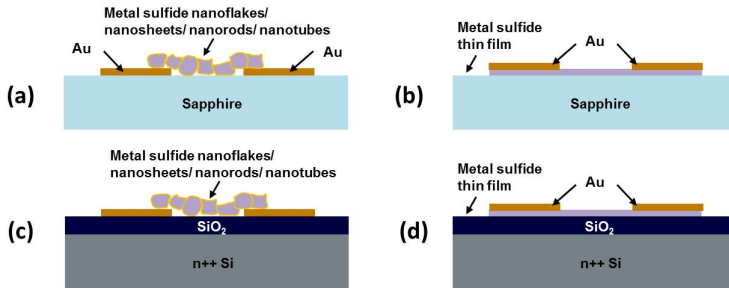


Figure 2.5: Schematic of the structure of metal sulfide-based gas sensor. (a) Dip coated and (b) bottom-up synthesized metal sulfide-based chemiresistor gas sensor. (c) Dip coated and (d) bottom-up synthesized metal sulfide-based transistor.

### 2.3.2. TRANSFER METHOD

To extend the applications of metal sulfides, people tried to transfer them to different target substrates to realize various functions. For wearable electronics applications, metal sulfides have excellent flexibility, thus they can be applied to polymer substrates such as poly(methyl methacrylate) (PMMA), polyaniline (PI), and polyethylene terephthalate (PET). However, they typically cannot be synthesized on the flexible substrates directly due to the high synthesis temperature. Therefore, it needs to be transferred onto flexible substrates from another (growth) substrate. There are mainly two transferring methods, dry transfer and wet transfer. Usually, a dry transfer is used for the ME bulk crystal, and wet transfer is used in the CVD-grown metal sulfides.

In the dry mechanical method, first ME is performed and then the method in Figure 2.6a,b is used to transfer this flake onto a target substrate.[95] For the wet transferring method, an adhesion layer (polystyrene or PMMA) is spin-coated on metal sulfides. Then, it separated the metal sulfides film from the original substrate through chemically etching or just through the film's surface tension. Then, the floating adhesion layer/ metal sulfides are picked up by the target substrate. Finally, the adhesion layer can be removed by acetone. (see Figure 2.6c). A large-size thin film of metal sulfide can be transferred to any substrate.

However, the surface of the thin film is easily broken during the process. For instance, the pressure from the stamp during the dry-transfer process or the surface tension of water or solution can induce the generation of a crack in the thin film. Besides, the removal of the polymer layer is usually incomplete and results in surface contamination because of undissolved polymer residues. The polymer contaminants have adverse effects on the intrinsic properties of metal sulfides, and the reliability of devices fabricated.

## 2.4. SENSING PARAMETERS

There are a set of parameters defined to evaluate and compare the performance of different sensors, including response, sensitivity, selectivity, limit of detection, dynamic range, working temperature, response and recovery time, and stability.

**Response.** The response is defined as the change in measured resistance ( $R$ ), current ( $I$ ), conductance ( $G=I/V$ ; the symbol is not to be confused with Gibbs free energy), capacitance ( $C$ ), power gain, and resonant frequency ( $f_0$ ) for a given analyte concentration unit with

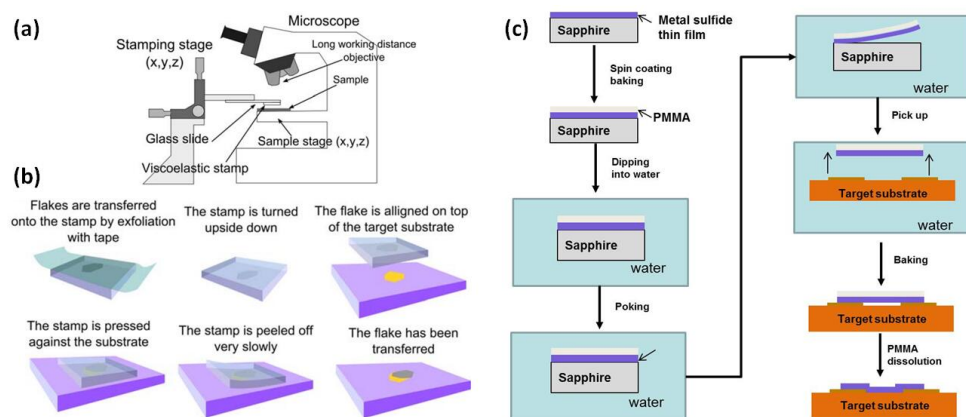


Figure 2.6: (a) Schematic diagram of the dry transfer setup. (b) Diagram of the dry transfer process.[96] (c) Schematic of the surface-functionalized wet transfer process.

respect to the signal under the absence of analyte molecules. It is defined as:

$$(X_{\text{gas}} - X_0)/X_0 = \Delta X/X_0 \quad (2.1)$$

where  $X=R, I, G, C$ , or gain,  $X_{\text{gas}}$  is the device's signal due to the presence of the target gas and  $X_0$  is the baseline signal (no analyte gas). Thus, it can be inferred from Eq. 2.1 that different gas concentrations will produce different sensor responses, as presented in Figure 2.7(a).

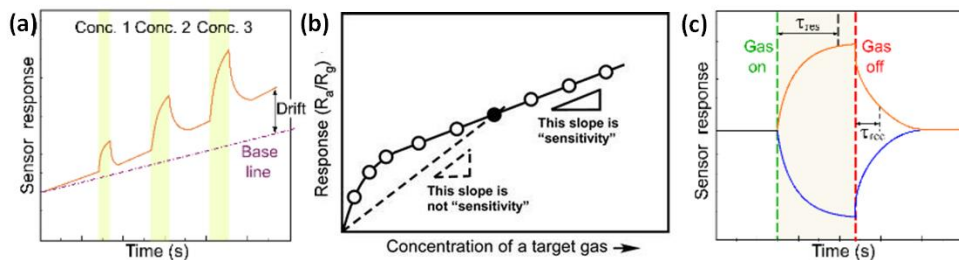


Figure 2.7: Sensing parameters (schematics). (a) Time dependence of the sensor response for different gas concentrations. (b) Response curve to chemical doping. Different responses can be observed for electron donating gas species (orange curve) and electron withdrawing gas species (blue curve). The response time and recovery time are shown as  $t_{\text{res}}$  and  $t_{\text{rec}}$ , respectively.[97] (c) Typical relationship between gas response and target gas concentration. [98]

**Sensitivity.** The gas sensitivity of a device is the slope of the calibration curve, that is, sensor response versus target gas concentration, according to the International Union of Pure and Applied Chemistry (IUPAC) definition. The maximum sensitivity is then achieved when working in the linear regime, as shown in Figure 2.7(b). Eventually, the sensor is reaching saturation when these curves flatten. If it is difficult to obtain a linear relationship,

for instance different slope values are observed in different concentration ranges, the term "response" is recommended to be used as a measure of sensor performance.

**Selectivity.** The selectivity refers to discrimination between gasses in a mixture, allowing adsorption of the desired species while remaining insensitive to others. The selectivity coefficient/factor ( $K$ ) of "target gas" to another gas is defined as:

$$K = S_A/S_B \quad (2.2)$$

where  $S_A$  and  $S_B$  are the sensitivities of the sensor to a specified target gas (A) and another gas (B), respectively.

**Limit of detection (LOD).** LOD is the smallest concentration of an analyte that can be detected concerning the noise level of the detector, under a given set of experimental conditions such as humidity, pressure, and temperature. Mathematically this is defined as:

$$\text{LOD} \geq 3\sigma/S \quad (2.3)$$

where  $S$  is the sensitivity and  $\sigma$  is the noise level in the absence of the analyte gas.

**Dynamic range** is the analyte concentration range between the LOD and the highest concentration detectable before saturation of the device response.

**Working temperature (T)** is the temperature that corresponds to maximum sensitivity.

The **response time** ( $t_{\text{res}}$ ) and the **recovery time** ( $t_{\text{rec}}$ ) are two critical response characteristics. As shown in (see Figure 2.7c), the ( $t_{\text{res}}$ ) is defined as the time taken to achieve 90% of the total response of the device. Initially, the response varies quite rapidly, stabilising when approaching to the equilibrium value. The ( $t_{\text{rec}}$ ) is defined as the time required for recovering 90% of the original value of the physical quantity to be measured. The response characteristics of a specific device might vary for different gases, but they are also highly dependent on the device architecture, the exposure time, and the analytical techniques used to generate the signal.

The **stability** describes the ability of a sensor to provide consistent and reproducible results for a specific time. This parameter becomes of high importance when sensors are exposed to hazardous, corrosive, or high-temperature atmospheres.

An ideal electrical sensor would possess high sensitivity, dynamic range, high selectivity, stability, low LOD, excellent linearity, and small recovery and response times. Ultimately, all these parameters are used to characterize a particular material or device's properties, determining its final application.

## 2.5. VARIOUS SENSING CONCEPT OF METAL SULFIDE-BASED DEVICES

### 2.5.1. CHEMIREISTOR GAS SENSORS

#### PRISTINE METAL SULFIDES-BASED GAS SENSORS

As mentioned in Section 1.3.3, the basic sensing principle of metal sulfides acts as charge acceptors or donors. Their shallow valence band, small effective mass, and diverse structures enable a robust quantum size effect and promising applications in gas sensing. The typical direct narrow band gap IV-VI compound semiconductors, such as SnS, PbS, and GeS, have similar puckered structures as black phosphorus.[99, 100] and used for detecting

toxic ( $\text{NO}_2$ ,  $\text{NH}_3$ ,  $\text{H}_2\text{S}$ ) and organic (acetone, ethanol) gas molecules. The response and recovery time is fast (5 s-36 s). [8, 101, 102] The classical II-VI compound semiconductors mostly have a direct wide band gap, including CdS and ZnS. They have high response and selectivity to VOCs gases, including isopropanol, methanol, ethanol, acetone, and methylbenzene. However, most of their operating temperature is relatively high (200 °C-300 °C). [103, 104] Other metal monosulfide-based gas sensors, like CuS, NiS also have potential applications in  $\text{H}_2$  and  $\text{SO}_2$  gas sensing. [105–107] According to Kim's research, 75% of publications up to 2017 are focused on  $\text{MoS}_2$  along with  $\text{WS}_2$  (14%),  $\text{SnS}_2$  (9%), etc. [108] The predominance of  $\text{MoS}_2$  over other metal disulfide is because the material is the easiest material to synthesize and the most stable among transition metal sulfides. As shown in Figure 2.8, most of the metal sulfides are composed of metal atoms sandwiched between two layers of hexagonally disposed of close-packed sulfur (S) atoms; the weak vdW forces connect the adjacent S layers. They have a larger electronegativity, potentially enhancing gas adsorption sites. Thus various transition metal sulfides, including  $\text{ReS}_2$ ,  $\text{TaS}_2$ , and  $\text{VS}_2$ , were used for gas sensing in  $\text{NO}_x$ ,  $\text{NH}_3$ ,  $\text{O}_2$ , and humidity, and have very low LOD, high response and low operation temperature (OT).

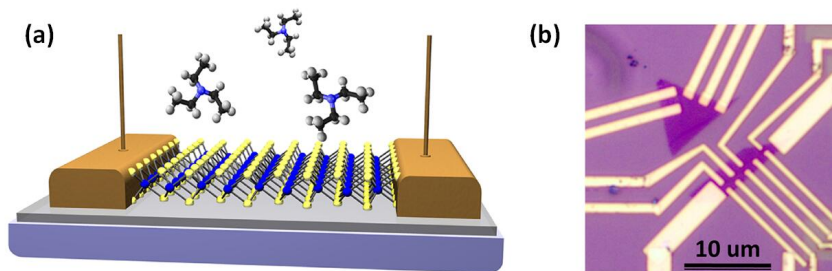


Figure 2.8: Typical pristine metal sulfide-based gas sensors. (a) Schematic and (b) optical image of the  $\text{MoS}_2$  monolayer sensor. [109]

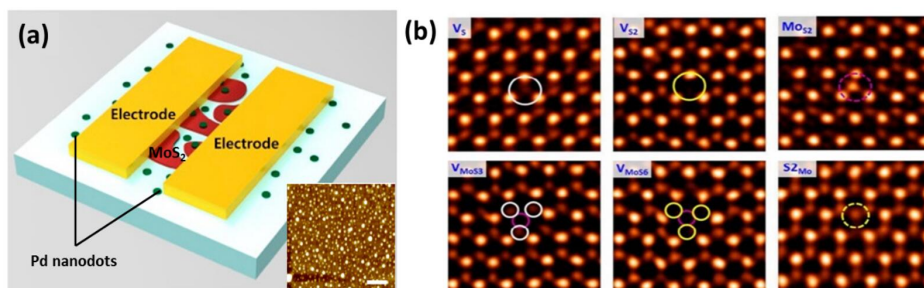


Figure 2.9: (a) Schematic of Pd-doped  $\text{MoS}_2$ -based sensor. Inset image is the AFM image Pd on  $\text{SiO}_2$  substrate. The scale bars indicate a distance of 400 nm. [110] (b) Image analysis for intrinsic point defects in ML  $\text{MoS}_2$ . [111]

Table 2.2: Literature study on gas sensing performance of doped or defective metal sulfide nanomaterials or devices.

Material	Type	Analyte	Method	Performance	Ref.
MoS <sub>2</sub>	Pd-doped	H <sub>2</sub>	Experiment	LOD: 50 ppm, RT	[110]
	Pt-doped	H <sub>2</sub> O	Experiment	Response:~4000 (85%RH), Response /recovery time 91.2 s/153.6 s	[112]
	Al-, Si-, P-doped	NO <sub>2</sub> , NH <sub>3</sub>	DFT	Si-doped MoS <sub>2</sub> is the most stable system.	[113]
	Ni-doped	H <sub>2</sub> S, SO <sub>2</sub>	DFT	Chemisorption	[114]
	Ni-doped	COF <sub>2</sub> , CF <sub>4</sub>	DFT	Interaction between COF <sub>2</sub> molecule and Ni-doped MoS <sub>2</sub> is stronger than that of CF <sub>4</sub> .	[115]
	Cu-doped	CO, NO	DFT	Strong interaction, low powered single electron transistor	[116]
	Au-, Pt-, Pd-, or Ni-doped	CO, NO	DFT	Chemisorption	[117]
	V-, Nb-, Ta-doped	CO, NO <sub>2</sub> , H <sub>2</sub> O, NH <sub>3</sub>	DFT	The doped metal atoms interact strongly on the S defect site of monolayer MoS <sub>2</sub> .	[118]
	B, N, P and Al doped	SO <sub>2</sub>	DFT	Al/MoS <sub>2</sub> has the best adsorption energy.	[119]
	Ni-, Fe-, Co-doped	SO <sub>2</sub>	Experiment		[120]
	Au-, Cu-, and AuxCuy-doped	CO, H <sub>2</sub> O	DFT	CO strongly binds to MoS <sub>2</sub> in presence of Au, Cu, atom or Au <sub>x</sub> Cu <sub>y</sub> clusters	[121]
	WS <sub>2</sub>	Ag nanowires	NO <sub>2</sub>	Experiment	Response (667%)
SnS <sub>2</sub>	2D (sulfur vacancies)	NH <sub>3</sub>	Experiment	Response (420%)	[123]

### FUNCTIONALIZED METAL SULFIDE-BASED GAS SENSORS

Doping and defect substitution is a versatile and new tool for changing the chemical and electronic properties of 2D layered materials and boosting these materials. Chemical doping is an effective way to alter the binding configurations, modify electronic and transport properties, and enhance the application of materials as a gas sensor. Chemisorption is found to be thermally more stable and enhanced by dopants. Similarly, the introduction of defects can change the electronic structure, and chemical reactivity of the metal sulfide's surface, more and more groups used defective metal sulfide to obtain greater sensitivity. Ma *et al.*[117] studied the adsorption of CO and NO molecules on the Au, Pt, Pd, or Ni-doped MoS<sub>2</sub> monolayer through first-principles analysis. The effect of non-metal doping of MoS<sub>2</sub> with boron, phosphorus and chlorine for NO, NO<sub>2</sub>, and NH<sub>3</sub>. [113] Figure 2.9 shows a hydrogen sensor with few-layered Pd-doped MoS<sub>2</sub> and various point defects in CVD-MoS<sub>2</sub>. [110, 111] The gas sensing performance has been improved after functionalization. [124] Qin *et al.*[123] demonstrated an enhanced NH<sub>3</sub> sensor based on 2D SnS<sub>2</sub> with sulfur vacancies, which are synthesized by chemical exfoliation. Compared with the bulk SnS<sub>2</sub> that shows none response to NH<sub>3</sub>, the gas sensors exhibit excellent NH<sub>3</sub> gas sensing performance at room temperature. When exposed to 500 ppm NH<sub>3</sub>, the response time, 16 s, is the shortest among all the NH<sub>3</sub> gas sensors based on metal sulfides. The enhanced sensitivity is dominated by the high energy defect sulfur vacancies on the surface of 2D SnS<sub>2</sub>. However, most of the gas sensing behaviours of functionalized metal sulfides were analyzed through

density functional theory (DFT) calculations, which are listed in Table 2.2. It is a lack of experimental reports on the influence of defects on the gas sensing performance of metal sulfide-based devices.

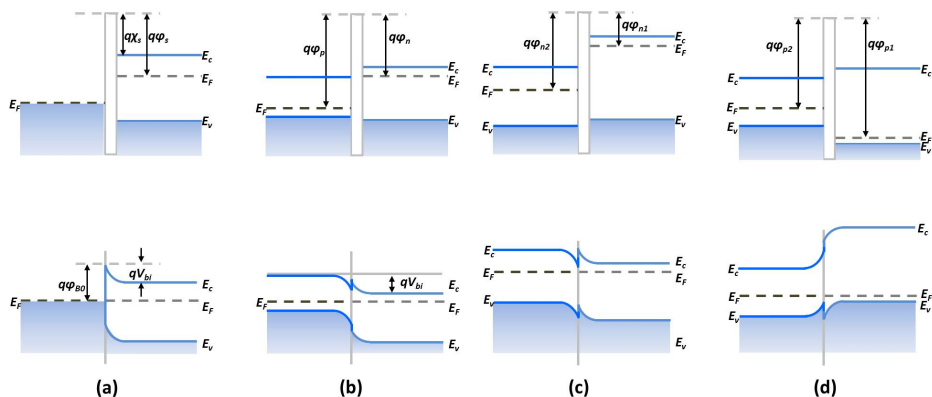


Figure 2.10: Band alignment of (a) Schottky diode, (b) p-n junction, (c) n-n junction, and (d) p-p junction.  $E_c$ ,  $E_F$ , and  $E_v$  are the conduction band edge, Fermi level, and valence band edge of the semiconductor, respectively.  $\phi_m$ ,  $\phi_s$ , and  $\phi_s$  are the metal work function (measured in volts), the semiconductor work function, and electron affinity, respectively.  $\phi_{B0}$ ,  $V_{bi}$ , and  $\chi_n$  are the barrier height, built-in potential barrier, and depletion width, respectively. Other symbols have their usual meaning.

### 2.5.2. SCHOTTKY DIODE

Typically, the metal-semiconductor (M-S) junction is a type of heterostructure where metal is in close contact with a semiconductor material. The rectifying M-S junction is called a Schottky junction, while the non-rectifying junction forms ohmic contact. Recently, researchers found that when atomically thin and semimetallic 2D graphene or rGO contact with a semiconductor, they can also create a Schottky or an Ohmic contact, which depends on their electron affinity values. As shown in Figure 2.10a, the electrons flow from the conduction band to the semiconductor layer until they reach equilibrium. A depletion region is generated when the charge flows across the junction. It forms a barrier of  $V_{bi}$  across the junction and impedes further charge transport across it. The barrier height from the metal side remains unchanged, while the change of barrier height ( $\phi_B$ ) of semiconductor could depend on the bias across the junction. The adsorption of analytes is a kind of dopants for the semiconducting material, which could change the doping level of materials and modulate the  $\phi_{B0}$  in turn. Because the formation of the Schottky junction enables high gas sensing performance, the modulation of band alignment has been widely used during Schottky diode-based gas sensor designing.

For metal-metal sulfide junction, many groups modulate the gas sensing behaviours through change the materials of electrodes. Kim *et al.*[125] demonstrated improved  $CO_x$  gas sensitivity of  $MoS_2$ -based gas sensor by controlling the  $\phi_B$ . They used different metal as the materials of electrodes, Au, Ag, and Al, and found that they have different selectivity of gas molecules. As shown in Figure 2.11, because of the Schottky barrier modulation (SBM) effect, the response to CO gas is improved in devices with an increase in  $\phi_B$ . Es-

pecially, the MoS<sub>2</sub> gas sensor on different electrodes shows responds selectively to CO and CO<sub>2</sub> gases, indicating the Schottky contacted metal sulfide-based sensor could be applied for improving the sensitivity. Besides, vdW vertical heterojunctions of graphene and semiconductors have attracted considerable attention as emerging transducers for chemical sensors. Similarly, an Schottky barrier can be formed in the interface due to the difference in the work function. Unlike conventional Schottky diode gas sensors, graphene/semiconductor heterojunction has more adsorption sites on the surface of graphene, inducing efficient transduction. Pham *et al.*[126] comparatively analyzed the gas sensing performances of CVD MoS<sub>2</sub> with Au metal electrodes (Au-MoS<sub>2</sub>-Au), graphene electrodes (Gr-MoS<sub>2</sub>-Gr), and graphene/Au electrodes (Au/Gr-MoS<sub>2</sub>-Gr/Au). The resulting Au/Gr-MoS<sub>2</sub>-Gr/Au optoelectronic gas sensor under red light illumination showed a significant enhancement of the device sensitivity toward ppb level of NO<sub>2</sub> gas exposure reaching 4.9%/ppb (4900%/ppm) after using graphene/Au electrodes.

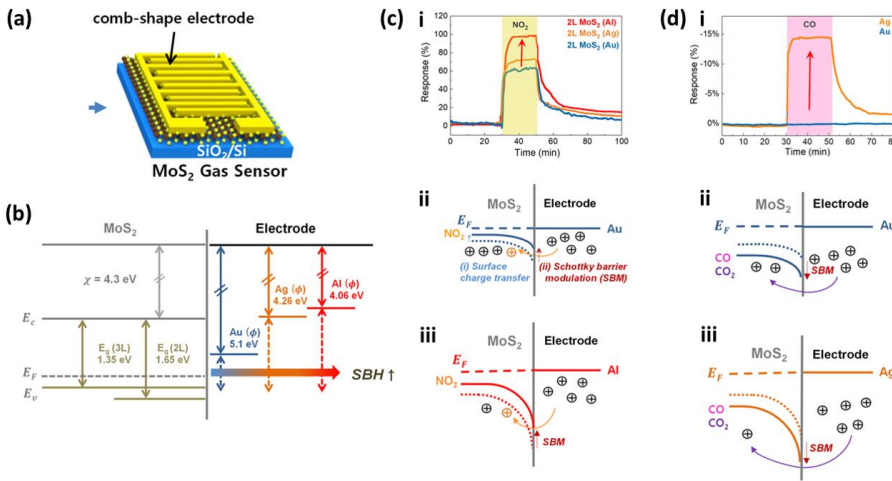


Figure 2.11: (a) Schematic of the fabrication of the metal-MoS<sub>2</sub> Schottky contacted gas sensor. (b) Band diagram of MoS<sub>2</sub> with metal electrodes. (c) i) Sensing characteristics of NO<sub>2</sub> for 2L MoS<sub>2</sub> with Al, Ag, and Au electrodes. Band diagram of ii) Au/MoS<sub>2</sub> gas sensor and iii) Al/MoS<sub>2</sub> gas sensor before and after NO<sub>2</sub> exposure. (d) Sensing characteristics of CO for 2L MoS<sub>2</sub> with Au and Ag electrodes. Band diagram of ii) Au/MoS<sub>2</sub> gas sensor and iii) Al/MoS<sub>2</sub> gas sensor before and after CO exposure. [125]

### 2.5.3. HETEROJUNCTIONS BASED GAS SENSOR

Heterojunctions based on metal sulfide can be easily constructed and present superior electric and photoelectric properties compared with pristine metal sulfide.[127, 128] 2D heterojunctions can be classified into three typical band alignments (Figure 2.12).[129] Type-I band alignment is with a straddling gap, resulting in both electrons and holes accumulating on the same side. Type-II band alignment is with a staggering gap and is the most widely investigated heterojunction, where the electrons and holes are separated into different layers. Type-III band alignment is with a broken gap and particularly appropriate for tunneling applications. Because the conduction band and the valence band overlap, the tunneling transport of electrons from one side to the other is feasible. Type-III alignment has a

stronger ability to separate electrons and holes than that of type-II, which can contribute to reducing the interfacial Coulomb scattering.

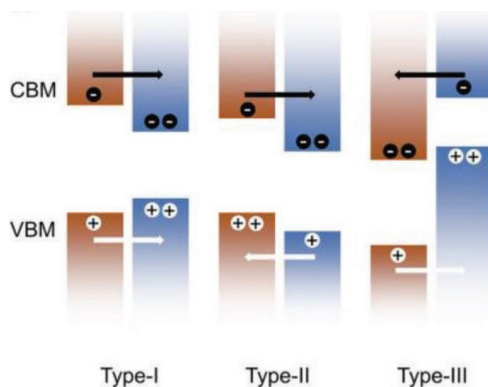


Figure 2.12: Schematic diagrams of type-I, II, and III band alignment heterojunctions. [129]

### P-N JUNCTION

A p-n heterojunction usually present type-II or type-III band alignment due to the special position of their Fermi levels in the bandgap. As shown in Figure 2.10b, electrons and holes flow in reverse directions until equilibrium is achieved, which forms a thick space-charge region that further narrows the electrical transport channels. Through the hydrothermal method, MoS<sub>2</sub>/SnO<sub>2</sub> p-n heterojunctions have been fabricated and used for ethanol, trimethylamine (TEA), and NO<sub>2</sub> gas sensing, see Figure 2.13.[130–132] They exhibited high sensitivity, lower OT, excellent sensing selectivity, and outstanding long-term stability. Mostly, in p-n heterostructure gas sensors, the main current often flows through either of two dissimilar materials. The major conduction path is determined by the difference in the areal coverage of the two materials present in the heterostructure devices. If the areal coverage of one material falls below a certain value compared to the other material with higher areal coverage, the sensing response of the heterostructures is dominated by the gas sensing properties of the material with higher areal coverage. Moreover, the effects of the interfacial bonds on the gas-sensing properties are necessary.[133] Since a random connection of two different crystals would lead to dangling bonds and voids in the interfacial region, the charge transfer is hindered to a large extent. Electrons can be trapped in the interfacial dangling bonds; thus, it needs additional energy to cross the electron-depletion layer induced by the interface states. It will reduce the number of electrons traveling across the interface. Therefore, a low density of the interface state at the contact interface is favored to promote the desired electron transfer and further enhance the gas-sensing performances of p-n junction-based devices.

### N-N OR P-P JUNCTION

Recently, various n-n and p-p heterostructures have been proposed to improve the gas sensing performances. Most of the n-n and p-p junction gas sensors are based on metal oxide nanomaterials, such as SnO<sub>2</sub>/TiO<sub>2</sub>, [134] SnO<sub>2</sub>/ZnO, [135] SnO<sub>2</sub>/Sn<sub>3</sub>O<sub>4</sub>, [136] TiO<sub>2</sub>/ZnO, [137]

CaO/ZnO,[138] and ZnO/In<sub>2</sub>O<sub>3</sub>,[139] whose enhanced performances are attributed to the heterocontact of the two semiconductor surfaces. Regards to metal sulfides-based n-n and p-p heterojunction, Zhang *et al.* [140] optimized the NH<sub>3</sub> sensing behaviour by using SnS<sub>2</sub>/ZnS hierarchical nanoflowers. Benefited from metal oxide hybrids, the gas sensors based on metal sulfide n-n junction, such as CdS/CeO<sub>2</sub>,[141] CdS/ZnO,[142] ZnS/ZnO,[143] and ZnS/CuO,[144] have been used for detecting VOC toxic gases. The electrons flow across the heterojunction from the higher Fermi level to the lower one, which induces band bending and the formation of depletion layer in the interface. It improves the transfer efficiency of the interfacial charge and increases the adsorption of oxygen species. A depletion layer and accumulation layer is formed in the case of n-n (Figure 2.10c) and p-p (Figure 2.10d) heterointerfaces, respectively. The depletion/accumulation layer could be further affected by the adsorption of oxygen gas onto the surface, which contracts the conduction channel by extracting (giving) electrons from the conduction band of the semiconductor and enhances the response toward the analytes. The semiconductor with a lower Fermi energy acts as a metal in the Schottky junction. At that point, introducing different analytes at the heterointerface could alter the conductivity in various ways depending on the types of analyte and heterointerface (n-n or p-p) present at the heterojunction.

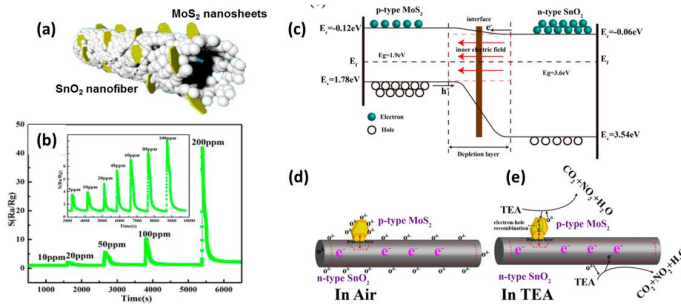


Figure 2.13: (a) Schematic of MoS<sub>2</sub>/SnO<sub>2</sub> heterojunctions. (b) Dynamic response of MoS<sub>2</sub>/SnO<sub>2</sub> heterojunction toward various TEA concentrations at 230 °C. (c) Schematic illustration of the energy band of MoS<sub>2</sub>/SnO<sub>2</sub> heterojunctions. Model for the MoS<sub>2</sub>/SnO<sub>2</sub> heterojunction sensors in air (d) and TEA vapor (e).[131]

#### 2.5.4. FIELD-EFFECT TRANSISTORS (FETs)

A field-effect transistor (FET) gas sensor has attracted many research interest because of its sensitive detection and miniaturization.[145, 146] As shown in Figure 2.14, a typical FET sensor consists of a sensing semiconductor as a channel material, and two metal electrodes served as the source and drain electrodes, respectively, through which the conductance of the channel can be modulated by applying different bias voltages on the gate electrode through a thin dielectric layer. Gas detection can be realized by measuring the change of drain current before and after exposure to the target gases under a constant voltage. The electronic structure of the sensing material will be changed when adsorbing the gas molecules, causing the change of its conductance. 2D semiconducting sheets are of particular interest in FETs due to their high charge carrier mobility and ultra-high surface-to-volume ratio, resulting in high sensitivity. FETs device has been used to detect many kinds of gases, such as CO, NO, NH<sub>3</sub>, NO<sub>2</sub>, SO<sub>2</sub>, H<sub>2</sub>, and VOCs. They can be characterized also

by low power requirement and can be miniaturized for the development of portable sensors, eventually supported on flexible foils. However, most of the FET gas sensors are still not enough in the aspects of device instability, poor reproducibility, and limited large-scale production, even though in a fast response and selectivity.[147]

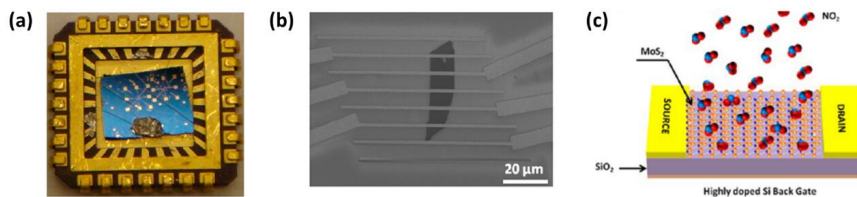


Figure 2.14: (a) Optical image of the MoS<sub>2</sub> transistor sensor on the chip. (b) SEM image of a two-layer MoS<sub>2</sub> transistor. (c) Schematic of MoS<sub>2</sub> transistor sensor.[148]

## 2.6. METAL SULFIDES-BASED DEVICES FOR NO<sub>2</sub> AND HUMIDITY SENSING APPLICATIONS

### 2.6.1. NITRIC DIOXIDE (NO<sub>2</sub>) SENSORS

The most abundant air pollutants, NO<sub>2</sub>, can irritate the human respiratory system at high concentrations. Long exposures in low NO<sub>2</sub> concentrations induce the development of asthma and respiratory symptoms. Different types of NO<sub>2</sub> gas sensors based on metal sulfides are summarised in Table 2.3. Wang *et al.*[101] synthesized large-size SnS thin crystals and used them for gas sensing. The devices present high sensitivity, superior selectivity, low detection limit ( $\ll 100$  ppb), and reversibility to NO<sub>2</sub> at room temperature. PbS thin films were synthesized and applied in NO<sub>2</sub> concentration detection, which exhibited a response of 35 % for 50 ppm NO<sub>2</sub> at 150 °C with a rapid response time of 6 s.[149] Recently, Sonker *et al.*[150] used a sol-gel method for fabricating CdS nanoparticles, which can detect 20 ppm NO<sub>2</sub> gas with a response of  $\sim 173$  at 70 °C. Donarelli's group [151] and Kim's group [152] prepared MoS<sub>2</sub> flakes-based chemiresistor gas sensors through LPE methods, and investigated the NO<sub>2</sub> and O<sub>2</sub> sensing behaviour, respectively, which showed low LOD of ppb level. Xu *et al.*[153] synthesized ultra-thin WS<sub>2</sub> nanosheets through hydrothermal and calcination process, which showed a high response of 9.3% after exposure to 0.1 ppm NO<sub>2</sub> gas at room temperature (RT). Kim *et al.*[154] proposed a gas sensor for detecting acetone and NO<sub>2</sub> based on large-area WS<sub>2</sub> nanosheets which were synthesized by sulfurizing the deposited WO<sub>3</sub> atomic layer. The response after exposure to 500 ppm NO<sub>2</sub> gas was about 16% but with incomplete recovery. The LPE-WS<sub>2</sub> flakes-based gas sensor showed p-type sensing behaviour and excellent detection limits in dry air for NH<sub>3</sub> and NO<sub>2</sub> (1 ppm and 100 ppb, respectively) operationally at 150 °C.[155] Ou *et al.*[156] fabricated SnS<sub>2</sub> flakes-based gas sensor, presenting high selective and reversible NO<sub>2</sub> sensing at 160 °C, where the LOD at ppb levels. Moreover, the gas-sensing performance of WS<sub>2</sub> was improved by surface functionalization. Ko *et al.*[122] proved that the WS<sub>2</sub> gas sensor showed a dramatically improved response (667%) and recovery upon NO<sub>2</sub> exposure after AgNW functionalization.

Regarding metal-metal sulfide Schottky junction, many groups modulate the gas sens-

ing behaviours through changing the electrodes. Liu *et al.*[157] noticed that there is a considerable level of Schottky barrier existing in the Ti/Au electrodes and CVD-MoS<sub>2</sub> contact interface because the output characteristics of the devices showed the rectifying characteristics typically. The devices showed conductance change by 2-3 orders of magnitude upon exposure to sub-ppb level concentrations of NO<sub>2</sub> and NH<sub>3</sub>. Besides, vdW vertical heterojunctions of graphene and semiconductors have attracted considerable attention as emerging transducers for chemical sensors. Similarly, an Schottky barrier ( $\phi_B$ ) can be formed in the interface due to the difference in the work function. Unlike conventional Schottky diode gas sensors, graphene/semiconductor heterojunction has more adsorption sites on the surface of graphene, inducing efficient transduction. Tabata *et al.*[158] deeply analyzed the NO<sub>2</sub> gas sensing performance of the Graphene/MoS<sub>2</sub> heterojunction-based gas sensor, where the  $\phi_B$  was modulated by bias- and gate-voltage.

Table 2.3: Literature Study on NO<sub>2</sub> Gas Sensing Performance of Metal Sulfide-based Heterostructures Devices.

Material	Sensing type	Synthesis method	C(NO <sub>2</sub> ) (ppm)	Response (%)	LOD (ppb)	$t_{res}$ (s)	$t_{rec}$ (s)	OT(°C)	Ref.
SnS	Chemiresistor	Solvothermal	0.1	20	/	NA	5	RT	[101]
CdS	Chemiresistor	Chemical route	20	17300	/	331	207	70	[150]
PbS	Chemiresistor	Chemical bath deposition	100	74	/	20	36	38	[8]
MoS <sub>2</sub>	FET	ME	5	15	/	~800	1500	RT (green light)	[148]
WS <sub>2</sub>	Chemiresistor	Hydrothermal	0.1	9.3	100	300	1500	RT	[153]
SnS <sub>2</sub>	Chemiresistor	HEBM	10	2000	/	6	40	250	[154]
	Chemiresistor	Solvothermal	10	3633	/	~170	~140	120	[152]
NbS <sub>2</sub>	Chemiresistor	CVD	10	2832	241.02	3000	9000	RT	[26]
Ag doped-WS <sub>2</sub>	Chemiresistor	ALD, deposition	500	667	/	300	600	RT	[124]
Al / MoS <sub>2</sub>	Chemiresistor	ME	10	~100	/	~300	~1200	RT	[125]
Au/Gr-MoS <sub>2</sub> -Gr/Au	Chemiresistor	CVD	0.025	3.3/ppb	0.1	~1000	~700	RT (red light)	[126]
MoS <sub>2</sub> / SnO <sub>2</sub>	Chemiresistor	Hydrothermal	5	18.7	/	75	NA	RT	[132]
MoS <sub>2</sub> /ZnO	Chemiresistor	Hydrothermal, CVD	50	31.2	200	3600	3900	200	[155]
rGO-MoS <sub>2</sub> -CdS	Chemiresistor	Hydrothermal	0.2	27.4	/	25	34	75	[156]
WS <sub>2</sub> / WO <sub>3</sub>	Chemiresistor	annealing	2	1010	1.0e5	/	/	150	[157]
WS <sub>2</sub> /ZnS	Chemiresistor	LPE	5	3250	10	4	~400	RT	[158]
SnS <sub>2</sub> / SnO <sub>2</sub>	Chemiresistor	CVD	8	530	1.0e3	159	297	80	[159]
SnS <sub>2</sub> / SiO <sub>2</sub>	Chemiresistor	CVD	10	701	408.9	272.8	3800.4	RT	[160]
SnS <sub>2</sub> / rGO	Chemiresistor	Hydrothermal	8	9.8	8.7	NA	76	RT	[161]
PbS QDs / MoS <sub>2</sub>	Chemiresistor	Hydrothermal	100	~23	/	30	235	RT	[6]
ZnS / CuO	Chemiresistor	Hydrothermal	5	1055	/	45	170	RT (UV light)	[144]

Benefited from the interfacial Coulomb scattering and strongly charged transfer, various types (p-n, n-n) of heterojunction-based devices have been used as NO<sub>2</sub> gas sensors.

MoS<sub>2</sub>/SnO<sub>2</sub> p-n heterojunctions have been fabricated and used for ethanol, TEA, and NO<sub>2</sub> gas sensing.[131, 132] They exhibited high sensitivity, lower OT, excellent sensing selectivity, and outstanding long-term stability. Shao *et al.*[159] fabricated RGO-MoS<sub>2</sub>-CdS nanocomposite films via solvothermal treatment and analyzed the sensing performance, which showed a largely enhanced response of 27.4% toward 0.2 ppm NO<sub>2</sub>, about 7 times higher than that of RGO-MoS<sub>2</sub> based sensor. Moreover, Guo's group and Xu's group synthesized SnO<sub>2</sub>-SnS<sub>2</sub> p-n heterojunction by the oxidation of SnS<sub>2</sub> at 300 °C, and used it for NO<sub>2</sub> and NH<sub>3</sub> gas sensing, respectively.[160] With respect to n-n heterojunction metal sulfide-based gas sensor, Li *et al.*[141] modified CdS nanowires (NWs) with CeO<sub>2</sub> nanoparticles, and found that the 5 wt% CeO<sub>2</sub>/CdS heterostructures exhibited a much higher response to 100 ppm ethanol (about 5200%), which was 2.6 times larger than that of pure CdS. It is also found that most of the metal sulfides heterojunction are constructed with metal oxides, which can be attributed to the strong interaction between the oxygen ions and gas analytes and the high adsorption energy of the defects (oxygen vacancies).

A FET gas sensor has been used for NO<sub>2</sub> gas sensing because the conductance of the channel can be modulated by applying different bias voltages on the gate electrode. Late *et al.*[148] comparatively analyzed the gas sensing behaviours of single-layer (SL) and multilayer (ML) MoS<sub>2</sub> transistor-based sensors towards NO<sub>2</sub>, NH<sub>3</sub>, and humidity in different conditions. They found that the SL-MoS<sub>2</sub> sensor was unstable, so they compared the sensing performances between 2L and five-layer (5L) devices. The resistance of both FETs decreases when exposed to NH<sub>3</sub> but increases upon exposure to NO<sub>2</sub>. The positive bias voltage enhanced the sensitivity of NO<sub>2</sub> but decreased that of NH<sub>3</sub>, and the 5L-MoS<sub>2</sub> sensor showed a stronger response to a bias voltage, suggesting that the carrier concentration in 5L-MoS<sub>2</sub> was more susceptible to the bias voltage. Similarly, WS<sub>2</sub>[161] and ReS<sub>2</sub>[162] FETs were used for detecting different gases, such as O<sub>2</sub>, NH<sub>3</sub>, and NO<sub>2</sub>. Alternatively, to further improve the gas sensing response, a gate-tunable gas sensor based on a graphene/MoS<sub>2</sub> vdW heterojunction had a high response to NO<sub>2</sub> of 10<sup>3</sup>, and the magnitude of the response strongly dependent on the bias and back-gate voltages.[158] Since the interaction between the gas molecule and sensitive layer (the FET channel material) enables an obvious electron transfer between them, which can further change the carrier concentration, mobility, and semiconductor work function of the device, and finally affect the transistor current.[147, 163]

### 2.6.2. HUMIDITY SENSORS

The humidity sensor can not only be used to monitor the patient's respiration profile continuously but also to determine the dehydration state. There is evidence that the changes in the humidity of exhaled air influence the asthmatic symptoms. Yang *et al.*[164] reported a humidity sensor based on ReS<sub>2</sub> nanosheets, and found the devices exhibit fast response/recovery time and excellent sensitivity. Feng *et al.*[165] fabricated a flexible touchless positioning interface based on the fast response and sensitive moisture detection through VS<sub>2</sub> nanosheets. Guo *et al.*[166] fabricated transparent and flexible WS<sub>2</sub> based humidity sensors for electronic skin, which wide relative humidity range (up to 90%) with fast response and recovery times in a few seconds.[166] To improve the performance, Burman *et al.*[112] decorated MoS<sub>2</sub> with Pt nanoparticles, and used it for humidity sensing. The sensor showed a high response of ~4000 times at 85% RH. The response and recovery

times were  $\sim 92$  s and  $\sim 154$  s, respectively, with repeatable behaviour. The sensor performance was found to be stable when tested over a few months.  $\text{MoS}_2/\text{ZnO}$  [167] and  $\text{MoS}_2/\text{VS}_2$  [165] were constructed and used for humidity detection, which exhibited fast response and recovery time in few seconds and ultra-high response of 579850%.

After comparing different pristine metal sulfides, it is found that SnS and  $\text{WS}_2$  can detect low gas concentration. Thus SnS and  $\text{WS}_2$  are chosen as gas sensing materials in my work. The sensing concept of metal-metal sulfides Schottky barrier, p-n heterojunction, and transistor will be introduced in my devices to improve gas sensing performance further.

## 2.7. CONCLUSIONS

In this chapter, I summarized the state-of-the-art of metal sulfides materials and their gas sensing applications. In the first section, the basic characteristics of various metal sulfides are listed. Different from many metal oxides, metal sulfides often have a shallow valence band and due to their availability in a variety of shapes, sizes, crystalline forms, chemical compositions, and their excellent response to external stimulation. Thus, metal sulfides have a range of potential novel properties that can contribute to high gas sensing behaviours. There are generally two preparation methods, the top-down and bottom-up techniques. The most common “top-down” approaches are mechanical exfoliation and liquid phase exfoliation methods, which can be used for obtaining high-quality 2D or nanomaterials. However, most of the exfoliated materials are of small size and fragmented. Regarding “bottom-up” processes, chemical vapor deposition and hydrothermal methods are used widely for synthesizing SL-, FL- or ML-metal sulfides thin films. After preparing metal sulfides, suspension and transfer methods can be used to fabricate different kinds of gas sensors. The critical sensing parameters are sensitivity, response time and recovery time, sensing range, selectivity, and LOD.

After comparing gas sensing performance of various metal sulfides-based gas sensors, it is found that the pristine metal sulfides (i.e., SnS and  $\text{WS}_2$ ) can detect ppb-level  $\text{NO}_2$  gas. To improve the sensitivity, a Schottky diode of  $\text{Ti}/\text{Au}-\text{MoS}_2$  showed 3 orders of gas sensing response. The Schottky barrier can be formed in the interface due to the difference in the work function between metal and metal sulfides, which can enable high gas sensing performance. Thus many groups modulate the gas sensing behaviours through change the materials of electrodes. To decrease the LOD, heterojunction is often used in metal sulfides-based devices. The  $\text{SnS}_2/\text{rGO}$  heterojunction device can detect sub-ppb  $\text{NO}_2$ . Most of the metal sulfides heterojunction are constructed with metal oxides, which can be attributed to the strong interaction between the oxygen ions and gas analytes and the high adsorption energy of the defects (oxygen vacancies). Furthermore, high response to  $\text{NO}_2$  of  $10^3$  was achieved by using FET mode, where the magnitude of the response strongly depends on the bias and back-gate voltages. It is attributed to the interaction between the gas molecule and sensitive layer (the FET channel material), which enables an obvious electron transfer between them, and further changes the carrier concentration, mobility, and semiconductor work function of the device, and finally affect the transistor current. In addition to improve their performance, researchers used UV light to stimulate the charge transfer between the gas molecules and metal sulfides. Thus the light source can be integrated into the device in the future.

Based on the summary of the metal sulfides gas sensors, SnS and  $\text{WS}_2$  as gas sens-

ing materials are chosen in my work. To improve the humidity sensing response and speed, the sensing concept of metal-metal sulfides Schottky barrier is introduced for SnS nanoflakes. The high-quality single-crystal SnS nanoflakes are obtained through ME methods. To achieve a large surface area and high-quality materials, the LPE method is applied for preparing SnS nanosheets, which are the foundation materials of SnO<sub>x</sub>/SnS heterostructures. The OV<sub>s</sub> in the SnO<sub>x</sub>/SnS heterostructures could enhance the sensing response and LOD. Finally, to improve charge transfer in the interface, few-layer WS<sub>2</sub> thin film grown through the CVD method is adapted for forming WS<sub>2</sub>/IGZO heterojunction and further fabricated as a transistor.

## REFERENCES

- [1] Sundaram Chandrasekaran, Lei Yao, Libo Deng, Chris Bowen, Yan Zhang, Sanming Chen, Zhiquan Lin, Feng Peng, and Peixin Zhang. Recent advances in metal sulfides: from controlled fabrication to electrocatalytic, photocatalytic and photoelectrochemical water splitting and beyond. *Chemical Society Reviews*, 48(15):4178–4280, 2019.
- [2] Yu Cui, Ziqi Zhou, Tao Li, Kaiyou Wang, Jingbo Li, and Zhongming Wei. Versatile crystal structures and (opto)electronic applications of the 2D metal mono-, di-, and tri-chalcogenide nanosheets. *Advanced Functional Materials*, 29(24):1900040, 2019.
- [3] Gang Wang, Baibiao Huang, Zhuji Li, Zaizhu Lou, Zeyan Wang, Ying Dai, and Myung-Hwan Whangbo. Synthesis and characterization of ZnS with controlled amount of S vacancies for photocatalytic H<sub>2</sub> production under visible light. *Scientific Reports*, 5(1):8544, 2015.
- [4] Chan Su Jung, Fazel Shojaei, Kidong Park, Jin Young Oh, Hyung Soon Im, Dong Myung Jang, Jeunghee Park, and Hong Seok Kang. Red-to-ultraviolet emission tuning of two-dimensional gallium sulfide/selenide. *ACS Nano*, 9(10):9585–9593, 2015.
- [5] Shiyong Guo, Lu Yuan, Xuhai Liu, Wenhan Zhou, Xiufeng Song, and Shengli Zhang. First-principles study of SO<sub>2</sub> sensors based on phosphorene and its isoelectronic counterparts: GeS, GeSe, SnS, SnSe. *Chemical Physics Letters*, 686:83–87, 2017.
- [6] Xin Xin, Yong Zhang, Xiaoxiao Guan, Juexian Cao, Wenli Li, Xia Long, and Xin Tan. Enhanced performances of PbS quantum-dots-modified MoS<sub>2</sub> composite for NO<sub>2</sub> detection at room temperature. *ACS Applied Materials & Interfaces*, 11(9):9438–9447, 2019.
- [7] M. F. Afsar, M. A. Rafiq, and A. I. Y. Tok. Two-dimensional SnS nanoflakes: synthesis and application to acetone and alcohol sensors. *RSC Advances*, 7(35):21556–21566, 2017.
- [8] S. T. Navale, D. K. Bandgar, M. A. Chougule, and V. B. Patil. Facile method of preparation of PbS films for NO<sub>2</sub> detection. *RSC Advances*, 5(9):6518–6527, 2015.
- [9] Sajedeh Manzeli, Dmitry Ovchinnikov, Diego Pasquier, Oleg V. Yazyev, and Andras Kis. 2D transition metal dichalcogenides. *Nature Reviews Materials*, 2:17033, 2017.
- [10] Wonbong Choi, Nitin Choudhary, Gang Hee Han, Juhong Park, Deji Akinwande, and Young Hee Lee. Recent development of two-dimensional transition metal dichalcogenides and their applications. *Materials Today*, 20(3):116–130, 2017.
- [11] Jianfeng Ping, Zhanxi Fan, Melinda Sindoro, Yibin Ying, and Hua Zhang. Recent advances in sensing applications of two-dimensional transition metal dichalcogenide nanosheets and their composites. *Advanced Functional Materials*, 27(19):1605817, 2017.

- [12] R. Kappera, D. Voiry, S. E. Yalcin, B. Branch, G. Gupta, A. D. Mohite, and M. Chhowalla. Phase-engineered low-resistance contacts for ultrathin MoS<sub>2</sub> transistors. *Nat Mater*, 13(12):1128–34, 2014.
- [13] Zhongjian Xie, Dou Wang, Taojian Fan, Chenyang Xing, Zhongjun Li, Wei Tao, Liping Liu, Shiyun Bao, Dianyuan Fan, and Han Zhang. Black phosphorus analogue tin sulfide nanosheets: synthesis and application as near-infrared photothermal agents and drug delivery platforms for cancer therapy. *Journal of Materials Chemistry B*, 6(29):4747–4755, 2018.
- [14] Summayya Kouser, Anagha Thannikoth, Uttam Gupta, Umesh V. Waghmare, and C. N. R. Rao. 2D-GaS as a photocatalyst for water splitting to produce H<sub>2</sub>. *Small*, 11(36):4723–4730, 2015.
- [15] Shengli Zhang, Ning Wang, Shangguo Liu, Shiping Huang, Wenhan Zhou, Bo Cai, Meiqiu Xie, Qun Yang, Xianping Chen, and Haibo Zeng. Two-dimensional GeS with tunable electronic properties via external electric field and strain. *Nanotechnology*, 27(27):274001, 2016.
- [16] Richard M. Martin. Elastic properties of ZnS structure semiconductors. *Physical Review B*, 1(10):4005–4011, 1970.
- [17] V. Lantto and V. Golovanov. A comparison of conductance behaviour between SnO<sub>2</sub> and CdS gas-sensitive films. *Sensors and Actuators B: Chemical*, 25(1):614–618, 1995.
- [18] Y. Rodriguez-Lazcano, H. Martinez, M. Calixto-Rodriguez, and A. Nunez Rodriguez. Properties of CuS thin films treated in air plasma. *Thin Solid Films*, 517(21):5951–5955, 2009.
- [19] Jeffrey Trahan, R. G. Goodrich, and S. F. Watkins. X-ray diffraction measurements on metallic and semiconducting hexagonal NiS. *Physical Review B*, 2(8):2859–2863, 1970.
- [20] Ziqian Wang, Shoucong Ning, Takeshi Fujita, Akihiko Hirata, and Mingwei Chen. Unveiling three-dimensional stacking sequences of 1T phase MoS<sub>2</sub> monolayers by electron diffraction. *ACS Nano*, 10(11):10308–10316, 2016.
- [21] Andrea Splendiani, Liang Sun, Yuanbo Zhang, Tianshu Li, Jonghwan Kim, Chi-Yung Chim, Giulia Galli, and Feng Wang. Emerging photoluminescence in monolayer MoS<sub>2</sub>. *Nano Letters*, 10(4):1271–1275, 2010.
- [22] Tamie A. J. Loh and Daniel H. C. Chua. Origin of hybrid 1T- and 2H-WS<sub>2</sub> ultrathin layers by pulsed laser deposition. *The Journal of Physical Chemistry C*, 119(49):27496–27504, 2015.
- [23] Lee A. Burton, Diego Colombara, Ruben D. Abellon, Ferdinand C. Grozema, Laurence M. Peter, Tom J. Savenije, Gilles Dennler, and Aron Walsh. Synthesis, characterization, and electronic structure of single-crystal SnS, Sn<sub>2</sub>S<sub>3</sub>, and SnS<sub>2</sub>. *Chemistry of Materials*, 25(24):4908–4916, 2013.
- [24] Liang Li, Xiaosheng Fang, Tianyou Zhai, Meiyong Liao, Ujjal K. Gautam, Xingcai Wu, Yasuo Koide, Yoshio Bando, and Dmitri Golberg. Electrical transport and high-performance photoconductivity in individual ZrS<sub>2</sub> nanobelts. *Advanced Materials*, 22(37):4151–4156, 2010.
- [25] Kai Xu, Zhenxing Wang, Feng Wang, Yun Huang, Fengmei Wang, Lei Yin, Chao Jiang, and Jun He. Ultrasensitive phototransistors based on few-layered HfS<sub>2</sub>. *Advanced Materials*, 27(47):7881–7887, 2015.

- [26] Yeonhoo Kim, Ki Chang Kwon, Sungwoo Kang, Changyeon Kim, Tae Hoon Kim, Seung-Pyo Hong, Seo Yun Park, Jun Min Suh, Min-Ju Choi, Seungwu Han, and Ho Won Jang. Two-dimensional NbS<sub>2</sub> gas sensors for selective and reversible NO<sub>2</sub> detection at room temperature. *ACS Sensors*, 4(9):2395–2402, 2019.
- [27] Qiyuan He, Qinglang Ma, Bo Chen, Zongyou Yin, Zhiyuan Zeng, Shixin Wu, Xiehong Cao, Xingyi Kong, and Hua Zhang. TaS<sub>2</sub> nanosheet-based room-temperature dosage meter for nitric oxide. *APL Materials*, 2(9):092506, 2014.
- [28] Houlong L. Zhuang and Richard G. Hennig. Stability and magnetism of strongly correlated single-layer VS<sub>2</sub>. *Physical Review B*, 93(5):054429, 2016.
- [29] Sijie Liu, Wenbo Xiao, Mianzeng Zhong, Longfei Pan, Xiaoting Wang, Hui-Xiong Deng, Jian Liu, Jingbo Li, and Zhongming Wei. Highly polarization sensitive photodetectors based on quasi-1D titanium trisulfide (TiS<sub>3</sub>). *Nanotechnology*, 29(18):184002, 2018.
- [30] You-Rong Tao, Xing-Cai Wu, and Wei-Wei Xiong. Flexible visible-light photodetectors with broad photoresponse based on ZrS<sub>3</sub> nanobelt films. *Small*, 10(23):4905–4911, 2014.
- [31] Wei-Wei Xiong, Jin-Qiang Chen, Xing-Cai Wu, and Jun-Jie Zhu. Individual HfS<sub>3</sub> nanobelt for field-effect transistor and high performance visible-light detector. *Journal of Materials Chemistry C*, 2(35):7392–7395, 2014.
- [32] Carmen C. Mayorga-Martinez, Zdenek Sofer, Jan Luxa, Stepan Huber, David Sedmidubsky, Petr Brazda, Lukas Palatinus, Martin Mikulics, Petr Lazar, Rostislav Medlin, and Martin Pumera. TaS<sub>3</sub> nanofibers: Layered trichalcogenide for high-performance electronic and sensing devices. *ACS Nano*, 12(1):464–473, 2018.
- [33] Wenjuan Huang, Lin Gan, Haotian Yang, Nan Zhou, Renyan Wang, Wanhui Wu, Huiqiao Li, Ying Ma, Haibo Zeng, and Tianyou Zhai. Controlled synthesis of ultrathin 2D  $\beta$ -In<sub>2</sub>S<sub>3</sub> with broadband photoresponse by chemical vapor deposition. *Advanced Functional Materials*, 27(36):1702448, 2017.
- [34] K. S. Novoselov, A. K. Geim, S. V. Morozov, D. Jiang, Y. Zhang, S. V. Dubonos, I. V. Grigorieva, and A. A. Firsov. Electric field effect in atomically thin carbon films. *Science*, 306(5696):666, 2004.
- [35] Min Yi and Zhigang Shen. A review on mechanical exfoliation for the scalable production of graphene. *Journal of Materials Chemistry A*, 3(22):11700–11715, 2015.
- [36] K. S. Novoselov and A. H. Castro Neto. Two-dimensional crystals-based heterostructures: materials with tailored properties. *Physica Scripta*, T146:014006, 2012.
- [37] Ruitao Lv, Joshua A. Robinson, Raymond E. Schaak, Du Sun, Yifan Sun, Thomas E. Malouk, and Mauricio Terrones. Transition metal dichalcogenides and beyond: Synthesis, properties, and applications of single- and few-layer nanosheets. *Accounts of Chemical Research*, 48(1):56–64, 2015.
- [38] Hai Li, Gang Lu, Yanlong Wang, Zongyou Yin, Chunxiao Cong, Qiyuan He, Lu Wang, Feng Ding, Ting Yu, and Hua Zhang. Mechanical exfoliation and characterization of single- and few-layer nanosheets of WSe<sub>2</sub>, TaS<sub>2</sub>, and TaSe<sub>2</sub>. *Small*, 9(11):1974–1981, 2013.

- [39] Naoki Higashitarumizu, Hayami Kawamoto, Masaru Nakamura, Kiyoshi Shimamura, Naoki Ohashi, Keiji Ueno, and Kosuke Nagashio. Self-passivated ultra-thin SnS layers via mechanical exfoliation and post-oxidation. *Nanoscale*, 10(47):22474–22483, 2018.
- [40] Kin Fai Mak, Changgu Lee, James Hone, Jie Shan, and Tony F. Heinz. Atomically thin MoS<sub>2</sub>: A new direct-gap semiconductor. *Physical Review Letters*, 105(13):136805, 2010.
- [41] Santanu Mukherjee, Zhongkan Ren, and Gurpreet Singh. Beyond graphene anode materials for emerging metal ion batteries and supercapacitors. *Nano-Micro Letters*, 10(4):70, 2018.
- [42] Yenny Hernandez, Valeria Nicolosi, Mustafa Lotya, Fiona M. Blighe, Zhenyu Sun, Sukanta De, I. T. McGovern, Brendan Holland, Michele Byrne, Yurii K. Gun'Ko, John J. Boland, Peter Niraj, Georg Duesberg, Satheesh Krishnamurthy, Robbie Goodhue, John Hutchison, Vittorio Scardaci, Andrea C. Ferrari, and Jonathan N. Coleman. High-yield production of graphene by liquid-phase exfoliation of graphite. *Nature Nanotechnology*, 3(9):563–568, 2008.
- [43] Valeria Nicolosi, Manish Chhowalla, Mercouri G. Kanatzidis, Michael S. Strano, and Jonathan N. Coleman. Liquid exfoliation of layered materials. *Science*, 340(6139):1226419, 2013.
- [44] Ali Jawaid, Dhriti Nepal, Kyoungweon Park, Michael Jespersen, Anthony Qualley, Peter Mirau, Lawrence F. Drummy, and Richard A. Vaia. Mechanism for liquid phase exfoliation of MoS<sub>2</sub>. *Chemistry of Materials*, 28(1):337–348, 2016.
- [45] Arlene O'Neill, Umar Khan, and Jonathan N. Coleman. Preparation of high concentration dispersions of exfoliated MoS<sub>2</sub> with increased flake size. *Chemistry of Materials*, 24(12):2414–2421, 2012.
- [46] Guan-Qun Han, Yan-Ru Liu, Wen-Hui Hu, Bin Dong, Xiao Li, Yong-Ming Chai, Yun-Qi Liu, and Chen-Guang Liu. WS<sub>2</sub> nanosheets based on liquid exfoliation as effective electrocatalysts for hydrogen evolution reaction. *Materials Chemistry and Physics*, 167:271–277, 2015.
- [47] Lijuan Shen, Mingbu Luo, Yuhao Liu, Ruowen Liang, Fenfen Jing, and Ling Wu. Noble-metal-free MoS<sub>2</sub> co-catalyst decorated UiO-66/CdS hybrids for efficient photocatalytic H<sub>2</sub> production. *Applied Catalysis B: Environmental*, 166-167:445–453, 2015.
- [48] H. S S Ramakrishna Matte, A. Gomathi, Arun K Manna, Dattatray J Late, Ranjan Datta, Swapan K Pati, and C. N R Rao. MoS<sub>2</sub> and WS<sub>2</sub> analogues of graphene. *Angewandte Chemie International Edition*, 49(24):4059–4062, 2010.
- [49] Zhengzong Sun, Zheng Yan, Jun Yao, Elvira Beitler, Yu Zhu, and James M. Tour. Growth of graphene from solid carbon sources. *Nature*, 468(7323):549–552, 2010.
- [50] Xuesong Li, Weiwei Cai, Jinho An, Seyoung Kim, Junghyo Nah, Dongxing Yang, Richard Piner, Aruna Velamakanni, Inhwa Jung, Emanuel Tutuc, Sanjay K. Banerjee, Luigi Colombo, and Rodney S. Ruoff. Large-area synthesis of high-quality and uniform graphene films on copper foils. *Science*, 324(5932):1312, 2009.
- [51] Yumeng Shi, Christoph Hamsen, Xiaoting Jia, Ki Kang Kim, Alfonso Reina, Mario Hofmann, Allen Long Hsu, Kai Zhang, Henan Li, Zhen-Yu Juang, Mildred S. Dresselhaus, Lain-Jong Li, and Jing Kong. Synthesis of few-layer hexagonal boron nitride thin film by chemical vapor deposition. *Nano Letters*, 10(10):4134–4139, 2010.

- [52] Lijie Ci, Li Song, Chuanhong Jin, Deep Jariwala, Dangxin Wu, Yongjie Li, Anchal Srivastava, Z. F. Wang, Kevin Storr, Luis Balicas, Feng Liu, and Pulickel M. Ajayan. Atomic layers of hybridized boron nitride and graphene domains. *Nature Materials*, 9(5):430–435, 2010.
- [53] Sefaattin Tongay, Wen Fan, Jun Kang, Joonsuk Park, Unsal Koldemir, Joonki Suh, Deepa S. Narang, Kai Liu, Jie Ji, Jingbo Li, Robert Sinclair, and Junqiao Wu. Tuning interlayer coupling in large-area heterostructures with CVD-grown MoS<sub>2</sub> and WS<sub>2</sub> monolayers. *Nano Letters*, 14(6):3185–3190, 2014.
- [54] Changyong Lan, Chun Li, Yi Yin, and Yong Liu. Large-area synthesis of monolayer WS<sub>2</sub> and its ambient-sensitive photo-detecting performance. *Nanoscale*, 7(14):5974–5980, 2015.
- [55] Jie Sun, Xuejian Li, Weiling Guo, Miao Zhao, Xing Fan, Yibo Dong, Chen Xu, Jun Deng, and Yifeng Fu. Synthesis methods of two-dimensional MoS<sub>2</sub>: A brief review. *Crystals*, 7(7), 2017.
- [56] Patrick J. Whitham, DenNiS P. Strommen, Sandra Lundell, Lisa D. Lau, and Rene Rodriguez. GeS<sub>2</sub> and GeSe<sub>2</sub> PECVD from GeCl<sub>4</sub> and various chalcogenide precursors. *Plasma Chemistry and Plasma Processing*, 34(4):755–766, 2014.
- [57] Xing Zhou, Qi Zhang, Lin Gan, Huiqiao Li, and Tianyou Zhai. Large-size growth of ultrathin SnS<sub>2</sub> nanosheets and high performance for phototransistors. *Advanced Functional Materials*, 26(24):4405–4413, 2016.
- [58] Tilman Zschechel, Wolfgang Wisniewski, and Christian Russel. Microstructure and texture of polycrystalline CVD-ZnS analyzed via EBSD. *Advanced Functional Materials*, 22(23):4969–4974, 2012.
- [59] Jakob Kibsgaard, Zhebo Chen, Benjamin N. Reinecke, and Thomas F. Jaramillo. Engineering the surface structure of MoS<sub>2</sub> to preferentially expose active edge sites for electrocatalysis. *Nature Materials*, 11(11):963–969, 2012.
- [60] Jianping Shi, Yang Yang, Yu Zhang, Donglin Ma, Wei Wei, Qingqing Ji, Yanshuo Zhang, Xiuju Song, Teng Gao, Cong Li, Xinhe Bao, Zhongfan Liu, Qiang Fu, and Yanfeng Zhang. Monolayer MoS<sub>2</sub> growth on Au foils and on-site domain boundary imaging. *Advanced Functional Materials*, 25(6):842–849, 2015.
- [61] Thomas F. Jaramillo, Kristina P. Jorgensen, Jacob Bonde, Jane H. Nielsen, Sebastian Horch, and Ib Chorkendorff. Identification of active edge sites for electrochemical H<sub>2</sub> evolution from MoS<sub>2</sub> nanocatalysts. *Science*, 317(5834):100, 2007.
- [62] Yi Rang Lim, Wooseok Song, Jin Kyu Han, Young Bum Lee, Sung Jun Kim, Sung Myung, Sun Sook Lee, Ki-Seok An, Chel-Jong Choi, and Jongsun Lim. Wafer-scale, homogeneous MoS<sub>2</sub> layers on plastic substrates for flexible visible-light photodetectors. *Advanced Materials*, 28(25):5025–5030, 2016.
- [63] Qingqing Ji, Yu Zhang, Yanfeng Zhang, and Zhongfan Liu. Chemical vapour deposition of group-VIB metal dichalcogenide monolayers: engineered substrates from amorphous to single crystalline. *Chemical Society Reviews*, 44(9):2587–2602, 2015.
- [64] Keng-Ku Liu, Wenjing Zhang, Yi-Hsien Lee, Yu-Chuan Lin, Mu-Tung Chang, Ching-Yuan Su, Chia-Seng Chang, Hai Li, Yumeng Shi, Hua Zhang, Chao-Sung Lai, and Lain-Jong Li. Growth of large-area and highly crystalline MoS<sub>2</sub> thin layers on insulating substrates. *Nano Letters*, 12(3):1538–1544, 2012.

- [65] N. Koteeswara Reddy, M. Devika, and E. S. R. Gopal. Review on tin (II) sulfide (SnS) material: Synthesis, properties, and applications. *Critical Reviews in Solid State and Materials Sciences*, 40(6):359–398, 2015.
- [66] Kibum Kang, Saien Xie, Lujie Huang, Yimo Han, Pinshane Y. Huang, Kin Fai Mak, Cheol-Joo Kim, David Muller, and Jiwoong Park. High-mobility three-atom-thick semiconducting films with wafer-scale homogeneity. *Nature*, 520(7549):656–660, 2015.
- [67] J. Etzkorn, H. A Therese, F. Rucker, N. Zink, U. Kolb, and W. Tremel. Metal-organic chemical vapor deposition synthesis of hollow inorganic-fullerene-type MoS<sub>2</sub> and MoSe<sub>2</sub> nanoparticles. *Advanced Materials*, 17(19):2372–2375, 2005.
- [68] Nicole Zink, Helen Annal Therese, Julien Pansiot, Aswani Yella, Florian Banhart, and Wolfgang Tremel. In situ heating TEM study of onion-like WS<sub>2</sub> and MoS<sub>2</sub> nanostructures obtained via MOCVD. *Chemistry of Materials*, 20(1):65–71, 2008.
- [69] Andrew J. Clayton, Stuart J. C. Irvine, Cecile M. E. Charbonneau, Peter Siderfin, and Vincent Barrioz. A new approach to thin-film SnS PV using MOCVD. *Materials Research Innovations*, 19(7):477–481, 2015.
- [70] Aswani Yella, Enrico Mugnaioli, Helen Annal Therese, Martin Panth fer, Ute Kolb, and Wolfgang Tremel. Synthesis of fullerene- and nanotube-like SnS<sub>2</sub> nanoparticles and Sn/S/carbon nanocomposites. *Chemistry of Materials*, 21(12):2474–2481, 2009.
- [71] Aswani Yella, Helen Annal Therese, Nicole Zink, Martin Panth fer, and Wolfgang Tremel. Large scale MOCVD synthesis of hollow ReS<sub>2</sub> nanoparticles with nested fullerene-like structure. *Chemistry of Materials*, 20(11):3587–3593, 2008.
- [72] Tokuo Yodo and Shuhei Tanaka. Growth of CdS by atmospheric pressure metalorganic vapor-phase epitaxy at low temperature. *Journal of Applied Physics*, 72(7):2781–2790, 1992.
- [73] Steven M. George. Atomic layer deposition: An overview. *Chemical Reviews*, 110(1):111–131, 2010.
- [74] Lee Kheng Tan, Bo Liu, Jing Hua Teng, Shifeng Guo, Hong Yee Low, and Kian Ping Loh. Atomic layer deposition of a MoS<sub>2</sub> film. *Nanoscale*, 6(18):10584–10588, 2014.
- [75] Ville Miikkulainen, Markku Leskel, Mikko Ritala, and Riikka L. Puurunen. Crystallinity of inorganic films grown by atomic layer deposition: Overview and general trends. *Journal of Applied Physics*, 113(2):021301, 2013.
- [76] Joice Sophia Ponraj, Giovanni Attolini, and Matteo Bosi. Review on atomic layer deposition and applications of oxide thin films. *Critical Reviews in Solid State and Materials Sciences*, 38(3):203–233, 2013.
- [77] Zhenyu Jin, Seokhee Shin, Do Hyun Kwon, Seung-Joo Han, and Yo-Sep Min. Novel chemical route for atomic layer deposition of MoS<sub>2</sub> thin film on SiO<sub>2</sub>/Si substrate. *Nanoscale*, 6(23):14453–14458, 2014.
- [78] Jukka T. Tanskanen, Jonathan R. Bakke, Stacey F. Bent, and Tapani A. Pakkanen. Ald growth characteristics of ZnS films deposited from organozinc and hydrogen sulfide precursors. *Langmuir*, 26(14):11899–11906, 2010.

- [79] T. W. Scharf, S. V. Prasad, T. M. Mayer, R. S. Goeke, and M. T. Dugger. Atomic layer deposition of tungsten disulphide solid lubricant thin films. *Journal of Materials Research*, 19(12):3443–3446, 2004.
- [80] Zhibin Yang and Jianhua Hao. Progress in pulsed laser deposited two-dimensional layered materials for device applications. *Journal of Materials Chemistry C*, 4(38):8859–8878, 2016.
- [81] J. D. Yao, Z. Q. Zheng, and G. W. Yang. Production of large-area 2d materials for high-performance photodetectors by pulsed-laser deposition. *Progress in Materials Science*, 106:100573, 2019.
- [82] Claudy R. Serrao, Anthony M. Diamond, Shang-Lin Hsu, Long You, Sushant Gadgil, James Clarkson, Carlo Carraro, Roya Maboudian, Chenming Hu, and Sayeef Salahuddin. Highly crystalline MoS<sub>2</sub> thin films grown by pulsed laser deposition. *Applied Physics Letters*, 106(5):052101, 2015.
- [83] Martha I. Serna, Seong H. Yoo, Salvador Moreno, Yang Xi, Juan Pablo Oviedo, Hyunjoo Choi, Husam N. Alshareef, Moon J. Kim, Majid Minary-Jolandan, and Manuel A. Quevedo-Lopez. Large-area deposition of MoS<sub>2</sub> by pulsed laser deposition with in situ thickness control. *ACS Nano*, 10(6):6054–6061, 2016.
- [84] Fan-Yong Ran, Zewen Xiao, Hidenori Hiramatsu, Hideo Hosono, and Toshio Kamiya. Growth of high-quality SnS epitaxial films by H<sub>2</sub>S flow pulsed laser deposition. *Applied Physics Letters*, 104(7):072106, 2014.
- [85] J. Johny, S. Sepulveda-Guzman, B. Krishnan, D. Avellaneda, and S. Shaji. Facile and fast synthesis of SnS<sub>2</sub> nanoparticles by pulsed laser ablation in liquid. *Applied Surface Science*, 435:1285–1295, 2018.
- [86] S. Yano, R. Schroeder, B. Ullrich, and H. Sakai. Absorption and photocurrent properties of thin ZnS films formed by pulsed-laser deposition on quartz. *Thin Solid Films*, 423(2):273–276, 2003.
- [87] Liang, Yoshiki Shimizu, Takeshi Sasaki, Hiroyuki Umehara, and Naoto Koshizaki. Au-mediated growth of wurtzite ZnS nanobelts, nanosheets, and nanorods via thermal evaporation. *The Journal of Physical Chemistry B*, 108(28):9728–9733, 2004.
- [88] Ming-Yen Lu, Jinhui Song, Ming-Pei Lu, Chung-Yang Lee, Lih-Juann Chen, and Zhong Lin Wang. ZnO-ZnS heterojunction and ZnS nanowire arrays for electricity generation. *ACS Nano*, 3(2):357–362, 2009.
- [89] Hui Miao, Xiaoyun Hu, Qian Sun, Yuanyuan Hao, Hao Wu, Dekai Zhang, Jintao Bai, Enzhou Liu, Jun Fan, and Xun Hou. Hydrothermal synthesis of MoS<sub>2</sub> nanosheets films: Microstructure and formation mechanism research. *Materials Letters*, 166:121–124, 2016.
- [90] Wensi Zhang, Panpan Zhang, Zhiqiang Su, and Gang Wei. Synthesis and sensor applications of MoS<sub>2</sub>-based nanocomposites. *Nanoscale*, 7(44):18364–18378, 2015.
- [91] Yinghan Yan, Cuiling Zhang, Wei Gu, Caiping Ding, Xinchang Li, and Yuezhong Xian. Facile synthesis of water-soluble WS<sub>2</sub> quantum dots for turn-on fluorescent measurement of lipoic acid. *The Journal of Physical Chemistry C*, 120(22):12170–12177, 2016.

- [92] John D. Lampkin, Anthony V. Powell, and Ann M. Chippindale. Solvothermal synthesis of a new 3-D mixed-metal sulfide framework,  $(\text{H}_{1.33}\text{tren})[\text{In}_{2.67}\text{Sb}_{1.33}\text{S}_8]\text{tren}$ . *Journal of Solid State Chemistry*, 243:44–49, 2016.
- [93] Jian Zhou, Litao An, Xing Liu, Lijun Huang, and Xijiao Huang. Solvothermal synthesis and characterization of two 2-D layered germanium thioantimonates with transition-metal complexes. *Dalton Transactions*, 40(43):11419–11424, 2011.
- [94] Ajinkya Bhorde, Amit Pawbake, Priyanka Sharma, Shruthi Nair, Adinath Funde, Prashant Bankar, Mahendra More, and Sandesh Jadkar. Solvothermal synthesis of tin sulfide (SnS) nanorods and investigation of its field emission properties. *Applied Physics A*, 124(2):133, 2018.
- [95] Yancong Qiao, Thomas Hirtz, Fan Wu, Ge Deng, Xiaoshi Li, Yao Zhi, He Tian, Yi Yang, and Tian-Ling Ren. Fabricating molybdenum disulfide memristors. *ACS Applied Electronic Materials*, 2019.
- [96] Andres Castellanos-Gomez, Michele Buscema, Rianda Molenaar, Vibhor Singh, Laurens Janssen, Herre S. J. van der Zant, and Gary A. Steele. Deterministic transfer of two-dimensional materials by all-dry viscoelastic stamping. *2D Materials*, 1(1):011002, 2014.
- [97] Buckley David, Black Nicola Charlotte Grant, Castanon Eli, Melios Christos, Hardman Melanie, and Kazakova Olga. Frontiers of graphene and 2D material-based gas sensors for environmental monitoring. *2D Materials*, 2020.
- [98] Yasuhiro Shimizu. *SnO<sub>2</sub> Gas Sensor*, pages 1974–1982. Springer New York, New York, NY, 2014.
- [99] Zhen Tian, Chenglei Guo, Mingxing Zhao, Ranran Li, and Jiamin Xue. Two-dimensional SnS: A phosphorene analogue with strong in-plane electronic anisotropy. *ACS Nano*, 11(2):2219–2226, 2017.
- [100] A. S. Rodin, Lidia C. Gomes, A. Carvalho, and A. H. Castro Neto. Valley physics in tin (II) sulfide. *Physical Review B*, 93(4):045431, 2016.
- [101] Jun Wang, Gang Lian, Zhenghao Xu, Chen Fu, Zhaojun Lin, Liyi Li, Qilong Wang, Deliang Cui, and Ching-Ping Wong. Growth of large-size SnS thin crystals driven by oriented attachment and applications to gas sensors and photodetectors. *ACS Applied Materials & Interfaces*, 8(15):9545–9551, 2016.
- [102] Huan Liu, Min Li, Gang Shao, Wenkai Zhang, Weiwei Wang, Huaibing Song, Hefeng Cao, Wanli Ma, and Jiang Tang. Enhancement of hydrogen sulfide gas sensing of PbS colloidal quantum dots by remote doping through ligand exchange. *Sensors and Actuators B: Chemical*, 212:434–439, 2015.
- [103] Xiao-Hua Liu, Peng-Fei Yin, Sergei A. Kulinich, Yu-Zhu Zhou, Jing Mao, Tao Ling, and Xi-Wen Du. Arrays of ultrathin CdS nanoflakes with high-energy surface for efficient gas detection. *ACS Applied Materials & Interfaces*, 9(1):602–609, 2017.
- [104] Xianfu Wang, Zhong Xie, Hongtao Huang, Zhe Liu, Di Chen, and Guozhen Shen. Gas sensors, thermistor and photodetector based on ZnS nanowires. *Journal of Materials Chemistry*, 22(14):6845–6850, 2012.

- [105] Fayroz A. Sabah, Naser M. Ahmed, Z. Hassan, and Hiba S. Rasheed. High performance CuS p-type thin film as a hydrogen gas sensor. *Sensors and Actuators A: Physical*, 249:68–76, 2016.
- [106] E. C. LingaNiSo, B. W. Mwakikunga, S. D. Mhlanga, N. J. Coville, B. T. Sone, and M. Maaza. Synthesis and hydrogen gas sensing properties of pure NiS and Au-coated NiS. In *SENSORS, 2012 IEEE*, pages 1–4, 2012.
- [107] N. Souda and Y. Shimizu. Sensing properties of solid electrolyte SO<sub>2</sub> sensor using metal-sulfide electrode. *Journal of Materials Science*, 38(21):4301–4305, 2003.
- [108] H. Tae Kim, H. Yeon Kim, Y. Seo Park, Y. Soo Kim, and W. Ho Jang. Two-dimensional transition metal disulfides for chemoresistive gas sensing: Perspective and challenges. *Chemosensors*, 5(2), 2017.
- [109] F. K. Perkins, A. L. Friedman, E. Cobas, P. M. Campbell, G. G. Jernigan, and B. T. Jonker. Chemical vapor sensing with monolayer MoS<sub>2</sub>. *Nano Letters*, 13(2):668–673, 2013.
- [110] Dae-Hyun Baek and Jongbaeg Kim. MoS<sub>2</sub> gas sensor functionalized by Pd for the detection of hydrogen. *Sensors and Actuators B: Chemical*, 250:686–691, 2017.
- [111] Wu Zhou, Xiaolong Zou, Sina Najmaei, Zheng Liu, Yumeng Shi, Jing Kong, Jun Lou, Pulickel M. Ajayan, Boris I. Yakobson, and Juan-Carlos Idrobo. Intrinsic structural defects in monolayer molybdenum disulfide. *Nano Letters*, 13(6):2615–2622, 2013.
- [112] Debasree Burman, Sumita Santra, Panchanan Pramanik, and Prasanta Kumar Guha. Pt decorated MoS<sub>2</sub> nanoflakes for ultrasensitive resistive humidity sensor. *Nanotechnology*, 29(11):115504, 2018.
- [113] Hao Luo, Yijiang Cao, Jing Zhou, Jumeng Feng, Jiamu Cao, and Hai Guo. Adsorption of NO<sub>2</sub>, NH<sub>3</sub> on monolayer MoS<sub>2</sub> doped with Al, Si, and P: A first-principles study. *Chemical Physics Letters*, 643:27–33, 2016.
- [114] Huangli Wei, Yingang Gui, Jian Kang, Weibo Wang, and Chao Tang. A dft study on the adsorption of H<sub>2</sub>S and SO<sub>2</sub> on Ni doped MoS<sub>2</sub> monolayer. *Nanomaterials*, 8(9):646, 2018.
- [115] Yi Li, Xiaoxing Zhang, Dachang Chen, Song Xiao, and Ju Tang. Adsorption behavior of COF<sub>2</sub> and CF<sub>4</sub> gas on the MoS<sub>2</sub> monolayer doped with Ni: A first-principles study. *Applied Surface Science*, 443:274–279, 2018.
- [116] A. Sharma, Anu, M. S. Khan, M. Husain, M. S. Khan, and A. Srivastava. Sensing of CO and NO on Cu-doped MoS<sub>2</sub> monolayer-based single electron transistor: A first principles study. *IEEE Sensors Journal*, 18(7):2853–2860, 2018.
- [117] Dongwei Ma, Weiwei Ju, Tingxian Li, Xiwei Zhang, Chaozheng He, Benyuan Ma, Zhansheng Lu, and Zongxian Yang. The adsorption of CO and NO on the MoS<sub>2</sub> monolayer doped with Au, Pt, Pd, or Ni: A first-principles study. *Applied Surface Science*, 383:98–105, 2016.
- [118] Jia Zhu, Hui Zhang, Yawen Tong, Ling Zhao, Yongfan Zhang, Yuzhi Qiu, and Xianning Lin. First-principles investigations of metal (V, Nb, Ta)-doped monolayer MoS<sub>2</sub>: Structural stability, electronic properties and adsorption of gas molecules. *Applied Surface Science*, 419:522–530, 2017.

- [119] Ruiyang Zhang, Da Fu, Jiaming Ni, Chunbao Sun, and Shaoxian Song. Adsorption for  $\text{SO}_2$  gas molecules on B, N, P and Al doped  $\text{MoS}_2$ : The dft study. *Chemical Physics Letters*, 715:273–277, 2019.
- [120] Dongzhi Zhang, Junfeng Wu, Peng Li, and Yuhua Cao. Room-temperature  $\text{SO}_2$  gas-sensing properties based on a metal-doped  $\text{MoS}_2$  nanoflower: an experimental and density functional theory investigation. *Journal of Materials Chemistry A*, 5(39):20666–20677, 2017.
- [121] Yelda Kadioglu, Gokhan Gokoglu, and Olcay uzengi Akturk. Molecular adsorption properties of CO and  $\text{H}_2\text{O}$  on Au-, Cu-, and  $\text{Au}_x\text{Cu}_y$ -doped  $\text{MoS}_2$  monolayer. *Applied Surface Science*, 425:246–253, 2017.
- [122] Kyung Yong Ko, Jeong-Gyu Song, Youngjun Kim, Taejin Choi, Sera Shin, Chang Wan Lee, Kyounghoon Lee, Jahyun Koo, Hoonkyung Lee, Jongbaeg Kim, Taeyoon Lee, Jusang Park, and Hyungjun Kim. Improvement of gas-sensing performance of large-area tungsten disulfide nanosheets by surface functionalization. *ACS Nano*, 10(10):9287–9296, 2016.
- [123] Ziyu Qin, Keng Xu, Huacong Yue, Hao Wang, Jian Zhang, Chao Ouyang, Changsheng Xie, and Dawen Zeng. Enhanced room-temperature  $\text{NH}_3$  gas sensing by 2D  $\text{SnS}_2$  with sulfur vacancies synthesized by chemical exfoliation. *Sensors and Actuators B: Chemical*, 262:771–779, 2018.
- [124] A. A. Ramanathan. Defect functionalization of  $\text{MoS}_2$  nanostructures as toxic gas sensors: A review. *IOP Conference Series: Materials Science and Engineering*, 305:012001, 2018.
- [125] Youngjun Kim, Sang-Koo Kang, Nan-Cho Oh, Hi-Deok Lee, Soo-Min Lee, Jusang Park, and Hyungjun Kim. Improved sensitivity in Schottky contacted two-dimensional  $\text{MoS}_2$  gas sensor. *ACS Applied Materials & Interfaces*, 11(42):38902–38909, 2019.
- [126] Tung Pham, Guanghui Li, Elena Bekyarova, Mikhail E. Itkis, and Ashok Mulchandani.  $\text{MoS}_2$ -based optoelectronic gas sensor with sub-parts-per-billion limit of  $\text{NO}_2$  gas detection. *ACS Nano*, 13(3):3196–3205, 2019.
- [127] Xiaorui Zheng, Annalisa Calo, Edoardo Albisetti, Xiangyu Liu, Abdullah Sanad M. Alharbi, Ghidewon Arefe, Xiaochi Liu, Martin Spieser, Won Jong Yoo, Takashi Taniguchi, Kenji Watanabe, Carmela Aruta, Alberto Ciarrocchi, Andras Kis, Brian S. Lee, Michal Lipson, James Hone, Davood Shahrjerdi, and Elisa Riedo. Patterning metal contacts on monolayer  $\text{MoS}_2$  with vanishing schottky barriers using thermal nanolithography. *Nature Electronics*, 2(1):17–25, 2019.
- [128] Meng-Lin Tsai, Sheng-Han Su, Jan-Kai Chang, Dung-Sheng Tsai, Chang-Hsiao Chen, Chih-I. Wu, Lain-Jong Li, Lih-Juann Chen, and Jr-Hau He. Monolayer  $\text{MoS}_2$  heterojunction solar cells. *ACS Nano*, 8(8):8317–8322, 2014.
- [129] Thomas Ihn. *Semiconductor Nanostructures: Quantum states and electronic transport*. Oxford University Press, 2010.
- [130] Huihui Yan, Peng Song, Su Zhang, Zhongxi Yang, and Qi Wang. Dispersed  $\text{SnO}_2$  nanoparticles on  $\text{MoS}_2$  nanosheets for superior gas-sensing performances to ethanol. *RSC Advances*, 5(97):79593–79599, 2015.

- [131] Xiu-Qing Qiao, Zhen-Wei Zhang, Dong-Fang Hou, Dong-Sheng Li, Yunlin Liu, Ya-Qian Lan, Jian Zhang, Pingyun Feng, and Xianhui Bu. Tunable  $\text{MoS}_2/\text{SnO}_2$  p-n heterojunctions for an efficient trimethylamine gas sensor and 4-nitrophenol reduction catalyst. *ACS Sustainable Chemistry & Engineering*, 6(9):12375–12384, 2018.
- [132] Yutong Han, Yujie Ma, Yang Liu, Shusheng Xu, Xinwei Chen, Min Zeng, Nantao Hu, Yanjie Su, Zhihua Zhou, and Zhi Yang. Construction of  $\text{MoS}_2/\text{SnO}_2$  heterostructures for sensitive  $\text{NO}_2$  detection at room temperature. *Applied Surface Science*, 493:613–619, 2019.
- [133] Keng Xu, Neng Li, Dawen Zeng, Shouqin Tian, Shasha Zhang, Die Hu, and Changsheng Xie. Interface bonds determined gas-sensing of  $\text{SnO}_2$ - $\text{SnS}_2$  hybrids to ammonia at room temperature. *ACS Applied Materials & Interfaces*, 7(21):11359–11368, 2015.
- [134] Xiaohang Wang, Yuanhua Sang, Dongzhou Wang, Shaosheng Ji, and Hong Liu. Enhanced gas sensing property of  $\text{SnO}_2$  nanoparticles by constructing the  $\text{SnO}_2$ - $\text{TiO}_2$  nanobelt heterostructure. *Journal of Alloys and Compounds*, 639:571–576, 2015.
- [135] Sunghoon Park, Soyeon An, Youngho Mun, and Chongmu Lee. UV-enhanced  $\text{NO}_2$  gas sensing properties of  $\text{SnO}_2$ -core/ $\text{ZnO}$ -shell nanowires at room temperature. *ACS Applied Materials & Interfaces*, 5(10):4285–4292, 2013.
- [136] Wenwen Zeng, Yingzhi Liu, Jun Mei, Changyu Tang, Kun Luo, Shaomin Li, Haoran Zhan, and Zhoukun He. Hierarchical  $\text{SnO}_2$ - $\text{Sn}_3\text{O}_4$  heterostructural gas sensor with high sensitivity and selectivity to  $\text{NO}_2$ . *Sensors and Actuators B: Chemical*, 301:127010, 2019.
- [137] Akash Katoch, Jae-Hun Kim, and Sang Sub Kim.  $\text{TiO}_2/\text{ZnO}$  inner/outer double-layer hollow fibers for improved detection of reducing gases. *ACS Applied Materials & Interfaces*, 6(23):21494–21499, 2014.
- [138] Gun-Joo Sun, Jae Kyung Lee, Seungbok Choi, Wan In Lee, Hyoun Woo Kim, and Chongmu Lee. Selective oxidizing gas sensing and dominant sensing mechanism of n-CaO-decorated n-ZnO nanorod sensors. *ACS Applied Materials & Interfaces*, 9(11):9975–9985, 2017.
- [139] Ehsan Espid and Fariborz Taghipour. Development of highly sensitive  $\text{ZnO}/\text{In}_2\text{O}_3$  composite gas sensor activated by UV-LED. *Sensors and Actuators B: Chemical*, 241:828–839, 2017.
- [140] Qixian Zhang, Shuyi Ma, Rong Zhang, Kaiming Zhu, Yue Tie, and Shitu Pei. Optimization  $\text{NH}_3$  sensing performance manifested by gas sensor based on Pr- $\text{SnS}_2/\text{ZnS}$  hierarchical nanoflowers. *Journal of Alloys and Compounds*, 807:151650, 2019.
- [141] Meishan Li, Wei Ren, Rong Wu, and Min Zhang.  $\text{CeO}_2$  enhanced ethanol sensing performance in a CdS gas sensor. *Sensors*, 17(7), 2017.
- [142] Jiali Zhai, Lingling Wang, Dejun Wang, Haiyan Li, Yu Zhang, Dong qing He, and Tengfeng Xie. Enhancement of gas sensing properties of CdS nanowire/ $\text{ZnO}$  nanosphere composite materials at room temperature by visible-light activation. *ACS Applied Materials & Interfaces*, 3(7):2253–2258, 2011.
- [143] Daejong Yang, Incheol Cho, Donghwan Kim, Mi Ae Lim, Zhiyong Li, Jong G. Ok, Moonjin Lee, and Inkyu Park. Gas sensor by direct growth and functionalization of metal oxide/metal sulfide core-shell nanowires on flexible substrates. *ACS Applied Materials & Interfaces*, 11(27):24298–24307, 2019.

- [144] Sunghoon Park, Gun-Joo Sun, Hyejoon Kheel, Taegyung Ko, Hyoun Woo Kim, and Chongmu Lee. Light-activated NO<sub>2</sub> gas sensing of the networked CuO-decorated ZnS nanowire gas sensor. *Applied Physics A*, 122(5):504, 2016.
- [145] F. Schedin, A. K. Geim, S. V. Morozov, E. W. Hill, P. Blake, M. I. Katsnelson, and K. S. Novoselov. Detection of individual gas molecules adsorbed on graphene. *Nature Materials*, 6(9):652–655, 2007.
- [146] Paolo Bondavalli, Pierre Legagneux, and Didier Pribat. Carbon nanotubes based transistors as gas sensors: State of the art and critical review. *Sensors and Actuators B: Chemical*, 140(1):304–318, 2009.
- [147] Kyung Su Kim, Cheol Hyoun Ahn, Sung Hyeon Jung, Sung Woon Cho, and Hyung Koun Cho. Toward adequate operation of amorphous oxide thin-film transistors for low-concentration gas detection. *ACS Applied Materials & Interfaces*, 10(12):10185–10193, 2018.
- [148] Dattatray J. Late, Yi-Kai Huang, Bin Liu, Jagaran Acharya, Sharmila N. Shirodkar, Jiajun Luo, Aiming Yan, Daniel Charles, Umesh V. Waghmare, Vinayak P. Dravid, and C. N. R. Rao. Sensing behavior of atomically thin-layered MoS<sub>2</sub> transistors. *ACS Nano*, 7(6):4879–4891, 2013.
- [149] Vishal V Burungale, Rupesh S Devan, Sachin A Pawar, Namdev S Harale, Vithoba L Patil, V. K Rao, Yuan Ron Ma, Jo Eun Ae, Jin H Kim, and Pramod S Patil. Chemically synthesized PbS nano particulate thin films for a rapid NO<sub>2</sub> gas sensor. *Materials Science-Poland*, 34(1):204–211, 2016.
- [150] Rakesh K. Sonker, B. C. Yadav, Vinay Gupta, and Monika Tomar. Synthesis of CdS nanoparticle by sol-gel method as low temperature NO<sub>2</sub> sensor. *Materials Chemistry and Physics*, 239:121975, 2020.
- [151] M. Donarelli, S. Prezioso, F. Perrozzi, F. Bisti, M. Nardone, L. Giancaterini, C. Cantalini, and L. Ottaviano. Response to NO<sub>2</sub> and other gases of resistive chemically exfoliated MoS<sub>2</sub>-based gas sensors. *Sensors and Actuators B: Chemical*, 207:602–613, 2015.
- [152] Yeon Hoo Kim, Kye Yeop Kim, You Rim Choi, Young-Seok Shim, Jong-Myeong Jeon, Jong-Heun Lee, Soo Young Kim, Seungwu Han, and Ho Won Jang. Ultrasensitive reversible oxygen sensing by using liquid-exfoliated MoS<sub>2</sub> nanoparticles. *Journal of Materials Chemistry A*, 4(16):6070–6076, 2016.
- [153] Tingting Xu, Yunyun Liu, Yongyong Pei, Yunpeng Chen, Zimin Jiang, Zhifeng Shi, Junmin Xu, Di Wu, Yongtao Tian, and Xinjian Li. The ultra-high NO<sub>2</sub> response of ultra-thin WS<sub>2</sub> nanosheets synthesized by hydrothermal and calcination processes. *Sensors and Actuators B: Chemical*, 259:789–796, 2018.
- [154] Young-Ho Kim, Duy-Thach Phan, Seungbae Ahn, Ki-Hun Nam, Cheol-Min Park, and Ki-Joon Jeon. Two-dimensional sns2 materials as high-performance no2 sensors with fast response and high sensitivity. *Sensors and Actuators B: Chemical*, 255:616–621, 2018.
- [155] F. Perrozzi, S. M. Emamjomeh, V. Paolucci, G. Taglieri, L. Ottaviano, and C. Cantalini. Thermal stability of WS<sub>2</sub> flakes and gas sensing properties of WS<sub>2</sub>/WO<sub>3</sub> composite to H<sub>2</sub>, NH<sub>3</sub> and NO<sub>2</sub>. *Sensors and Actuators B: Chemical*, 243:812–822, 2017.

- [156] Jian Zhen Ou, Wanyin Ge, Benjamin Carey, Torben Daeneke, Asaf Rotbart, Wei Shan, Yichao Wang, Zhengqian Fu, Adam F. Chrimes, Wojtek Wlodarski, Salvy P. Russo, Yong Xiang Li, and Kourosh Kalantar-zadeh. Physisorption-based charge transfer in two-dimensional SnS<sub>2</sub> for selective and reversible NO<sub>2</sub> gas sensing. *ACS Nano*, 9(10):10313–10323, 2015.
- [157] Bilu Liu, Liang Chen, Gang Liu, Ahmad N. Abbas, Mohammad Fathi, and Chongwu Zhou. High-performance chemical sensing using schottky-contacted chemical vapor deposition grown monolayer MoS<sub>2</sub> transistors. *ACS Nano*, 8(5):5304–5314, 2014.
- [158] Hiroshi Tabata, Yuta Sato, Kouhei Oi, Osamu Kubo, and Mitsuhiro Katayama. Bias- and gate-tunable gas sensor response originating from modulation in the schottky barrier height of a graphene/MoS<sub>2</sub> van der waals heterojunction. *ACS Applied Materials & Interfaces*, 10(44):38387–38393, 2018.
- [159] Shaofeng Shao, Leisheng Che, Yunyun Chen, Min Lai, Shenbei Huang, and Ralf Koehn. A novel RGO-MoS<sub>2</sub>-CdS nanocomposite film for application in the ultrasensitive NO<sub>2</sub> detection. *Journal of Alloys and Compounds*, 774:1–10, 2019.
- [160] Ding Gu, Xiaogan Li, Yangyang Zhao, and Jing Wang. Enhanced NO<sub>2</sub> sensing of SnO<sub>2</sub>/SnS<sub>2</sub> heterojunction based sensor. *Sensors and Actuators B: Chemical*, 244:67–76, 2017.
- [161] Nengjie Huo, Shengxue Yang, Zhongming Wei, Shu-Shen Li, Jian-Bai Xia, and Jingbo Li. Photoresponsive and gas sensing field-effect transistors based on multilayer WS<sub>2</sub> nanoflakes. *Scientific Reports*, 4(1):5209, 2014.
- [162] Shengxue Yang, Jun Kang, Qu Yue, J. M. D. Coey, and Chengbao Jiang. Defect-modulated transistors and gas-enhanced photodetectors on ReS<sub>2</sub> nanosheets. *Advanced Materials Interfaces*, 3(6):1500707, 2016.
- [163] Hwan-Seok Jeong, Min-Jae Park, Soo-Hun Kwon, Hyo-Jun Joo, and Hyuck-In Kwon. Highly sensitive and selective room-temperature NO<sub>2</sub> gas-sensing characteristics of SnOx-based p-type thin-film transistor. *Sensors and Actuators B: Chemical*, 288:625–633, 2019.
- [164] Aijun Yang, Jian Gao, Baichang Li, Jiawei Tan, Yu Xiang, Tushar Gupta, Lu Li, Shrvan Suresh, Juan Carlos Idrobo, Toh-Ming Lu, Mingzhe Rong, and Nikhil Koratkar. Humidity sensing using vertically oriented arrays of ReS<sub>2</sub> nanosheets deposited on an interdigitated gold electrode. *2D Materials*, 3(4):045012, 2016.
- [165] Jun Feng, Lele Peng, Changzheng Wu, Xu Sun, Shuanglin Hu, Chenwen Lin, Jun Dai, Jinlong Yang, and Yi Xie. Giant moisture responsiveness of VS<sub>2</sub> ultrathin nanosheets for novel touchless positioning interface. *Advanced Materials*, 24(15):1969–1974, 2012.
- [166] Huayang Guo, Changyong Lan, Zhifei Zhou, Peihua Sun, Dapeng Wei, and Chun Li. Transparent, flexible, and stretchable WS<sub>2</sub> based humidity sensors for electronic skin. *Nanoscale*, 9(19):6246–6253, 2017.
- [167] Lu Ze, Gong Yueqiu, Li Xujun, and Zhang Yong. MoS<sub>2</sub>-modified ZnO quantum dots nanocomposite: Synthesis and ultrafast humidity response. *Applied Surface Science*, 399:330–336, 2017.

# 3

## SnS NANOFLLAKES-BASED SCHOTTKY CONTACTED HUMIDITY SENSOR

*In this chapter, an SnS nanoflakes-based sensor presents high humidity sensing behaviour both in the rigid and flexible substrate. The device is designed to promote SnS-metal Schottky contacts and improve the sensitivity of the device. It is based on the Schottky nature of SnS-metal contact. Besides expanding its application in wearable devices, we fabricate the flexible SnS nanoflakes-based humidity sensor with polyimide substrate, which can be well attached to the skin and exhibits stable humidity sensing performance in the natural flat state and under bending loading. Moreover, the first-principles analysis is performed to prove the high specificity of SnS to the moisture ( $H_2O$ ) in the air. Benefit from its promising advantages, we explore some application of the SnS nanoflakes-based sensors in the detection of breathing patterns and noncontact fingertips sensing behaviour. Finally, a smart home system based on the sensors is proposed to process the signal from breath and finger touch experiments for noncontact controlling and respiration monitoring.*

---

Parts of this chapter have been published in: "High-performance humidity sensor using Schottky-contacted SnS nanoflakes for noncontact healthcare monitoring", *Nanotechnology*, **31**, 5, 2019.

### 3.1. INTRODUCTION

SINCE the 18th century, lots of studies on humidity sensors have continued for more than 100 years owing to the substantial value of humidity control in many application fields, such as industrial production, agriculture, and medical practice.[1] The humidity sensor's key parameters for detecting human breath are the sensitivity and response/recovery time. According to the literature review in Chapter 1 and 2, it is found that tin sulfide (SnS) is an ideal for humidity sensing due to its similar puckered structure as black phosphorus and layered materials. It has been used for detecting ppb-level NO<sub>2</sub> [2] and ppm-level alcohol.[3] Our group proved that the gas sensing between polar gas and SnS, the strong charge transfer and the adsorption-induced band gap states could affect the carrier density in SnS and lead to outstanding sensing performances.[4] Water vapor is one kind of maximal proportion of polar gases in the air, however, the application of moisture sensing based on SnS remaining exclusive. Moreover, the SnS nanosheet exhibited good biocompatibility has been used for cancer therapy, which makes it a good potential material for human healthcare.[5] The excellent flexibility of SnS nanomaterials can be used for wearable electronics.

Here, resistive humidity sensors based on mechanical exfoliated SnS nanoflakes placed on a SiO<sub>2</sub> and flexible substrate are proposed. The as-fabricated humidity sensors show a room temperature humidity-sensing behaviour with short response/recovery time and broad RH range. Besides, the devices fabricated on flexible substrates are also illustrated, which show comparable sensing behaviour to the devices on rigid substrates. The humidity sensing mechanism is explained by the interactions of gas molecules (CO<sub>2</sub>, O<sub>2</sub>, H<sub>2</sub>O, and N<sub>2</sub>) and SnS through first principle analysis. Finally, the fast response speed of these sensors allows us to observe a real-time dynamic monitoring of human breath and fingertip touch to demonstrate potential utilization in respiration monitoring and noncontact controlling. The achieved SnS nanoflakes-based humidity sensor with outstanding performances in the air enables its potential intelligent noncontact healthcare application.

### 3.2. DESIGN AND FABRICATION

The schematic diagram of the SnS nanoflakes-based sensor's fabricating steps is shown in Figure 3.1, which consists of mechanical exfoliation, transferring, and a lift-off process. The SnS bulk crystal was bought from 6Carbon Corp., China. The SnS nanoflakes were mechanically exfoliated (ME) from the bulk crystal through thermal release tape, and then transferred onto the SiO<sub>2</sub>/Si substrate. Due to the non-uniform distributed SnS nanoflakes, we designed eight non-interconnected interdigital electrodes in one sensor for covering most of the nanoflakes. The space between the adjacent electrodes was around 5 μm. After standard photolithography, the electrodes were magnetron sputtered of Ti/Au (10/30 nm) in a vacuum with a chamber pressure <math>6 \times 10^{-6}</math> Torr, and contacted with the top of SnS nanoflakes. After the lift-off process, the devices were annealed at 200 °C for 2 h in argon atmosphere before testing. To fabricate the flexible sensors, we transferred the SnS nanoflakes onto a polyimide (PI) membrane by a thermal release tape (TRT)-assisted transferring technique. The PI membrane was pre-pasted on a Si wafer. After removing the residual of TRT by using acetone solution, the Ti/Au electrodes were deposited onto SnS/PI substrates.

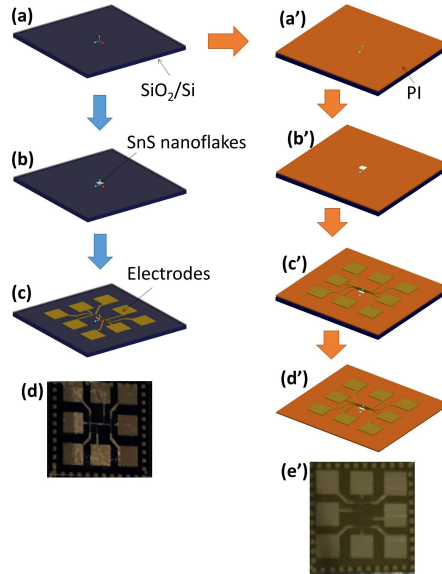


Figure 3.1: Fabrication process of the SnS nanoflakes-based humidity sensor. (a–c) Schematic diagrams of the fabrication process for the sensor with rigid substrate. (a) Cleaning the  $\text{SiO}_2/\text{Si}$  wafer. (b) Transferring the SnS nanoflakes on the surface of substrate. (c) Sputtering Ti/Au electrodes. (d) The optical image of SnS nanoflakes-based humidity sensor with rigid substrate. (a'–d') Schematic diagrams of the fabrication process for the sensor with flexible substrate. (a') Pasting PI film on the top of Si wafer. (b') Transferring the SnS nanoflakes on the surface of PI. (c') Sputtering Ti/Au electrodes. (d') Removing the Si wafer. (e') The optical image of SnS nanoflakes-based humidity sensor with flexible substrate.

### 3.3. CHARACTERIZATION

The optical microscopic images were acquired with an optical microscope (OLYMPUS TH4-200) imager with white light illumination using bright-field imaging modes and objectives. The thickness of ME-SnS was determined by using an atomic force microscope (AFM, Bruker, Santa Barbara, CA, USA) and a Raman spectrometer (Raman, HORIBA, LabRAM HR Evolution) excited by a 532 nm laser. The crystalline microstructure was characterized by transmission electron microscope (TEM, JEOL JEM-2100). An optical image of the SnS nanoflakes transferred on a 300 nm  $\text{SiO}_2/\text{Si}$  substrate is shown in Figure 3.2a. Figure 3.2b shows the AFM scanning image of SnS-nanoflakes between two electrodes. The inset image shows the corresponding quantitative AFM height profile. The SnS nanoflake height is about 30 nm. The Raman spectra for the SnS nanoflake and bulk SnS were measured using a confocal Raman microprobe (see Figure 3.2c). It shows the Raman peaks of SnS nanoflakes detected at 95, 163, 194, and 217  $\text{cm}^{-1}$ , all of which match well with those from single-crystal SnS in previous literature.[6, 7] As shown in Figure 3.2d, the high resolution transmission electron microscopy (HRTEM) image of the SnS nanoflake shows a typical d-spacing of 0.292 nm, corresponding to the distance between (101) planes of the orthorhombic phase of SnS. The inset image shows the selected area electron diffraction (SAED) pattern of SnS, which reveals a single-crystalline orthorhombic phase projected along the  $\langle 010 \rangle$  direction. The interplanar angles defined by the intersection

of the (101) planes of the nanoflake is  $92^\circ$  and  $88^\circ$ , which is consistent with the calculated dihedral angle between (001) and (101).[8]

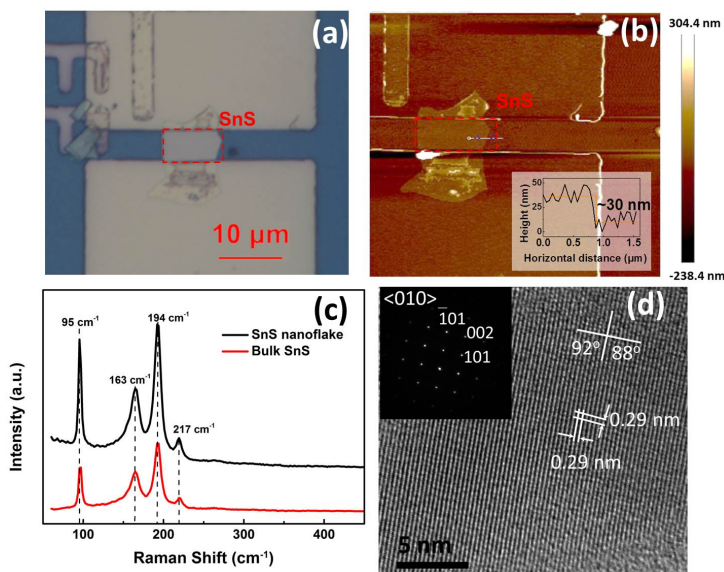


Figure 3.2: SnS nanoflakes deposited on 300 nm  $\text{SiO}_2/\text{Si}$  substrate using the mechanical exfoliation method. (a) Optical image, (b) AFM image, inset image is the corresponding AFM height profile. (c) Raman image. And (d) HRTEM image with SEAD diffraction image.

### 3.4. HUMIDITY SENSING PERFORMANCES

To investigate the effects of humidity on the electronic properties of SnS nanoflakes-based sensor, we performed the gas sensing experiments in the AES-4TH Testing System (Beijing Elite Tech Co. Ltd.). The atmospheric conditions changing in the following order: ambient (25 °C, 30% RH), dry air, gradually increasing humidity (RH= 3-99%), and ambient condition. All the gas-sensing experiments were carried out at room temperature and atmospheric pressure. Figure 3.3a shows the experimental setup used for humidity sensing performance. As shown in Figure 3.3b, the dry air was used as a carrier gas and injected into the chamber for 12 min to reduce the water vapour from about 80% RH down to 3% RH. Then, we varied the RH of 3%, 10%, 30%, 50%, 75%, and 99% in the chamber through a mass flow controller. However, the response/recovery time is limited by the large volume of the chamber, which is about 1.5L and needs a few minutes to be stabilized. Thus, we moved the sensor in/out from the bottle with dry air (3% RH) to the gas collecting container (99% RH) very fast for achieving accurate response/recovery time (see Figure 3.3c). The RH inside gas collecting bottle was controlled by using saturated salt solutions of potassium sulfate anhydrous (AR  $\text{K}_2\text{SO}_4$ ) as described in previous literature.[9]

The electrical characterization of the SnS-based device was performed by using an electrical analysis system (Beijing Elite Tech Co., Ltd, SA6101) to record the current change in real-time (data acquisition time  $\sim 30$  ms). Before the gas-sensing test, the SnS-based

devices were stabilized in  $N_2$  in the system about 30 min for fully recovering to the initial state. For the flexible SnS nanoflakes gas sensor, we applied the silver glue and fine Cu wire in the electrodes and put the flexible sensor into a  $150\text{ }^\circ\text{C}$  temperature chamber for 5 min. After curing and dry, the sensor was pasted to the target surface. The fixed Cu wires in the positive and negative electrodes were then connected with the electrical analysis system. The current-voltage (I-V) measurements were taken from  $-1\text{ V}$  to  $+1\text{ V}$ , and the current were calculated from the slope of the plot through the least square method. The response (S%) of SnS nanoflakes-based humidity sensor is defined as the percent change in current.  $S\% = (\Delta I / I_x) \times 100$ , where  $\Delta I = (I_x - I_{\text{dry}})$ ,  $I_{\text{dry}}$  and  $I_x$  are the resistance of the sensor at dry air (3% RH) and x% RH, respectively.

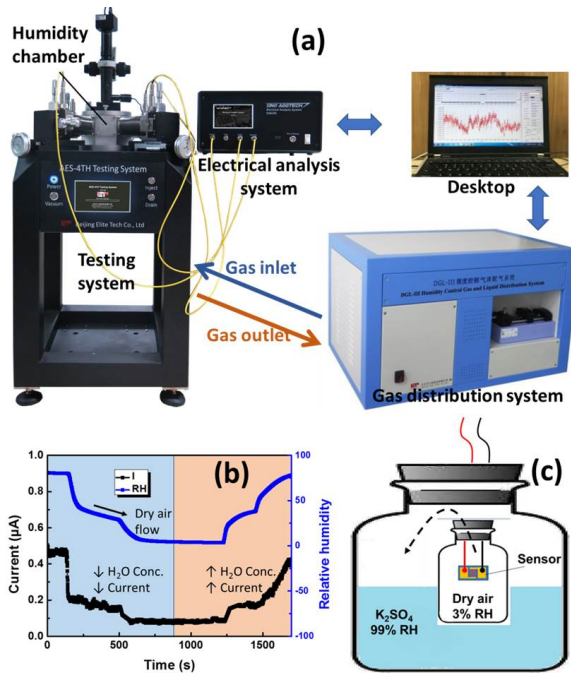


Figure 3.3: (a) Experimental setup used for humidity sensing performance. (b) Current change of the SnS device versus the relative humidity (% RH) in the humidity chamber. The dry air flows into the chamber in the blue area to decrease the % RH inside the chamber. (c) Setup for response/recovery time testing.

The sensing behaviours of SnS nanoflakes-based humidity sensor were measured under different RH of 3%, 10%, 30%, 50%, 75% and 99% at  $25\text{ }^\circ\text{C}$ . Figure 3.4a shows the rectifying output characteristics (I-V) of the device, which indicates the presence of a Schottky barrier between the SnS and the electrode. The maximum power consumption is about  $4.8\text{ }\mu\text{W}$ . As shown in Figure 3.4b, it is found that the resistance decreased with increasing humidity. Since  $H_2O$  is a type of charge acceptor for SnS nanoflakes, the electrons transfer from SnS to  $H_2O$ , inducing the current of SnS increases. With increasing  $H_2O$  concentration, more and more electrons discharged from SnS, thus the current gain. From this plot, we noted that there is almost four orders of magnitude resistance variation exist in the as-

fabricated sensor from 3% RH to 99% RH. The sensor presents a high response of 67600 % under 10% RH and 2491000% under 99% RH. The device is highly sensitive to environmental humidity may be attributed to the Schottky barrier modulation upon gas molecule adsorption, which will be discussed in Section 3.5.

For evaluating the response kinetics and cycling performance, the sensor was moved in/out from the dry air (3% RH) to the gas collecting bottle ( $\sim 99\%$  RH) very fast according to the saturated salt solutions method several times. The cycle performance of the sensor in 3% RH and 99% RH at a bias voltage +1 V is shown in Figure 3.4c, indicating a repeatable and stable response of the sensor. Figure 3.4d shows the current-time (I-t) plot through which the response and recovery time between 3% RH and 99% RH were noted as 6 s and 4 s respectively. Compared with the reported 2D material humidity sensors (see Table 3.1), the SnS nanoflakes-based sensor response is as high as that of the graphene-based humidity sensor. The response speed is faster than many tin-based humidity sensors.[10, 11] The sensing range is larger than those of most reported metal sulfides-based[12, 13], nanofibers[14], and porous membrane[15] humidity sensors.

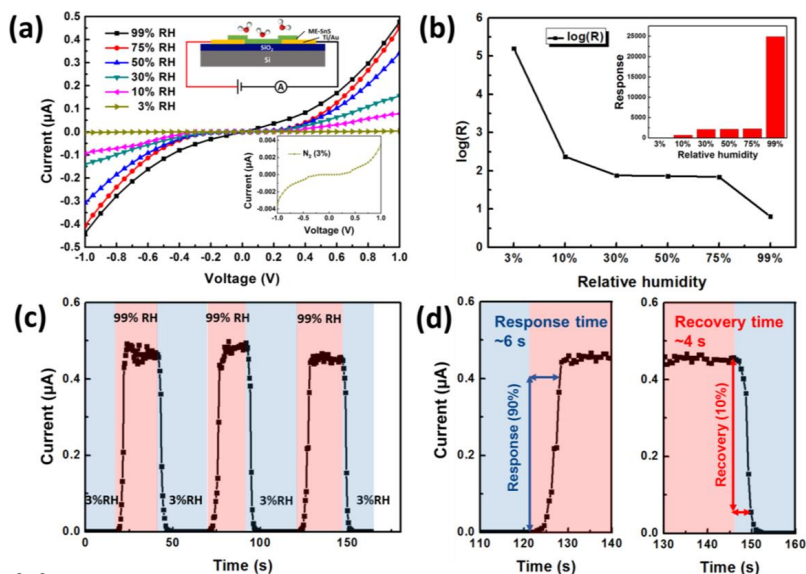


Figure 3.4: Humidity sensing performance of the SnS nanoflakes-based sensor on rigid substrate. (a) I-V curve measured at various RH conditions, showing an obvious slope increasing with the increasing of RH. Inset top image is the schematic of SnS nanoflakes device, and the inset bottom image is the magnified curve of the 3% RH. (b) The derived RH-dependent resistance changes. Inset image is the response under different RH. (c) Time-dependent response current of three cycles of humidity switching between dry air (3% RH) and 99% RH. (d) The response and recovery time of the sensor.

Motivated by the highly sensitive and fast response performance of the SnS nanoflakes-based sensor, we explored the possibility of whether the sensor can be fabricated on a flexible substrate and enable wearable health monitoring applications. Hence, the SnS nanoflakes-based sensors on PI membrane substrate was demonstrated to verify the application in flexible electronics. As shown in Figure 3.1(a'-e'), the fabrication process is

similar to the sensor on a rigid substrate except for the step of pasting and separating PI film. The sensor can be well laminated to many curved surfaces due to the excellent flexibility of the SnS and the substrate. For instance, we pasted the flexible sensor on the surface of a finger with double-side PI tape thickness of about 200  $\mu\text{m}$  and tested its current response in flat and bend states at various RH conditions (see Figure 3.5a,b). It was observed that the current response was slightly affected under the lower RH. When the RH exceeds 50 %RH, the current response was enhanced. In general, the distorted structure of SnS applies less adsorption site for  $\text{H}_2\text{O}$  gas molecules, while the adsorption properties of a gas molecule on SnS can be significantly enhanced by using strain.[16] Under low RH, the gas adsorption of SnS is not saturated. Thus fewer occupied adsorption sites induced less charge transfer between  $\text{H}_2\text{O}$  and SnS, and the current decreased slightly. Under high RH, most of the adsorption sites were occupied, the high surface reactivity induced by mechanical strain can improve gas sensing behaviour. Thus the current is higher than that of flat state.[17] For the dynamic RH changing test, as shown in Figure 3.5c, the sensor under both flat and bent conditions exhibits a repeatable response to a periodical humidity changing between 10% RH and 75% RH, showing similar sensing behaviour.

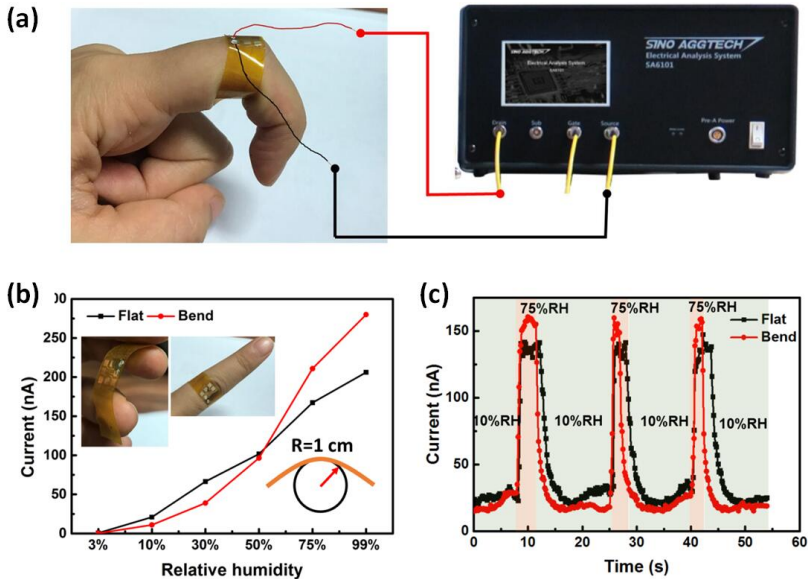


Figure 3.5: (a) The testing setup for SnS nanoflakes-based flexible sensor. (b) The current response of the flexible sensor working in flat and bent states, respectively. Top left inset: Image of SnS nanoflakes transferred onto the PI membrane. Top right inset: Image of the flexible sensors pasted to a finger. Bottom inset: Illustration of the bent state. (c) Dynamic response of the flexible humidity sensor in flat and bent states with the RH level periodically changing between 10% RH and 75% RH. All tests were conducted at room temperature of 25  $^{\circ}\text{C}$  and with a bias voltage of 1V.

Moreover, the bending performances of the SnS nanoflakes-based sensor under different bending angles and bending cycles were investigated. The results are summarized in Figure 3.6. There is no appreciable resistance change of the flexible sensor under different bending angles. Besides, we successively carried out a bending cycle test of 500 cycles of 30 $^{\circ}$ , 500

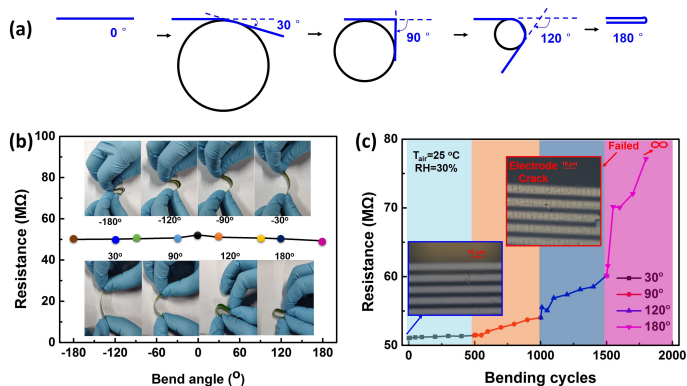


Figure 3.6: (a) Schematic of different bending angle. (b) The resistance of the SnS nanoflakes-based flexible sensor under different bending angles. (c) The bending performance of SnS nanoflakes-based flexible humidity sensor for 500 cycles at different bending angle. Bottom inset: Image of the as-fabricated flexible sensors before bending cycle test. Top inset: Image of the sensors after bending cycle test of 500 cycles of 30°, 500 cycles of 90°, 500 cycles of 120°, and 300 cycles of 180° in sequence.

cycles of 90°, 500 cycles of 120°, and 300 cycles of 180°. It found that the sensor can also be bent many times (above 500 cycles with the bending angle of 30°, 90°) without apparent degradation of response after the mechanical test (see Figure 3.6b). However, the current response of the sensor decreased after 50 bending cycles of 120° and finally failed after 300 bending cycles of 180°. It should be induced by the crack of the electrodes of the sensor, which reminds us to use high flexible electrodes to enhance the long-term reliability of the device. These results clearly illustrate its ability to withstand the stress of human wear in daily life, and its potential as a wearable sensing device.

## 3.5. HUMIDITY SENSING MECHANISM

### 3.5.1. FIRST PRINCIPLE ANALYSIS

To understand the mechanism of the high humidity sensitivity of the SnS-based device, we performed density functional calculations on the SnS-gas system. From all the gases comprising air, four types of gas molecules/SnS interaction, including CO<sub>2</sub>, N<sub>2</sub>, O<sub>2</sub>, and H<sub>2</sub>O, simulations can provide insight into the sensing mechanism more comprehensive. All the calculations were carried out by DMol3 code of Materials Studio.[23] Based on the density functional theory (DFT), we carried out the first-principles calculations within the generalized gradient approximated (GGA) to the Perdew-Burke-Ernzerhof (PBE) exchange-correlation functional. To better describe the van der Waals (vdW) interaction, the dispersion corrected density functional theory (DFT-D) proposed by Grimme was employed because the standard PBE functional cannot well describe the weak interactions. The all-electron double numerical atomic orbital plus polarization (DNP) was used as the basis set. The kinetic energy cutoff the plane wave was set to 500 eV on a Monkhorst-Pack k-point scheme of 8×8×1 for geometry optimization and 16×16×1 k-points for accurate electric properties calculations. The self-consistent convergence accuracy, the maximum displacement and the convergence criterion for the force between atoms were set to be 1×10<sup>-6</sup> eV

Table 3.1: Comparison of various resistive humidity sensor technologies with respect to reported %RH ranges, response and recovery times, and response.

	Material	Measured %RH range	$t_{res}$ (s)	$t_{rec}$ (s)	Response (%)	Ref.
Tang	SnS nanoflake	3-99	6	4	2491 000	This work
Bharatula	SnS <sub>2</sub> nanoflakes	10-97	85	6	11300	[18]
Parthibavarman	SnO <sub>2</sub>	5-95	32	25	3200	[10]
Late	MoS <sub>2</sub>	4-84	9	17	1100	[9]
Guo	WS <sub>2</sub>	11-97	0.18	0.38	235700	[12]
Feng	VS <sub>2</sub> nanosheets	0-98	5	12	320	[13]
Lin	Supramolecular nanofibers	10-80	0.008	0.024	400	[14]
Li	Porous Ionic Membrane	10.89-81.75	6	4	/	[15]
Smith	Graphene	5-95	0.6	0.4	0.31	[19]
Borini	GO	30-80	0.03	0.03	100	[20]
Zhen	Wrinkled graphene	11-95	0.0125	0.0125	/	[21]
He	Graphene confined poly(dopamine)	0-97	0.02	0.017	28380	[22]

per atom,  $1.0 \times 10^{-3}$  Å,  $0.03$  eV Å<sup>-1</sup>, respectively. Periodic boundary conditions were applied in the x- and y- directions. A supercell with an adequate 20 Å vacuum region was introduced in the z-direction to prevent the interactions between the adjacent SnS layers, and all of the atomic positions were optimized until the maximum force is less than  $0.002$  Ha Å<sup>-1</sup> (see Figure 3.7).

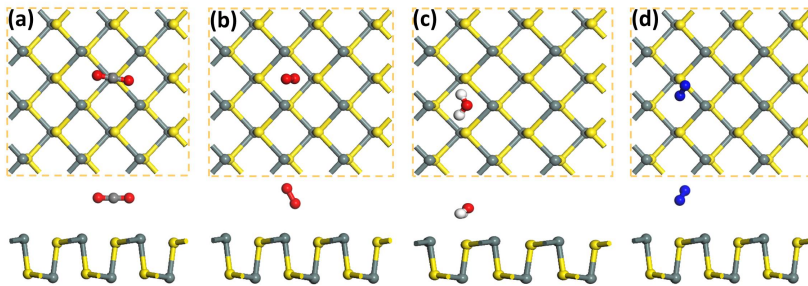


Figure 3.7: Top and side views of the most favorable configurations of (a) CO<sub>2</sub>, (b) O<sub>2</sub>, (c) H<sub>2</sub>O and (d) N<sub>2</sub> adsorbed on the SnS monolayer. The balls in greyish-green and yellow balls represent the Sn and S atoms, where grey, white, red, and blue represent the Sn, S atoms, H, O, and N atoms, respectively.

To better understand the interaction and quantitative determination, the amount of charge transfer between gas molecule and SnS monolayer at 0 K, the charge density difference (CDD) diagram of the O atom S site configuration is plotted in Figure 3.8(a-d). The blue region represents the charge accumulation, while the yellow region shows the charge depletion. It is seen that four types of gas molecule in the air (CO<sub>2</sub>, N<sub>2</sub>, O<sub>2</sub> and H<sub>2</sub>O) act

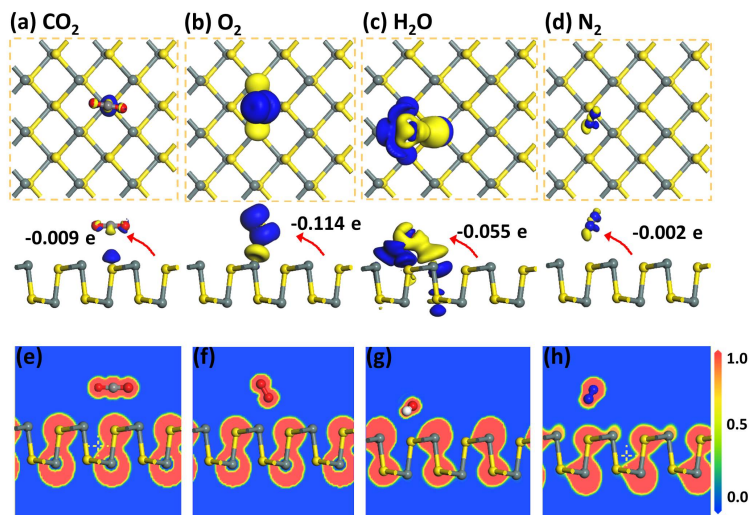


Figure 3.8: Top and side views of the CDD calculation for (a)  $\text{CO}_2$ , (b)  $\text{O}_2$ , (c)  $\text{H}_2\text{O}$  and (d)  $\text{N}_2$  adsorbed on the SnS monolayer at 0 K. The isosurface is taken as  $3 \times 10^{-3} \text{ e } \text{\AA}^{-3}$ . The blue (yellow) region represents the charge accumulation (depletion). The negative sign of  $Q$  indicates charge transfers from SnS to the gas molecule. Electronic localization function (ELF) of (e)  $\text{CO}_2$ , (f)  $\text{O}_2$ , (g)  $\text{H}_2\text{O}$  and (h)  $\text{N}_2$  adsorbed on the SnS monolayer. The reference bar for ELF value is provided at the right side. The balls in greyish-green and yellow balls represent the Sn and S atoms, where grey, white, red, and blue represent the Sn, S atoms, H, O, and N atoms, respectively.

as charge acceptors, and receive 0.009 e, 0.114 e, 0.055 e, and 0.002 e from single-layer SnS, respectively. In addition, as shown in Figure 3.8(e-h), it is seen that the electron localization function (ELF) has no remarkable electron sharing between gas molecules and SnS sheet, which indicates that the chemical bond is unformed. More detailed information from the simulation of different gas-SnS systems, including adsorption energy ( $E_A$ ), equilibrium distances ( $d$ ), and charge transfer ( $\Delta Q$ ) are listed in Table 3.2. The  $d$  is the shortest distance between the atoms of monolayer SnS and molecules. The negative sign of  $Q$  indicates charge transfers from SnS to the gas molecule. The adsorption of  $\text{H}_2\text{O}$  on monolayer SnS produces relatively high binding energies (-0.388 eV) with charge transfer of -0.055 eV, indicating that SnS has good specificity and sensitivity for detecting water vapour in the air. Besides, strong interaction with water molecules via physical absorption makes it possible for repeatable utilization.

Table 3.2: The adsorption energy ( $E_A$ ), adsorption distance ( $d$ ), and change transfer ( $\Delta Q$ ) of different gases on SnS.

Gas	$E_A$ (eV)	$d$ ( $\text{\AA}$ )	$\Delta Q$ (e)	Gas type
$\text{CO}_2$	-0.207	3.34	-0.009	acceptor
$\text{O}_2$	-0.229	3.28	-0.114	acceptor
$\text{H}_2\text{O}$	-0.388	2.72	-0.055	acceptor
$\text{N}_2$	-0.135	3.41	-0.002	acceptor

### 3.5.2. SCHOTTKY BARRIER ANALYSIS

From the experimental sensing results, we find that the current increase is more for high RH levels than that of lower RH levels. The sensing mechanism is relevant to the Schottky nature of SnS-metal contact (see Figure 3.9a, b). The Schottky barrier height of the SnS nanoflakes-based device,  $\phi_B$ , is equal to the sum of the semiconductor band gap ( $E_g$ ) and electron affinity ( $\chi$ ) minus the work function of the metal ( $\Phi_M$ ). The work function of Ti and SnS is 4.33 eV and 4.88 eV, respectively.[24] As shown in Figure 3.9a, it is the Schottky-Mott band alignment of Ti/Au contacts on SnS without gas adsorption. H<sub>2</sub>O adsorption moves the Fermi level of SnS toward the conduction band, decreases the Schottky barrier ( $\phi_B$ ) by  $\Delta\phi_B$ , resulting in thinning of the  $\phi_B$  and an increase of the device current (see Figure 3.9b). For lower RH levels, because of the non-uniform distribution of water layer and non-significant charge transfer through the sensing layer, the  $\Delta\phi_B$  is small, and the response is low. At higher RH levels, the SnS continuously physical adsorbs water layers, which increase the  $\Delta\phi_B$  significantly, inducing high sensitivity of the device. The recovery mechanism is also attributed to the  $\phi_B$ . When air flows out of the chamber, the water molecule shifts from the adsorption sites and the conductivity decreases due to the increased  $\phi_B$ . [25].

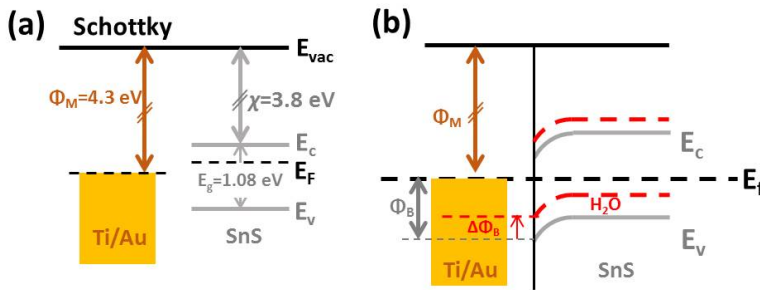


Figure 3.9: (a) Energy diagram of the Ti/Au and SnS before contact. (b) Band realignment and energy diagram of the Ti/Au and SnS after contact and the formation of Schottky barrier. Gray and red lines indicate the energy band of the pristine SnS (solid gray), and after exposure to H<sub>2</sub>O (dashed red), respectively.  $\chi$  is the electron affinity of SnS,  $E_g$  is the band gap,  $E_{vac}$  is the vacuum level,  $E_c$  is the conduction band minimum, and  $E_v$  is the valence band maximum. H<sub>2</sub>O adsorption decreases the Schottky barrier ( $\phi_B$ ) by  $\Delta\phi_B$ , resulting in thinning of the  $\phi_B$  width and an increase of the device current.

## 3.6. APPLICATIONS

### 3.6.1. RESPIRATION MONITORING

Benefit from its excellent performance, we intend to apply SnS nanoflakes-based humidity sensor into some medical applications, such as respiration monitoring. To investigate the respiration performance, the flexible SnS nanoflakes-based humidity sensor was used and pasted inside breath receiving mask (see Figure 3.10). The sensor is sensed and recorded the breath rate and depth to the periodic exercise of normal, deep, and fast breathing successfully. The apnea process was employed during the breathing, and there is no sudden saltation for current, indicating no airflow force effects on the humidity sensor. Besides, the

impact of breathing temperature difference on the humidity sensor response can be ignored if it works on normal body temperature (see Figure 3.11). Therefore, the as-fabricated sensor is only sensitive to humidity variation at atmospheric pressure. In all, the SnS nanoflakes-based humidity sensor shows excellent monitoring and distinction abilities for various breathing process. It is beneficial for real-time monitoring of breath change during extreme sports, hazardous working environments, and medical treatment. According to the signal of the breath pattern, the people can roughly predict the health condition without a region restriction, and the doctors can make a diagnosis of the breath pattern-related disease timely, such as obstructive sleep apnea syndrome (OSAS) and asthma, etc.[26, 27]

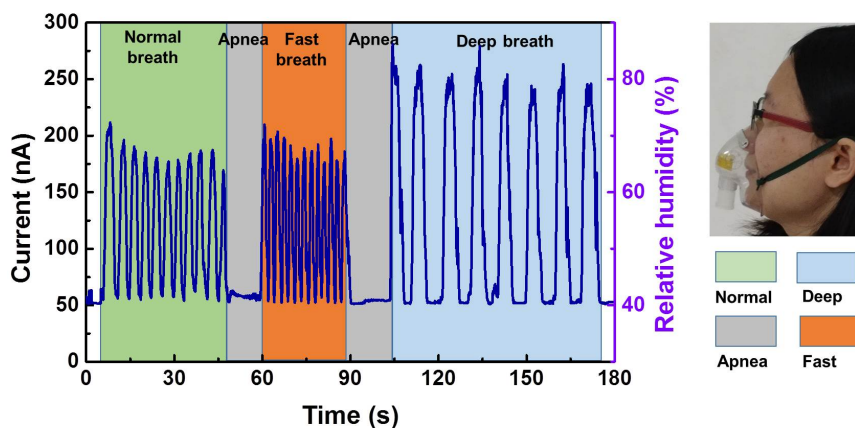


Figure 3.10: The current variation response to normal, deep and fast breathing at room temperature (25 °C).

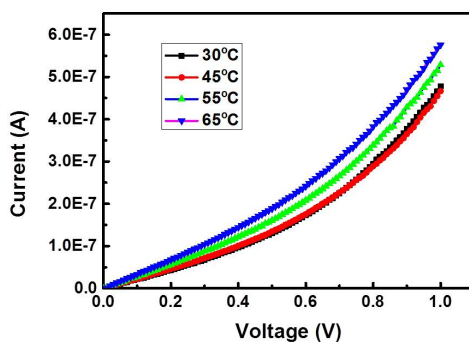


Figure 3.11: The I-V curves of SnS nanoflakes-based humidity sensor at different temperatures.

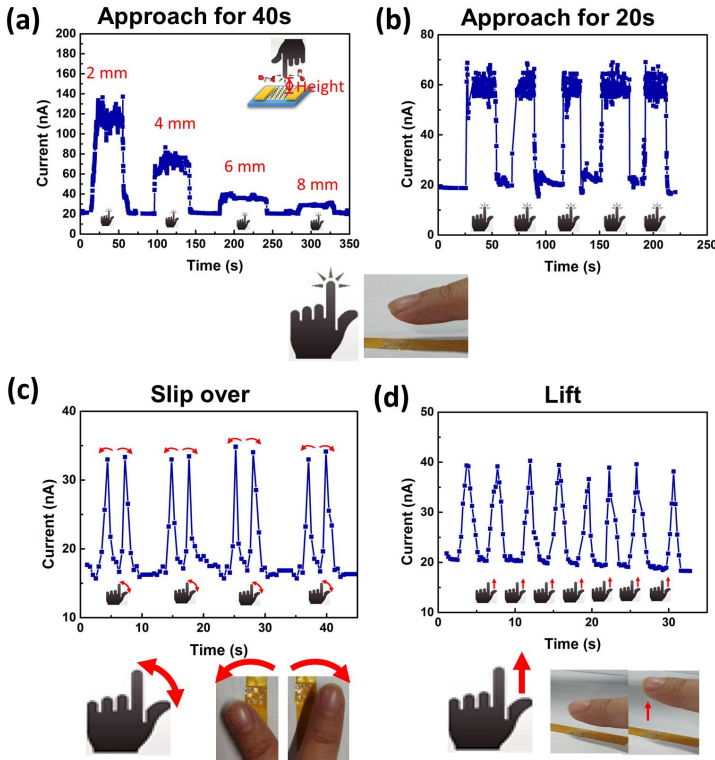


Figure 3.12: (a) Time-dependent response current with a fingertip vertically approaching and retracting away from the device surface at different distances. Inset: The corresponding diagram showing the configuration of the fingertip-sample distance related sensing properties. The RH of the test environment is about 30%. (b) Finger approaching for a short duration of time. (c) Quick Finger slipping over the sensor. (d) Sudden finger lifting.

### 3.6.2. MOVEMENT OF FINGERTIP

Since the SnS nanoflake-based sensor has a high sensitivity under a low-humidity environment, it has a potential application for detecting the surface water evaporation from a fingertip. The RH and temperature near the fingertip are  $\sim 40\%$  RH and  $\sim 30^\circ\text{C}$ , respectively. With the fingertip vertically approaching and retracting away from the device at an increasing distance, the RH of the surface of the sensor decreases, thus the response current decreases (Figure 3.12a). It means that the sensor can detect small humidity changes upon a surface, implying its potential application for noncontact detection and touchscreen. As shown in Figure 3.12b, the sensor shows the periodical response of the finger approaching for 20 s duration time at the same height (5 mm), which is stable and repeatable. Figure 3.12c shows quick slips of fingertip back and forth near the top of the sensor, and sharp two peaks were observed, indicating a sudden shift in humidity level and a high resolution for the change of movement. Conversely, Figure 3.12d shows the signals of the fast lifting of a fingertip. All of the fast and stable sensing behaviour is owing to the fast adsorption of the SnS nanoflakes to the released water vapour of the finger surface. The overall performance

suggests a responsive sensitivity of the SnS nanoflakes sensor in monitoring skin evaporation for applications such as detecting gestures, physiological and physical evaluation based on perspiration, and non-invasive diagnostic of skin conditions.

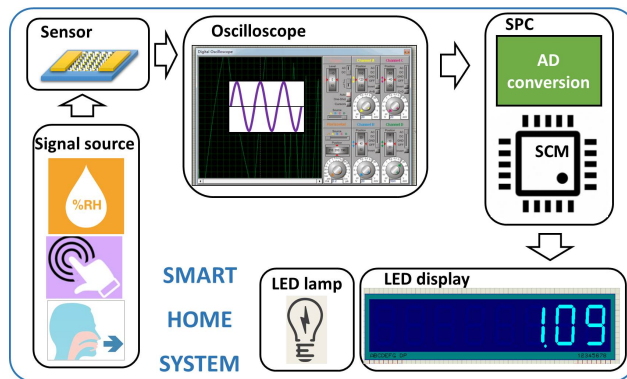


Figure 3.13: The schematic diagram of a SnS nanoflakes-based humidity sensor for smart home system. From left to right, three types of signal source, including environment humidity vibration, human breath, and finger touch; SnS nanoflakes-based sensor, for detecting signal and generating the V-t curve; The curve is shown in oscilloscope; SPC, for signal processing; and one type of electrical appliances, LED lamp.

### 3.6.3. A SMART HOME SYSTEM BASED ON SNS NANOFKAKES-BASED SENSOR

Based on the substantial advantages of the SnS nanoflakes-based sensor demonstrated above, we design a smart home system, comprising of a signal source, humidity sensor, a simple signal processing circuit (SPC), and electrical appliances (see in Figure 3.13). The signal source includes environment humidity variation, human breath, and finger touch. The input signal is the original voltage curve of varied finger touch, which was detected from the signal source by SnS nanoflakes-based humidity sensor, followed by the signals being analog-digital converted and processed in SPC. Then, the latching relay's output terminal is connected with a LED lamp and a LED display. To verify the feasibility of the system, we built and carried it in Proteus Pro7.8 software (Labcenter Electronics Ltd.). The procedure of signal processing based on these circuits is presented in Figure 3.14. When a user is breathing towards the sensor or moving finger upon it, the signal is detected by the sensor and converted into a switching signal for the electrical appliances. The oscilloscope shows the voltage-time (V-t) curve as the voltage change, and the LED display shows the voltage value in real-time. Moreover, the SPC analyzes the sensor's signal and controls the LED lamp to light up if the voltage exceeds the preset threshold. This demonstration further verifies that the SnS nanoflakes-based humidity sensor is able to be used in a smart home system and has excellent potential in daily life, such as touch screen, noncontact controller, and portable diagnosis system so on.

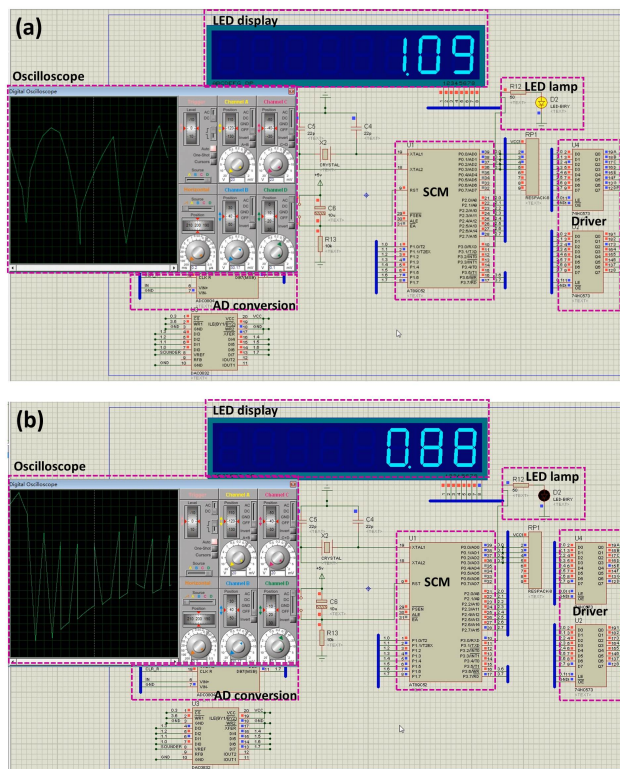


Figure 3.14: After simple processing through single chip microcomputer (SCM), breathe or finger touch signal can be converted into a trigger signal to control the appliances. (a) For breathing signal, if the voltage exceeds the preset threshold of 1 V, the LED lamp lights up. (b) If not, the lamp lights off. The LED display shows the voltage value in real-time.

### 3.7. CONCLUSION

In this chapter, we reported ease of fabricated Schottky-contacted SnS nanoflakes-based humidity sensors on a rigid and flexible substrate. The as-fabricated sensor exhibited good body temperature moisture sensing performance with a high response of 67600% under 10% RH and 2491000% under 99% RH, wide RH range from 3% RH to 99% RH, and fast response/recovery time of 6 s /4 s, competing with tin-based and TMDs-based humidity sensors. The DFT analysis results suggest that the adsorption of H<sub>2</sub>O on SnS produces relatively larger binding energies (-0.388 eV) with charge transfer of -0.055 eV than other gas molecules in the air. The fast response and recovery performances result from the Schottky nature of SnS-Ti contact. More importantly, its wide RH range, quick response time, and excellent biocompatibility enable real-time monitoring of finger touch without contact and different breathing patterns. Finally, we propose a smart home system based on the sensors to process the signal from breath and finger touch experiments for noncontact controlling and respiration monitoring, which presents intelligent potential applications for noncontact healthcare monitoring.

## REFERENCES

- [1] Huiling Tai, Si Wang, Zaihua Duan, and Yadong Jiang. Evolution of breath analysis based on humidity and gas sensors: Potential and challenges. *Sensors and Actuators B: Chemical*, page 128104, 2020.
- [2] Hyeongsu Choi, Jeongsu Lee, Seokyeon Shin, Juhyun Lee, Seungjin Lee, Hyunwoo Park, Sejin Kwon, Namgwe Lee, Minwook Bang, Seung-Beck Lee, and Hyeongtag Jeon. Fabrication of high crystalline SnS and SnS<sub>2</sub> thin films, and their switching device characteristics. *Nanotechnology*, 29(21):215201, 2018.
- [3] M. F. Afsar, M. A. Rafiq, and A. I. Y. Tok. Two-dimensional SnS nanoflakes: synthesis and application to acetone and alcohol sensors. *RSC Advances*, 7(35):21556–21566, 2017.
- [4] F. Hu, H. Tang, C. Tan, H. Ye, X. Chen, and G. Zhang. Nitrogen dioxide gas sensor based on monolayer SnS: A first-principle study. *IEEE Electron Device Letters*, 38(7):983–986, 2017.
- [5] Zhongjian Xie, Dou Wang, Taojian Fan, Chenyang Xing, Zhongjun Li, Wei Tao, Liping Liu, Shiyun Bao, Dianyuan Fan, and Han Zhang. Black phosphorus analogue tin sulfide nanosheets: synthesis and application as near-infrared photothermal agents and drug delivery platforms for cancer therapy. *Journal of Materials Chemistry B*, 6(29):4747–4755, 2018.
- [6] Bao-Zhen Sun, Zuju Ma, Chao He, and Kechen Wu. Enhanced thermoelectric performance of layered SnS crystals: the synergetic effect of temperature and carrier concentration. *RSC Advances*, 5(69):56382–56390, 2015.
- [7] In-Hwan Baek, Jung Joon Pyeon, Young Geun Song, Taek-Mo Chung, Hae-Ryoung Kim, Seung-Hyub Baek, Jin-Sang Kim, Chong-Yun Kang, Ji-Won Choi, Cheol Seong Hwang, Jeong Hwan Han, and Seong Keun Kim. Synthesis of SnS thin films by atomic layer deposition at low temperatures. *Chemistry of Materials*, 29(19):8100–8110, 2017.
- [8] Zhengtao Deng, Di Cao, Jin He, Su Lin, Stuart M. Lindsay, and Yan Liu. Solution synthesis of ultrathin single-crystalline SnS nanoribbons for photodetectors via phase transition and surface processing. *ACS Nano*, 6(7):6197–6207, 2012.
- [9] Dattatray J. Late, Yi-Kai Huang, Bin Liu, Jagaran Acharya, Sharmila N. Shirodkar, Jiajun Luo, Aiming Yan, Daniel Charles, Umesh V. Waghmare, Vinayak P. Dravid, and C. N. R. Rao. Sensing behavior of atomically thin-layered MoS<sub>2</sub> transistors. *ACS Nano*, 7(6):4879–4891, 2013.
- [10] M. Parthibavarman, V. Hariharan, and C. Sekar. High-sensitivity humidity sensor based on SnO<sub>2</sub> nanoparticles synthesized by microwave irradiation method. *Materials Science and Engineering: C*, 31(5):840–844, 2011.
- [11] Jian Zhen Ou, Wanyin Ge, Benjamin Carey, Torben Daeneke, Asaf Rotbart, Wei Shan, Yichao Wang, Zhengqian Fu, Adam F. Chrimes, Wojtek Wlodarski, Salvy P. Russo, Yong Xiang Li, and Kourosh Kalantar-zadeh. Physisorption-based charge transfer in two-dimensional SnS<sub>2</sub> for selective and reversible NO<sub>2</sub> gas sensing. *ACS Nano*, 9(10):10313–10323, 2015.
- [12] Huayang Guo, Changyong Lan, Zhifei Zhou, Peihua Sun, Dapeng Wei, and Chun Li. Transparent, flexible, and stretchable WS<sub>2</sub> based humidity sensors for electronic skin. *Nanoscale*, 9(19):6246–6253, 2017.

- [13] Jun Feng, Lele Peng, Changzheng Wu, Xu Sun, Shuanglin Hu, Chenwen Lin, Jun Dai, Jinlong Yang, and Yi Xie. Giant moisture responsiveness of VS<sub>2</sub> ultrathin nanosheets for novel touchless positioning interface. *Advanced Materials*, 24(15):1969–1974, 2012.
- [14] Umesh Moger, Abhay A. Sagade, Subi J. George, and Giridhar U. Kulkarni. Ultrafast response humidity sensor using supramolecular nanofibre and its application in monitoring breath humidity and flow. *Scientific Reports*, 4:4103, 2014.
- [15] Tie Li, Lianhui Li, Hongwei Sun, Yan Xu, Xuewen Wang, Hui Luo, Zheng Liu, and Ting Zhang. Porous ionic membrane based flexible humidity sensor and its multifunctional applications. *Advanced Science*, 4(5):1600404, 2017.
- [16] Fafei Hu, Huaiyu Ye, Hongyu Tang, and Xianping Chen. Modulation of gas adsorption on SnS by strain, 2018.
- [17] Pankaj B. Agarwal, Bayazeed Alam, Daya Shankar Sharma, Sumit Sharma, Soumen Mandal, and Ajay Agarwal. Flexible NO<sub>2</sub> gas sensor based on single-walled carbon nanotubes on polytetrafluoroethylene substrates. *Flexible and Printed Electronics*, 3(3):035001, 2018.
- [18] Lakshmi Deepika Bharatula, Manisha B. Erande, Imtiaz S. Mulla, Chandra Sekhar Rout, and Dattatray J. Late. SnS<sub>2</sub> nanoflakes for efficient humidity and alcohol sensing at room temperature. *RSC Advances*, 6(107):105421–105427, 2016.
- [19] Anderson D. Smith, Karim Elgammal, Frank Niklaus, Anna Delin, Andreas C. Fischer, Sam Vaziri, Fredrik Forsberg, Mikael R sander, Hakan Hugosson, Lars Bergqvist, Stephan Schroder, Satender Kataria, Mikael Ostling, and Max C. Lemme. Resistive graphene humidity sensors with rapid and direct electrical readout. *Nanoscale*, 7(45):19099–19109, 2015.
- [20] Stefano Borini, Richard White, Di Wei, Michael Astley, Samiul Haque, Elisabetta Spigone, Nadine Harris, Jani Kivioja, and Tapani Ryh nen. Ultrafast graphene oxide humidity sensors. *ACS Nano*, 7(12):11166–11173, 2013.
- [21] Zhen Zhen, Zechen Li, Xuanliang Zhao, Yujia Zhong, Li Zhang, Qiao Chen, Tingting Yang, and Hongwei Zhu. Formation of uniform water microdroplets on wrinkled graphene for ultrafast humidity sensing. *Small*, 14(15):1703848, 2018.
- [22] Jiang He, Peng Xiao, Jiangwei Shi, Yun Liang, Wei Lu, Yousi Chen, Wenqin Wang, Patrick Theato, Shiao-Wei Kuo, and Tao Chen. High performance humidity fluctuation sensor for wearable devices via a bioinspired atomic-precise tunable graphene-polymer heterogeneous sensing junction. *Chemistry of Materials*, 30(13):4343–4354, 2018.
- [23] B. Delley. From molecules to solids with the DMol<sub>3</sub> approach. *The Journal of Chemical Physics*, 113(18):7756–7764, 2000.
- [24] Jenifer R. Hajzus, Adam J. Biacchi, Son T. Le, Curt A. Richter, Angela R. Hight Walker, and Lisa M. Porter. Contacts to solution-synthesized SnS nanoribbons: dependence of barrier height on metal work function. *Nanoscale*, 10(1):319–327, 2018.
- [25] Debasree Burman, Sumita Santra, Panchanan Pramanik, and Prasanta Kumar Guha. Pt decorated MoS<sub>2</sub> nanoflakes for ultrasensitive resistive humidity sensor. *Nanotechnology*, 29(11):115504, 2018.

- [26] Yu Pang, Jinming Jian, Tao Tu, Zhen Yang, Jiang Ling, Yuxing Li, Xuefeng Wang, Yancong Qiao, He Tian, Yi Yang, and Tian-Ling Ren. Wearable humidity sensor based on porous graphene network for respiration monitoring. *Biosensors and Bioelectronics*, 116:123–129, 2018.
- [27] Hao Jin, Xiang Tao, Shurong Dong, Yiheng Qin, Liyang Yu, Jikui Luo, and M. Jamal Deen. Flexible surface acoustic wave respiration sensor for monitoring obstructive sleep apnea syndrome. *Journal of Micromechanics and Microengineering*, 27(11):115006, 2017.

# 4

## SnO<sub>x</sub>/SnS HETEROSTRUCTURES GAS SENSOR

*To further improve the sensing performance, firstly, I comparatively analyzed the humidity sensing responses between LPE-SnS nanosheets, SnO<sub>2</sub> nanosheets, SnO<sub>2</sub>/SnS nanocomposites, and SnO<sub>x</sub>/SnS heterostructure devices. The results show that the sensor based on SnO<sub>x</sub>/SnS heterostructure that formed by the post-oxidation of LPE-SnS nanosheets in air has excellent humidity sensing response among these four types of sensors. Accordingly, the SnO<sub>x</sub>/SnS is used for detecting NO<sub>2</sub> gas, which exhibits a high response of 161% towards 1 ppb NO<sub>2</sub>, wide detecting range (from 1 ppb to 1 ppm), an ultra-low theoretical detection limit of 5 ppt, and excellent repeatability. The sensor also shows superior gas selectivity to NO<sub>2</sub> with comparison to several other gas molecules, such as NO, H<sub>2</sub>, CO, NH<sub>3</sub>, and H<sub>2</sub>O. We have systematically investigated the gas sensing mechanism based on experiments and density functional theory simulation. The results show that the outstanding NO<sub>2</sub> sensing behaviour is attributed to numerous oxygen vacancies generated in the post-oxidation process, which provides more adsorption sites, superior band gap modulation, and more active charge transfer in the sensing interface layer. .*

---

Parts of this chapter have been published in: "Liquid-phase exfoliated SnS as a semiconductor coating filler to enhance corrosion protection performance", *Physical Chemistry Chemical Physics*, **21**, 33, 2019.

## 4.1. INTRODUCTION

NUMEROUS studies have proved that the sensing performance of nanomaterials-based gas sensors can be improved through using different morphologies (i.e., nanoflakes, nanosheets or nanorods) to increase the surface area, constructing heterojunction to enhance the charge transfer in the interface, and introducing defects to improve the adsorption energy between gas molecules and nanomaterials. Many metal sulfides-based heterojunction is constructed with metal oxides, which can be attributed to the strong interaction between the oxygen ions of metal oxides and gas analytes and the high adsorption energy of the defects (oxygen vacancies). Tin oxides (i.e.,  $\text{SnO}_2$ ,  $\text{SnO}$ , etc.) is the most commonly used metal oxide materials for gas sensor. Cui *et al.*[1] reported a  $\text{SnO}_2/\text{MoS}_2$  hybrids  $\text{NO}_2$  gas sensor that has a lower detection limit of 0.5 ppm. Hao *et al.*[2] presented hierarchical  $\text{SnS}_2/\text{SnO}_2$  nanocomposites to improve the sensing performance toward 1 ppm  $\text{NO}_2$  at 100 °C and a detection limit of 125 ppb (response of 90%). In addition, The groups of Epifani [3] and Li [4] have proved that  $\text{SnO}_2$  with oxygen vacancies (OVs) for  $\text{NO}_2$  gas detection exhibited ultrahigh response at room temperature. They also found that the higher operation temperature, the lower the gas sensing response. It indicates that introducing OVs is an efficient way of enhancing gas sensing performance.

Herein, firstly, the liquid-phase exfoliation (LPE) method is employed to prepare SnS nanosheets with a large surface area. The  $\text{SnO}_2$  is combined with SnS nanosheets for constructing  $\text{SnO}_2/\text{SnS}$  nanocomposites. Simultaneously,  $\text{SnO}_x/\text{SnS}$  heterostructures were synthesized by oxidizing pristine SnS in air at 350 °C. The humidity sensing performances of ME-SnS nanoflakes, LPE-SnS nanosheets,  $\text{SnO}_2$  nanosheets,  $\text{SnO}_2/\text{SnS}$  nanocomposites, and  $\text{SnO}_x/\text{SnS}$  heterostructure devices are comparatively analyzed. Then, the response, selectivity and LOD of  $\text{SnO}_x/\text{SnS}$  heterostructures towards  $\text{NO}_2$  are tested at room temperature. Finally, the gas sensing mechanism is analyzed based on density functional theory (DFT).

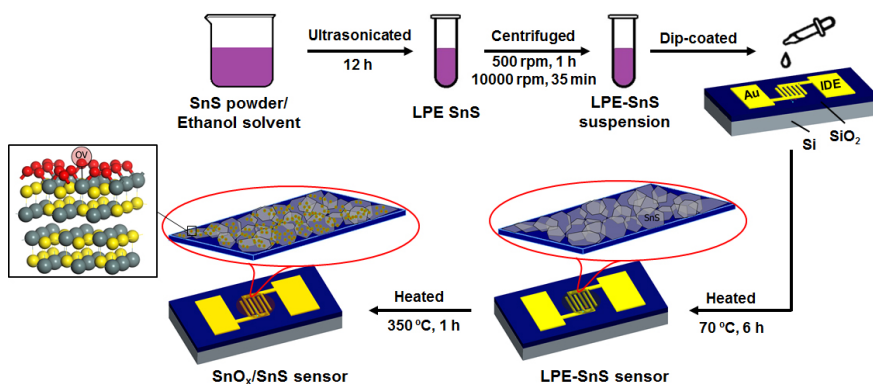


Figure 4.1: Fabrication process of the  $\text{SnO}_x/\text{SnS}$  heterostructure-based gas sensor.

## 4.2. FABRICATION OF GAS SENSORS

**Preparation of SnS nanosheets.** The SnS nanomaterial was purchased directly from 6Carbon Corp., China, and all chemicals were used as received without further purification. SnS (mg) was uniformly dispersed in ethanol (ml) and subsequently stirred for 20 min to form a suspension. The suspensions were ultrasonicated in a KH-500B benchtop ultrasonic bath (250 W) operating at 40 kHz frequency and 100% power for 12 h. The bath was modified by the addition of a water-cooling coil to maintain the water temperature below 30 °C during sonication. Upon completion of the exfoliation step, the dispersion was centrifuged at a rate of 500 rpm for 45 min to remove the remaining bulk material. The top two-thirds of the supernatant was collected for analysis. Then, we dried the supernatant in a temperature chamber and cleaned them through distilled (DI) water several times, and the LPE-SnS nanosheets were obtained.

**Fabrication of gas sensor.** The obtained SnS nanosheets (20 mg) were uniformly dispersed in ethanol (20 ml) and subsequently stirred for 20 min to form a suspension. The resulting suspension was deposited onto the SiO<sub>2</sub>/Si substrate pre-printed with Au interdigitated electrodes (IDEs). After the ethanol evaporated, the sensors were dried at 70 °C for 2 h to purify the samples. And the SnS-based gas sensor was obtained. Then, the SnO<sub>x</sub>/SnS was synthesized by the in-situ high-temperature oxidation method. The oxidation of the SnS nanosheets was conducted at 350 °C for one hour in the air. According to previous reports, the oxidation of SnS to SnO<sub>x</sub> occurred at temperatures above 325 °C through the reaction  $\text{SnS} + (1 + x/2) \text{O}_2 \rightarrow \text{SnO}_x + \text{SO}_2$ . [5] In addition, to quantitatively investigate the change of SnS flake under different annealing temperatures, Higashitarumizu *et al.* [6] calculated the optical contrasts of the SnS after post-oxidation. They found that the optical contrasts were almost constant after 6 h at temperatures below 350 °C, indicating that the SnS can not be oxidized below 350 °C. Therefore, in this work, the SnS nanosheets were oxidized under 350 °C for one hour to form SnO<sub>x</sub>/SnS heterostructure. The samples of SnO<sub>x</sub>/SnS heterostructure-based gas sensors were obtained, as shown in Figure 4.1. The SnO<sub>2</sub> nanosheets (20 mg) were purchased directly from Shanghai Aladdin Biochemical Technology Co., Ltd., China. They were uniformly dispersed in ethanol (20 ml) and subsequently stirred for 20 min to form a suspension. The suspension was deposited onto the Au IDEs and dried at 70 °C for 2 h. This is the SnO<sub>2</sub>-based humidity sensor. The fabrication process of the SnO<sub>2</sub>/SnS nanocomposites sensor is the mixture of SnS (10 mg) and SnO<sub>2</sub> (10 mg) in ethanol (20 ml) with magnetic mixer for 1 h, and the dip coating process of the SnO<sub>2</sub>/SnS suspension to the Au IDEs.

## 4.3. HUMIDITY SENSING PERFORMANCES

The morphology of the SnS nanosheets, SnO<sub>2</sub> nanosheets, SnO<sub>2</sub>/SnS nanocomposites, and SnO<sub>x</sub>/SnS heterostructure was characterized by a field-emission scanning electron microscopy (FESEM, JEOL JSM-7610FPlus) using an acceleration voltage of 5 kV and a working distance of 8 mm. As shown in Figure 4.2a and b, SnS has a flake-shaped morphology, while the SnO<sub>x</sub>/SnS heterostructure is constructed by the SnS nanosheets and decorated with small SnO<sub>x</sub> nanoparticles. Figure 4.2c illustrated that the size of SnO<sub>2</sub> nanosheets is about 50 nm. Figure 4.2d show that the SnO<sub>2</sub>/SnS nanocomposites is composed of SnS nanoflakes with mixed SnO<sub>2</sub> nanosheets.

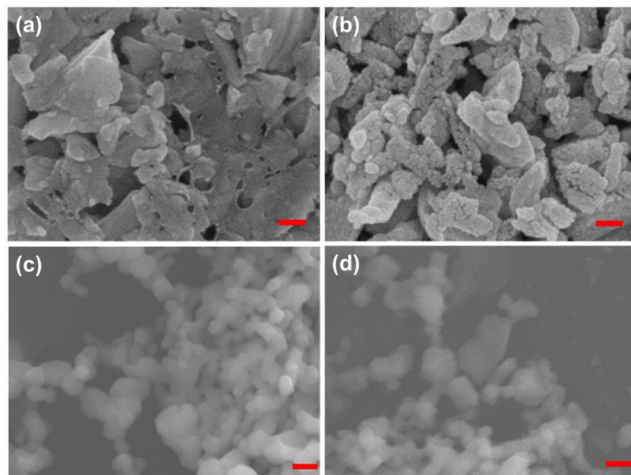


Figure 4.2: SEM characterization of (a) SnS nanosheets, (b)  $\text{SnO}_x/\text{SnS}$  heterostructure, (c)  $\text{SnO}_2$  nanosheets, and (d)  $\text{SnO}_2/\text{SnS}$  nanocomposites. The red bar indicates 50 nm.

Humidity sensing measurement was performed at the ambient temperature of 25 °C. Various RH levels inside gas-collecting bottles were controlled by using several saturated salt solutions, as described in previous literature.[7] Saturated solutions of LiCl,  $\text{MgCl}_2$ ,  $\text{Mg}(\text{NO}_3)_2$ , NaCl, and  $\text{K}_2\text{SO}_4$  in a closed vessel were used to yield approximately 11%, 33%, 52%, 75%, 85% and 99% RH levels, respectively. Then, we moved the sensor in/out from the gas collecting bottle ( $\sim 25$  °C,  $\sim 99\%$  RH) to the ambient ( $\sim 25$  °C,  $\sim 30\%$  RH) fast for achieving accurate response/recovery time. Electrical characterizations of SnS-based device were performed by using a semiconductor parameter analyzer (Keithley 4200, Tektronix Corp.) to record the current change in real time (data acquisition time  $\sim 30$  ms). Before the gas-sensing test, all the samples were stabilized at 70 °C inside a temperature chamber about 30 min for fully recovering to the initial state.

As shown in Figure 4.3, under 75%RH humidity condition, the SnS nanosheets-based device response and recovery very fast, while their response is low (1260%). Even if it is not ultrahigh as that of the ME-SnS nanoflakes-based sensor (2491000 @ 99%RH, 229000 @ 75%RH), the fast response time and sensitivity can meet the requirement of humidity sensing. The gas sensing response of the  $\text{SnO}_2$ -based device is much higher than that of the SnS nanosheets sensor, while the recovery time is 50 s. To combine the fast response of SnS and high sensitivity of  $\text{SnO}_2$ , we mixed SnS and  $\text{SnO}_2$  for achieving  $\text{SnO}_2/\text{SnS}$  nanocomposites-based device, which shows the high response of 9950% while the recovery time is more than 210 s. Alternatively, the  $\text{SnO}_x/\text{SnS}$  heterostructure shows a high response of 10200%, and very short response and recovery times (5 s/3 s). It is much better than that of ME-SnS nanoflakes sensors. The  $\text{SnO}_x/\text{SnS}$  heterostructure-based sensor exhibits excellent repeatability and wide sensing range (11%RH-99%RH), see Figure 4.4. The results indicate that tin oxides can contribute to the high response to humidity, and SnS is helpful for response and recovery time. Comparing the response of  $\text{SnO}_x/\text{SnS}$  heterostructure with  $\text{SnO}_2/\text{SnS}$  nanocomposites, it is found that the high sensing performance

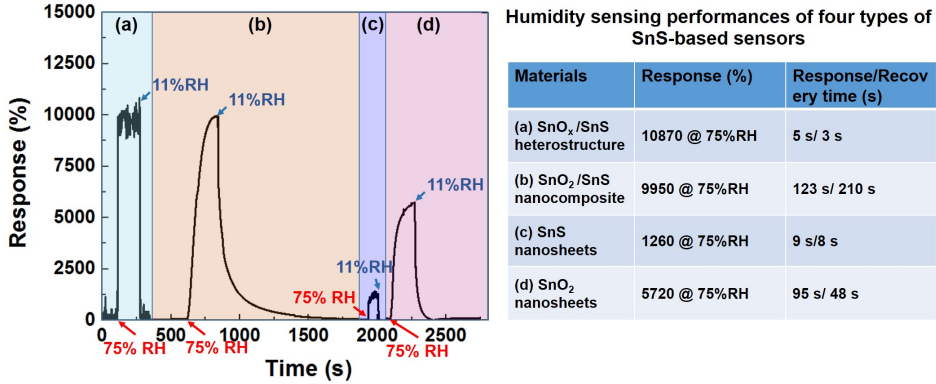


Figure 4.3: Dynamic response-recovery curves of (Left) (a) SnO<sub>x</sub>/SnS heterostructure, (b) SnO<sub>2</sub>/SnS nanocomposites, (c) SnS nanosheets, and (d) SnO<sub>2</sub> nanosheets to humidity in the concentration of 75% RH at room temperature. (Right) Humidity sensing response and speed of SnO<sub>x</sub>/SnS heterostructure, SnO<sub>2</sub>/SnS nanocomposites, SnS nanosheets, and SnO<sub>2</sub> nanosheets.

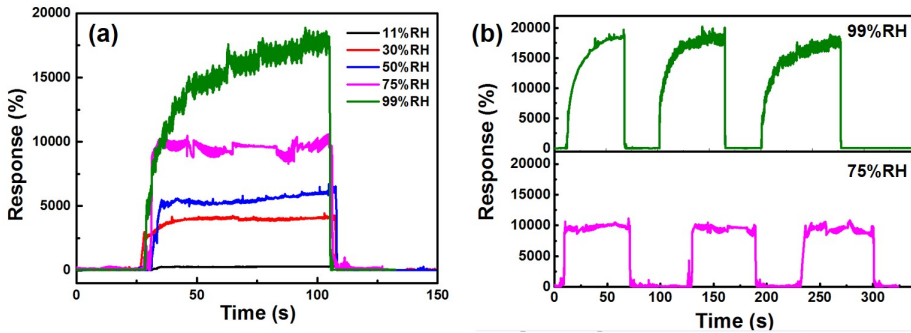


Figure 4.4: (a) Dynamic response-recovery curves of SnO<sub>x</sub>/SnS heterostructure to moisture in the concentration range from 11% to 99% RH at room temperature. (b) Repetitive dynamic response-recovery curves of SnO<sub>x</sub>/SnS heterostructure under 75% RH and 99% RH.

of SnO<sub>x</sub>/SnS heterostructure should not only be attributed to the heterojunction between SnO<sub>x</sub> and SnS, but also to the morphology.

## 4.4. NO<sub>2</sub> GAS SENSING PERFORMANCE

### 4.4.1. CHARACTERIZATION

To understand the characteristics of SnO<sub>x</sub>/SnS heterostructures, a series of material characterizations were carried out. The crystal structures of SnS nanosheets and SnO<sub>x</sub>/SnS heterostructure collected from sensing film were measured on a Philips X'pert X-ray diffractometer (XRD) with Cu K $\alpha$ 1 radiation in the 2 $\theta$  range from 10° to 80°. X-ray photoelectron spectroscopy (XPS) was used to investigate surface modification. The chemical mappings of the SnS nanosheets and SnO<sub>x</sub>/SnS heterostructure were also obtained by energy dispersive spectroscopy (EDS, Oxford X-Max<sup>N</sup>-50) using an accelerating voltage of 20 kV

with a working distance of 10 mm. The crystalline microstructure was characterized by transmission electron microscope (TEM, JEOL JEM-2100).

The nanocrystal structures were observed using a transmission electron microscope (TEM), as shown in Figure 4.5a, the SnS nanosheets with a diameter of 10-100 nm. After the oxidation process, the  $\text{SnO}_x/\text{SnS}$  heterostructure is shown in Figure 4.5b, the typical size of the resulting heterostructure is 50 nm. Figure 4.5c shows the typical HRTEM image of SnS nanoflakes, and the magnified HRTEM image presents the lattice spacing of 0.292 nm corresponding to the distance between (101) planes of the orthorhombic phase of SnS. The left inset image shows the selected area electron diffraction (SAED) rings of SnS, which reveals a single-crystalline orthorhombic phase projected along the  $\langle 010 \rangle$  direction and indexes to the reflections of the SnS (002) and (101) planes. Figure 4.5c shows that the fringe interval of 0.292 nm corresponds to the d-spacing of (101) SnS. Meanwhile, the fringe interval of 0.334 nm and 0.176 nm agrees well with the d-spacing of (011) and (211) crystal planes of  $\text{SnO}_2$ , respectively. The fringe interval of 0.299 nm corresponds to the d-spacing of (101) SnO. The HRTEM image demonstrates that many nanocrystals grow densely on the SnS nanoflakes and form  $\text{SnO}_x/\text{SnS}$  heterostructure. The SAED rings (left inset of Figure 4.5d) further confirms that the heterostructures are polycrystalline structures. To further analyze the interfacial evolution from SnS to  $\text{SnO}_x/\text{SnS}$ , atomic resolution high-angle annular dark-field (HAADF) STEM in combination with dispersive X-ray spectroscopy (EDX) elemental mapping and electron energy loss spectroscopy (EELS) are shown in Figure 4.6, respectively. The elemental mapping results show that there is only O, S, and Sn in the  $\text{SnO}_x/\text{SnS}$  heterostructure and all of the elements are uniformly distributed, further confirming the existence and uniform distribution of  $\text{SnO}_x$  nanoparticles in the SnS nanosheets.

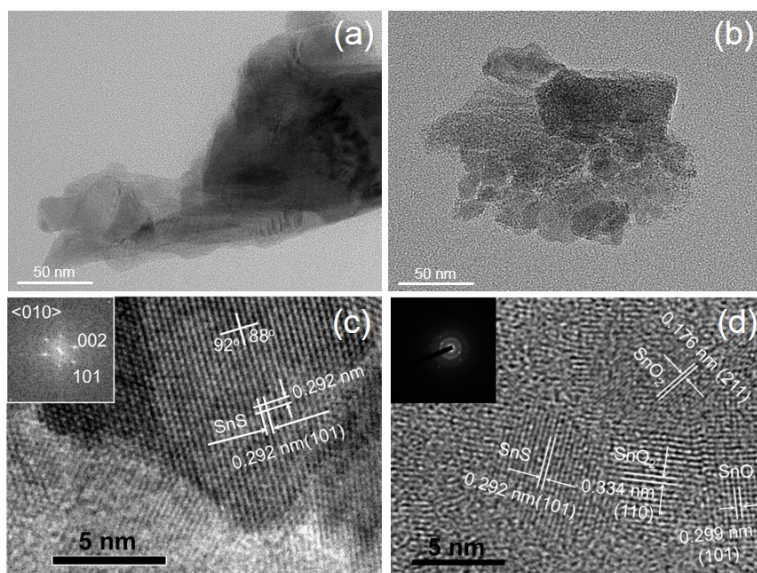


Figure 4.5: (a) TEM image, (b) HRTEM image of SnS nanosheets. (c) TEM image, (d) HRTEM image of  $\text{SnO}_x/\text{SnS}$  heterostructure.

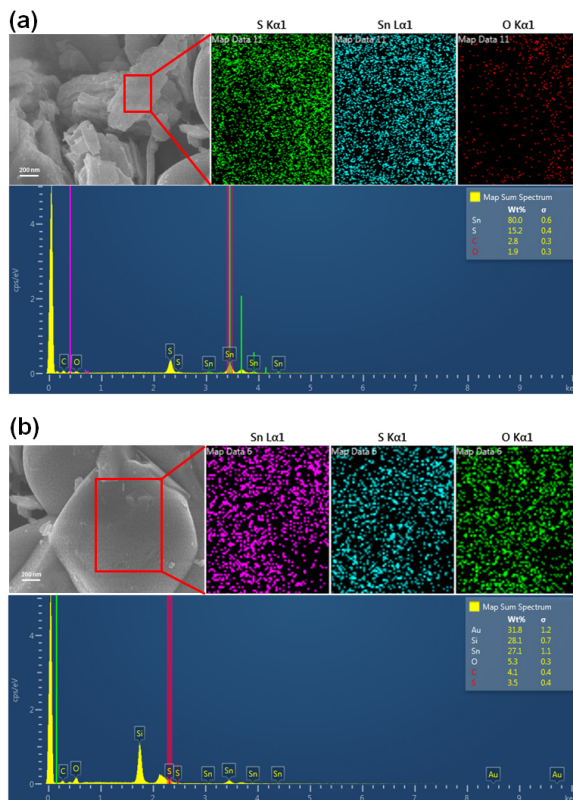


Figure 4.6: SEM image and corresponding elemental mappings of O, S, and Sn of (a) the SnS nanosheet and (b) SnO<sub>x</sub>/SnS heterostructure. The inset images are the elemental compositions.

Since the EDX results of a light element (O) is inaccurate, the X-ray photoelectron spectroscopy (XPS) analysis was applied to acquire the elemental ratios of oxygen to the tin. It can also show the chemical states and chemical composition of the fabricated SnO<sub>x</sub>/SnS nanosheets (see Figure 4.7). From the deconvolution of the Sn 3d spectra in Figure 4.7b, the binding energies at 486.4 and 494.7 eV correspond to the Sn 3d<sup>5/2</sup> and Sn 3d<sup>3/2</sup> of Sn<sup>2+</sup> species, respectively, while the peaks at 487.1 and 495.4 eV are ascribed to the Sn 3d<sup>5/2</sup> and Sn 3d<sup>3/2</sup> of Sn<sup>4+</sup> species. It confirms the formation of SnO<sub>2</sub> and might be formed SnO. We further check the peak of O 1s, which can be split into three different peaks at 530.1, 530.9, and 532.0 eV, corresponding to the Sn-O-Sn, Sn-O, and hydroxyl groups respectively (Figure 4.7c). The S 2p spectrum is fitted with two peaks at 161.0 and 162.2 eV, which are attributed to the S 2p<sup>3/2</sup> and 2p<sup>1/2</sup> peaks for S<sub>2</sub><sup>-</sup> ions in SnS (Figure 4.7d). Overall, it can confirm that SnO<sub>x</sub>/SnS contains SnS, SnO, and SnO<sub>2</sub>. Since the atomic percentages of Sn, S and O are 40%, 16.67%, and 43.33%, respectively, the ratio of lattice oxygen to Sn is approximately 1.86. According to the ratio of lattice oxygen to Sn, SnO<sub>x</sub> is denoted as SnO<sub>1.86</sub>, indicating the heterostructure has different kinds of oxidation and rich OV. From the electron paramagnetic resonance (EPR) investigation in Figure 4.7e, it is observed that

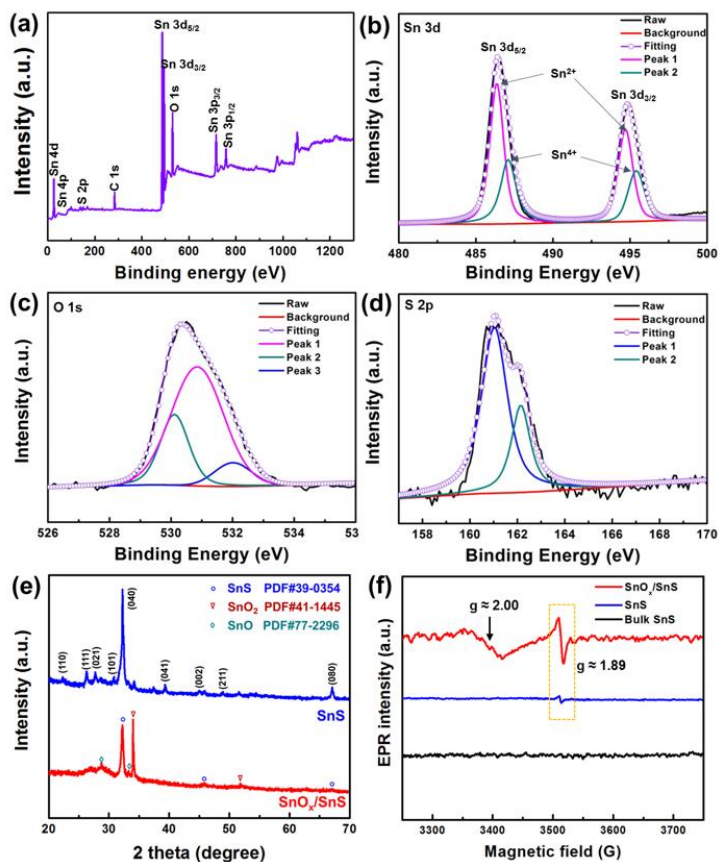


Figure 4.7: (a) XPS survey, and high-resolution (b) Sn 3d, (c) O 1s and (d) S 2p spectra of  $\text{SnO}_x/\text{SnS}$  heterostructure. (e) XRD patterns of the SnS nanosheets (blue) and  $\text{SnO}_x/\text{SnS}$  heterostructure (red). (f) EPR spectra comparison of bulk SnS, SnS nanosheets and  $\text{SnO}_x/\text{SnS}$  heterostructure.

there are symmetrical resonance lines in the spectra located at  $g \approx 1.89$  in  $\text{SnO}_x/\text{SnS}$  and SnS nanosheets samples except for bulk SnS, which are assigned as singly ionized oxygen vacancies ( $\text{V}_{\text{O}}^-$ ). [8] After LPE and  $70^\circ\text{C}$  annealing process, there are few vacancies on the surface of SnS. Moreover, the intensity of  $\text{SnO}_x/\text{SnS}$ 's resonance line is higher than that of SnS, which reveals that post-oxidation can introduce more OVs to the surface of SnS. In addition, there is another resonance line located at  $g \approx 2.00$  that corresponding to surface superoxide centers  $\text{Sn}_4^+-\text{O}_2^-$ , which are formed by the transfer of trapped electrons present in oxygen vacancies to the surface adsorbed  $\text{O}_2$  molecule in the reaction:  $(\text{Sn} + (1 + x/2) \text{O}_2 \rightarrow \text{SnO}_x + \text{SnO}_2)$ . [9] These superoxide radicals are strongly attached to  $\text{Sn}_4^+$  or  $\text{Sn}_2^+$  species on the surface. The XRD patterns of the obtained  $\text{SnO}_x/\text{SnS}$  heterostructure (Figure 4.7f) display peaks at  $28.6^\circ$ ,  $32.3^\circ$  correspond to the (101), (021) planes of SnO (JCPDS Card No. 77-2296), and peaks at  $33.9^\circ$ ,  $51.8^\circ$  from the (101), (211) planes of  $\text{SnO}_2$  (JCPDS Card No. 41-1445), respectively, and other peaks at  $32^\circ$ ,  $45.5^\circ$  and  $66.8^\circ$  are

indexed to the (040), (002) and (080) planes of SnS (JCPDS Card No. 39-0354). Overall, the diffraction patterns correspond to SnO, SnO<sub>2</sub>, and SnS, which further illustrates the structure of SnO<sub>x</sub>/SnS hybrids.

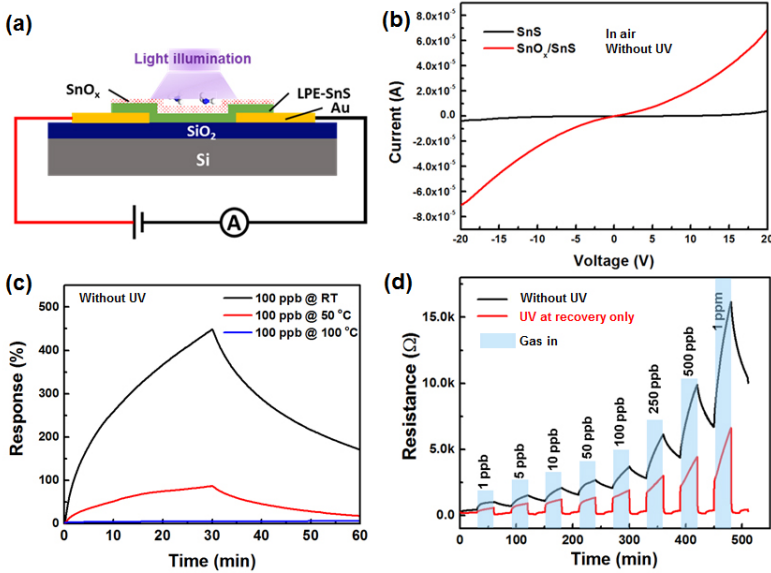


Figure 4.8: (a) Schematic test setup of SnO<sub>x</sub>/SnS heterostructure-based gas sensor. (b) I-V curve of SnS-based and SnO<sub>x</sub>/SnS heterostructures-based gas sensor measured at room temperature in air. (c) Dynamic sensing performances of SnO<sub>x</sub>/SnS gas sensor toward 100 ppb NO<sub>2</sub> gas concentration at room temperature, 50 °C and 100 °C. (d) Dynamic changes of resistance of SnO<sub>x</sub>/SnS sensor toward NO<sub>2</sub> gas under concentrations ranging from 1 ppb to 1 ppm at room temperature without UV and UV at recovery only. (The bias voltage is 10V.)

#### 4.4.2. GAS SENSING PROPERTIES

Figure 4.8a shows the test set-up for SnO<sub>x</sub>/SnS heterostructure-based gas sensor. The IV curves of pure SnS-based and SnO<sub>x</sub>/SnS heterostructure-based gas sensor are shown in Figure 4.8b, which reveals that the conductivity of the device increases after oxidation. The maximum power consumption in the air and NO<sub>2</sub> is 0.21 mW and 0.5 W, respectively. Figure 4.8c shows that the lower the operating temperature, the higher the gas response, which is attributed to rich OV<sub>s</sub> according to the previous work. In Figure 4.8d, the resistance changes of the device towards different NO<sub>2</sub> gas concentrations were measured under two conditions: without UV and with UV illumination (1.3 W UV lamp with 365 nm wavelength, the light intensity is 19 mW/cm<sup>2</sup>) with at the recovery phase only. When the UV light is applied during the recovery process, the device recovers more rapidly. Because UV light can shift the gas sensor's baseline, we applied UV illumination for the first 15 minutes, then in the dark for 15 minutes. Thus, it can recover to the initial value. The responses of the sensors (*S*) are defined as the relative change in the resistance of the sensors in the background and those in the tested gas  $S = (R_{\text{gas}} - R_{\text{air}})/R_{\text{air}} \times 100\%$ , where  $R_{\text{air}}$  and  $R_{\text{gas}}$  are the resistance in air and the tested gases, respectively. The response and recovery

Table 4.1: Comparison of various gas sensor technologies with respect to reported  $\text{NO}_2$  ranges, response and recovery times, and response (%).

Sensing materials	$\text{C}(\text{NO}_2)$ (ppb)	LOD (ppb)	Temperature (°C)	$t_{\text{res}}$ (s)	$t_{\text{rec}}$ (s)	Response (%)	Ref.
$\text{WO}_3$	500	10	200	~3600	~1800	150	[13]
HOF	1	40	25	17.6	19.1	~34	[14]
CNT	1	0.1	25	120	/	~25	[15]
$\text{SnO}_2$	1	0.2	25	~1800	~900	~90	[12]
$\text{SnO}_2/\text{SnO}$	100	100	50	~150	~400	26 ppm <sup>-1</sup>	[16]
$\text{SnO}_2/\text{ZnO}$	400	/	200	~300	~300	600	[17]
$\text{SnO}_2/\text{Graphene}$	10	0.024	150	43	408	200-300	[18]
$\text{MoS}_2/\text{SnO}_2$	500	/	25	408	162	0.6	[1]
$\text{SnS}_2/\text{SnO}_2$	125	/	100	299	143	~90	[2]
$\text{SnS}_2$	10 000	/	120	~170	~140	~3600	[19]
SnS	1000	/	25	~25	~25	60	[20]
$\text{SnS}_2/\text{SnS}$	400	75	25	365	1216	660	[21]
$\text{SnO}_2$ with OVs	500	/	25	/	/	3525000	[4]
$\text{SnO}_x/\text{SnS}$	1	0.005	25	1800	36 (UV)	161	This work

Notes: HOF= hydrogen-bonded organic framework material, CNT= carbon nanotubes.

times of the sensors were defined as the time required for a 90% change in the gas response factor's full magnitude change. The recovery time is only 36 s after applied UV, which is much faster than that without UV. In Figure 4.7c, the maximum responses of the sensor without and with UV towards different  $\text{NO}_2$  concentrations are similar, which means that UV illumination has slight effects on the gas sensing response. Figure 4.9a illustrates the responses of  $\text{SnO}_x/\text{SnS}$  heterostructures as a function of the  $\text{NO}_2$  concentrations range from 1 ppb to 1 ppm. The experimental data were fitted by exponential function as Response ( $S$ ) =  $69.42 \times C^{0.34}$ , where  $C$  is the gas concentration of  $\text{NO}_2$ . The inset image of Figure 4.9b shows the linear fitting  $\log(S) - \log(C)$  plot, revealing the surface coverage of adsorbed  $\text{NO}_2$  molecules follows Freundlich isotherm adsorption, which is the most important multisite adsorption isotherm for rough surfaces.[10] Moreover, our device exhibits a response of ~161% to the 1 ppb  $\text{NO}_2$  (limited by our gas mixture system). This is much lower than the recommended ambient air quality guidelines of WHO (20 ppb). As shown in Figure 4.9c and Table A.1, the signal of the as-fabricated sensor is three times more than the noise ( $0.39e^{-3}$ ). Thus the theoretical limit of detection can be calculated from the slope of the linear region of the response curve and the root-mean-square deviation ( $\text{RMS}_{\text{noise}}$ ) at the baseline according to the International Union of Pure and Applied Chemistry (IUPAC). The calculated LOD is as low as 5 ppt, which is much lower than that of carbon nanotubes-based, metal oxide-based, and metal sulfide-based sensors (see Table A.2)[11–14].

Repeatability and fast response/recovery time are also critical parameters for practical gas sensing. Figure 4.10a shows three cycles of measurements of SnS nanosheets-based and  $\text{SnO}_x/\text{SnS}$  heterostructures-based gas sensors. It is found that the repeatability of them is excellent, while the response of  $\text{SnO}_x/\text{SnS}$  heterostructures-based device is much higher than that of the SnS device. The superior gas sensing performance is determined by the large amount of  $\text{Sn}_4^+ - \text{O}_2^-$  centers in the heterostructures. It is essential to highlight that the recovery time of gas sensors after applying UV illumination is only 0.3 s, which is much faster than that of most  $\text{SnO}_2$ -based sensors ( $\text{SnO}_2$  modified CNTs, 408 s @ 100 ppb, and  $\text{SnO}_2$  NPs, 2400 s @ 100 ppb).[3, 22] Furthermore, we checked the selectivity of

the sensors in the air for finding more practical application capability (see Figure 4.10b). The device's responses to several other gasses, including a reducing gas  $\text{NH}_3$  and  $\text{H}_2$ , oxidizing gases of  $\text{NO}$  and  $\text{CO}$  with 500 ppm gas concentration, were measured. With the gas concentration of 500 ppm, the sensor response toward  $\text{NO}$  and  $\text{CO}$  are 371% and 170%, respectively, while for  $\text{NH}_3$  and  $\text{H}_2$  are -50% and -40%, respectively. Besides, the sensor shows responses of -271% under 11%RH. Therefore, the  $\text{SnO}_x/\text{SnS}$  heterostructures is an ideal sensing platform with excellent selectivity, sensitivity, reversibility, ultra-low LOD, and low operation temperature.

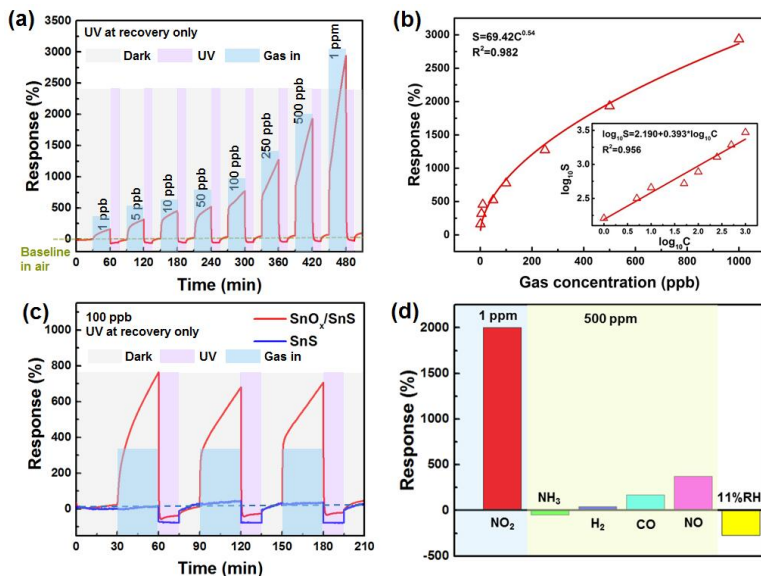


Figure 4.9: (a) Dynamic sensing performance of  $\text{SnO}_x/\text{SnS}$  sensor under different gas concentrations. (b) The sensor response as a function of the concentration of  $\text{NO}_2$  gas. (c) Time-dependent response current of three cycles of  $\text{NO}_2$  gas switching between the air and 100 ppb. (d) The gas sensor responses toward different types of gas molecules. (The bias voltage is 10V.)

## 4.5. GAS SENSING MECHANISM

In the previous section, it is known that the high gas sensing performance is mainly associated with the large and rich-OVs surface and high-density charge transfer inside nanostructures. Oxidation increases the surface area and the defects on the nanostructure's surface, which enable abundant adsorption sites and higher binding energy. Thus a large number of  $\text{NO}_2$  and  $\text{H}_2\text{O}$  gas molecules can be adsorbed by the nanostructures, and several charges transfer between gas molecules and nanostructures consequently.

### 4.5.1. COMPUTATIONAL METHODS

All the calculations were carried out by DMol3 code of Materials Studio.[23] The calculation methods and parameters refers to Section 3.5.1. To understand the charge transfer and energy distribution between them, the DFT calculations were conducted and compared

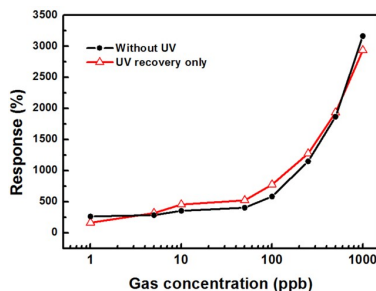


Figure 4.10: The maximum response of  $\text{SnO}_x/\text{SnS}$  gas sensor toward  $\text{NO}_2$  gas under concentrations ranging from 1 ppb to 1 ppm at room temperature without UV and with UV at recovery only. (The bias voltage is 10V.)

4

with those of monolayer  $\text{SnS}$ . Firstly, we simulated the oxidation process between the top  $\text{SnS}$  layer and  $\text{O}_2$  gas molecule in the unit cell. After the oxidizing reaction, the  $\text{SnO}_x$  layer is obtained, where the Sn-S bond disconnects and new Sn-O bond is formed (see Figure 4.11). Since  $\text{SnS}$  is a kind of layered material, the  $\text{SnO}_x/\text{SnS}$  heterojunction could be a layered structure. The most stable adsorption configurations of  $\text{NO}_2$  molecule adsorbed on the monolayer  $\text{SnS}$  and  $\text{SnO}_x/\text{SnS}$  heterojunction with OV are shown in Figure 4.12.

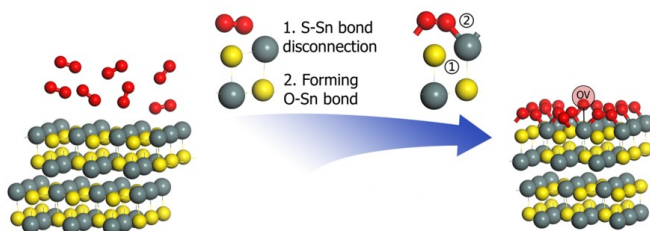


Figure 4.11: Modelling procedure of  $\text{SnO}_x/\text{SnS}$  heterojunction with O atom vacancy. From left to right:  $\text{SnS}$  reacts with oxygen; Formation of  $\text{SnO}_x$  layer. The bond between Sn and S atom becomes disconnected, new bond is formed between O and Sn atom;  $3 \times 3$  supercell of  $\text{SnO}_x/\text{SnS}$  heterojunction with O atom vacancy.

#### 4.5.2. COMPUTATIONAL RESULTS

The adsorption energy ( $E_A$ ), charge transfer ( $\Delta Q$ ), and change of the band gap after adsorption are listed in Table 4.2. The results show that  $\Delta Q$  of pure  $\text{SnS}$  and  $\text{SnO}_x/\text{SnS}$  heterojunction with OV adsorbed with  $\text{NO}_2$  are at a negative level, indicating that charge transfers from the substrate to  $\text{NO}_2$  gas molecule. On the contrary, charge transfers from  $\text{H}_2\text{O}$  to  $\text{SnO}_x/\text{SnS}$  ( $\Delta Q = 0.172 e$ ). The charge density difference (CDD) presented in Figure 4.13b,c further confirms that  $\text{NO}_2$  and  $\text{H}_2\text{O}$  act as charge acceptor and donor with larger charge transfer, respectively. Thus  $\text{NO}_2$  and  $\text{H}_2\text{O}$  can induce the current of the working device to decrease and increase, respectively. For the adsorption of  $\text{NO}_2$ , the  $E_A$  and  $\Delta Q$  of pure  $\text{SnS}$  is higher than that of heterojunction with OV, indicating that  $\text{SnS}$  can trap the  $\text{NO}_2$  gas molecule much easier. For the adsorption of  $\text{H}_2\text{O}$ , the  $E_A$  and  $\Delta Q$  of pure  $\text{SnS}$  is lower, which reveals that  $\text{SnO}_x/\text{SnS}$  has more sensitive detection behaviour for humidity, is consistent with the humidity testing results in Section 4.3.

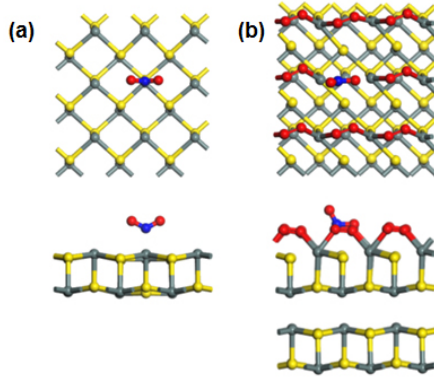


Figure 4.12: Top and side views of the most favorable configurations of  $\text{NO}_2$  adsorbed on the (a) monolayer SnS and (b)  $\text{SnO}_x/\text{SnS}$  heterjunction. The balls in greyish-green and yellow balls represent the Sn and S atoms, where red and blue represent O and N atoms, respectively.

Table 4.2: The adsorption energy ( $E_A$ ), adsorption distance ( $d$ ), and charge transfer ( $\Delta Q$ ) of different gases on monolayer SnS and  $\text{SnO}_x/\text{SnS}$  heterjunction.

Gas	$E_A$ (eV)	$d$ (Å)	$\Delta Q$ (e)	$E_g$ (eV)
SnS	/	/	/	0.927
$\text{NO}_2 + \text{SnS}$	-0.900	2.47	-0.382	0.986
$\text{H}_2\text{O} + \text{SnS}$	-0.388	2.72	-0.055	/
$\text{SnO}_x/\text{SnS}$ with OVs	/	/	/	0.037
$\text{NO}_2 + \text{SnO}_x/\text{SnS}$ with OVs	-0.314	2.45	-0.283	0.219
$\text{H}_2\text{O} + \text{SnO}_x/\text{SnS}$ with OVs	-0.426	2.303	+0.172	0.126

According to the classical relation between  $E_g$  and electrical conductivity of a materials,[24]

$$\sigma \propto e^{(-E_g/2kT)} \quad (4.1)$$

where  $k$  and  $T$  are the Boltzmann's constant and the temperature, respectively. It is clear that the smaller the value of  $E_g$ , the higher the electrical conductivity at a given temperature. Thus the conductivity of the  $\text{SnO}_x/\text{SnS}$  heterostructure device increased significantly after introducing  $\text{SnO}_x$  to the top of SnS nanosheets (see Figure 4.8). After the adsorption of  $\text{NO}_2$  gas molecule over the SnS and  $\text{SnO}_x/\text{SnS}$  heterojunction surface, an increase in the band gap indicates a decrease of conductivity. Based on the Eq.4.1, the response ( $S$ ) of the device can be expressed as:

$$S \propto e^{(\Delta E_g/2kT)} \quad (4.2)$$

From Table 4.2, the  $\Delta E$  of pure SnS and  $\text{SnO}_x/\text{SnS}$  heterojunction with OV after the adsorption of  $\text{NO}_2$  can be calculated as 0.059 eV and 0.182 eV respectively. Thus the response of  $\text{SnO}_x/\text{SnS}$  heterojunction with OV after exposure to  $\text{NO}_2$  is higher than that of SnS nanosheets according to Eq.4.2. It reveals that both of SnS and heterojunction with OV can enhance the  $S$  of the device. For as-fabricated devices, the SnS substrate has a large surface area, which can easily trap lots of gas molecules and increase the  $S$ . Meanwhile, the  $\text{SnO}_x/\text{SnS}$  heterojunction with OV contributes large  $S$  to the device even with less adsorbed gas molecules. Therefore, the device with a high response to  $\text{NO}_2$  gas molecule.

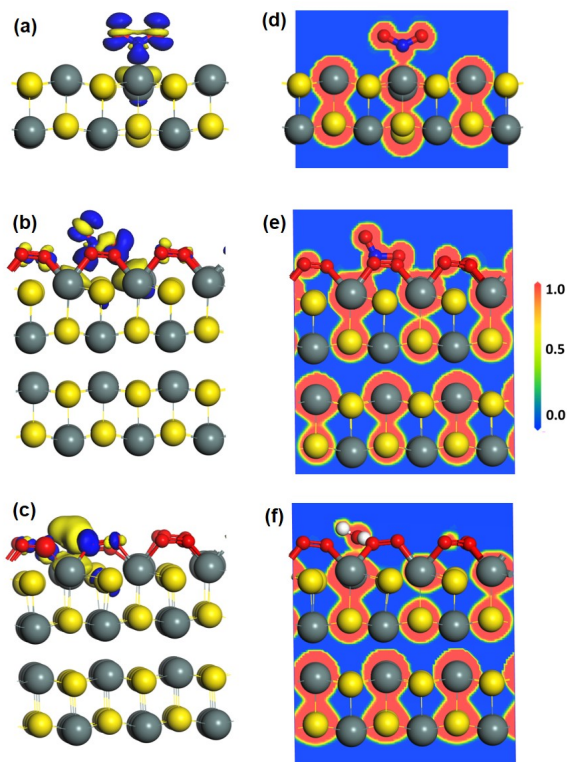


Figure 4.13: The CDD plots for  $\text{NO}_2$  on (a) monolayer SnS and (b)  $\text{SnO}_x/\text{SnS}$  heterojunction. (c) The CDD plots for  $\text{H}_2\text{O}$  on  $\text{SnO}_x/\text{SnS}$  heterojunction. The blue and yellow regions show charge accumulation and depletion, respectively. The ELF plots for  $\text{NO}_2$  on (d) monolayer SnS and (e)  $\text{SnO}_x/\text{SnS}$  heterojunction. (f) The ELF plots for  $\text{H}_2\text{O}$  on  $\text{SnO}_x/\text{SnS}$  heterojunction. The isosurface is taken as  $0.015 \text{ e} \text{ \AA}^{-3}$ .

To further explore the interaction between the gas molecule and heterojunction, the grade of ELF is encoded using a color scheme in which high values correspond to orange and low values to blue (see Figure 4.13d). The ELF plot clearly shows that few-electron sharing between  $\text{NO}_2$  gas molecules and heterojunction proves a chemical adsorption nature powerfully. However, due to the chemisorption nature, the desorption of  $\text{NO}_2$  gas molecule is difficult for  $\text{SnO}_x/\text{SnS}$  heterostructures. Thus we accelerated the desorption process through UV irradiation for the heterostructure. The ultra-narrow band gap of  $\text{SnO}_x/\text{SnS}$  heterostructures with OVs means that the photo-induced electrons can easily transfer from the conduction band to the valence band. It leads to the absorption of more photons in the UV light region to produce more electron-hole pairs, resulting in more  $\text{O}_2^-$  and  $\text{NO}_2^-$  is photoexcited to be  $\text{O}_2$  and  $\text{NO}_2$ . Finally, it accelerates the gas desorption from the surface of  $\text{SnO}_x/\text{SnS}$ . On the other side, the ELF plot shows no electron-sharing between  $\text{H}_2\text{O}$  and heterojunction, indicating physical adsorption between them. Consequently, the recovery time of humidity sensing is much faster than that for  $\text{NO}_2$ .

## 4.6. CONCLUSION

Four types of SnS-based sensors, LPE-SnS nanosheets, SnO<sub>2</sub> nanosheets, SnO<sub>2</sub>/SnS nanocomposites, and SnO<sub>x</sub>/SnS heterostructure, are comparatively analyzed with respect to their humidity sensing responses. The results show that the sensor based on SnO<sub>x</sub>/SnS heterostructure has excellent humidity sensing response among them. The SnS decorated with SnO<sub>x</sub> nanoparticle was synthesized by the post-oxidation of LPE-SnS nanosheets in air at 350 °C. The SnO<sub>x</sub>/SnS heterostructure-based NO<sub>2</sub> gas sensor exhibits excellent humidity and NO<sub>2</sub> sensing performance. The device shows a high response of 10870% at 75%RH, and fast response and recovery time in seconds. It has a high response of 500% towards 500 ppt and 5800% towards 1 ppm NO<sub>2</sub> gas concentration, wide detecting range from 500 ppt to 1 ppm, competing with related 2D-materials based gas sensors. The sensor shows superior gas selectivity toward NO<sub>2</sub> with comparison to several gas vapors such as NO, SO<sub>2</sub>, H<sub>2</sub>, CO, NH<sub>3</sub> and C<sub>2</sub>H<sub>5</sub>OH. Besides, humidity has slight effects on the gas sensing performance towards NO<sub>2</sub>. The outstanding NO<sub>2</sub> sensing behaviours could be attributed to the post-oxidation process of the SnO<sub>x</sub> particles which provide more adsorption site for NO<sub>2</sub> gas molecule and the formed SnO<sub>x</sub>/SnS heterostructure can be efficiently modulated by the gas concentration due to the active electrons transfer in the sensing interface layer. Upon UV irradiation, the heterostructures can lead to the absorption of more photons in the UV light region to produce more electron-hole pairs, resulting in more O<sub>2</sub><sup>-</sup> and NO<sub>2</sub><sup>-</sup> is photoexcited to be O<sub>2</sub> and NO<sub>2</sub>. The present study shows that fabricating semiconductor materials with multiple heterojunction structures is an efficient way to make gas sensors with high sensing performances, and UV-enhanced recovery behaviour, and low operation temperature.

## REFERENCES

- [1] Shumao Cui, Zhenhai Wen, Xingkang Huang, Jingbo Chang, and Junhong Chen. Stabilizing MoS<sub>2</sub> nanosheets through SnO<sub>2</sub> nanocrystal decoration for high-performance gas sensing in air. *Small*, 11(19):2305–2313, 2015.
- [2] Juanyuan Hao, Dan Zhang, Quan Sun, Shengliang Zheng, Jianyong Sun, and You Wang. Hierarchical SnS<sub>2</sub>/SnO<sub>2</sub> nanoheterojunctions with increased active-sites and charge transfer for ultrasensitive NO<sub>2</sub> detection. *Nanoscale*, 10(15):7210–7217, 2018.
- [3] Mauro Epifani, Joan Daniel Prades, Elisabetta Comini, Eva Pellicer, Manuel Avella, Pietro Siciliano, Guido Faglia, Albert Cirera, Roberto Scotti, Franca Morazzoni, and Joan Ramon Morante. The role of surface oxygen vacancies in the NO<sub>2</sub> sensing properties of SnO<sub>2</sub> nanocrystals. *The Journal of Physical Chemistry C*, 112(49):19540–19546, 2008.
- [4] Yuxiang Li, Baiyi Zu, Yanan Guo, Kun Li, Haibo Zeng, and Xincun Dou. Surface superoxide complex defects-boosted ultrasensitive ppb-level NO<sub>2</sub> gas sensors. *Small*, 12(11):1420–1424, 2016.
- [5] P. K. Nair, M. T. S. Nair, Ralph A. Zingaro, and Edward A. Meyers. XRD, XPS, optical and electrical studies on the conversion of SnS thin films to SnO<sub>2</sub>. *Thin Solid Films*, 239(1):85–92, 1994.
- [6] Naoki Higashitarumizu, Hayami Kawamoto, Masaru Nakamura, Kiyoshi Shimamura, Naoki

- Ohashi, Keiji Ueno, and Kosuke Nagashio. Self-passivated ultra-thin SnS layers via mechanical exfoliation and post-oxidation. *Nanoscale*, 10(47):22474–22483, 2018.
- [7] Dattatray J. Late, Yi-Kai Huang, Bin Liu, Jagaran Acharya, Sharmila N. Shirodkar, Jiajun Luo, Aiming Yan, Daniel Charles, Umesh V. Waghmare, Vinayak P. Dravid, and C. N. R. Rao. Sensing behavior of atomically thin-layered MoS<sub>2</sub> transistors. *ACS Nano*, 7(6):4879–4891, 2013.
- [8] D. Zwingel. The electronic structure of trapped hole centres in SnO<sub>2</sub>. *physica status solidi (b)*, 77(1):171–180, 1976.
- [9] Pawan Chetri, Biswajit Choudhury, and Amarjyoti Choudhury. Room temperature ferromagnetism in SnO<sub>2</sub> nanoparticles: an experimental and density functional study. *Journal of Materials Chemistry C*, 2(43):9294–9302, 2014.
- [10] Herbert Freundlich. *Kapillarchemie, eine Darstellung der Chemie der Kolloide und verwandter Gebiete, von Dr. Herbert Freundlich*. akademische Verlagsgesellschaft, 1909.
- [11] Leandro Sacco, Salome Forel, Ileana Florea, and Costel-Sorin Cojocar. Ultra-sensitive NO<sub>2</sub> gas sensors based on single-wall carbon nanotube field effect transistors: Monitoring from ppm to ppb level. *Carbon*, 157:631–639, 2020.
- [12] Xiaoli Wang, Noppadol Aroonyadet, Yuzheng Zhang, Matthew Mecklenburg, Xin Fang, Haitian Chen, Edward Goo, and Chongwu Zhou. Aligned epitaxial SnO<sub>2</sub> nanowires on sapphire: Growth and device applications. *Nano Letters*, 14(6):3014–3022, 2014.
- [13] L. Parellada-Monreal, S. Gherardi, G. Zonta, C. Malagu, D. Casotti, G. Cruciani, V. Guidi, M. Martinez-Calderon, I. Castro-Hurtado, D. Gamarra, J. Lozano, L. Presmanes, and G. G. Mandayo. WO<sub>3</sub> processed by direct laser interference patterning for NO<sub>2</sub> detection. *Sensors and Actuators B: Chemical*, 305:127226, 2020.
- [14] Yijie Wang, Di Liu, Jianbo Yin, Yanxue Shang, Juan Du, Zixi Kang, Rongming Wang, Yanli Chen, Daofeng Sun, and Jianzhuang Jiang. An ultrafast responsive NO<sub>2</sub> gas sensor based on a hydrogen-bonded organic framework material. *Chemical Communications*, 56(5):703–706, 2020.
- [15] Pengfei Qi, Ophir Vermesh, Mihai Grecu, Ali Javey, Qian Wang, Hongjie Dai, Shu Peng, and K. J. Cho. Toward large arrays of multiplex functionalized carbon nanotube sensors for highly sensitive and selective molecular detection. *Nano Letters*, 3(3):347–351, 2003.
- [16] Lei Li, Chunmei Zhang, and Wei Chen. Fabrication of SnO<sub>2</sub>-SnO nanocomposites with p-n heterojunctions for the low-temperature sensing of NO<sub>2</sub> gas. *Nanoscale*, 7(28):12133–12142, 2015.
- [17] Jin-Ah Park, Jaehyun Moon, Su-Jae Lee, Seong Hyun Kim, Hye Yong Chu, and Taehyoung Zyung. SnO<sub>2</sub>-ZnO hybrid nanofibers-based highly sensitive nitrogen dioxides sensor. *Sensors and Actuators B: Chemical*, 145(1):592–595, 2010.
- [18] Vu Van Quang, Nguyen Van Dung, Ngo Sy Trong, Nguyen Duc Hoa, Nguyen Van Duy, and Nguyen Van Hieu. Outstanding gas-sensing performance of graphene/SnO<sub>2</sub> nanowire schottky junctions. *Applied Physics Letters*, 105(1):013107, 2014.

- [19] Jian Zhen Ou, Wanyin Ge, Benjamin Carey, Torben Daeneke, Asaf Rotbart, Wei Shan, Yichao Wang, Zhengqian Fu, Adam F. Chrimes, Wojtek Wlodarski, Salvy P. Russo, Yong Xiang Li, and Kourosh Kalantar-zadeh. Physisorption-based charge transfer in two-dimensional SnS<sub>2</sub> for selective and reversible NO<sub>2</sub> gas sensing. *ACS Nano*, 9(10):10313–10323, 2015.
- [20] Jun Wang, Gang Lian, Zhenghao Xu, Chen Fu, Zhaojun Lin, Liyi Li, Qilong Wang, Deliang Cui, and Ching-Ping Wong. Growth of large-size SnS thin crystals driven by oriented attachment and applications to gas sensors and photodetectors. *ACS Applied Materials & Interfaces*, 8(15):9545–9551, 2016.
- [21] Quan Sun, Jiaxin Wang, Juanyuan Hao, Shengliang Zheng, Peng Wan, Tingting Wang, Haitao Fang, and You Wang. SnS<sub>2</sub>/SnS p-n heterojunctions with an accumulation layer for ultrasensitive room-temperature NO<sub>2</sub> detection. *Nanoscale*, 11(29):13741–13749, 2019.
- [22] Anjali Sharma, Monika Tomar, and Vinay Gupta. Room temperature trace level detection of NO<sub>2</sub> gas using SnO<sub>2</sub> modified carbon nanotubes based sensor. *Journal of Materials Chemistry*, 22(44):23608–23616, 2012.
- [23] B. Delley. From molecules to solids with the DMol<sub>3</sub> approach. *The Journal of Chemical Physics*, 113(18):7756–7764, 2000.
- [24] Basant Roondhe and Prafulla K. Jha. "Haeckelite", a new low dimensional cousin of boron nitride for biosensing with ultra-fast recovery time: a first principles investigation. *Journal of Materials Chemistry B*, 6(42):6796–6807, 2018.



# 5

## WS<sub>2</sub>/IGZO HETEROJUNCTION GAS SENSOR

*In chapter 4, it is proved that metal sulfide/metal oxide heterojunction has enhanced NO<sub>2</sub> gas sensing behaviour. In this chapter, one typical transition metal sulfide, WS<sub>2</sub>, is vertically stacked with wide bandgap metal oxide semiconductor (IGZO) to form a heterojunction. In section 5.2, the structural, electronic, optical, and gas sensing properties of WS<sub>2</sub>/IGZO heterojunction are studied by density functional calculation. Based on the theoretical results, we design and fabricate a p-N WS<sub>2</sub>/IGZO heterojunction device in section 5.3, and analyze the NO<sub>2</sub> gas sensing performance in chemiresistor and transistor mode, respectively.*

---

Parts of this chapter have been published in: "Tunable electronic and optical properties of the WS<sub>2</sub>/IGZO heterostructure via an external electric field and strain: a theoretical study", *Physical Chemistry Chemical Physics*, **21**, 27, 2019, and "Ultra-High Sensitive NO<sub>2</sub> Gas Sensor Based on Tunable Polarity Transport in CVD-WS<sub>2</sub>/IGZO p-N Heterojunction", *ACS Applied Materials & Interfaces*, **11**, 43, 2019.

## 5.1. INTRODUCTION

**T**UNGSTEN sulfide (WS<sub>2</sub>), as a typical transition metal sulfide material, is a semiconductor with an S-W-S sandwiches structure and an indirect band gap of  $\sim 1.9$  eV. These features enable WS<sub>2</sub> to have great potential for a transistor, photodetector, solar cell, and gas sensor application.[1–3] Xu *et al.* [4] synthesized ultra-thin WS<sub>2</sub> nanosheets through hydrothermal and calcination process, which showed gas sensing response of 9.3% after exposure to 100 ppb NO<sub>2</sub> gas at room temperature (RT). To improve the sensing response of pristine WS<sub>2</sub>-based device, gas sensors based on metal oxide/WS<sub>2</sub> heterojunction have been developed. Because there exists synergistic effect, spontaneous electron transfer, and heterojunction barriers in the interface,[5, 6] it is very sensitive to a slight external disturbance (electric field, illumination, strain and gas adsorption).[7] SnO<sub>2</sub>, ZnO, WO<sub>3</sub>, and TiO<sub>2</sub> are currently prominent materials that account for about 70% of the metal sulfide gas sensors and often used for metal oxide/metal sulfides heterojunction gas sensor. [8–10] The NO<sub>2</sub> gas sensor based on p-n MoS<sub>2</sub>/ZnO hetero-nanostructure designed by Han *et al.*[11] exhibited high response of 3050% toward 5 ppm NO<sub>2</sub> and low LOD of 50 ppb, which is much greater than that of pure MoS<sub>2</sub>. Through experimental and theoretical analysis, they found that the enhanced sensing performance can be attributed to the 2D/0D structures, synergistic effects, and p-n heterojunctions between ZnO nanoparticles and MoS<sub>2</sub> nanosheets.

Indium-gallium-zinc-oxide (IGZO), an n-type metal-oxide complex semiconductor, for constructing p-n heterojunction with WS<sub>2</sub>. The large indium (In) content results in a high n-type carrier concentration and high electron mobility( $\sim 35.8$  cm<sup>2</sup>/Vs) due to the large overlap of the In 5s orbitals, thus IGZO is more stable than ZnO and used for electronic device.[12–14] IGZO has a wide band gap ( $\sim 3.5$  eV at 300K)[15], which can be formed a Type-I band alignment with WS<sub>2</sub>, resulting in both electrons and holes accumulating on the same side. Moreover, IGZO is lattice-matched to WS<sub>2</sub> in the orient of (001), IGZO would, therefore, be advantageous for enhancing the electrical, optical and sensing properties of the WS<sub>2</sub>. [16] Additionally, because the conductance of the sensitive layer (the thin film transistor (TFT) channel material) can be modulated by applying different bias voltages on the gate electrode, the interaction between the gas molecule and channel material enables an obvious electron transfer between them. Therefore, TFT provides an excellent platform to improve device sensitivity. Thus, high-performance TFT-type NO<sub>2</sub> gas sensors based on IGZO or WS<sub>2</sub> as the channel material were successfully fabricated by researchers.[17–19]

In this chapter, we design a 2D WS<sub>2</sub>/IGZO heterostructure and systematically study the different stacking orders, electronic, and optical properties of the composites without and with the external field through first-principle analysis. Moreover, the gas sensing performance of the heterostructure was comparatively analyzed with different gas species. Then, based on the DFT results, the gas sensor based on p-N heterojunction is fabricated by vertically stacking the sputtered amorphous IGZO film and 2D WS<sub>2</sub> film synthesized by CVD. The performance of CVD-WS<sub>2</sub>/IGZO gas sensor device under different NO<sub>2</sub> gas concentration is investigated by adopting two different device configurations: chemiresistor and transistor mode. In both cases, the mechanisms involved in the sensing process are deeply discussed using the electronic band theory.

## 5.2. THEORETICAL STUDY OF WS<sub>2</sub>/IGZO HETEROSTRUCTURE

### 5.2.1. COMPUTATIONAL METHODS

All the first-principle calculations for structural relaxation and electronic properties were carried out within the DFT method as implemented in the DMol3 package of Materials Studio.[20, 21] The exchange and correlation energy in our calculations were performed using the generalized gradient approximation (GGA) with Perdew-Burke-Ernzerhof (PBE) functional. The DFT-D (D stands for dispersion) method with TS correction was employed to describe the van der Waals (vdW) interactions.[22] Double numerical atomic orbital plus polarization (DNP) was chosen as the basis set, and the global orbital cutoff was set to be 5.0 Å. The k-points mesh of 12×12×1 was utilized in the geometry optimizations and accurate electronic characteristics calculations. The maximum force and convergence tolerance of energy was set to be 0.002 Ha Å<sup>-1</sup> and 1.0 e<sup>-5</sup> Ha, respectively. To eliminate the effect of periodic interaction between IGZO and WS<sub>2</sub> monolayer, a 35 Å vacuum region was introduced in the direction normal to the WS<sub>2</sub> surface (z-direction). Moreover, we used CASTEP code to calculate the optical properties of each heterostructure with a plane-wave energy cutoff of 450 eV.[23] The k-points mesh was adopted 12×12×1 Monkhorst-Pack grid considering the limited computational resources. All the calculations were applied to dipole slab correction.

To evaluate the interaction between single-layer WS<sub>2</sub> and IGZO accurately, the binding energy ( $E_b$ ) is gained by use of the following equation:

$$E_b = E_{\text{total}} - E_{\text{WS}_2} - E_{\text{IGZO}} \quad (5.1)$$

where  $E_{\text{total}}$ ,  $E_{\text{WS}_2}$ ,  $E_{\text{IGZO}}$  are the total energy of the hybrid, individual layer of IGZO, and WS<sub>2</sub>, respectively. A negative  $E_b$  stands for a stable structure. In addition, we calculated the imaginary part of the dielectric function ( $\epsilon_2$ ) of WS<sub>2</sub>/IGZO heterostructure, which relates to its optical properties and is defined as follows,

$$\epsilon_2(\omega) = \frac{8\pi^2 e^2}{L \cdot A \cdot m^2 \omega^2} \sum_{c,v} \sum_{\mathbf{K}} |\langle v, \mathbf{K} | p_\alpha | c, \mathbf{K} \rangle|^2 \delta(E_c(\mathbf{K}) - E_v(\mathbf{K}) - \hbar\omega) \quad (5.2)$$

where  $c$  and  $v$  represents the conduction and valance states associated with the energies  $E_c(K)$  and  $E_v(K)$ , delta function  $\delta$  ensures the conservation of energy,  $A$ , is the sheet area,  $L$  is the vertical height between the sheets in the periodic supercell,  $\langle \rangle$  is the momentum transition matrix,  $e$  is the charge of an electron,  $m$ , and  $\hbar$  are the effective mass and Planck constantly, respectively. The absorption coefficient of  $\alpha$  can be calculated as:

$$\alpha(\omega) = \sqrt{2} [\sqrt{\epsilon_1^2(\omega) + \epsilon_2^2(\omega)} - \epsilon_2(\omega)]^{1/2} \quad (5.3)$$

To study the properties of WS<sub>2</sub>/IGZO heterostructure, we discuss the geometric and electronic structures of the individual WS<sub>2</sub> and IGZO firstly. The WS<sub>2</sub> considered in this work have hexagonal lattices with a honeycomb structure, which is obtained by cleaving the (001) plane of its bulk structures. The c-InGaZnO<sub>4</sub> with YbFe<sub>2</sub>O<sub>4</sub>-type layered structure has been chosen as the calculation object of pristine IGZO whose atomic positions are cited from Ref.[24]. As shown in Figure 5.1, after structural optimizations, the lattice constants

of the pristine monolayer IGZO and  $\text{WS}_2$  are 5.696 Å and 5.616 Å, respectively. The calculated results agree well with the reported values of 5.707 Å and 5.606 Å.[13, 25] The unit cell of the  $\text{WS}_2/\text{IGZO}$  heterostructure is composed of unit cells for both  $\text{WS}_2$  and IGZO, which presents 1.4% lattice mismatch between  $\text{WS}_2$  and IGZO layers. Because the mismatch is much smaller than that of the other heterostructure reported previously and would not affect the calculation results,[26], which is acceptable.

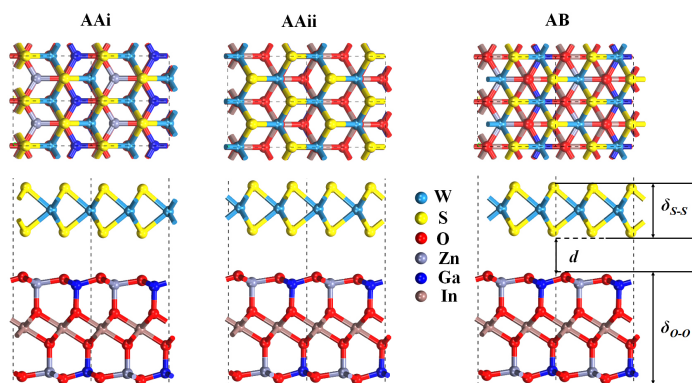


Figure 5.1: Top and side views of the atomic structure of the  $\text{WS}_2/\text{IGZO}$  heterostructure labeled as AAi, AAii and AB.

## 5.2.2. TUNABLE ELECTRONICAL AND OPTICAL PROPERTIES

### ELECTRONIC PROPERTIES

With different stacking conformations, the monolayer  $\text{WS}_2$  and IGZO can construct three possible configurations, separately named as AAi, AAii, and AB stacking, as shown in Figure 5.1. The AA-stacking of  $\text{WS}_2$  and IGZO are matched well in the  $xy$  plane. For AAi-stacking, the S atoms of  $\text{WS}_2$  were placed on the top of the O atoms of IGZO, whereas for AAii-stacking, the S atoms of  $\text{WS}_2$  were placed on the top of the Zn atoms. For AB-stacking, one of the O atoms of IGZO was placed at the center of a hexagon of  $\text{WS}_2$ . After geometry optimization, the corresponding structural and electronic properties of  $\text{WS}_2/\text{IGZO}$  heterostructure are calculated and listed in Table 5.1. It can be found that the buckling height of  $\text{WS}_2$  ( $\delta_{\text{S-S}}$ ) and IGZO ( $\delta_{\text{O-O}}$ ) layers in all patterns decrease slightly compared with the initial height of 3.210 Å and 7.446 Å, respectively. It indicates that there exists large interface binding between  $\text{WS}_2$  and IGZO. Besides, all the binding energy ( $E_b$ ) of heterostructures are negative, suggesting that the heterostructures are energetically favoured. The  $E_b$  of AAi-, AB-, and AAii-stacking patterns varies from -0.483 eV to -0.677 eV per atom. The interlayer distance  $d$  follows the order of AAii (2.589 Å) < AB (2.732 Å) < AAi (3.296 Å), which corresponds to the  $E_b$ . Since the shortest distance between the S atom of  $\text{WS}_2$  and the O atom of IGZO of all three patterns are larger than that of the bonding distance ( $\sim 1.74$  Å), revealing the absence of S-O covalent bonds in the heterostructures. Furthermore, the charge transfer ( $Q$ ) (0.029 eV) from  $\text{WS}_2$  to IGZO in AAii-stacking is higher than that in AAi-stacking (0.027 eV) and AB-stacking (0.004 eV), which further demonstrates that the interface binding force of AAii-stacking pattern

is much higher. The positive  $Q$  denotes that the charges transfer WS<sub>2</sub> (upper layer) from to IGZO (lower layer). All the binding energy is considerably higher than that of weak vdW interaction, which means that the WS<sub>2</sub> and IGZO are bound to each other via other mechanisms.[27, 28]

Table 5.1: Structure/electronic properties of IGZO/WS<sub>2</sub> heterostructure with different patterns.

Model	$d$ (Å)	$\delta_{O-O}$ (Å)	$\delta_{S-S}$ (Å)	$E_b$ (eV)	$Q$ (e)	$E_g$ (eV)
AAi	3.296	7.323	3.192	-0.483	0.027	1.102
AAii	2.589	7.296	3.183	-0.677	0.029	1.643
AB	2.732	7.321	3.224	-0.638	0.004	1.234

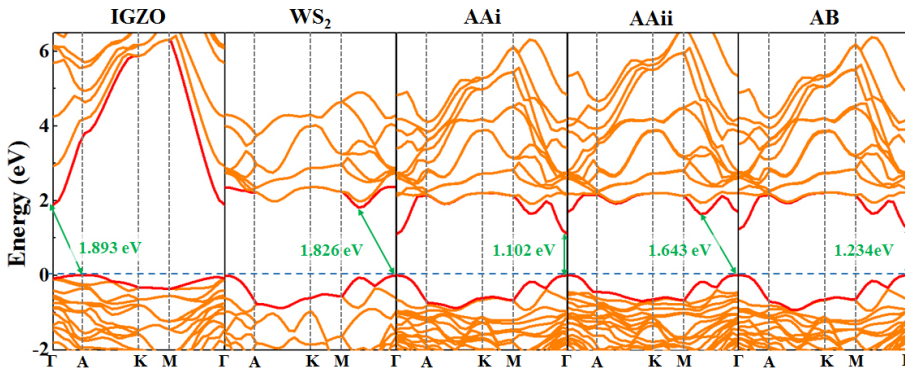


Figure 5.2: Electronic band structures of IGZO, single-layer WS<sub>2</sub>, AAI-, AAii- and AB-stacking of WS<sub>2</sub>/IGZO heterostructure.

The electronic structures of the three patterns of WS<sub>2</sub>/IGZO heterostructures were computed and shown in Figure 5.2. All energies are relative to the Fermi level. Band structure along the high symmetry k-points in the Brillouin zone,  $\Gamma(0, 0, 0)$ ,  $A(1/2, 0, 0)$ ,  $K(1/2, 1/2, 0)$ ,  $M(0, 1/2, 0)$  are displayed. The calculated energy gap of pristine IGZO is an indirect-gap of 1.893 eV, which is consisted of the previous results.[29] This is determined by the conduction band maximum (CBM) located in the  $\Gamma$  point in the Brillouin zone (BZ) and valence band minimum (VBM) located in the A point. For freestanding WS<sub>2</sub> monolayer, it is an indirect band gap of 1.826 eV with the CBM located in the M- $\Gamma$  region and VBM located at  $\Gamma$  point. The band structure we obtained agrees with the reported value of 1.801 eV.[30] Notably, when the heterostructures are formed, the band structure of AAI- and AB-stacking become direct band gap of 1.102 eV and 1.234 eV, respectively. Since the direct band gap would allow a high absorption efficient under photoexcitation, AAI- and AB-stacking patterns are suitable for applications in optoelectric devices.[31] For the AAii-stacking, the CBM is located in the M- $\Gamma$  region and VBM located at  $\Gamma$  point of the BZ. The CBM and VBM are similar to pristine WS<sub>2</sub> except for the narrow band gap of 1.643 eV. Besides, a broad-gap to narrow-gap transition is observed in three patterns, indicating that the optical properties of the three types of heterostructures are superior to those of individual WS<sub>2</sub> and IGZO.[32]

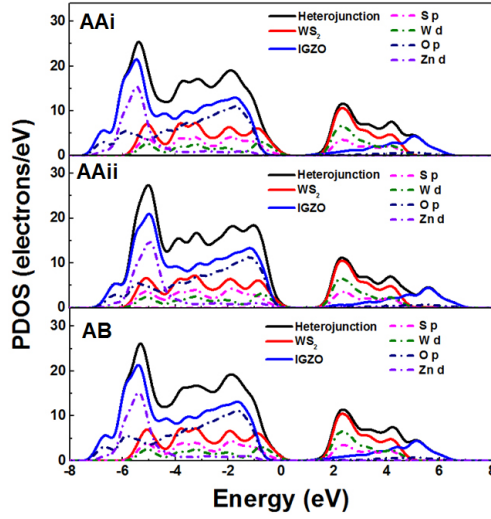


Figure 5.3: The density of states for the AAi- (upper), AAii- (middle) and the AB- (bottom) stacking of  $WS_2/IGZO$  heterostructure. The Fermi level is set to zero.

To further explore the interaction mechanism between  $WS_2$  and IGZO, the total and atom projected density of states (PDOS) of AAi-, AAii- and the AB-stacking heterostructures are plotted in Figure 5.3. It can be seen that the characteristic peak in the valence bands (VBs) from -8 to -4 eV are mainly dominated by the IGZO and partly from the  $WS_2$  monolayer. The peak in the VBs from -4 to 0 eV is primarily dominated by the  $WS_2$  and partly from the IGZO, whereas the  $WS_2$  only contributes the peak in the conduction bands (CBs) from 0 to 8 eV. Besides, the p orbitals of S and O atoms, and the d orbitals of W and Zn atoms make the largest contribution to the states of the peak around the Fermi level. The CB near the Fermi level is entirely contributed by the S p orbital and the W d orbital. In addition, there exists an evident orbital overlap between the W d orbital and the O p orbital of AAii-stacking in the energy range from -1.0 eV to 0 eV. It demonstrates that the interlayer interaction between  $WS_2$  and IGZO is strong, corresponding to the results of the highest binding energy for AAii-stacking pattern as listed in Table 5.2.

In order to comprehensively understanding of the electrostatic interaction between IGZO and  $WS_2$  layers, the charge density difference (CDD) of AAi-, AAii- and AB-stacking were calculated based on the following equation:

$$\Delta\rho = \rho_{\text{heterostructure}} - \rho_{WS_2} - \rho_{IGZO} \quad (5.4)$$

where  $\rho_{\text{heterostructure}}$ ,  $\rho_{WS_2}$ ,  $\rho_{IGZO}$  are the total charge densities of the heterostructure, single-layer  $WS_2$  and IGZO, respectively. As shown in Figure 5.4(a-c), the blue area denotes charge accumulation, while the yellow area represents charge depletion. The charge rearrangement localized in the interlayer region, which is the result of orbital overlaps.[2] The majority of charge is depleted at lower S atoms of  $WS_2$  and upper O atoms of IGZO and accumulated at the interface between  $WS_2$ , and IGZO induces the enhanced interlayer interaction. The interaction of the AAii-stacking pattern is larger than that of the other pat-

terns, which is in agreement with the  $Q$  and  $E_b$  results. Besides, since the charge transfer of the heterostructures is positive, IGZO acts as an electron donor to the WS<sub>2</sub>. To get a precise evaluation of the bonding nature between the IGZO and WS<sub>2</sub> layer, the electron localization function (ELF) of heterostructures is also calculated. As shown in Figure 5.4(e-f), the grades of ELF are characterized by a color scheme in which red shows that the electrons are highly localized and blue corresponds to the electrons with non-localized. The ELF for heterostructures is close to zero in the interlayer region, suggesting the electrons are incapable of forming covalent bonds between IGZO and monolayer WS<sub>2</sub>.

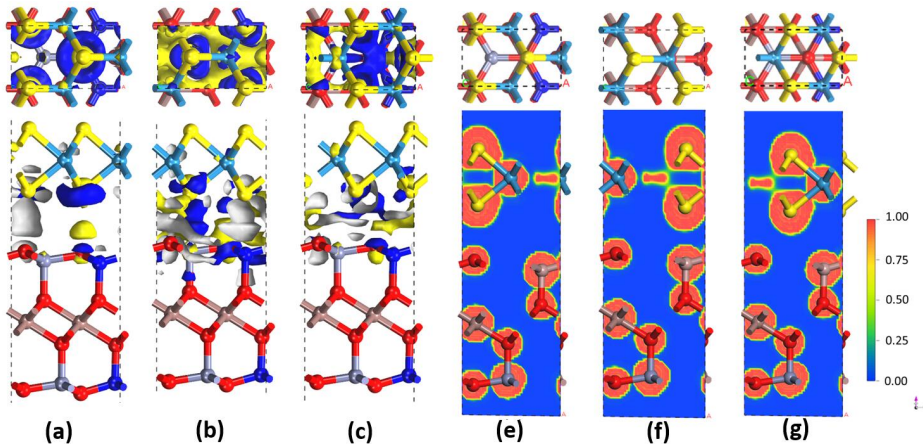


Figure 5.4: Top and side view of charge density difference of the (a) AAi-, (b) AAii- and (c) AB- stacking of WS<sub>2</sub>/IGZO heterostructure. The blue and yellow balls represent charge accumulation and depletion, respectively. The isovalue is set to be  $0.0015 \text{ e } \text{\AA}^{-3}$ . ELF contour plots for the (e) AAi-, (f) AAii- and (g) AB- stacking of WS<sub>2</sub>/IGZO heterostructure. Red (blue) regions correspond to large (small) ELF values.

**Tunable electronic properties under external electric field.** Many groups have demonstrated that the electronic properties of 2D materials can be modified or tuned efficiently by applying an external electric field (E-field).[33, 34] The modulation mechanism under a vertical electric field mainly attributed to the giant Stark effect, which can lead to splitting of degenerate energy levels and induce charge transfer between layers.[35] Moreover, electronic band engineering is experimentally meaningful, and thus, we investigate the effect of an E-field on the heterostructure's electrical behaviors. Figure 5.5 shows the band gap of WS<sub>2</sub>/IGZO heterostructure as a function of vertical E-field magnitude. Two orientations of E-field (+z, -z) along the normal direction of the infinite heterostructure plane were adopted. The positive direction of the E-field is denoted by the arrows, as shown in Figure 5.5(a). The strength of the E-field changes from  $-0.007$  to  $0.006 \text{ a.u.}$  ( $1 \text{ a.u.} = 51.36 \text{ V } \text{\AA}^{-1}$ ). Interestingly, the band gap of heterostructure depends on the external E-field after fully system optimization. The band gap decreases gradually with the increase of the E-field, resulting in a semiconductor-metal transition (see Figure 5.5b). To further analyzing the modulation mechanism of the E-field, we investigate the changes in the band gap, charge transfer, and binding energy under different E-field, as shown in Figure 5.5c and d. The more negative binding energy means that the heterostructure is more stable, and the positive  $Q$  means the charge transfer from WS<sub>2</sub> to the IGZO. Different from the effect of the band gap as found

above, the charge transfer from  $WS_2$  to the IGZO decreases monotonically with the increase of the E-field strength in the  $+z$  direction. For AAii pattern,  $WS_2$  no longer denotes charge to the IGZO at E-field = 0.006 a.u.. Correspondingly, the binding energy increases with increasing strength of the E-field. These results demonstrate that the band structure of the  $WS_2/IGZO$  heterostructure can be efficiently tuned, and the semiconductor-metal transition can be achieved by applying an external E-field.

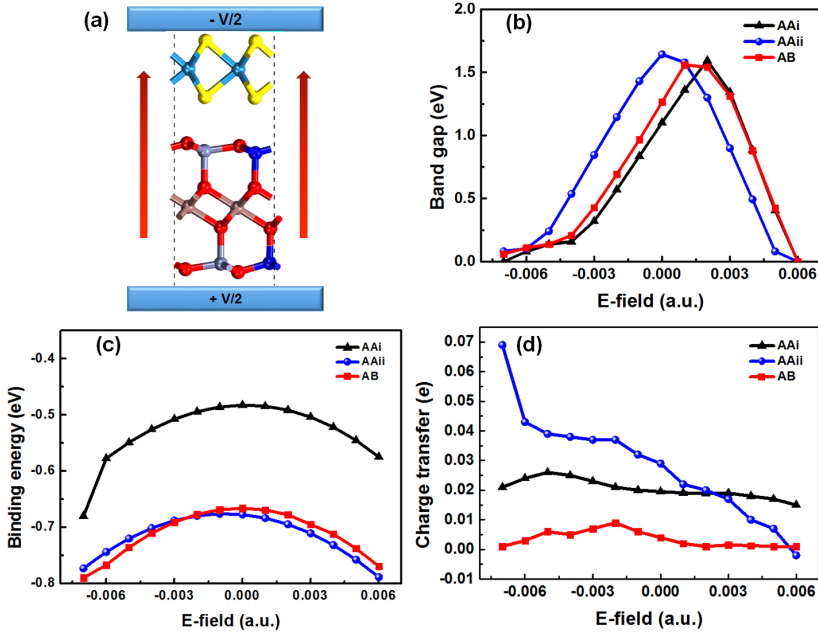


Figure 5.5: (a) Schematic diagram of the  $WS_2/IGZO$  heterostructure with applied E-field. The two arrows demonstrate the positive direction of the E-field. (b) The band gap and (c) binding energy of the  $WS_2/IGZO$  heterostructure as a function of E-field. (d) Charge transfer from  $WS_2$  to IGZO as a function of E-field.

**Tunable electronic properties under mechanical strain.** In addition to the E-field can tune the electronic properties of 2D materials, lots of previous theoretical and experimental results showed that mechanical strain is a powerful tool in effectively modulating it.[36–38] Since the energy bands around the Fermi level have high sensitivity to orbital coupling/interaction-neighboring atoms within the crystal, the magnitude of mechanical strain can determine the strength of orbital interaction.[39] Thus the electronic properties of the  $WS_2/IGZO$  heterostructure under various mechanical strains are analyzed. The external tensile and compressive strain is changing the lattices as  $\varepsilon = (a - a_0)/a_0$ , where  $a$  and  $a_0$  are the strained and equilibrium lattice constants of the heterobilayer. Moreover, the strain energy is also considered and can be expressed as  $\Delta E = E_d - E_p$ , where  $E_d$  and  $E_p$  are the total energy of deformed and pristine heterostructure, respectively. There are three types of mechanical strain: the first one is uniaxial strain along  $a$  vector of the unit cell, the second one is uniaxial strain along  $b$  vector of the unit cell, and the last one is biaxial strain along both  $a$  and  $b$  vectors of the unit cell. The ranges of uniaxial and biaxial strains

are from -10% to 10%. After applying external mechanical strain, the heterostructures have been fully optimized.

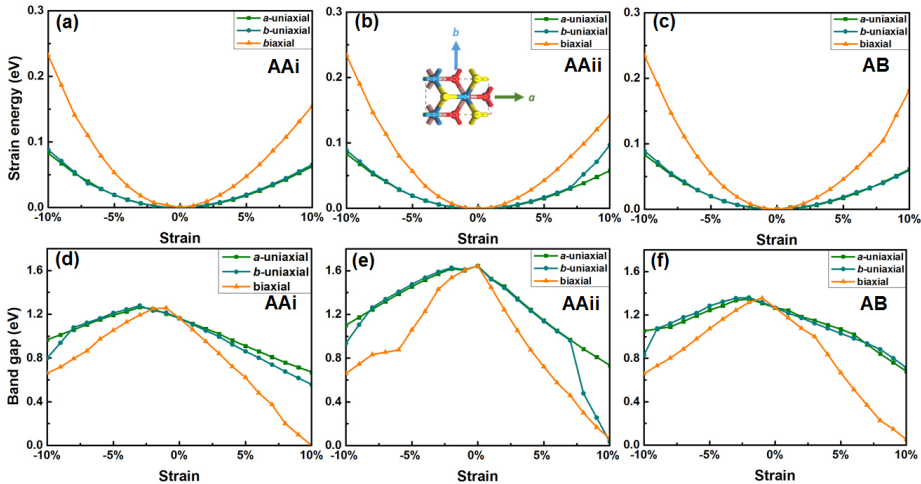


Figure 5.6: Variation of the strain energy (a-c) and bandgap (d-f) for the AAi-, AAii- and AB- stacking of the WS<sub>2</sub>/IGZO heterostructure as a function of mechanical strain. The inset image of (b) is the schematic diagram of the AAii pattern with applied mechanical strain in *a*- and *b*- direction.

Figure 5.6 demonstrates that the electronic band structures and strain energy can be significantly affected by applying in-plane strain for the WS<sub>2</sub>/IGZO heterostructure. The strain energy as a function of external strain is plotted in Figure 5.6(a-c). It is found that the strain energy of three types of heterostructure increases monotonously with the increased mechanical strain within the range of -10 to 10% both under uniaxial and biaxial strain. It indicates that the strain is in the range of elastic deformation. Thus the deformed structure can be restored to its initial state when external strain is removed. Therefore, WS<sub>2</sub>/IGZO heterostructure can be a promising candidate for a pressure sensor. The changes of band gap values upon applying uniaxial and biaxial strains are illustrated in Figure 5.6(d-f). For the biaxial tensile strain, the band gap decreases rapidly with an increasing strain from 0 to 10% for three types of heterostructures. For AAii stacking pattern, the band gap amounts to the maximum value of 1.643 eV at the strain of 0%, and then decreases linearly with increasing the compressive strain from 0% (0.613 eV) to -10% (0 eV). While for AAi and AB, the maximum band gap is 1.258 eV and 1.355 eV at the strain of -1%, respectively. And then the band gap decreases monotonically with increasing the compressive strain from -1% to -10%. Under the applied biaxial tensile strain, the band gap of the AAi decreases to a minimum value of 0 eV at  $\varepsilon = 10\%$ . The band gap decreases linearly with increasing tensile strain under the applied tensile uniaxial strain in both *a*- and *b*- direction. But for the uniaxial compressive strain, the band gap of the AAi-stacking firstly increases from the original 1.163 eV to 1.264 eV under  $\varepsilon = -3\%$  strain, and then decreases linearly to 0.967 eV under -10% strain. A similar phenomenon also occurs in the case of AAii and AB pattern. Benefit from the elastic deformation under large external strain and high tunability of the bandgap, WS<sub>2</sub>/IGZO heterostructure has the potential application of wearable electronics.

## OPTICAL PROPERTIES

Since the dielectric function and the absorption coefficient play crucial roles in characterization and optical applications of 2D material, we discuss the optical properties of the  $WS_2/IGZO$  heterostructure with a comparison to the  $WS_2$  and  $IGZO$  monolayers in this section.[40] Our calculated imaginary part ( $\epsilon_2$ ) of the dielectric function and adsorption coefficient ( $\alpha$ ) of the  $WS_2$  monolayer are similar to the calculated result of Wei *et al.*,[41] indicating our calculation is reasonable. As shown in Figure 5.7, for the single-layer  $WS_2$ , the  $\epsilon_2(\omega)$  spectrum of  $<1.2$  eV is approximately zero due to the transition between VBM and CBM being forbidden. The first peak locates around 2.9 eV and extends to 1.5 eV, indicating that the  $WS_2$  can absorb visible light. Besides, it exhibits the two prominent peaks located in the UV light range ( $>3$  eV). While the  $\epsilon_2(\omega)$  spectrum of the single-layer  $IGZO$  is smaller than that of  $WS_2$ , which means that  $IGZO$  has relatively weak absorption for visible and UV light, notably, it exhibits one peak located in the deep UV light range ( $>13$  eV). Benefit from the optical properties of  $WS_2$  and  $IGZO$  monolayer, the photoresponse characteristics of  $WS_2/IGZO$  heterostructure are extended to cover most of the visible range and all the UV light. Moreover, the  $\epsilon_2$  of three types of heterostructure is much higher than that of  $IGZO$  monolayer, showing remarkably enhanced photons. Notably,  $WS_2/IGZO$  heterostructure has a broad range of photoresponse, from visible light to deep UV light, which is wider than that of  $WS_2/ZnO$ ,  $MoS_2/ZnO$  heterostructure.[42, 43] It can be concluded the  $WS_2/IGZO$  heterostructure holds the typical optical characteristics of individual single-layer  $IGZO$  and  $WS_2$  and also exhibits some unique optical properties, such as the unique dielectric function and absorption spectrum in the visible light range and wide range of photoresponse, which shows great potential applications in optical transmission and photoelectric devices.

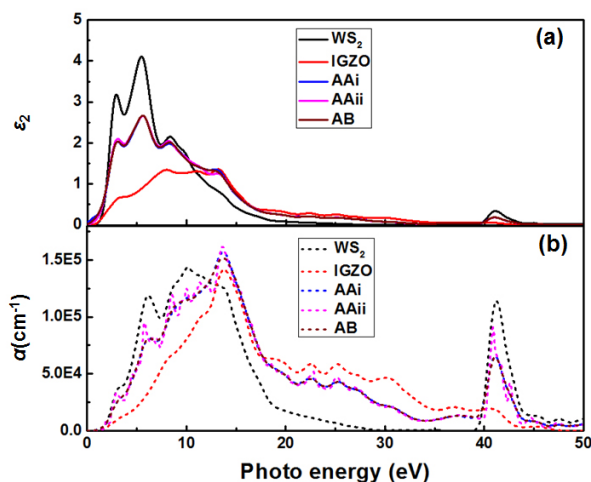


Figure 5.7: (a) Imaginary part of dielectric function ( $\epsilon_2$ ) and (b) adsorption coefficient ( $\alpha$ ) of free-standing  $WS_2$  monolayer, pristine  $IGZO$ , and AAi-, AAii- and AB- stacking heterostructure for the polarization vectors parallel to the two dimensional plane.

**Tunable optical properties under mechanical strain.** In addition to tuning up the elec-

tronic properties, the external strain can modulate the optical properties of WS<sub>2</sub>/IGZO heterostructure. Since the dielectric function and the absorption coefficient of three types of heterostructures are similar, we only discuss the modulation mechanism of AAI- and AB-stacking, which has a direct band gap. Figure 5.8 show that the peak position and intensity of the  $\epsilon_2$  curve are slightly altered with the increased strain. For both AAI- and AB-stacking, redshift behavior is observed in the primary two peaks when mechanical strain is applied. The range of photoresponse is narrowed and mainly focuses on visible light, UVA, and UVB (0 to 10 eV). For tensile strain, with increasing applied strain, the intensity of  $\epsilon_2$  in  $\sim 6$  eV decreases, while the intensity of  $\epsilon_2$  in  $\sim 2$  eV increases. It means that the tensile strain can weaken the photoresponse of the heterostructure to the UV light (the main peak located in  $\sim 6$  eV), and enhance the response for the visible light (the first peak located in  $\sim 2$  eV). Besides, the higher the applied tensile strain, the larger the redshift for the heterostructure. Notably, this phenomenon is more remarkable for the uniaxial strain in b- direction and biaxial strain in AAI- and AB- stacking. For compressive strain, with increasing applied strain, the intensity of  $\epsilon_2$  in all response photon energy is enhanced. And the uniaxial compressive strain in a-direction induces more obvious changes in  $\epsilon_2$ . As shown in Figure 5.8c and f, it is notable that the corresponding  $\epsilon_2$  curve for the UV light region (4-8 eV) exhibits a strong absorption peak when the compressive magnitude reaches -6% to -10%. The capability of the biaxial strain to modulate the heterostructure's optical properties is superior to that of the uniaxial strain. Accordingly, the heterostructure would exhibit a high capability of absorbing UV light, an ideal nanocomposite for applications in UV-driven photocatalysis. According to the above analysis results, it can be concluded that WS<sub>2</sub>/IGZO heterostructure could be well tuned by external mechanical strain and has great potential for photodetector, photocatalysis, and other optical device applications.

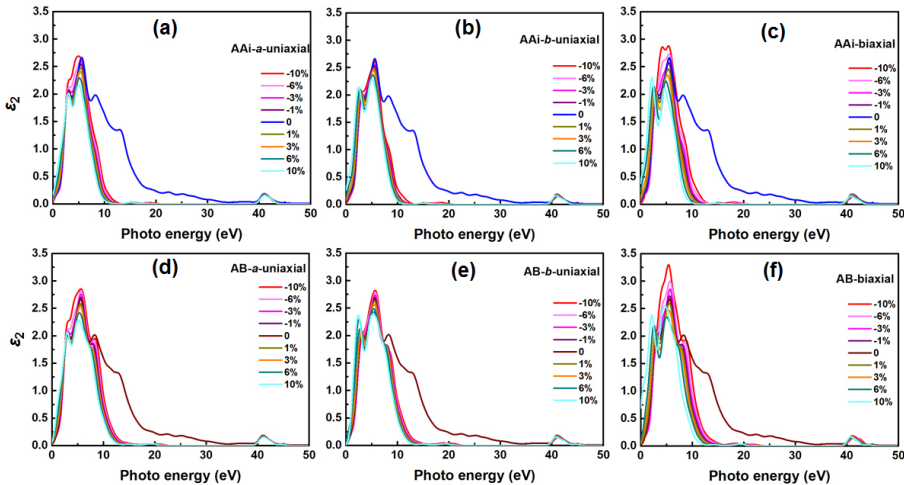


Figure 5.8: The effect of external mechanical strain on the imaginary part of dielectric function ( $\epsilon_2$ ) of (a-c) AAI- and (d-f) AB- pattern of WS<sub>2</sub>/IGZO heterostructure under (a, d) uniaxial strain in a-direction, (b, e) uniaxial strain in b-direction, and (c, f) biaxial strain.

### 5.2.3. GAS SENSING PROPERTIES

Here, the gas sensing behavior of WS<sub>2</sub>/IGZO heterostructure was comparatively analyzed with that of WS<sub>2</sub> monolayer. In order to characterize the adsorption strength between gas molecules and substrate, the adsorption energy ( $E_A$ ) is defined as  $E_A = E_{\text{substrate+gas}} - E_{\text{substrate}} - E_{\text{gas}}$ , where  $E_{\text{substrate+gas}}$ ,  $E_{\text{substrate}}$ , and  $E_{\text{gas}}$  represent the total energy of gas-adsorbed on substrate system, pristine substrate, and free gas molecules, respectively. The negative value of  $E_A$  indicates the adsorption is exothermic. Charge transfer in the adsorption systems of gas molecules adsorbed on the substrate was evaluated based on Hirshfeld charge analysis, which provides an intuitive way of separating the charge related to each atom using first-principles calculations.[44] More detailed information from the simulation of different molecule-substrate systems, i.e.  $E_A$ , and charge transfer ( $\Delta Q$ ), the change of bandgap ( $\Delta E_g$ ) are listed in Table 5.2. The negative sign of  $Q$  indicates charge transfers from the substrate to the molecule. This structure has the  $E_A$  of -0.308 eV and  $\Delta Q$  of 0.024. Because NO<sub>2</sub> is a paramagnetic molecule, the adsorption introduces stronger doping and produces larger  $E_A$ . The  $\Delta E_g$  of WS<sub>2</sub>/IGZO heterostructure is larger than that of monolayer WS<sub>2</sub>, indicating a higher level gas response can be achieved using heterostructure based sensors compared to WS<sub>2</sub> according to Eq.4.2.

Table 5.2: The adsorption energy ( $E_A$ ), change transfer ( $\Delta Q$ ), band gap ( $E_g$ ), and the change of band gap ( $\Delta E_g$ ) after adsorption

Material	Gas	$E_A$ (eV)	$\Delta Q$ (e)	$E_g$ (eV)	$\Delta E_g$ (eV)
WS <sub>2</sub>	NH <sub>3</sub>	-0.167	0.056	0.797	1.029
	NO <sub>2</sub>	-0.261	-0.027	1.727	0.101
WS <sub>2</sub> /IGZO	NH <sub>3</sub>	-0.214	0.057	1.595	0.361
	NO <sub>2</sub>	-0.308	-0.024	0.787	0.447

To further explore the interaction between the gas molecule and substrate, the charge density difference (CDD) are presented in Figure 5.9. The blue and yellow regions show charge accumulation and depletion, respectively. The CDD for NH<sub>3</sub>/substrate system shows that the charge is depleted on NH<sub>3</sub> molecule (Figure 5.9a) and charge accumulated on the substrate surface. As a result, NH<sub>3</sub> acts as a charge donor and provides 0.057 e to the substrate. In the case of NO<sub>2</sub> (Figure 5.9b), the most charge accumulated on NO<sub>2</sub> molecule surface, while charge depleted on the top surface of the substrate. The results reveal that NO<sub>2</sub> acts as a charge acceptor with large charge transfer (-0.024 e) because the spin-induced magnetic moment leads to stable doping. The density of states (DOS) profiles is presented in Figure 5.10. The total DOS of NH<sub>3</sub>/substrate system (Figure 5.10a) does not change much compared with the pristine substrate, indicating that the outstanding electronic properties of substrate stay unaffected after adsorption. The contribution of NH<sub>3</sub> electronic level to the total DOS is localized between -4 eV to -2 eV in the valence band, which is far away from the Fermi level. Similar to NH<sub>3</sub>, for NO<sub>2</sub>/substrate system (Figure 5.10b), the DOS of the substrate with gas adsorption is almost unchanged at the Fermi level. Thus, the electronic properties of the substrate can be well-retained.

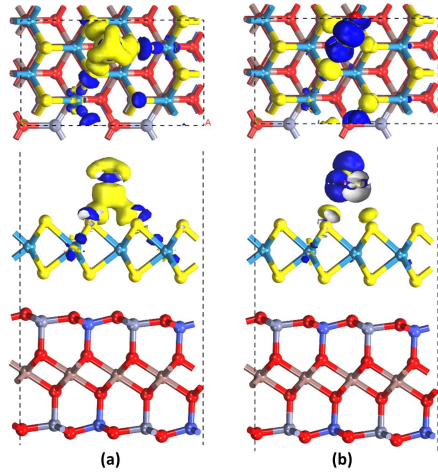


Figure 5.9: Charge density difference of the (a) NO<sub>2</sub>-adsorbed and (b) NH<sub>3</sub>-adsorbed on WS<sub>2</sub>/IGZO heterostructure. The isosurface is taken as  $3 \times 10^{-3} e \text{ \AA}^{-3}$ .

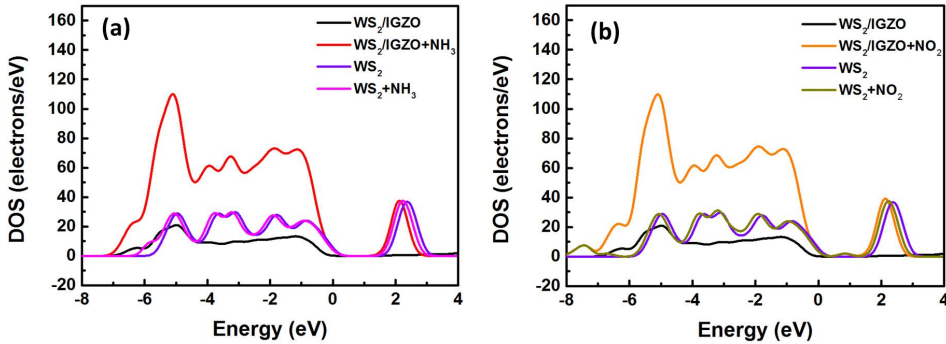


Figure 5.10: DOS of (a) NH<sub>3</sub>-adsorbed and (b) NO<sub>2</sub>-adsorbed on WS<sub>2</sub> and WS<sub>2</sub>/IGZO heterostructure.

## 5.3. NO<sub>2</sub> GAS SENSOR BASED ON CVD-WS<sub>2</sub>/IGZO P-N HETEROJUNCTION

### 5.3.1. DESIGN AND FABRICATION

**Device fabrication.** An IGZO film (10 nm) was deposited onto an Si/SiO<sub>2</sub> substrate through RF magnetron sputtering. Then, source/drain (S/D) electrodes were formed through thermal evaporation of Ti (10 nm)/Au (30 nm). After the photolithographic lift-off process, an IGZO thin film transistor (TFT) was obtained. To fabricate a WS<sub>2</sub>/IGZO heterojunction TFT, the monolayer WS<sub>2</sub> film grown by the CVD process was transferred onto the fixed position of the IGZO surface and covered on the top of S/D electrodes by using a poly(methyl methacrylate) (PMMA) supporting layer with a custom fixture. Finally, the PMMA was removed by dipping in acetone for 10 min and ethanol for 5 min. For comparison, we also fabricated a WS<sub>2</sub> TFT, whose procedure is similar to that of WS<sub>2</sub>/IGZO heterojunction TFT

except for the deposition of IGZO film. The schematics and optical images of  $WS_2$  TFT, IGZO TFT, and  $WS_2/IGZO$  heterojunction TFT are shown in Figure 5.11.

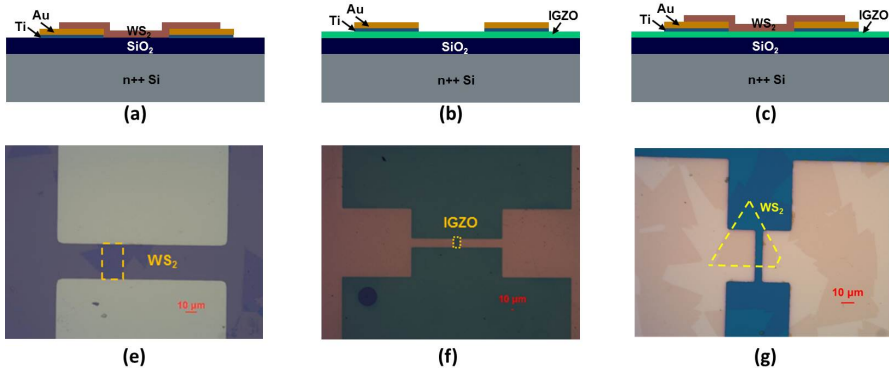


Figure 5.11: Schematic diagram of the (a)  $WS_2$ -only, (b) IGZO-only and (c)  $WS_2/IGZO$  heterojunction transistor. Optical image of (e)  $WS_2$ -only, (f) IGZO-only and (g)  $WS_2/IGZO$  heterojunction transistor.

5

**Characterization.** The optical microscopic images were obtained from an optical microscope (OLYMPUS TH4-200) imager with white light illumination. The thickness of CVD- $WS_2$  and IGZO was measured by using an atomic force microscope (AFM, Bruker, Santa Barbara, CA, USA). The Raman and photoluminescence (PL) spectra of the  $WS_2$ , IGZO, and  $WS_2/IGZO$  heterojunction were obtained through a Raman spectroscope meter (Raman, HORIBA, LabRAM HR Evolution) excited by a 532 nm laser. The film morphology was characterized by field-emission scanning electron microscopy (SEM; SUPRA 55VP, Carl Zeiss, Germany).

**Gas test setup.** For the investigation of the effects of gas on the electronic properties of  $WS_2/IGZO$  heterostructure on  $SiO_2$ , experiments were performed in the DGL-III Testing System (Beijing Elite Tech Co., Ltd) with the atmospheric conditions changing in the following order: dry air, gradually increasing  $NO_2$  concentration, and dry air. All the gas-sensing experiments were carried out at room temperature and atmospheric pressure. Figure 5.12 shows the experimental setup used for gas sensing performance.

**Electrical Characterization.** Mott-Schottky measurements were performed on a CHI660C electrochemical workstation using a three-electrode cell system. In this measurement, 0.5 M  $Na_2SO_4$  was used as the electrolyte, while  $WS_2$ , platinum, and Ag/AgCl were used as the cathode, the anode, and reference electrode, respectively. The frequency was fixed at 1 kHz. Electrical characterization of  $WS_2/IGZO$  heterojunction device was performed by using an electrical analysis system (two Keithley 2450 Source Meter, one for supplying drain-source voltage ( $V_{ds}$ ), and the other for supplying gate-source voltage ( $V_{gs}$ ) to record the real-time change of current (data acquisition time  $\sim 30$  ms) using the three-probe in the gas chamber. Before the gas-sensing test, the  $WS_2/IGZO$ -based devices were stabilized in the air in the system for about 30 min to restore to the initial state fully. The current-voltage ( $I_{ds}-V_{ds}$ ) measurements were taken from -1 V to +1 V. The transfer characteristics ( $I_{ds}-V_{gs}$ ) were recorded with constant  $V_{ds}$  of 0.5 V. The transistor electrical parameters, namely, the field-effect mobility ( $\mu$ ), threshold voltage ( $V_{th}$ ), and on/off current ratio ( $I_{on}/I_{off}$ ), were

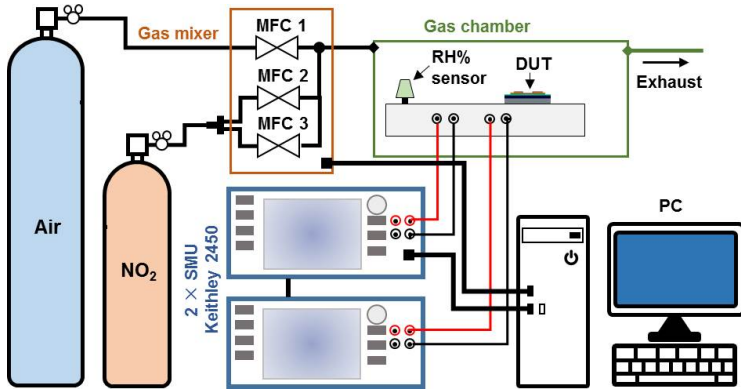


Figure 5.12: Experimental setup used for gas sensing measurements.

extracted from the characteristic curves in the saturation regime. The sensing performance of WS<sub>2</sub>/IGZO heterojunction was evaluated according to the response ( $S$ ) and response time. Here,  $S$  is defined by the relative current change as the percent change in current divided by the initial current in different gas concentrations.

$$S = (I_{g(V_{gs})} - I_0(V_{gs})) / I_0(V_{gs}) \times 100\% \quad (5.5)$$

where  $I_{g(V_{gs})}$  and  $I_0(V_{gs})$  are the drain-source current of the device upon the introduction of NO<sub>2</sub> gas and in dry air under different  $V_{gs}$ , respectively. When  $V_{gs} = 0$  V,  $S$  is the response on the chemiresistor mode; when  $V_{gs} < 0$  V,  $S$  is the response on the transistor mode.

### 5.3.2. CHARACTERIZATION

The cross-section SEM images of the WS<sub>2</sub>/IGZO device are shown in Figure 5.13a, which confirms that the vertical stacking structure and the thickness of WS<sub>2</sub> and IGZO. The AFM scanning images of WS<sub>2</sub> and IGZO film are shown in Figure 5.13 b and c, respectively. It can be found that the height of the WS<sub>2</sub> is  $\sim 1.2$  nm, indicating that it is a monolayer WS<sub>2</sub>. [45] The device has a channel length of 5  $\mu\text{m}$  and a width of 20  $\mu\text{m}$ . The top surface of IGZO contact with the Ti metal layer, and the bottom surface of WS<sub>2</sub> contact with Au film affects the band alignment of the semiconductor materials and metals. As shown in Figure 5.14, the Raman spectra for both WS<sub>2</sub>/IGZO and WS<sub>2</sub> have two main bands at 354 and 419  $\text{cm}^{-1}$ , which correspond to the E<sub>1</sub><sup>2g</sup> and A<sub>1g</sub> modes of the WS<sub>2</sub> crystal. [16] It indicates that the transferring process in both substrates (IGZO and SiO<sub>2</sub>) is equivalent. Moreover, the PL intensity of heterojunction is lower than that of WS<sub>2</sub>, which further confirms that the electrons and holes generated from separated excitons transferred from WS<sub>2</sub> and IGZO effectively. [46]

To explain the contact barrier between semiconductors and Ti/Au metal in more detail, we analyzed the band structures of WS<sub>2</sub> and IGZO and the work functions of Ti, Au through first-principle calculations. Figure 5.2 shows the calculated band structures of WS<sub>2</sub> and IGZO crystals, respectively. The band diagram structure provides the band gap values of the metal electrodes to estimate the type-I band alignment between WS<sub>2</sub> and IGZO, as well

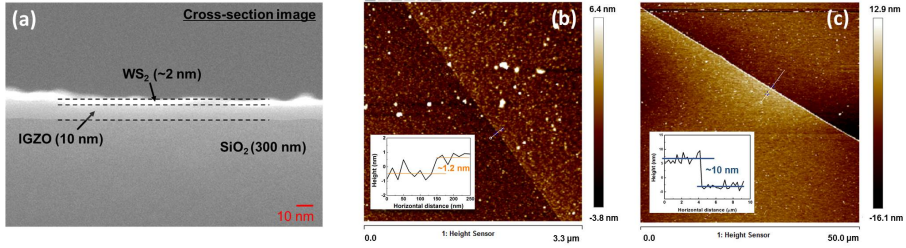


Figure 5.13: (a) SEM cross-sections of the  $WS_2/IGZO$  heterojunction. The AFM results of (b)  $WS_2$  layer and (c) IGZO layer.

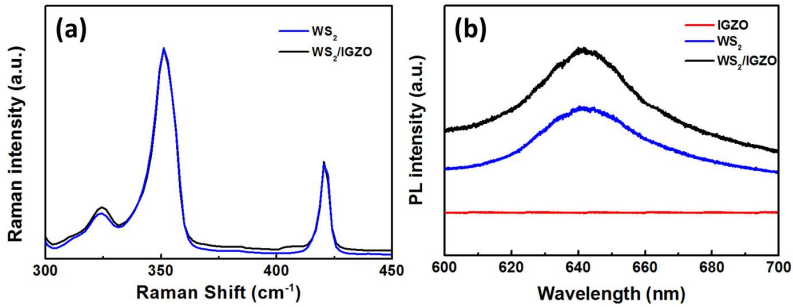


Figure 5.14: (a) Raman and (b) PL image under 532 nm laser.

as the position of Au and Ti work function.  $WS_2$  has a narrower band gap, whose Fermi level ( $E_f$ ) is almost equal to that of Au and much lower than that of IGZO. Concerning the Ti, their  $E_f$  is lower than that of IGZO. It indicates the contact barrier between Au and  $WS_2$  is small and negligible, while the barrier between Ti and IGZO is large and positive. Thus, the I-V curve under the air environment shows rectification characteristics consisting of an Au/ $WS_2$  near-Ohmic contact and Ti/IGZO Schottky contact (see Figure 5.15). In this work,  $WS_2$  shows p-type semiconductor nature according to the Mott-Schottky plot drawn between  $1/C^2$  and the potential with respect to saturated calomel electrode (SCE) (see Figure 5.16). The flat band potential ( $E_{FB}$ ) is found to be  $0.43 V_{SCE}$  with acceptor density ( $N_A$ ) in the range of  $9.8 \times 10^{17}/cm^3$ , which agrees with the reported value ( $0.45 V_{SCE}$  with  $N_A$  of  $10^{18}/cm^3$  by Tonti *et al.*[47], and  $0.44 V_{SCE}$  with  $N_A$  of  $9.7 \times 10^{17}/cm^3$  by Devadasan *et al.*[48]). Accordingly, three regions of the device configuration, including heterojunction, p-channel of  $WS_2$ , and n-channel of IGZO, can dominate the electrical transport of the systems.

According to its output (Figure 5.17a) and transfer (Figure 5.17b) characteristics, the  $WS_2/IGZO$  heterojunction-based TFT show excellent and symmetrical ambipolar behaviour, which can be attributed to the p-channel of  $WS_2$  and n-channel of IGZO. Gate-induced holes in  $WS_2$  will dominate the system's electrical conductivity after applying negative  $V_{gs}$ , and the transistor shows p-type behaviour. However, the positive  $V_{gs}$  induces the increment of electrons and finally leads to the transistor show n-type behaviour. In general, the emerging ambipolar properties with both p- and n-type conducting channels reveal

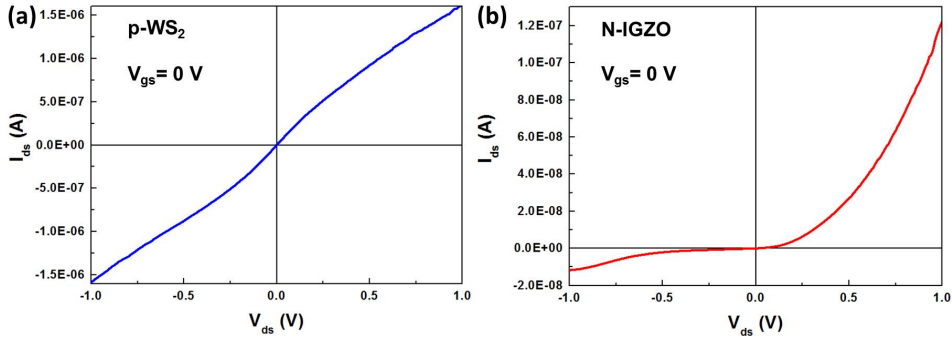


Figure 5.15: I-V characteristics of the individual WS<sub>2</sub> (a) and IGZO (b) without gate bias, showing a near-ohmic behaviour and Schottky behaviour for Au/WS<sub>2</sub> contact and Ti/IGZO contact, respectively.

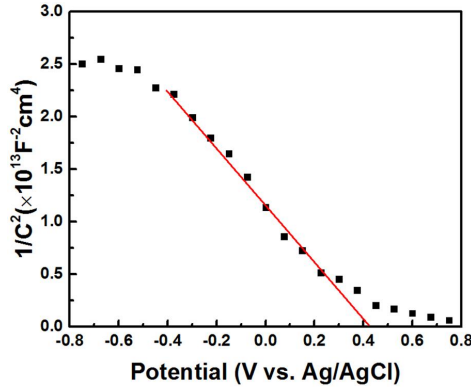


Figure 5.16: Mott-Schottky plot for p-WS<sub>2</sub> thin film in 0.5M Na<sub>2</sub>SO<sub>4</sub>.

great potential applications in future electronics and oscillators for the WS<sub>2</sub>/IGZO hetero-junction. The current between gate and source ( $I_{gs}$ ) is far less than  $I_{ds}$ , indicating there is no current leakage. The on/off current ratio of the WS<sub>2</sub>/IGZO hetero-junction-based TFT is 5090. This ratio degrades compared to the device based on IGZO, which on/off current ratio is 25530. This is induced by the wet transfer process of CVD-WS<sub>2</sub>, which enlarge the distance of the interface between WS<sub>2</sub> and IGZO.[49, 50] The mobility of transistors are obtained using  $\mu = [L/(WC_i V_{ds})] \cdot [(dI_{ds}/dV_{gs})]$ , where  $(dI_{ds}/dV_{gs})$  is the slope of linear region of transfer curves,  $C_i$  is the gate capacitance of the gate insulator per unit area,  $L$  and  $W$  are the length and width of the channel, respectively ( $L=5 \mu\text{m}$  and  $W=20 \mu\text{m}$ , as shown in Figure 5.11c).[51] The field-effect mobility increased from  $\sim 0.3$  to  $23.8 \text{ cm}^2/\text{Vs}$  after the WS<sub>2</sub> film is introduced. The maximum power consumption is  $1.3 \mu\text{W}$ .

### 5.3.3. GAS SENSING PROPERTIES OF WS<sub>2</sub>/IGZO CHEMIREซิสТОР

The responses to NO<sub>2</sub> gas among WS<sub>2</sub>-only, IGZO-only and WS<sub>2</sub>/IGZO based devices were investigated firstly. As shown in Figure 5.19a, WS<sub>2</sub>, IGZO, and WS<sub>2</sub>/IGZO based

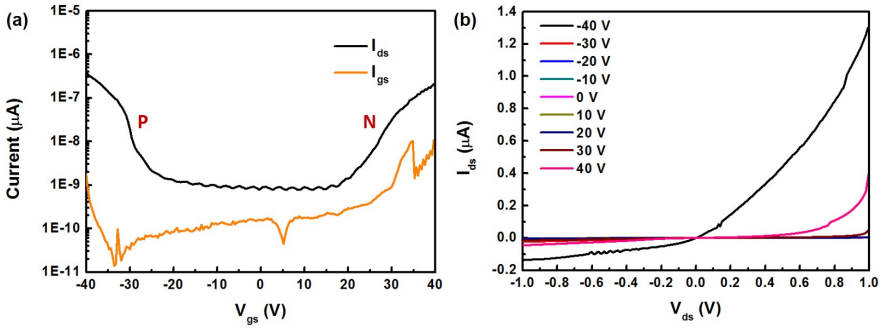


Figure 5.17: (a) Output characteristics of the device, showing the symmetrical ambipolar behavior. (b) Transfer characteristics during the period of sweeping gate voltage in linear (black line) and logarithmic (blue line) scales. ( $V_{ds} = 0.5$  V,  $V_{gs} = -40$  V to 40 V).

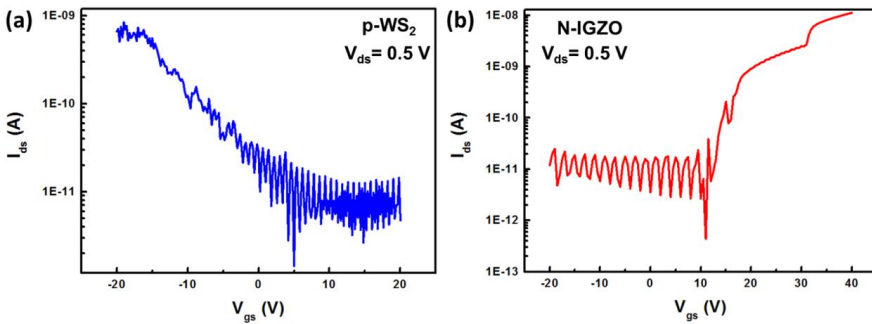


Figure 5.18: Transfer characteristics of (a) WS<sub>2</sub> and (b) IGZO with logarithmic scale of y-axis, showing the p-type behaviour, respectively.

sensor has  $S_{WS_2} = 430\%$ ,  $S_{IGZO} = -70\%$ , and  $S_{WS_2/IGZO} = 5470\%$  when exposed to 50 ppm NO<sub>2</sub>, confirming that WS<sub>2</sub>/IGZO has much better NO<sub>2</sub> sensing behaviour than that of only WS<sub>2</sub> and IGZO. The superior gas sensing performance could benefit from the hetero-junction structure. However, three types of devices have a very long recovery time, which might be related to the chemical adsorption of NO<sub>2</sub> on the surface. Then, to evaluate the NO<sub>2</sub> sensing performance of the WS<sub>2</sub>/IGZO hetero-junction chemiresistor sensor, the dynamic current change was measured under the different gas concentrations of NO<sub>2</sub> ranging from 1 ppm to 300 ppm. As shown in Figure 5.19b, with increasing gas concentration, the current of the device increases. The response of the device after exposure to different concentration NO<sub>2</sub> are shown in Figure 5.19c. It can be found that the lower the concentration, the longer the recovery time needed. Thus we unified the recovery time with 30 minutes for ease of comparison. The device presents high response ( $S$ ) of 230% under 5 ppm and 18170% under 300 ppm NO<sub>2</sub>, which is much higher than that of ultra-thin WS<sub>2</sub> nanosheets ( $S = 9.3\%$  @ 1 ppm NO<sub>2</sub>) and WS<sub>2</sub> nanosheets decorated by Ag nanowires ( $S = 667\%$  @ 500 ppm NO<sub>2</sub>). [4, 52] Figure 5.19d shows the responses of WS<sub>2</sub>/IGZO hetero-junction as a function of the NO<sub>2</sub> concentrations in 1 ppm to 300 ppm. The experimental data were

fitted by exponential function as:

$$\text{Response}(S) = 648.28 \times C^{0.6} \quad (5.6)$$

where C is the gas concentration of NO<sub>2</sub>. Also, the linear fitting results of log(S) versus log(C) (see the inset image of Figure 5.19d) further illustrates that the surface coverage of adsorbed NO<sub>2</sub> molecules follows Freundlich isotherm adsorption, which is the most important multisite adsorption isotherm for rough surfaces.[53] Besides, since the signal is three times greater than the noise, we calculated the limit of detection (LOD) of the as-fabricated sensor according to the International Union of Pure and Applied Chemistry (IUPAC). The theoretical LOD can be calculated from the slope of the linear region of the response curve and the root-mean-square (RMS) deviation at the baseline, according to the equation:

$$\text{LOD}(\text{ppb}) = 3 \times \text{RMS}_{\text{noise}}/\text{Slope} \quad (5.7)$$

where RMS<sub>noise</sub> is the standard deviation of noise and is calculated as 0.0023, according to 200 data points in the baseline of the response curve (Figure A.2 a,b). The calculation process and results are present in Appendix-a, Table A.3,A.4. The calculated LOD for NO<sub>2</sub> is 29 ppb at room temperature, which is much better than the reported values.

In addition, the response and recovery kinetics are critical to the reliability and sustainability of gas sensor. Thus, we quantitatively investigated the recovery characteristics of WS<sub>2</sub>/IGZO-based gas sensors by calculating the percent recovery. The percent recovery is expressed as:

$$\text{Recovery}(\%) = (I_{\text{g}}(V_{\text{gs}}) - I_{\text{r}}(V_{\text{gs}}))/I_{\text{r}}(V_{\text{gs}}) \times 100\% \quad (5.8)$$

where  $I_{\text{r}}(V_{\text{gs}})$  and  $I_{\text{g}}(V_{\text{gs}})$  are the current value in dry air and after 30 min exposure to NO<sub>2</sub> gas under different  $V_{\text{gs}}$ , respectively.  $I_{\text{r}}(V_{\text{gs}})$  is the recovered current value after exposure to dry air for 30 min under different  $V_{\text{gs}}$ . As shown in Figure 5.19e, the higher gas concentration, the larger the percent recovery, indicating that under high NO<sub>2</sub> the device can recover faster than that under lower gas concentration. Under low NO<sub>2</sub> gas concentration, gas molecules are easily and mostly adsorbed by the edge-sites and defects of the heterojunction and the interface.[9] Due to the high adsorption energy of the edge-sites and defects, the device recovers so slowly. With increasing gas concentration, most of the gas molecules are adsorbed by the surface of WS<sub>2</sub>/IGZO heterojunction, which easily escapes from the adsorption site under airflow. Accordingly, we investigated the dynamic response of the device after 3 cycles under 50 ppm NO<sub>2</sub>. Here, the device was exposed to 50 ppm NO<sub>2</sub> for 30 minutes, and then with the flow of dry air for 90 minutes to make the sensor fully recovered. As shown in Figure 5.19f, the result shows that the chemiresistor sensor has good repeatability.

To study the selectivity, we measured the responses of the device to several other gases, including a reducing gas NH<sub>3</sub> (100 ppm) oxidizing gases of CO (100 ppm). As shown in Figure 5.20a, the sensor response toward NH<sub>3</sub> and CO under 100 ppm are -137% and 94%, respectively, which are far lower than that of NO<sub>2</sub>. Then, the device was measured under different humidity environments (with a relative humidity of 10%, 30%, 50%, 65%, and 80%). The sensor presents the maximum response of 33% (see Figure 5.20b). It is

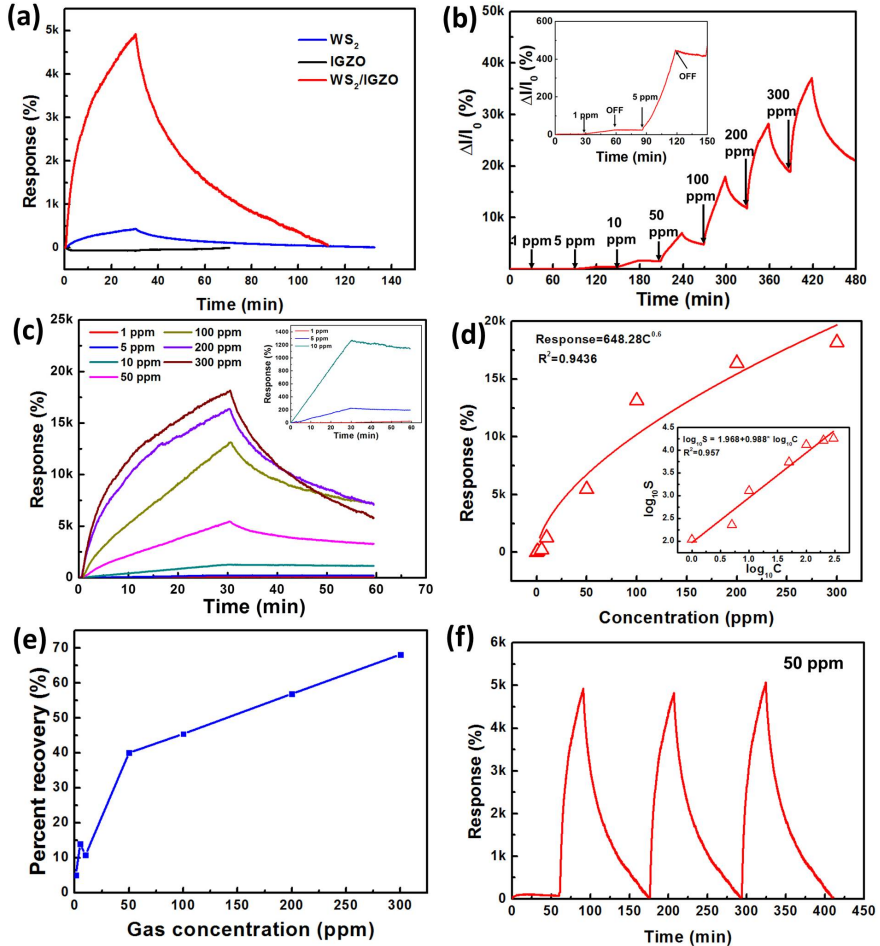


Figure 5.19: (a) Response of IGZO-only,  $WS_2$ -only, and  $WS_2/IGZO$  devices after exposure to 50 ppm  $NO_2$ . (b) Real time response of a  $WS_2/IGZO$  device after exposure to  $NO_2$  under different concentration. Inset image is the magnified curve of current change under 1 and 5 ppm  $NO_2$  gas concentration. (c) Response of the device after exposure to  $NO_2$  under different concentration. Inset image is the magnified curve of normalized response under 1, 5 and 10 ppm  $NO_2$  gas concentration. (d) Response versus  $NO_2$  concentrations fitted by using Freundlich isotherm adsorption model. Inset:  $\log_{10} S$  versus  $\log_{10} C$  with linear line fitting. (e) Percent recovery of the device after exposure to  $NO_2$  under different concentration. (f) Dynamic response of a sensor during 3 successive cycles of exposure to 50 ppm  $NO_2$ . All the test were carried out at room temperature.

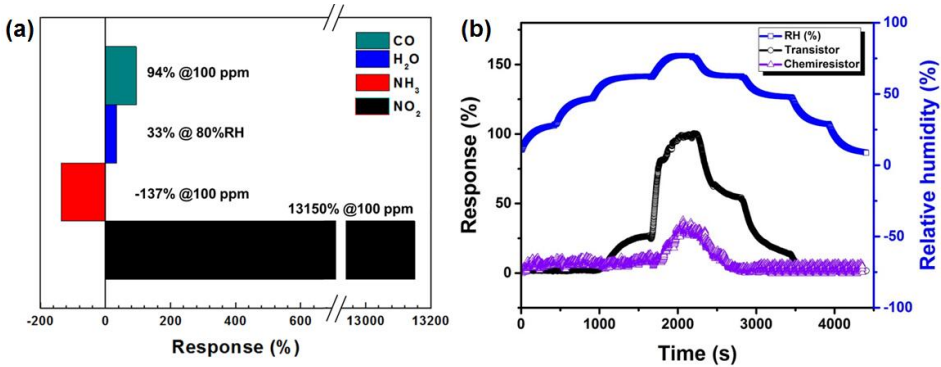


Figure 5.20: (a) The WS<sub>2</sub>/IGZO heterojunction chemiresistor gas sensor response of different types of gas molecules. (b) Dynamic response of the WS<sub>2</sub>/IGZO heterojunction (black) chemiresistor sensor and (purple) transistor sensor to humidity. The relative humidity in the test chamber were set to 80% RH, 65% RH, 50% RH, 30% RH, 10% RH, 30% RH, 50% RH, 65% RH, and 80% RH in sequence.

much less than that towards NO<sub>2</sub>, indicating that humidity has slight effects on the gas sensing performance towards NO<sub>2</sub>. Accordingly, it can be concluded that the WS<sub>2</sub>/IGZO heterojunction has good selectivity, sensitivity, low operation temperature, and unaffected by the RH of environments.

#### 5.3.4. GAS SENSING PROPERTIES OF WS<sub>2</sub>/IGZO TFT

The semiconducting behavior is particularly attractive for modulating the transport characteristics with exposure to light or gate bias to enhance sensing performance.[54, 55] Thus we investigated the sensing behavior of the WS<sub>2</sub>/IGZO TFT under different NO<sub>2</sub> gas concentration after applying different gate biases. Figure 5.21a shows the transfer characteristics of the device under air and increasing NO<sub>2</sub> gas concentration. By applying the gate bias, the response of the as-fabricated gas sensor was modulated by the carrier concentration. Along with increasing NO<sub>2</sub> gas concentration, more electrons are accepted by WS<sub>2</sub>/IGZO vertical stacked heterojunction, the hole current from the p-channel of WS<sub>2</sub> will gradually strengthen. Notably, when the concentration is higher than 50 ppm, the expected tunable polarity behaviors ranging from ambipolar to p-type behavior is observed. Since the surface of WS<sub>2</sub> adsorbs more and more NO<sub>2</sub> gas molecules, the current in p-channel of WS<sub>2</sub> increases obviously and dominates the electrical transport. Thus the transistor shows weakened ambipolar behavior and distinct p-type characteristics. As shown in Figure 5.21b, the electrical properties of the devices are tunable under different gas concentrations. When the gas concentration of NO<sub>2</sub> increases, the mobility of the TFT increase and reach 138 cm<sup>2</sup>/Vs under 300 ppm; while the on/off ratio decrease from 696 (1 ppm) to 72 (300 ppm).

Figure 5.21c shows the response of the WS<sub>2</sub>/IGZO transistors after exposure to NO<sub>2</sub> with different concentration, which was measured at fixed V<sub>gs</sub> ranging from -35 V to 35 V with a step of 5 V. After exposure to different NO<sub>2</sub> concentration, the maximum response occurs at different gating potentials depending on the gas concentrations. The gating potential-dependence behaviour is mainly induced by the gas doping effects, which modifies the transistor's operation ranges compared with the regime for the same gate bias under

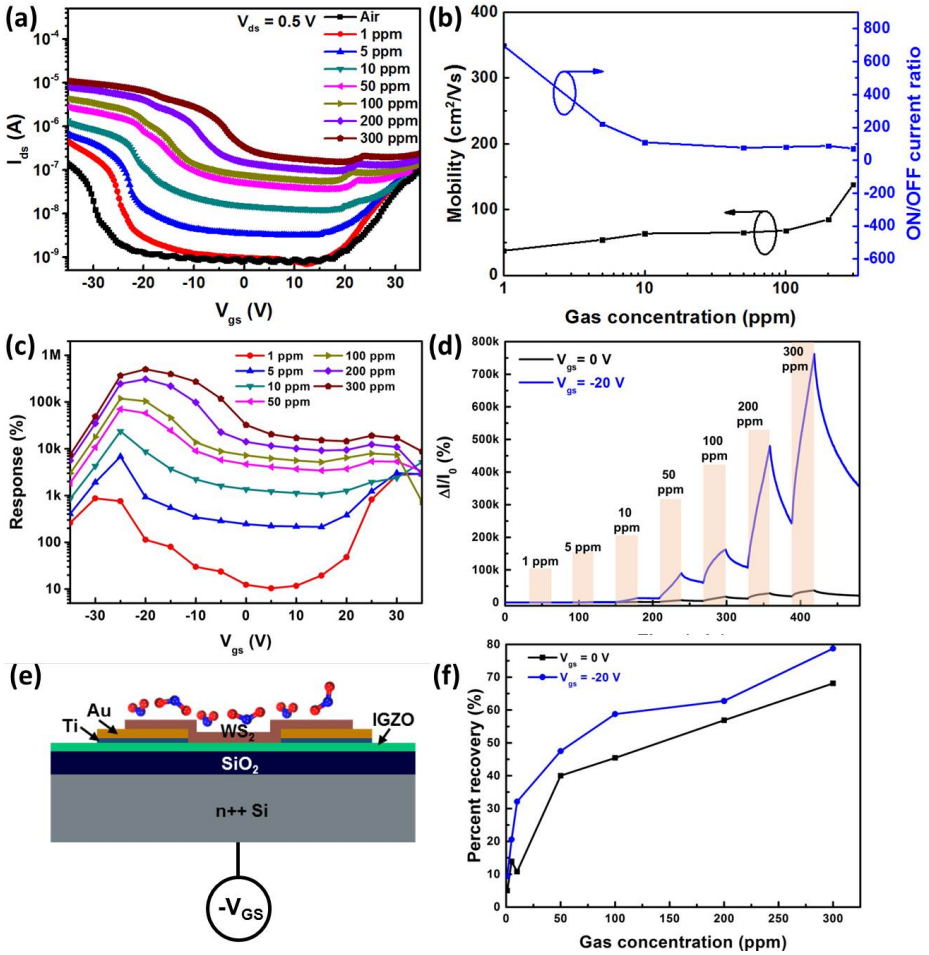


Figure 5.21: (a) Transfer curves of WS<sub>2</sub>/IGZO TFT under different NO<sub>2</sub> concentration. (b) Mobility and ON/OFF current ratio of devices under different NO<sub>2</sub> concentration. (c) Gas response of the devices under different NO<sub>2</sub> concentration after applying different gate bias. (d) Dynamic response of the device under different NO<sub>2</sub> concentration at 0 V and -20 V gate bias. (e) Schematic of WS<sub>2</sub>/IGZO TFT under negative gate bias. (f) Percent recovery of the device under different NO<sub>2</sub> concentration at 0 V and -20 V gate bias.

Table 5.3: Comparison of various gas sensor materials with respect to reported NO<sub>2</sub> ranges (ppm), LOD (ppm), working temperature (°C) and response (%).

Sensing materials	Sensor type	NO <sub>2</sub> (ppm)	LOD (ppm)	Temperature (°C)	Response (%)	Ref.
WS <sub>2</sub> /IGZO	TFT	300	0.026	RT	499400@-20V <sub>gs</sub>	This work
		5			6820@-25V <sub>gs</sub>	
WS <sub>2</sub> nanosheets	Chemiresistor	0.1	0.1	RT	9.3	[4]
WS <sub>2</sub> /Ag	TFT	500	/	RT	667	[52]
WS <sub>2</sub> /WO <sub>3</sub>	Chemiresistor	100	/	150	1000	[9]
WS <sub>2</sub> /ZnS heterostructure	Chemiresistor	5	0.053	RT	3250	[56]
MoS <sub>2</sub> /ZnO heterostructure	Chemiresistor	5	/	RT	3035	[11]
monolayer MoS <sub>2</sub>	TFT	0.1	0.1	RT	50	[57]
<i>a</i> -IGZO	Chemiresistor	5	/	200	3300	[58]
Photo-induced IGZO	TFT	5	/	RT	20	[18]

the air atmosphere. For instance, at high concentrations (200-300 ppm), with a gating voltage of -20 V, the transistor is nearly on the saturation regime while under air at the same gate bias, the transistors are on the linear regime. At low concentrations, the maximum responses are obtained with a gating tension larger than -20 V, because the TFT is in the linear regime. In all cases, the responses decrease for more negative gate bias because the transistor is operational in the saturation regime with and without NO<sub>2</sub> gas molecules. Figure 5.21d shows that the response of the device is improved to be 499400% at 300 ppm, and the recovery time is shortened after applying -20 V gate bias. As shown in Figure 5.21f, the higher gas concentration, the larger the percent recovery, which is similar to that of WS<sub>2</sub>/IGZO heterojunction chemiresistor devices. While the TFT gas sensor is with higher percent recovery, indicating that the surface activity can be enhanced under gate voltage. The gas-sensing performance is much higher than that of WS<sub>2</sub>-based, MoS<sub>2</sub>-based, and IGZO-based TFT gas sensors (see Table 5.1). The results illustrated that WS<sub>2</sub>/IGZO TFT is also a promising candidate for NO<sub>2</sub> gas sensor. To the best of our knowledge, the TFT device has the best NO<sub>2</sub> gas sensor response comparing to all the gas sensors based on TMDs materials.

### 5.3.5. GAS SENSING MECHANISM

When the WS<sub>2</sub> is combined with the IGZO, the p-N type WS<sub>2</sub>/IGZO heterojunctions are formed, inducing a different electron transport mechanism from that of individual WS<sub>2</sub> and IGZO. The band diagrams of WS<sub>2</sub> and IGZO before and after equilibrium is shown in Figure 5.22. IGZO has a higher work function of 7.01 eV compared to WS<sub>2</sub> (5.89 eV), and a higher E<sub>f</sub> compared to that of WS<sub>2</sub>. Thus electrons flow from the IGZO to the WS<sub>2</sub> while holes from WS<sub>2</sub> to IGZO, until their E<sub>f</sub> align, resulting in the energy band bending in the depletion region at the interface between WS<sub>2</sub> and IGZO.[59] As shown in Figure 5.22a, the region beneath the p-N interface creates an internal electric field, which acts as a potential barrier for further carrier diffusion. The potential barriers and depletion layers contribute to the low conductivity of the WS<sub>2</sub>/IGZO heterojunction in air. As shown in Figure 5.22b, when the sensor is exposed to air, oxygen species are adsorbed on the surface and interface layer of WS<sub>2</sub>/IGZO heterojunctions. Then, oxygen molecules can

easily trap the free electrons from their conduction band ( $E_c$ ) to form ionic oxygen species ( $O_2^-$  or  $O^-$ ). [60] When the sensor is exposed to  $NO_2$ , the oxidizing  $NO_2$  reacts with ionic oxygen species as well as adsorbed on the surface of heterojunctions. The adsorbed  $NO_2$  molecules attract the electrons from the heterojunction, produce  $NO_3^-$  or  $NO_2^-$ , and decrease its carrier concentration. The built-in electric field is non-equilibrium, inducing extra holes to slip from the IGZO and accumulate at the surface of  $WS_2$ , and the width of the heterojunction barriers decreases. It also leads to a decrease in depletion layer thickness and an increase in the conductivity of the device consequently.

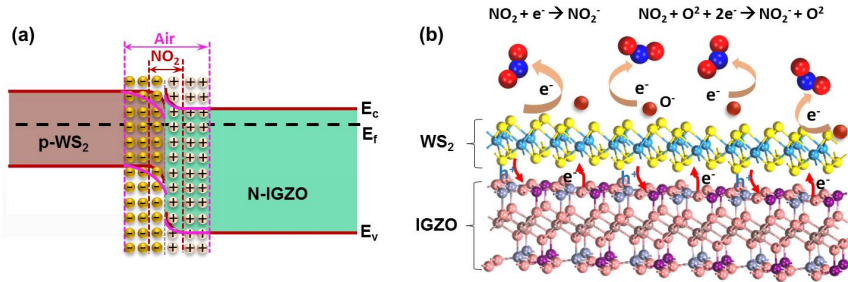


Figure 5.22: (a) Energy band structure of  $WS_2/IGZO$  heterojunction in air and a  $NO_2$  atmosphere, and (b) Schematic of sensing mechanisms of  $WS_2/IGZO$  heterojunction to  $NO_2$  molecules.

In general, the band shape and barrier height of heterojunction can be effectively modulated by applying an external gate voltage on the back-gate silicon electrode. [61, 62] As shown in Figure 5.23a,b, the N-IGZO has a large number of electrons, the electron drifts from IGZO to  $WS_2$  to overcome the  $WS_2/IGZO$  barrier under a constant positive  $V_{ds}$ . With a negative  $V_{gs}$ , the electron concentrations of IGZO near the  $SiO_2$  dielectric substrate decrease, which induces the  $E_c$  of IGZO decrease according to the equation of electron concentrations [63],

$$n_0 = N_c \times \exp(-(E_c - E_F)/k_0T), \quad (5.9)$$

where  $N_c$  is the effective density of states of the conduction band,  $k_0$  is Boltzman constant,  $T$  is temperature and results in the upward band bending between the  $SiO_2$  and IGZO films. On the contrary, after applying a positive  $V_{gs}$ , the electrons concentration in IGZO increase near the  $SiO_2$  substrate and shift the Fermi level downwards, forming a downward band bending (see Figure 5.23c,d). Therefore, the junction effect and gate-induced band bending dominate the electrical transport and lead to the ambipolar behaviours. When the TFT exposures to  $NO_2$  gas, the adsorption energy and charge transfer between gas molecules and  $WS_2/IGZO$  heterojunction increase obviously due to the effects of the external electric field from back gate voltage. [64, 65] Thus, the depletion layer thickness of TFT decreases greater than that in chemiresistor mode, and the current of heterojunction increases with the rising back gate voltage.

Moreover, the conductivity of the TFT increase with increasing gas concentration, and a lateral shift of  $V_{th}$  and a change of subthreshold slope can be observed, as shown in Figure 5.24a. Usually, chemical doping by gas molecules can induce massive charge transfer between the sensing materials and dopant, and finally lead to current increase and  $V_{th}$  shift in

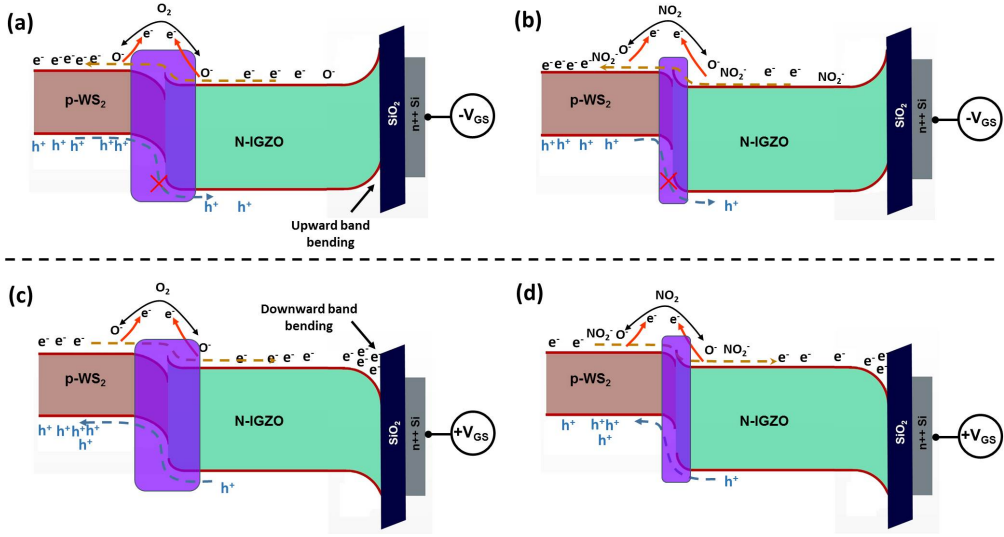


Figure 5.23: After applying negative  $V_{gs}$ , the band diagram of WS<sub>2</sub>/IGZO TFT (a) in air and (b) a NO<sub>2</sub> atmosphere. After applying positive  $V_{gs}$ , the band diagram of WS<sub>2</sub>/IGZO TFT (c) in air and (d) a NO<sub>2</sub> atmosphere. The purple region represents depletion layer.

a TFT-type gas sensor.[66, 67] For as-fabricated WS<sub>2</sub>/IGZO TFT, the transfer curves of p-type behaviour shift towards the positive gate voltage direction, while the n-type behaviour towards the negative direction. It is mainly attributed to the high gas doping effects on the WS<sub>2</sub>/IGZO heterojunction, which leads to massive charge transfer between gas molecules and heterojunction. Thus the device is difficult to go back to off-state under high gas concentration, and the on/off ratio decreases (see Figure 5.24,b). Moreover, since the WS<sub>2</sub> film at the top layer of the vertically stacking WS<sub>2</sub>/IGZO heterojunction, most of the NO<sub>2</sub> gas molecules can be adsorbed by p-channel WS<sub>2</sub> at first. It results in high current density inside WS<sub>2</sub>, and the device presents enhanced p-type behavior.

A change of subthreshold slope is usually found in a TFT with metal/semiconductor contact because gas concentration.[68, 69] The WS<sub>2</sub>/IGZO heterojunction TFT's subthreshold slope ( $K_{th} = dV_{gs}/d\log(I_{ds})$ ) for both p- and n-type behaviour decrease sharply from 0 ppm to 10 ppm and then increase slightly when the gas concentration is higher than 50 ppm. These results can be attributed to two types of sensing mechanisms: Schottky barrier modulation and doping of the transistor channel. As shown in Figure 5.24b, when the device exposures to low NO<sub>2</sub> gas concentration, the adsorption sites are sufficient for detecting many gas molecules, thus a Schottky barrier built-up between the WS<sub>2</sub>, IGZO, and metal in the contact region is changed obviously and so does the  $K_{th}$ . For high NO<sub>2</sub> gas concentration, the adsorption sites reach saturation, which induces slight changes in  $K_{th}$  and  $V_{th}$ . Both shifts of the  $V_{th}$  and changes of the  $K_{th}$  can be associated to the fact that the sensing mechanism of the WS<sub>2</sub>/IGZO transistor is affected by the doped of NO<sub>2</sub> and the modulated Schottky barrier value at the WS<sub>2</sub> and IGZO with a metal contact interface. Therefore, with the increase in the concentration of NO<sub>2</sub>, more charges are transferred to heterojunction,

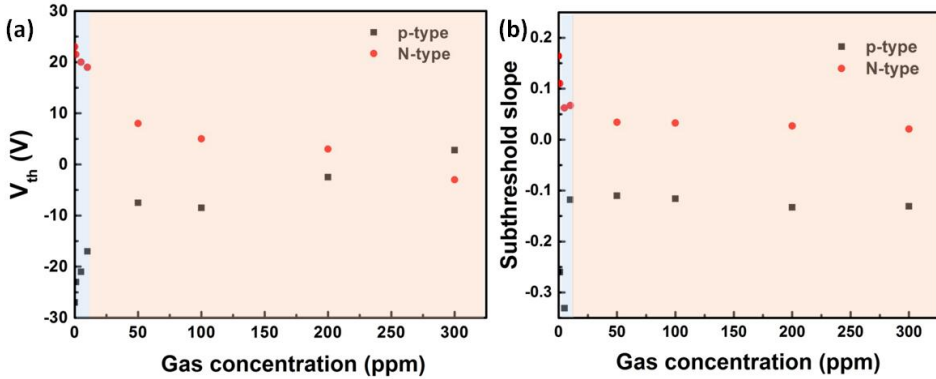


Figure 5.24:  $WS_2/IGZO$  sensing mechanism study. (a) Threshold voltage ( $V_{th}$ ) and (b) Subthreshold slope ( $K_{th}$ ) versus gas concentrations for  $NO_2$ .

5

and the  $WS_2/IGZO$  heterojunction-based sensor shows an ultra-high response to  $NO_2$  under gate voltage. The proposed sensing mechanism is in agreement with the fact that the device is more difficult to recover at low concentrations, as is previously mentioned, the metal electrodes interfaces and the edges are more favourable for binding  $NO_2$  molecules, the molecules adsorbed in the metal electrode interface with the junctions will contribute to the Schottky barrier modulation. In contrast, those located at edges will contribute to the doping because both kinds of sites possess higher binding energy, these molecules will be more difficult to desorb. However, to identify where the predominant gas sensing behaviour is taking place, further studies must be performed, it might be interesting to analyze the gas response and the recovery time with a passivate device in the interface between the metal electrodes and the heterojunction, and compare with a response with a passivate device in the channel (where just the metal electrode area is exposed).

## 5.4. CONCLUSIONS

In conclusion, the structural, electronic, and optical properties of  $WS_2/IGZO$  heterostructure have been studied by density functional calculation. The binding energy and inter-layer distance indicate that the  $WS_2$  and  $IGZO$  monolayers are bound to each other via non-covalent interactions with enhanced binding strength. The results demonstrate that the AAii stacking pattern has an indirect band gap of 1.643 eV, while the AAi and AB stacking pattern has a direct-gap of 1.102 eV and 1.234 eV, respectively. The band gap shows a near-linear decrease behavior with the increase of the E-field both in the negative and positive direction, resulting in a semiconductor-metal transition. Besides, the structure of the heterostructure is very robust under different E-field, revealing a great potential application for the field-effect transistor. For mechanical strain, all the heterostructures show elastic deformation within the range of -10% to 10% under uniaxial and biaxial strain. With the increase of compressive strain, the band gap first increases and then decreases. While the relationship between the band gap and tensile strain is a linear function. Moreover, we find that the heterostructure exhibits much broad spectral responsivity (from visible light

to deep UV light) and more pronounced optical absorption than WS<sub>2</sub> and IGZO monolayers. Also, the optical properties of the heterostructure can be enhanced obviously under an external strain. The tensile strain can weaken the photoresponse of the heterostructure to the UV light and improve the response for the visible light, while for compressive strain, the heterostructure shows a strong absorption peak in UV light. Besides, a red-shift is observed when the external strain exists. The unique and tunable properties endow that the WS<sub>2</sub>/IGZO heterostructure is a good candidate for nanoelectronic and photoelectronic devices, such as FETs, flexible devices, sensors, photocatalysis, and photonic devices.

Based on the DFT simulation results, CVD-WS<sub>2</sub>/IGZO heterojunction-based devices were fabricated, and their gas sensing performances were investigated in two modes, chemiresistor and transistor mode. The as-fabricated gas sensor has a maximum response of 18170% on the chemiresistor mode, and 499400% on the TFT mode under 300 ppm NO<sub>2</sub> after applying -20 V gate bias. It is much better than that of only WS<sub>2</sub> and IGZO. Moreover, the sensor shows excellent gas selectivity toward NO<sub>2</sub> with comparison to several gas vapors such as CO, NH<sub>3</sub>, and humidity. The superior gas sensing performance could benefit from the heterojunction of WS<sub>2</sub> and IGZO and the external electric field under the back gate voltage. Besides, the transistor notably presents a typical ambipolar-behaviour under dry air, while the transistor becomes p-type as the amount of NO<sub>2</sub> increases. The mobility, on/off ratio, and the NO<sub>2</sub> gas concentration modulates the subthreshold slope of the device. The unique tunable behaviour can be associated with the doping effects of NO<sub>2</sub> on the heterojunction and the modulated Schottky barrier value at the WS<sub>2</sub> and IGZO with a metal contact interface. Consequently, the WS<sub>2</sub>/IGZO-based device is a potential candidate for the NO<sub>2</sub> gas sensor and tunable engineering application.

However, some issues need to be studied in our future work: (1) It needs to quantitatively analyze the effects of the Schottky barrier and doping of gas molecules. Thus we need to separate the sensing area into two parts, one part will be covered with PMMA in the contact region of metal/heterojunction, and the other one will be only covered with PMMA in the heterojunction; (2) the device has long recovery time which needs to be improved for future work, such as attaching functional groups or applying UV illumination; (3) the long-term response stability is essential for practical application, which we will deeply study in our future works.

## REFERENCES

- [1] Jake D Mehew, Selim Unal, Elias Torres Alonso, Gareth J F Jones, Saad Fadhil Ramadhan, Monica F Craciun, and Saverio Russo. Fast and highly sensitive ionic-polymer-gated WS<sub>2</sub>-graphene photodetectors. *Advanced Materials*, 29(23):1700222, 2017.
- [2] Guichao Wang, Liang Li, Weihao Fan, Renyan Wang, Shasha Zhou, Jing-Tao Lu, Lin Gan, and Tianyou Zhai. Interlayer coupling induced infrared response in WS<sub>2</sub>/MoS<sub>2</sub> heterostructures enhanced by surface plasmon resonance. *Advanced Functional Materials*, 28(22):1800339, 2018.
- [3] Kyunghnam Kang, Kyle Godin, Young Duck Kim, Shichen Fu, Wujoon Cha, James Hone, and Eui-Hyeok Yang. Graphene-assisted antioxidation of tungsten disulfide monolayers: Substrate and electric-field effect. *Advanced Materials*, 29(18):1603898, 2017.
- [4] Tingting Xu, Yunyun Liu, Yongyong Pei, Yunpeng Chen, Zimin Jiang, Zhifeng Shi, Junmin

- Xu, Di Wu, Yongtao Tian, and Xinjian Li. The ultra-high NO<sub>2</sub> response of ultra-thin WS<sub>2</sub> nanosheets synthesized by hydrothermal and calcination processes. *Sensors and Actuators B: Chemical*, 259:789–796, 2018.
- [5] Diyu Fu, Chunling Zhu, Xitian Zhang, Chunyan Li, and Yujin Chen. Two-dimensional net-like SnO<sub>2</sub>/ZnO heteronanostructures for high-performance H<sub>2</sub>S gas sensor. *Journal of Materials Chemistry A*, 4(4):1390–1398, 2016.
- [6] Longtao Ma, Huiqing Fan, Hailin Tian, Jiawen Fang, and Xuezhu Qian. The n-ZnO/n-In<sub>2</sub>O<sub>3</sub> heterojunction formed by a surface-modification and their potential barrier-control in methanal gas sensing. *Sensors and Actuators B: Chemical*, 222:508–516, 2016.
- [7] Xiaoyang Zhu, Nicholas R. Monahan, Zizhou Gong, Haiming Zhu, Kristopher W. Williams, and Cory A. Nelson. Charge transfer excitons at van der waals interfaces. *Journal of the American Chemical Society*, 137(26):8313–8320, 2015.
- [8] Shufen Zhao, Guojing Wang, Jiecuai Liao, Shasha Lv, Zhenan Zhu, and Zhengcao Li. Vertically aligned MoS<sub>2</sub>/ZnO nanowires nanostructures with highly enhanced NO<sub>2</sub> sensing activities. *Applied Surface Science*, 456:808–816, 2018.
- [9] F. Perrozzi, S. M. Emamjomeh, V. Paolucci, G. Taglieri, L. Ottaviano, and C. Cantalini. Thermal stability of WS<sub>2</sub> flakes and gas sensing properties of WS<sub>2</sub>/WO<sub>3</sub> composite to H<sub>2</sub>, NH<sub>3</sub> and NO<sub>2</sub>. *Sensors and Actuators B: Chemical*, 243:812–822, 2017.
- [10] Yutong Han, Yujie Ma, Yang Liu, Shusheng Xu, Xinwei Chen, Min Zeng, Nantao Hu, Yanjie Su, Zhihua Zhou, and Zhi Yang. Construction of MoS<sub>2</sub>/SnO<sub>2</sub> heterostructures for sensitive NO<sub>2</sub> detection at room temperature. *Applied Surface Science*, 493:613–619, 2019.
- [11] Yutong Han, Da Huang, Yujie Ma, Guili He, Jun Hu, Jing Zhang, Nantao Hu, Yanjie Su, Zhihua Zhou, Yafei Zhang, and Zhi Yang. Design of hetero-nanostructures on MoS<sub>2</sub> nanosheets to boost NO<sub>2</sub> room-temperature sensing. *ACS Applied Materials & Interfaces*, 10(26):22640–22649, 2018.
- [12] Dong Hun Kim, Seung-Hoon Choi, Nam Gyu Cho, YoungEun Chang, Ho-Gi Kim, Jae-Min Hong, and Il-Doo Kim. High stability InGaZnO<sub>4</sub> thin-film transistors using sputter-deposited PMMA gate insulators and PMMA passivation layers. *Electrochemical Solid-State Letters*, 12(8):H296–H298, 2009.
- [13] Youngho Kang, Sanghyun Lee, Hasung Sim, Chang Hee Sohn, Won Goo Park, Seul Ji Song, Un Ki Kim, Cheol Seong Hwang, Seungwu Han, and Deok-Yong Cho. The impact of orbital hybridization on the electronic structure of crystalline InGaZnO: a new perspective on the compositional dependence. *Journal of Materials Chemistry C*, 2(43):9196–9204, 2014.
- [14] R. A. Rodriguez-Davila, I. Mejia, R. A. Chapman, C. D. Young, and M. Quevedo-Lopez. Performance and reliability comparison of ZnO and IGZO thin-film transistors and inverters fabricated at a maximum process temperature of 115 °C. *IEEE Transactions on Electron Devices*, 66(9):3861–3866, 2019.
- [15] Hiromichi Godo, Daisuke Kawae, Shuhei Yoshitomi, Toshinari Sasaki, Shunichi Ito, Hiroki Ohara, Hideyuki Kishida, Masahiro Takahashi, Akiharu Miyayama, and Shunpei Yamazaki. Temperature dependence of transistor characteristics and electronic structure for amorphous In-Ga-Zn-Oxide thin film transistor. *Japanese Journal of Applied Physics*, 49(3):03CB04, 2010.

- [16] Edgars Butanovs, Sergei Vlassov, Alexei Kuzmin, Sergei Piskunov, Jelena Butikova, and Boris Polyakov. Fast-response single-nanowire photodetector based on ZnO/WS<sub>2</sub> core/shell heterostructures. *ACS Applied Materials & Interfaces*, 10(16):13869–13876, 2018.
- [17] Kyung Su Kim, Cheol Hyoun Ahn, Sung Hyeon Jung, Sung Woon Cho, and Hyung Koun Cho. Toward adequate operation of amorphous oxide thin-film transistors for low-concentration gas detection. *ACS Applied Materials & Interfaces*, 10(12):10185–10193, 2018.
- [18] Stefan Knobelspies, Benedikt Bierer, Alwin Daus, Alain Takabayashi, A. Giovanni Salvatore, Giuseppe Cantarella, Alvaro Ortiz Perez, Jurgen Wollenstein, Stefan Palzer, and Gerhard Troster. Photo-induced room-temperature gas sensing with *a*-IGZO based thin-film transistors fabricated on flexible plastic foil. *Sensors*, 18(2), 2018.
- [19] Nengjie Huo, Shengxue Yang, Zhongming Wei, Shu-Shen Li, Jian-Bai Xia, and Jingbo Li. Photoresponsive and gas sensing field-effect transistors based on multilayer WS<sub>2</sub> nanoflakes. *Scientific Reports*, 4(1):5209, 2014.
- [20] B. Delley. From molecules to solids with the DMol3 approach. *The Journal of Chemical Physics*, 113(18):7756–7764, 2000.
- [21] K. Zheng, Q. Yang, C. J. Tan, H. Y. Ye, and X. P. Chen. A two-dimensional van der waals CdS/germanene heterojunction with promising electronic and optoelectronic properties: DFT + NEGF investigations. *Physical Chemistry Chemical Physics*, 19(28):18330–18337, 2017.
- [22] L. Debbichi, O. Eriksson, and S. Lebegue. Electronic structure of two-dimensional transition metal dichalcogenide bilayers from ab initio theory. *Physical Review B*, 89(20):205311, 2014.
- [23] S J Clark, M D Segall, Chris J Pickard, Phil Hasnip, Matt Probert, Keith Refson, and M C Payne. First principles methods using castep. *Zeitschrift Fur Kristallographie*, 220:567–567, 2005.
- [24] Hideyuki Omura, Hideya Kumomi, Kenji Nomura, Toshio Kamiya, Masahiro Hirano, and Hideo Hosono. First-principles study of native point defects in crystalline indium gallium zinc oxide. *Journal of Applied Physics*, 105(9):093712, 2009.
- [25] N. Gao, J. C. Li, and Q. Jiang. Tunable band gaps in silicene-MoS<sub>2</sub> heterobilayers. *Physical Chemistry Chemical Physics*, 16(23):11673–11678, 2014.
- [26] Ning Lu, Hongyan Guo, Lei Li, Jun Dai, Lu Wang, Wai-Ning Mei, Xiaojun Wu, and Xiao Cheng Zeng. MoS<sub>2</sub>/MX<sub>2</sub> heterobilayers: bandgap engineering via tensile strain or external electrical field. *Nanoscale*, 6(5):2879–2886, 2014.
- [27] Thomas Steiner and Gautam R. Desiraju. Distinction between the weak hydrogen bond and the van der waals interaction. *Chemical Communications*, (8):891–892, 1998.
- [28] Ralph H Petrucci, F Geoffrey Herring, Carey Bissonnette, and Jeffry D Madura. *General chemistry: principles and modern applications*. Pearson, Toronto, 2011.
- [29] Il-Joon Kang and Chul-Hong Park. First-principles study of the electronic structure of single-crystalline InGaZnO<sub>4</sub>. *Journal of the Korean Physical Society*, 56(1):476–479, 2010.
- [30] Huayang Guo, Changyong Lan, Zhifei Zhou, Peihua Sun, Dapeng Wei, and Chun Li. Transparent, flexible, and stretchable WS<sub>2</sub> based humidity sensors for electronic skin. *Nanoscale*, 9(19):6246–6253, 2017.

- [31] S. Lebegue and O. Eriksson. Electronic structure of two-dimensional crystals from ab initio theory. *Physical Review B*, 79(11):115409, 2009.
- [32] Chunjian Tan, Qun Yang, Ruishen Meng, Qihua Liang, Junke Jiang, Xiang Sun, Huaiyu Ye, and X. P. Chen. An AlAs/germanene heterostructure with tunable electronic and optical properties via external electric field and strain. *Journal of Materials Chemistry C*, 4(35):8171–8178, 2016.
- [33] Hafiz M. W. Khalil, Muhammad Farooq Khan, Jonghwa Eom, and Hwayong Noh. Highly stable and tunable chemical doping of multilayer WS<sub>2</sub> field effect transistor: Reduction in contact resistance. *ACS Applied Materials & Interfaces*, 7(42):23589–23596, 2015.
- [34] Dattatray J. Late, Yi-Kai Huang, Bin Liu, Jagaran Acharya, Sharmila N. Shirodkar, Jiajun Luo, Aiming Yan, Daniel Charles, Umesh V. Waghmare, Vinayak P. Dravid, and C. N. R. Rao. Sensing behavior of atomically thin-layered MoS<sub>2</sub> transistors. *ACS Nano*, 7(6):4879–4891, 2013.
- [35] Harald Friedrich and H Friedrich. *Theoretical atomic physics*, volume 2. Springer, Switzerland, fourth edition edition, 2017.
- [36] Keliang He, Charles Poole, Kin Fai Mak, and Jie Shan. Experimental demonstration of continuous electronic structure tuning via strain in atomically thin MoS<sub>2</sub>. *Nano Letters*, 13(6):2931–2936, 2013.
- [37] Liangzhi Kou, Aijun Du, Changfeng Chen, and Thomas Frauenheim. Strain engineering of selective chemical adsorption on monolayer MoS<sub>2</sub>. *Nanoscale*, 6(10):5156–5161, 2014.
- [38] Vitor M. Pereira and A. H. Castro Neto. Strain engineering of graphene’s electronic structure. *Physical Review Letters*, 103(4):046801, 2009.
- [39] Shengxue Yang, Cong Wang, Hasan Sahin, Hui Chen, Yan Li, Shu-Shen Li, Aslihan Suslu, Francois M. Peeters, Qian Liu, Jingbo Li, and Sefaattin Tongay. Tuning the optical, magnetic, and electrical properties of ReSe<sub>2</sub> by nanoscale strain engineering. *Nano Letters*, 15(3):1660–1666, 2015.
- [40] H. Sahin and F. M. Peeters. Adsorption of alkali, alkaline-earth, and 3D transition metal atoms on silicene. *Physical Review B*, 87(8):085423, 2013.
- [41] Jian-wei Wei, Zeng-wei Ma, Hui Zeng, Zhi-yong Wang, Qiang Wei, and Ping Peng. Electronic and optical properties of vacancy-doped WS<sub>2</sub> monolayers. *AIP Advances*, 2(4):042141, 2012.
- [42] Min Su Kim, Shrawan Roy, Jubok Lee, Byung Gu Kim, Hyun Kim, Ji-Hoon Park, Seok Joon Yun, Gang Hee Han, Jae-Young Leem, and Jeongyong Kim. Enhanced light emission from monolayer semiconductors by forming heterostructures with ZnO thin films. *ACS Applied Materials & Interfaces*, 8(42):28809–28815, 2016.
- [43] Changyong Lan, Chun Li, Shuai Wang, Yi Yin, Huayang Guo, Nishuang Liu, and Yong Liu. ZnO-WS<sub>2</sub> heterostructures for enhanced ultra-violet photodetectors. *RSC Advances*, 6(72):67520–67524, 2016.
- [44] F. L. Hirshfeld. Bonded-atom fragments for describing molecular charge densities. *Theoretica chimica acta*, 44(2):129–138, 1977.
- [45] Sajedeheh Manzeli, Dmitry Ovchinnikov, Diego Pasquier, Oleg V. Yazyev, and Andras Kis. 2D transition metal dichalcogenides. *Nature Reviews Materials*, 2:17033, 2017.

- [46] Young Jun Tak, Dong Jun Kim, Won-Gi Kim, Jin Hyeok Lee, Si Joon Kim, Jong Hak Kim, and Hyun Jae Kim. Boosting visible light absorption of metal-oxide-based phototransistors via heterogeneous In-Ga-Zn-O and  $\text{CH}_3\text{NH}_3\text{PbI}_3$  films. *ACS Applied Materials & Interfaces*, 10(15):12854–12861, 2018.
- [47] D Tonti, F Varsano, F Decker, C Ballif, M Regula, and M Rem?kar. Preparation and photoelectrochemistry of semiconducting  $\text{WS}_2$  thin films. *The Journal of Physical Chemistry B*, 101(14):2485–2490, 1997.
- [48] J. Jebaraj Devadasan, C. Sanjeeviraja, and M. Jayachandran. Electrodeposition of p- $\text{WS}_2$  thin film and characterisation. *Journal of Crystal Growth*, 226(1):67–72, 2001.
- [49] Jin-Seong Park, Jae Kyeong Jeong, Hyun-Joong Chung, Yeon-Gon Mo, and Hye Dong Kim. Electronic transport properties of amorphous indium-gallium-zinc oxide semiconductor upon exposure to water. *Applied Physics Letters*, 92(7):072104, 2008.
- [50] Jaehyun Yang, Hyena Kwak, Youngbin Lee, Yu-Seon Kang, Mann-Ho Cho, Jeong Ho Cho, Yong-Hoon Kim, Seong-Jun Jeong, Seongjun Park, Hoo-Jeong Lee, and Hyoungsub Kim.  $\text{MoS}_2$ -InGaZnO heterojunction phototransistors with broad spectral responsivity. *ACS Applied Materials & Interfaces*, 8(13):8576–8582, 2016.
- [51] Sung Hee Lim, Joohee Kim, Sang-gi Lee, and Youn Sang Kim. Water-soluble polymer dielectric with potential for high performance organic thin-film transistors. *Chemical Communications*, 46(22):3961–3963, 2010.
- [52] Kyung Yong Ko, Jeong-Gyu Song, Youngjun Kim, Taejin Choi, Sera Shin, Chang Wan Lee, Kyounghoon Lee, Jahyun Koo, Hoonkyung Lee, Jongbaeg Kim, Taeyoon Lee, Jusang Park, and Hyungjun Kim. Improvement of gas-sensing performance of large-area tungsten disulfide nanosheets by surface functionalization. *ACS Nano*, 10(10):9287–9296, 2016.
- [53] Herbert Freundlich. *Kapillarchemie, eine Darstellung der Chemie der Kolloide und verwandter Gebiete, von Dr. Herbert Freundlich*. akademische Verlagsgesellschaft, 1909.
- [54] Sunghoon Park, Soyeon An, Youngho Mun, and Chongmu Lee. UV-enhanced  $\text{NO}_2$  gas sensing properties of  $\text{SnO}_2$ -core/ $\text{ZnO}$ -shell nanowires at room temperature. *ACS Applied Materials & Interfaces*, 5(10):4285–4292, 2013.
- [55] Hiroshi Tabata, Yuta Sato, Kouhei Oi, Osamu Kubo, and Mitsuhiro Katayama. Bias- and gate-tunable gas sensor response originating from modulation in the schottky barrier height of a graphene/ $\text{MoS}_2$  van der waals heterojunction. *ACS Applied Materials & Interfaces*, 10(44):38387–38393, 2018.
- [56] Yutong Han, Yang Liu, Chen Su, Shutang Wang, Hong Li, Min Zeng, Nantao Hu, Yanjie Su, Zhihua Zhou, Hao Wei, and Zhi Yang. Interface engineered  $\text{WS}_2/\text{ZnS}$  heterostructures for sensitive and reversible  $\text{NO}_2$  room temperature sensing. *Sensors and Actuators B: Chemical*, 296:126666, 2019.
- [57] Bilu Liu, Liang Chen, Gang Liu, Ahmad N. Abbas, Mohammad Fathi, and Chongwu Zhou. High-performance chemical sensing using schottky-contacted chemical vapor deposition grown monolayer  $\text{MoS}_2$  transistors. *ACS Nano*, 8(5):5304–5314, 2014.
- [58] Dae Jin Yang, George C. Whitfield, Nam Gyu Cho, Pyeong-Seok Cho, Il-Doo Kim, Howard M. Saltsburg, and Harry L. Tuller. Amorphous InGaZnO<sub>4</sub> films: Gas sensor response and stability. *Sensors and Actuators B: Chemical*, 171-172:1166–1171, 2012.

- [59] Pallab Bhattacharya and Lily Y Pang. *Semiconductor optoelectronic devices*, volume 613. prentice hall Upper Saddle River, NJ, 1997.
- [60] Yonghui Deng. *Semiconducting Metal Oxides for Gas Sensing*. Springer, 2019.
- [61] Nengjie Huo, Juehan Yang, Le Huang, Zhongming Wei, Shushen Li, Suhuai Wei, and Jingbo Li. Tunable polarity behavior and self-driven photoswitching in p-WSe<sub>2</sub>/n-WS<sub>2</sub> heterojunctions. *Small*, 11(40):5430–5438, 2015.
- [62] Hongyu Tang, Chunjian Tan, Huiru Yang, Kai Zheng, Yutao Li, Huaiyu Ye, Xianping Chen, Xuejun Fan, Tianling Ren, and Guoqi Zhang. Tunable electronic and optical properties of the WS<sub>2</sub>/IGZO heterostructure via an external electric field and strain: a theoretical study. *Physical Chemistry Chemical Physics*, 21(27):14713–14721, 2019.
- [63] Karlheinz Seeger. *Semiconductor physics*. Springer Science & Business Media, 2013.
- [64] Xiong-Yi Liang, Ning Ding, Siu-Pang Ng, and Chi-Man Lawrence Wu. Adsorption of gas molecules on Ga-doped graphene and effect of applied electric field: A DFT study. *Applied Surface Science*, 411:11–17, 2017.
- [65] Hai Li, Zongyou Yin, Qiyuan He, Hong Li, Xiao Huang, Gang Lu, Derrick Wen Hui Fam, Alfred Iing Yoong Tok, Qing Zhang, and Hua Zhang. Fabrication of single- and multilayer MoS<sub>2</sub> film-based field-effect transistors for sensing NO at room temperature. *Small*, 8(1):63–67, 2012.
- [66] Jing Kong, Nathan R. Franklin, Chongwu Zhou, Michael G. Chapline, Shu Peng, Kyeongjae Cho, and Hongjie Dai. Nanotube molecular wires as chemical sensors. *Science*, 287(5453):622, 2000.
- [67] Suhyun Kim, Geonyeop Lee, and Jihyun Kim. Chemical doping effects of gas molecules on black phosphorus field-effect transistors. *ECS Journal of Solid State Science and Technology*, 7(7):Q3065–Q3069, 2018.
- [68] S. Auvray, J. Borghetti, M. F. Goffman, A. Filoramo, V. Derycke, J. P. Bourgoin, and O. Jost. Carbon nanotube transistor optimization by chemical control of the nanotube-metal interface. *Applied Physics Letters*, 84(25):5106–5108, 2004.
- [69] Paolo Bondavalli, Pierre Legagneux, and Didier Pribat. Carbon nanotubes based transistors as gas sensors: State of the art and critical review. *Sensors and Actuators B: Chemical*, 140(1):304–318, 2009.

# 6

## CONCLUSION AND RECOMMENDATION

### CONCLUSION

The aim of my research for the last four years was to explore a high-performance gas sensor for detecting the changes in the environment (air pollutions, humidity). In this section, I summarize the key findings of this thesis.

**Chapter 2** describes the state-of-the-art of metal sulfide-based gas sensor, including the basic crystal structures, synthesis methods, devices fabrication methods, and the gas sensing performances of various types of metal sulfides-based sensor. Metal sulfides have great potential in gas sensing because they often have a shallow valence band and different shapes, sizes, crystalline forms, and chemical compositions. After comparing gas sensing performance of various metal sulfides-based gas sensors, it is found that the devices based on Schottky diode, metal oxide/metal sulfide heterojunction, and transistor have enhanced gas-sensing performance. Thus in this work, I analyzed the sensing behaviour of SnS-Ti Schottky contact humidity sensor and used SnO<sub>x</sub>/SnS heterostructures with rich OV<sub>s</sub> to increase the NO<sub>2</sub> sensing response and decrease the LOD. Finally, a WS<sub>2</sub>/IGZO heterojunction-based thin film transistor is proposed to improve the NO<sub>2</sub> gas sensing performance.

**Chapter 3** describes our effort in the humidity sensing behaviours of Schottky-contacted SnS nanoflakes-based sensors. We employ a mechanical exfoliation method to obtain SnS nanoflakes and use dry-transferring and photolithography process to fabricate the sensors on the rigid and flexible substrate. The as-fabricated sensor exhibited good body temperature moisture sensing performance with a high response of 67600% under 10% RH and 2491000% under 99% RH, wide RH range from 3% RH to 99% RH, and fast response/recovery time of 6 s /4 s, competing with tin-based and TMDs-based humidity sensors. The density functional theory (DFT) analysis results suggest that the adsorption of H<sub>2</sub>O on SnS produces relatively larger binding energies (-0.388 eV) with charge transfer of -0.055 eV than other gas molecules in the air. The fast response and recovery performances

result from the Schottky nature of SnS-Ti contact. H<sub>2</sub>O absorption moves the Fermi level of SnS toward the conduction band, decreasing the Schottky barrier ( $\phi_B$ ) by  $\Delta\phi_B$ , resulting in thinning of the  $\phi_B$  and an increase of the device current. Different RH levels induce different  $\Delta\phi_B$  and sensitivity. The recovery mechanism is also attributed to the  $\phi_B$ . When air flows out of the chamber, the water molecule shift from the adsorption sites, and the conductivity decreases due to the increased  $\phi_B$ . More importantly, its wide RH range, fast response time, and excellent biocompatibility enable real-time monitoring of finger touch without contact and different breathing patterns. Finally, we propose a smart home system based on the sensors to process the signal from breath and finger touch experiments for noncontact controlling and respiration monitoring, which presents intelligent potential applications for noncontact healthcare monitoring.

To further improve the gas sensing performance, such as the limit of detection (LOD) and response for NO<sub>2</sub> gas, in the **Chapter 4** we explore the SnO<sub>x</sub>/SnS heterostructures with large surface area and rich OV. They were synthesized by the post-oxidation of LPE-SnS nanosheets in the air at 350 °C. To accelerate recovery time, UV illumination is applied during the recovery process. The SnO<sub>x</sub>/SnS-based sensor exhibits excellent sensing performance with high response of 161% at 1 ppb and 2952% at 1 ppm NO<sub>2</sub> gas concentration, respectively, excellent repeatability, ultra-low theoretical LOD of 5 ppt, and a wide detecting range from 1 ppb to 1 ppm. The heterostructures with OVs contribute a significant response to the gas molecules due to a large number of adsorption sites, band gap modulation, and active electrons transfer in the sensing interface layer. The DFT results show that there is few-electron sharing between NO<sub>2</sub> gas molecules and heterojunction, which proves a chemical adsorption nature powerfully. Thus the sensor can detect low concentration NO<sub>2</sub> gas molecules. However, due to the chemisorption nature, the desorption of NO<sub>2</sub> gas molecule is difficult, which needs UV illumination to accelerate recovery time. Both experimental and DFT simulation results support that these factors conduce to the superior gas sensing properties in terms of higher sensitivity and ultra-low theoretical LOD toward ppt-level NO<sub>2</sub> at room operation temperature.

The third way of increasing NO<sub>2</sub> gas sensing response is based on the FET device. In section 1 of **Chapter 5**, we studied the structural, electronic, and optical properties of WS<sub>2</sub>/IGZO heterostructure by DFT calculation. The results demonstrate that the band gap of WS<sub>2</sub>/IGZO heterostructure shows a near-linear decrease behavior with the increase of the E-field both in the negative and positive direction, resulting in a semiconductor-metal transition, revealing a great potential application for the field-effect transistor. The heterostructure exhibits much broad spectral responsivity (from visible light to deep UV light) and more pronounced optical absorption than WS<sub>2</sub> and IGZO monolayers. The heterostructures show elastic deformation within the range of -10 to 10% both under uniaxial and biaxial strain, and their optical properties can be enhanced obviously under an external strain. The tensile strain can weaken the photoresponse of the heterostructure to the UV light and improve the response for the visible light, while for compressive strain, the heterostructure shows a strong absorption peak in UV light. Moreover, the gas adsorption energy of NH<sub>3</sub> and NO<sub>2</sub> on the WS<sub>2</sub>/IGZO heterostructure were calculated, which shows high gas adsorption energy with NO<sub>2</sub>, indicating the potential application in NO<sub>2</sub> gas sensor.

The unique and tunable properties based on DFT calculation endow that the WS<sub>2</sub>/IGZO heterostructure is a good candidate for nanoelectronic and photoelectronic devices, such as

FETs, flexible devices, sensors, photocatalysis, and photonic devices. Thus, we fabricate CVD-WS<sub>2</sub>/IGZO heterojunction-based devices in the second section of **Chapter 5**. The as-fabricated gas sensor is investigated in two modes, chemiresistor, and transistor mode. It has a maximum response of 18170% on the chemiresistor mode, and 499400% on the transistor mode under 300 ppm NO<sub>2</sub> after applying -20 V gate bias. It is much better than that of only WS<sub>2</sub> and IGZO. Moreover, the sensor shows excellent gas selectivity toward NO<sub>2</sub> with comparison to several gas vapors such as CO, NH<sub>3</sub>, and humidity. The superior gas sensing performance could benefit from the heterojunction of WS<sub>2</sub> and IGZO and the external electric field under the back gate voltage. Besides, the transistor notably presents a typical ambipolar-behaviour under dry air, while the transistor becomes p-type as the amount of NO<sub>2</sub> increases. The mobility, on/off ratio, and the NO<sub>2</sub> gas concentration modulates the subthreshold slope of the device. The unique tunable behaviour can be associated with the doping effects of NO<sub>2</sub> on the heterojunction and the modulated Schottky barrier value at the WS<sub>2</sub> and IGZO with a metal contact interface. Consequently, the WS<sub>2</sub>/IGZO-based device is a potential candidate for the NO<sub>2</sub> gas sensor and tunable engineering application. However, some issues need to be studied in our future work: (1) It needs to quantitatively analyze the effects of the Schottky barrier and doping of gas molecules. Thus we need to separate the sensing area into two parts, one part will be covered with PMMA in the contact region of metal/heterojunction, and the other one will be only covered with PMMA in the heterojunction; (2) the device has long recovery time which needs to be improved for future work, such as attaching functional groups or applying UV illumination; (3) the long-term response stability is important for practical application, which we will deeply study in our future works.

From the results in this thesis, I conclude that metal sulfide-based heterostructures are an excellent candidate for gas sensing applications. Build up semiconductor-metal Schottky junction, p-N heterojunction, oxygen-rich heterostructures, and the transistor can significantly improve the gas sensing performances.

## RECOMMENDATIONS IN FUTURE WORKS

Even though the results reported in this work are encouraging, there are lots of shortcomings to be improved in our future works.

1. New nanomaterials are emerging, and different material properties can be obtained by combining different types of materials with building various heterostructures. However, there are also problems such as lattice mismatch, interface stress, and band bending. It is not yet possible to determine what impact these problems will have on the final device characteristics, but it is necessary to start with material preparation, interface science, and combine material design with simulation.

2. The matching between materials and circuit electrodes, such as energy band and work function, needs to be considered in terms of device design. At the same time, applications such as low energy consumption and flexibility need to be considered.

3. At present, gas sensors still have reliability and stability problems, which are related to the characteristics of nanomaterials. Therefore, in the future, it is necessary to protect the surface of nanomaterials by designing materials, such as adding a passivation layer or a non-oxidizable layer, to enhance device stability and long-term reliability.

4. TFT devices can effectively improve gas sensing performance, but in the future, it

is necessary to control their energy consumption and turn-on voltage reasonably. Device performance can be enhanced by designing the device structure (shape and size of gate-drain electrodes), selecting the dielectric layer, and selecting the substrate. Some metal sulfides (such as MoS<sub>2</sub>, WS<sub>2</sub>) could play an important role in electronics for logic, memory, and connections, enabling the extension for Moore's law,[1] even More than Moore.[2, 3] There are mainly three challenges for these materials to meet industry needs in practical devices, such as the accuracy of predicting properties, the methods of growing and testing high-quality materials, and the assessment of the device's performance.

5. In the future, the application of new nanomaterial devices still has a long way to go. For example, the current of the metal sulfide device is too small, and it is necessary to implement signal acquisition and intelligent control through a precise amplifier circuit. Defective materials are difficult to desorb, and additional UV light sources are needed to achieve rapid desorption, increasing the overall size and cost of the device.

## REFERENCES

- [1] Ming-Yang Li, Sheng-Kai Su, H. S. Philip Wong, and Lain-Jong Li. How 2D semiconductors could extend Moore's law. *Nature*, 567:169–170, 2019.
- [2] G. Q. Zhang, M. Graef, and F. van Roosmalen. Strategic research agenda of "More than Moore". In *EuroSime 2006 - 7th International Conference on Thermal, Mechanical and Multiphysics Simulation and Experiments in Micro-Electronics and Micro-Systems*, pages 1–6, 2006.
- [3] Guo Qi Zhang and Alfred van Roosmalen. *More than Moore: creating high value micro/nanoelectronics systems*. Springer Science Business Media, 2010.

# A

## APPENDIX A

### A.1. CALCULATION METHODS

The calculation procedure of LOD:

1. Perform linear fitting for the response versus NO<sub>2</sub> concentration curve of the SnO<sub>x</sub>/SnS heterostructure-based gas sensor, followed by obtaining the slope and standard error in the linear region.

2. Plot the response  $\Delta R/R$  or  $\Delta I/I$  as a function of time (sec) at the baseline before NO<sub>2</sub> exposure, followed by executing polynomial fit (5th order) .

3. Extract N = 10 data points at the baseline before NO<sub>2</sub> exposure ( $Y_i$ ).

4. Calculate statistical parameters and regular residual ( $Y_i - \bar{Y}$ ) of 5th order polynomial fit and the root-mean squared deviation (RMS<sub>noise</sub>) and LOD using Equations (1) and (2).

$$\text{RMS}_{\text{noise}}(\text{ppb} - 1) = (V_x^2/(N))^{1/2} \quad (\text{A.1})$$

$$V_x^2 = \Sigma(Y_i - \bar{Y})^2 \quad (\text{A.2})$$

$$\text{LOD}(\text{ppb}) = 3\text{RMS}_{\text{noise}}/\text{Slope} \quad (\text{A.3})$$

## A.2. DATA OF LOD CALCULATION FOR $\text{SnO}_x/\text{SnS}$ SENSOR

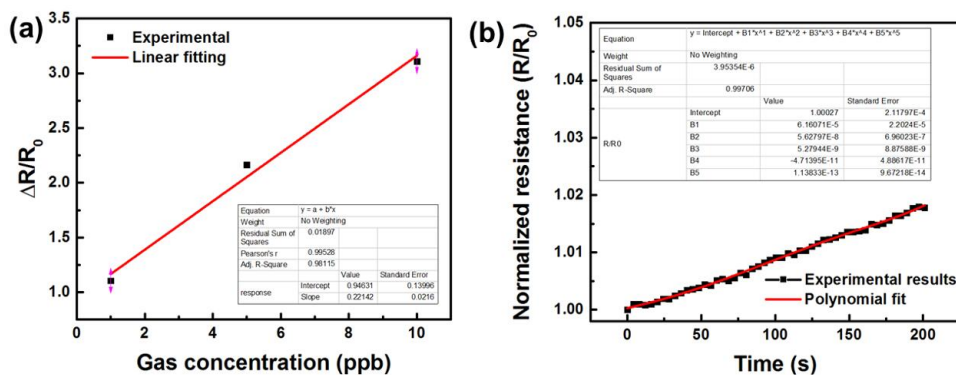


Figure A.1: Fitted response of the  $\text{SnO}_x/\text{SnS}$  sensor to  $\text{NO}_2$ . (a) Plots of response as a function of  $\text{NO}_2$  concentration. (b) Plots of 5th order polynomial fitted normalized resistance at the baseline before  $\text{NO}_2$  exposure as a function of time.

Table A.1: Polynomial fitting data of the  $\text{SnO}_x/\text{SnS}$  gas sensor.

Time (s)	$Y_i - \bar{Y}$	$(Y_i - \bar{Y})^2$
20	-1.766E-04	3.119E-08
40	3.464E-04	1.200E-07
60	3.130E-04	9.796E-08
80	-7.007E-04	4.910E-07
100	3.737E-04	1.397E-07
120	-4.423E-04	1.957E-07
140	3.864E-05	1.493E-09
160	-4.176E-04	1.744E-07
180	3.117E-04	9.717E-08
200	-4.139E-04	1.713E-07

Table A.2: Calculation of  $\text{RMS}_{\text{noise}}$  and LOD of the  $\text{SnO}_x/\text{SnS}$  gas sensor.

Sensing gas	Slope (%)	(Response) Standard error (ppb-1)	$V_x^2$	$\text{RMS}_{\text{noise}}$	LOD (ppt)
$\text{NO}_2$	0.22	0.0216	1.52E-06	0.39E-03	0.005 ( $\approx 5$ ppt)

### A.3. DATA OF LOD CALCULATION FOR WS<sub>2</sub>/IGZO GAS SENSOR

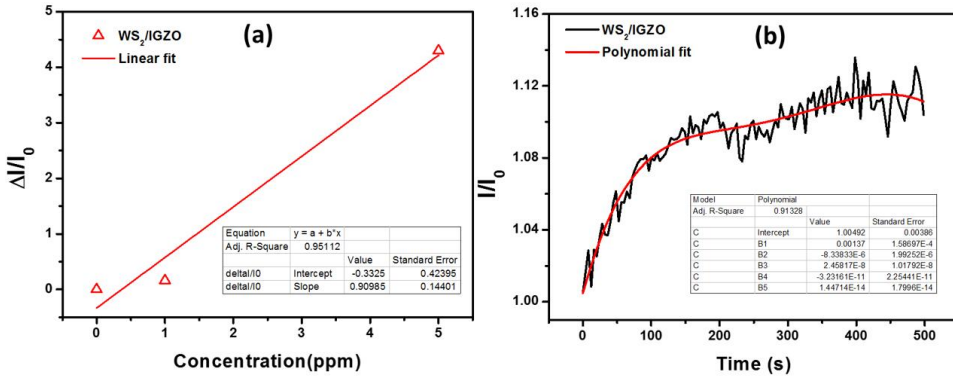


Figure A.2: Fitted response of the WS<sub>2</sub>/IGZO LOD sensor to NO<sub>2</sub>. (a) Plots of response as a function of NO<sub>2</sub> concentration. (b) Plots of 5th order polynomial fitted normalized resistance at the baseline before NO<sub>2</sub> exposure as a function of time.

Table A.3: Polynomial fitting data of WS<sub>2</sub>/IGZO gas sensor.

Time (s)	$Y_i - \bar{Y}$	$(Y_i - \bar{Y})^2$
50	7.200E-03	5.184E-05
100	-1.800E-04	3.239E-08
150	4.180E-03	1.747E-05
200	1.320E-03	1.742E-06
250	2.110E-03	4.452E-06
300	-1.580E-03	2.496E-06
350	9.150E-03	8.372E-05
400	2.261E-02	5.112E-04
450	-5.740E-03	3.295E-05
500	-7.490E-03	5.610E-05

Table A.4: Calculation of RMS<sub>noise</sub> and LOD of WS<sub>2</sub>/IGZO gas sensor.

Sensing gas	Slope (%)	(Response) (ppb-1) Standard error (ppb-1)	$V_x^2$	RMS <sub>noise</sub>	LOD (ppb)
NO <sub>2</sub>	0.90985	0.14401	7.620E-4	8.729E-3	29



# ACKNOWLEDGEMENTS

My dissertation was completed in June 2020. Writing this final part of my dissertation, I realize this could never happen without the full support and concerted efforts of all crew members.

First of all, I would like to express my deepest appreciation to my promoter Prof. dr. Guoqi Zhang for the continuous support of my Ph.D. study and related research, for his patience, motivation, and immense knowledge. You gave me a precious opportunity to enroll in the Ph.D. program in Beijing Research Center (BRC). Working with all the talented peers in this group, I can easily find everything I need to do world-class science. Your constant passion and wisdom inspire us to explore breakthroughs in microelectronics. Expanding the concept of “More than Moore” proposed by Kouchi and Alred is my research target for the novel 2D materials-based devices. Thanks to his extensive networking efforts to ensure collaboration with universities and research institutes, I could work in several locations across China (Beijing, Changzhou, Nanjing, Chongqing, and Shenzhen). I could not have imagined having a more insightful promoter for Ph.D. study.

I would like to dedicate my sincere gratitude to Prof. Huaiyu Ye, my daily supervisor. He has always been by my side, answering my questions in detail. Thanks for your innumerable long phone discussion for my working progress and plan. When I decided to change my research topic after two years of PhD study, he fully understood and supported me with no hesitation. Without the technical and financial support from his group, it would be hard to conduct this research. Thanks for trusting me that I can finish my project, and also thanks for the students in his group, Qipeng Liu, Huiru Yang, Chenshan Gao, Yang Liu, Quan Zhou, Lian Liu, and Fafei Hu, for teaching me first principle analysis and tasting the “hot” Chongqing cuisine.

My sincere thanks go to Prof. Xuejun Fan, who is a rigorous and obliging researcher. He is always available for discussion regardless of time, location, and distance. Without your word-by-word revision of my manuscript and your valuable comments, it would not have been possible to publish a decent journal paper and this dissertation. Besides working, Prof. Fan gave me a lot of precious advice in the aspect of career development and life.

I am grateful to the help of colleagues from ECTM and EKL. Thanks for the guidance of paper writing from Prof. Pasqualina M. Sarro, Dr. Sten Vollebreg, and Dr. Leandro Sacco. Their suggestions on how to improve my manuscripts and abstracts were always valuable. My gratitude also goes out to Hitham Amin Hassan and Robert Verhoeven for the comprehensive training in the lab. Thanks for Drs. Jia Wei, Jiajie Fan, Amir Mirzagheytaghi, and Robert Sokolovskij, who gave me valuable comments on my projects. I owe sincere thankfulness to Dr. Boyao Zhang and Can Han for their advice on my research and selfless help in my life in the Netherlands. Thanks to my colleagues Fengze Hou and Jianwen Sun, it is unforgettable to do our project and revise paper overnight as well as the nice trip in "Nice". Many thanks to Joost Romijn, Joost van Ginkel, and Leo Guo for helping me translate the summary and proposition of this thesis. It was a happy time to watch a volleyball

game, to learn Dutch, and to talk about different interesting topics. It was pleasure work with brilliant colleagues: Jianlin Huang, Mingzhi Dong, Bo Sun, Guangjun Lu, Yuan Gao, Hao Zhang, Chunjian Tan, Yue Sun, Xu Liu, Xueming Li, Hengqian (Daniel) Yi, Zhen Cui, Tianyi Jin, Dong Hu, Jiarui Mo, Manjunath Ramachandrappa Venkatesh, Romina Sattari, Zahra Sheykhifard, Luke Middelburg, Hande Aydogmus, and Milica Dostanic.

I am especially grateful to Mrs. L. Wu, the secretary-general of China SSL Alliance (CSA) and the chairman of the board of China State Key Laboratory of Solid-State Lighting (SKL-SSL), who has been inspiring and stimulating all BRC students to pursue our PhD passion and ambitions. Great appreciations go to all of my colleagues in SKL-SSL, Drs. Changann Yuan, Stanely Leung, Cell Wong, Bob Li, Mingming Wang, and Weiqiao Yang, for their professional support in the laboratory, for their unforgettable training about social skills. Thanks to Dr. Yuan and Leung supporting me a precious opportunity to participate in the Sino-German workshop, which broadened my international horizons and strengthened the confidence for PhD study. It was pleasure work with excellent colleagues: Yanjian Xiong, Lei Li, Min Jia, Liangliang Luo, Yanbin Li, Dehong Wang, Tao Fang, and Yun Li.

I would like to thank Prof. Tianling Ren and his group in Tsinghua University. When I needed the experimental platform the most, he supported me with significant experimental resources. During the one year in his team, I learned various processes in the cleanroom, the mechanical exfoliations of two-dimensional materials, nanodevice fabrication, and measurements. I benefited from his profound knowledge and missionary spirit. My thanks also go to the colleagues in his group, Prof. He Tian, Prof. Yi Yang, Dr. Yuxing Li, Dr. Yu Pang, Dr. Yutao Li, Dr. Jinming Jian, Dr. Jun Ren, Guangyang Gou, Xiangshun Geng, Qi Lu, Tao Tu, Minghao Shao, Linlin Ren, Fan Wu, and other students. They inspired the creativity of my project and gave me lots of hands to my life in Beijing.

I would like to thank Prof. Zuopeng Qu and his group at North China Electric Power University. Thanks for supporting me with the experimental setup for the research of corrosion protection with nanocomposites, and inspired my future career planning. Thanks for the help of Lei Wang, and Shengtian Xu in his group.

Many thanks to Prof. Zeng Haibo and his team at Nanjing University of Science and Technology. I learned the synthesis method of CVD-TMDs and the wet transfer process of 2D materials under the guidance of Prof. Xiufeng Song. Thanks to Prof. Shengli Zhang, Yujie Gao, and Yuan Chen for their help.

Many thanks to Prof. Xianping Chen, Prof. Luqi Tao, and their students at Chongqing University. Zeping Wang, Kai Zheng, Heping Cui, Jing Qian, and Feng Luo, I am honored to have academic exchanges with them.

I would like to thank Prof. Hongyu Yu and his team at the Southern University of Science and Technology for supporting me with some excellent testing platforms. Thanks to Hongze Zheng for his assistance in gas testing.

I would like to thank Weili Yang of Mapu Institute to help me bring some precious 2D materials from China to Germany and then send it to the Netherlands, which is so important for my experiments. And thanks to Anne in TNW of TUDelft for her enthusiastically help for the synthesis of SnS nanosheets.

Many thanks to Prof. Daoguo Yang and Prof. Leo J. Ernst for broadening my research and worldviews. During my master's study, Prof. Yang provided me many opportunities for academic exchange and internship. During my PhD period, he gave me lots of practical

suggestions, which made me be more confident to defend hard topics.

I am thankful for my best friend, Dr. Lei Xie. He always helps me to think about scientific problems and life philosophy in different ways.

I would like to give the greatest thanks to my family. Without their understandings and encouragement, I will not be able to finish my PhD research.



# CURRICULUM VITÆ

## Hongyu TANG

25-08-1987      Born in Guangxi, China.

### EDUCATION

2006–2010      Undergraduate in Microelectronics Manufacturing Engineering  
Guilin University of Electronics Technology

2010–2013      Postgraduate in Mechatronics  
Guilin University of Electronics Technology  
*Thesis:*      Research on Multi-physics Coupling of LED Lumi-  
naire under Temperature and Humidity Environment  
*Supervisor:* Prof. dr. D.G. Yang

2015–2020      PhD in Microelectronics  
Delft University of Technology  
*Thesis:*      Metal sulfides for gas sensing applications: devices  
and mechanisms  
*Promotor:*   Prof. dr. G.Q. Zhang

### AWARDS

2012              Cisco Best Student Paper Award  
the 13th IEEE International Conference on Electronic Packaging Technology  
& High Density Packaging (ICEPT-HDP). Guilin, China

## RESEARCH EXPERIENCE

- 2013–2020      State Key Laboratory of Solid State Lighting, Changzhou, China  
The Sino-German cooperation project:  
Lighting LED beyond conventional: off-grid application
- 2019            North China Electric Power University, Beijing, China  
Anti-corrosion performance of nanocomposites coating
- 2018            Tsinghua University, Beijing, China  
Tunable electronic and optical behaviours of TMDs-based devices
- 2017            Nanjing University of Science and Technology, Nanjing, China  
Synthesis of TMDs materials and 2D materials transferring process

# LIST OF PUBLICATIONS

## JOURNAL PAPERS

13. **H. Tang**, L. Sacco, S. Vollebregt, H. Ye, X. Fan, G. Zhang, *Recent advances in metal sulfide nanomaterials-based gas sensors*, in preparation.
12. **H. Tang**, J. Sun, F. Hou, S. Vollebregt, P. Sarro, X. Fan, G. Zhang, *Recent advance in biosensing technologies for the detection of respiratory virus.*, submitted.
11. **H. Tang**, C. Gao, L. Sacco, R. Sokolovskij, H. Zheng, H. Ye, H. Yu, S. Vollebregt, X. Fan, G. Zhang, *Room temperature ppt-level NO<sub>2</sub> gas sensors based on SnOx/SnS nanostructures.*, submitted.
10. **H. Tang**, Y. Li, R. Sokolovskij, L. Sacco, H. Zheng, H. Ye, H. Yu, X. Fan, T.L. Ren, G. Zhang, *Ultra-high Sensitive NO<sub>2</sub> Gas Sensor based on Tunable Polarity Transport in CVD-WS<sub>2</sub>/IGZO p-N Heterojunction.*, *ACS applied materials & interfaces*, **11**, 43, 2019.
9. **H. Tang**, Y. Li, H. Ye, F. Hu, C. Gao, L. Tao, T. Tao, G. Gou, X. Chen, X. Fan, T.L. Ren, G. Zhang, *High-performance humidity sensor using Schottky-contacted SnS nanoflakes for noncontact healthcare monitoring.*, *Nanotechnology*, **31**, 5, 2019.
8. **H. Tang**, C. Tan, H. Yang, K. Zheng, Y. Li, H. Ye, X. Chen, X. Fan, T.L. Ren, G. Zhang, *Tunable electronic and optical properties of the WS<sub>2</sub>/IGZO heterostructure via an external electric field and strain: a theoretical study.*, *Physical Chemistry Chemical Physics*, **21**, 27, 2019.
7. **H. Tang**, Z. Qu, Z. Wang, H. Ye, X. Fan, G. Zhang, *Liquid-phase exfoliated SnS as a semiconductor coating filler to enhance corrosion protection performance.*, *Physical Chemistry Chemical Physics*, **21**, 33, 2019.
6. Z. Qu,\* Z. Wang,\* **H. Tang**,\* H. Ye, M. Li, *Effect of Nano-SnS and Nano-MoS<sub>2</sub> on the Corrosion Protection Performance of the Polyvinylbutyral and Zinc-Rich Polyvinylbutyral Coatings.*, *Nanomaterials*, **9**, 7, 2019.
5. C. Qian, A.M. Gheitaghy, J. Fan, **H. Tang**, B. Sun, H. Ye, G. Zhang, *Thermal management on IGBT power electronic devices and modules.*, *IEEE Access*, **6**, 2018.
4. H. Ye, F. Hu, **H. Tang**, L. Yang, X. Chen, L. Wang, G. Zhang, *Germanene on single-layer ZnSe substrate: novel electronic and optical properties.*, *Physical Chemistry Chemical Physics*, **23**, 2018.
3. **H. Tang**, H. Ye, C.K. Wong, S.Y. Leung, J. Fan, X. Chen, X. Fan, G. Zhang, *Overdriving reliability of chip scale packaged LEDs: Quantitatively analyzing the impact of component.*, *Microelectronics Reliability*, **78**, 2017.
2. **H. Tang**, H. Ye, X. Chen, C. Qian, X. Fan, G. Zhang, *Numerical thermal analysis and optimization of multi-chip LED module using response surface methodology and genetic algorithm.*, *IEEE Access*, **5**, 2017.

1. F. Hu, **H. Tang**, C. Tan, H. Ye, X. Chen, G. Zhang, *Nitrogen dioxide gas sensor based on monolayer SnS: A first-principle study.*, *IEEE Electron Device Letters*, **38**, 7, 2017.

## CONFERENCE PAPERS

4. Z. Qu,\* **H. Tang**,\* H. Ye, X. Fan, G. Zhang, *Electrical and optical characterization of MoS<sub>2</sub> thin film transistors and the effect of strain on their performances*, In 2019 20th International Conference on Thermal, Mechanical and Multi-Physics Simulation and Experiments in Microelectronics and Microsystems (EuroSimE), Hannover, Germany, March, 2019..
3. F. Hu, **H. Tang**, H. Ye, X. Chen, *Modulation of Gas Adsorption on SnS by strain.*, In 2018 19th International Conference on Electronic Packaging Technology (ICEPT), Shanghai, China, August, 2018..
2. **H. Tang**, H. Ye, X. Chen, X. Fan, G. Zhang, *Thermal conductivity of functionalized graphene-polymer nanocomposite: A non-equilibrium molecular dynamics study.*, In 2017 18th International Conference on Thermal, Mechanical and Multi-Physics Simulation and Experiments in Microelectronics and Microsystems (EuroSimE), Dresden, Germany, April, 2017..
1. **H. Tang**, H. Ye, M. Wang, X. Fan, G. Zhang, *Thermal analysis and optimization of IGBT power electronic module based on layout model.*, In 2016 17th International Conference on Electronic Packaging Technology (ICEPT), Wuhan, China, August, 2016..

## PATENTS

5. **H. Tang**, Y. Leung, G. Zhang, *A disinfection device for electrothermal acupuncture needles*, China, CN201821778571.8, Oct 2018.
4. **H. Tang**, J. Fan, H. Ye, M. Wang, X. Fan, G. Zhang, *A multifunctional gas sensitive dynamic test device*, China, CN201821778552.5, Oct 2018.
3. **H. Tang**, L. Li, G. Qi, T. Fang, J. Fan, C. Qian, M. Wang, X. Fan, G. Zhang, *An efficient and stable ultraviolet purification system*, China, CN201721430713.7, Nov 2017.
2. **H. Tang**, C. Qian, H. Ye, M. Wang, X. Fan, G. Zhang, *A platform for testing material light-heat conversion efficiency*, China, CN201620957676.4, Aug 2016.
1. **H. Tang**, Y. Leung, G. Zhang, *Temperature measuring system for flexible display device*, China, CN201521129270.9, Dec 2015.